I

CHANNELING STUDIES OF SILICON INTERFACES

II

DIFFUSION BARRIER PROPERTIES OF TITANIUM NITRIDE

Thesis by

Woontong Nathan Cheung

In Partial Fulfillment of the Requirements

for the Degree of

Doctor of Philosophy

California Institute of Technology

Pasadena, California

1980

(Submitted May 12, 1980)

ACKNOWLEDGEMENTS

It gives me great pleasure to express my gratitude to members of the Caltech ion-beam group for providing the stimulative environment which has made this research possible. I gratefully acknowledge Professors James W. Mayer and Marc-Aurele Nicolet for their guidance, encouragement and suggestions throughout this work. I would like to thank Dr. Silvanus Lau for his friendship and many strenuous badminton games. It has been my pleasure to collaborate with Drs. Hermann von Seefeld and Martti Mäenpää on the titanium nitride project and Paula Grunthaner in the study of Si interfaces. Technical support of Rob Gorris, Rouel Fernandez and Jeff Mallory and moral support of Michell Parks are also appreciated.

I would like to thank Amy C. Ng for her expert assistance in SEM and EDAX analysis. I also thank Professors T. Vreeland, Jr. and W. L. Johnson for access to their X-ray diffraction equipments.

Special thanks are due to members of Dept. 1131 of Bell Telephone Laboratories, Murray Hill, New Jersey, for their hospitality during my stay as a resident visitor. I would like to thank Dr. Len Feldman for his contributions to my understanding of ion channeling. I enjoyed the collaborations

with R. J. Culbertson, P. J. Silverman and I. Stensgaard. I also thank Dr. Walter Brown for his encouragement and helpful discussions. The TEM work of T. T. Sheng is gratefully acknowledged.

Thanks also go to Drs. Peter Iles and Frank Ho of Applied Solar Energy Corporation, City of Industry, California, for their interest in solar cell metallization schemes. Their co-operation has benefited our understanding of the diffusion barrier properties of titanium nitride.

The author is indebted to the Office of Naval Research, the Department of Energy and Bell Telephone Laboratories for their financial support of this research.

ABSTRACT

PART I

The channeling effect of MeV ions in crystalline materials has been applied to study the interfaces of metals, silicides and oxides with single-crystal Si substrates. The study was facilitated by the development of thin (1500-5000Å) Si crystals which enabled channeled ions to probe the interfacial region without first traversing the metal or silicide layers. These investigations revealed that a reaction occurs between the silicon and as-deposited metal layers. For the Ni-Si system, about three monolayers of Ni penetrate into Si and occupy interstitial sites. An interfacial layer is also found between silicides and Si. In contrast, an abrupt interface is found between SiO_2 and Si.

With conventional channeling techniques, the ion beam traverses first the overlayer and then the Si substrate. A Si peak is observed in the energy spectrum and the area of the peak can be converted to Si atoms/cm^2 from known Rutherford scattering cross-sections. The Si peak corresponds to the first few monolayers of crystalline Si (the "surface peak"), the non-registered Si at the interface and the amount of Si in the silicide or oxide. From recent theoretical and experimental studies on surfaces, the surface peak contribution can be accurately predicted.

Using different overlayer thicknesses, the stoichiometry of silicides and oxides and the interfacial disordered Si can be determined. In the case of metal-Si interfaces, the

interfacial reactivity can be monitored by measuring the amount of non-registered Si at the interface. However, the conventional channeling technique is applicable only when the multiple scattering of the incident beam by the overlayer is small (i.e. thin overlayers and low atomic number elements).

Additional information on the nature of the interfacial disordered Si can be obtained by the thin-crystal channeling technique which involves the use of thin (<1μm), self-supporting Si crystals. With the ions first traversing the Si thin crystal along a channeling direction, the channeled ions are steered away from the atomic rows. At the interfacial region, the channeled ions only interact with the interfacial Si atoms which are displaced ≳0.7Å laterally from the atomic rows. There is no contribution from the first few crystalline Si layers to the measured Si peak; as there is in the case of conventional channeling. The combination of both conventional and thin-crystal channeling techniques provides further information about the interfacial disorder because of the different sensitivities of the two techniques to lateral displacements. Thin-crystal channeling has also been used to locate the relative position of foreign atoms with respect to the Si lattice near the interfacial region. This technique requires angular scan experiments along various axial and planar channeling directions.

For metal-Si interfaces, channeling results show that an interfacial reaction is initiated at room temperature with as-deposited metal layers (Ni, Pd, Cr, V and Au); Ag is the only

exception. With the Ni-Si system, the interfacial reaction can be greatly reduced by cooling the substrate to $170^{\circ}K$ during Ni deposition and ion beam analysis. The temperature dependence of the interfacial reactivity emphasizes the kinetic nature of the metal-Si interfaces and the importance of interfacial studies at low temperatures for meaningful comparison with abrupt metal-semiconductor interface models. The amount of disordered interfacial Si is observed to be high for metals which are dominant diffusion species in silicide formation (e.g. Ni and Pd). A lattice location experiment on the Ni-Si interface shows that $\sim$3 monolayers of Ni atoms are situated interstitially at the tetrahedral sites of crystalline Si. This observation supports the interstitial diffusion model which was proposed by Tu to explain the low-temperature formation of silicides.

Interfaces between Si and Pd_2Si, Ni_2Si, NiSi or $NiSi_2$ have also been investigated by thin-crystal channeling. The Ni_2Si-Si interface shows $\sim 4 \times 10^{16}$ atoms/cm^2 of excess Si above an "ideal" Ni_2Si-Si interface. The other silicide-Si interfaces all show disordered interfacial Si of $< 8 \times 10^{15}$ atoms/cm^2. The amount of interfacial disorder correlates with the transformation temperature for the next stable silicide phase. For example, the Ni_2Si phase (which exhibits the highest interfacial disorder) transforms to NiSi at $\sim 350^{\circ}C$. In contrast, the other silicide phases, Pd_2Si and NiSi, require a much higher transformation temperature ($\sim 700^{\circ}C$).

The SiO_2-Si interface has been studied by both conventional and thin-crystal channeling. The results show that thermally

grown oxides on (110)Si are stoichiometric SiO_2 at least down to a thickness of 4Å. By comparing the channeling data with predictions based on a various number of reconstructed Si layers, an abrupt SiO_2-Si interface is deduced with 2 monolayers of the Si single crystal being reconstructed at the interface.

PART II

This part of the thesis is concerned with the deposition and evaluation of titanium nitride (TiN) layers as diffusion barriers in contact metallization on Si devices. The application of TiN to Si solar cell contacts (i.e., the TiN-Ti-Ag metallization scheme) has been demonstrated to withstand a 600°C, 10 min anneal without degrading the cell's performance.

Titanium nitride films have been prepared by reactive sputtering of Ti in a nitrogen plasma. The nitride films are identified by TEM and X-ray diffraction to have the NaCl structure with a lattice parameter of 4.24 ± 0.02Å. Electrical properties and atomic composition of the films have been studied as a function of sputtering RF power (500-1500 W) and nitrogen pressure (3-100 mT). Backscattering analysis shows that the films have a composition close to stoichiometric TiN but with a slight tendency for higher nitrogen content. Oxygen is the major contaminant in the nitride films. The oxygen content strongly depends on the sputtering parameters and a high oxygen content corresponds to high electrical resistivity of the TiN films. The lowest resistivity ($\sim 170 \mu\Omega$-cm) is obtained by

sputtering with high RF power and low nitrogen pressure.

The effectiveness of titanium nitride films as a diffusion barrier between various metals and single-crystal Si substrate or Ti on single-crystal Si substrate is investigated by backscattering spectrometry, SEM and EDAX. The temperature range of interest is from 400°C to 700°C. Various metals of high electrical conductivity such as Au, Ag, Al, Cu and Pd are used as the top metal layer. By interposing a thin layer of TiN ($\lesssim$ 1000 Å) between the metal and substrate, the failure temperature (i.e., the temperature at which metal-substrate interdiffusion becomes significant) can be greatly increased. The failure temperature of the TiN layers as a diffusion barrier is related to the metal-silicon eutectic temperature. SEM studies show that the interdiffused layer is laterally non-uniform and is initiated at isolated spots across the sample's surface. It is believed that grain boundaries or pinholes in the TiN films are the weak links in the diffusion barrier properties of TiN.

As an application for high-temperature diffusion barriers, the Ag-Ti-TiN metallization scheme has been tested on shallow-junction ($\sim$2000A) Si solar cells. The conventional Ti-Pd-Ag metallization scheme has been shown to fail after a 600°C, 10 min anneal which is required for a glass encapsulation process. With the TiN-Ti-Ag scheme, no degradation of cell performance can be observed after the 600°C, 10 min anneal if the TiN layer is $\gtrsim$1500Å.

TABLE OF CONTENTS

	Page
Acknowledgments	ii
Abstract	iv
Table of Contents	ix
PART I: CHANNELING STUDIES OF SILICON INTERFACES	1
Chapter 1 Introduction	2
References to Chapter 1	9
Chapter 2 Channeling Analysis of Interfaces	11
2.1 The Surface Peak	11
2.2 Conventional Channeling - Thin Overlayers	16
2.2.1 Introduction	16
2.2.2 Multiple Scattering	18
2.3 Thin-Crystal Channeling	21
2.3.1 Introduction	21
2.3.2 Transmission Geometry	24
2.3.3 Backscattering Geometry	26
2.3.4 Transmission versus Backscattering Geometry	27
2.3.5 Comparison between Conventional and Thin-Crystal Channeling.	29
2.4 Lattice Location Experiment of Interfaces by Thin-Crystal Channeling	30
2.5 Effects of Ion Beam Dose and Current on Channeling Analysis	33
References to Chapter 2	48

Page

Chapter 3 Metal-Silicon Interfaces 51

3.1 The Ni-Si Interface-an UHV Experiment 51

3.2 Other Metal-Si Interfaces 59

3.2.1 Conventional Channeling 59

3.2.2 Thin-Crystal Channeling 66

3.2.3 The Ag-Si Interface 67

3.3 Lattice Location Experiment of the Ni-Si Interface 68

References to Chapter 3 99

Chapter 4 Silicide-Silicon Interfaces 102

4.1 The Pd_2Si-Si Interface 102

4.2 The Ni_2Si-Si Interface 108

4.3 The NiSi-Si Interface 111

4.4 The $NiSi_2$-Si Interface 112

4.5 Summary 117

References to Chapter 4 131

Chapter 5 The SiO_2-Si Interface 134

References to Chapter 5 149

Appendix 1 Preparation of Large-Area Monocrystalline Silicon Thin Windows. 150

A1.1 Introduction 150

A1.2 Experimental 151

A1.3 Characterization of Si Thin Crystals 155

A1.4 Discussion 158

References to Appendix 1 167

	Page
Appendix 2 Characterization of Si Surfaces Cleaned by Hydrofluoric Acid	168
A2.1 Introduction	168
A2.2 Nuclear Resonance Techniques	169
A2.3 X-ray Photoemission Spectroscopy	172
References to Appendix 2	177
PART II: DIFFUSION BARRIER PROPERTIES OF TITANIUM NITRIDE	178
Chapter 1 Introduction	179
References to Chapter 1	185
Chapter 2 Preparation and Characterization of Titanium Nitride Films	188
2.1 Experimental	188
2.2 Results and Discussion	190
2.3 Summary	194
References to Chapter 2	201
Chapter 3 Titanium Nitride as a Diffusion Barrier in Metallization Schemes for Silicon	202
3.1 Sample Preparation and Analytical Techniques	202
3.2 Results	205
3.2.1 Silver	205
3.2.2 Gold	206
3.2.3 Aluminum	208
3.2.4 Copper	209
3.2.5 Palladium	209
3.3 Discussion	210
References to Chapter 3	229

Page

Chapter 4 Application of Titanium Nitride To Si Solar Cell Metallization Schemes 230

4.1 Introduction 230

4.2 Thermal Instability of the Ti-Pd-Ag System 232

4.3 TiN as a Diffusion Barrier on Si Solar Cells. 235

References to Chapter 4 248

PART I

CHANNELING STUDIES OF SILICON INTERFACES

CHAPTER 1
INTRODUCTION

The structure of the interface between a semiconductor and a metal or oxide layer has long been a subject of experimental challenge. Modern electronic or optical spectroscopic techniques can in principle provide such structural information, but the data extraction is generally formidable and often requires theoretical assumptions. In view of the relevance of such structural information for the understanding of Schottky barrier heights and for theoretical calculations on interfaces, numerous techniques such as LEED, Auger, XPS, UPS, ion-channeling, ellipsometry, and cross-sectional TEM have been applied to the study of such interfaces[1-10]. Recently, such studies have revealed that interfaces between metals and semiconductors such as Si, GaSb, InP, and GaAs are chemically reactive even at room temperatures and that the interfaces are far from being abrupt as modeled by various theoretical studies. Instead, an interfacial layer of different composition from the pure metal and semiconductor components has been verified. On the other hand, Si interfaces with SiO_2 and some epitaxial silicides are almost atomically abrupt. The chemical and physical properties of the interface are not yet well understood and fundamental questions such as the variation of stoichiometry

and chemical bonding schemes across the interfacial region are still under current investigation.

The biggest advantage of electron spectroscopic methods is that they provide chemical states information about the interfacial atoms. Because most electron spectroscopic techniques are limited by the electron escape depth (5-20Å), several approaches have been taken to bring the interface towards the surface until the interfacial region is within the examination depth. One technique is to remove the topmost material by ion-milling and to monitor the interfacial signal as the surface approaches the interface. The limit in depth resolution is about 20 to 50Å and is set by atomic mixing and enhanced diffusion within the collision cascade volume around the sputtering ion track[11]. Depending on the sputtering ion and the substrate material, the depth penetration of ions can be greater than the analysis depth of most surface sensitive analytical techniques. In this case the signal obtained is no longer representative of an unperturbed interface. Alternatively, the interface can be created by sequential deposition of submonolayers of the overlayer. This type of experiment is very useful to study interfacial reactivity of the first few monolayers of deposited materials. With the build-up of a thicker over-layer, the interfacial signal will fade out exponentially as a function of the layer thickness. Hence, there is no assurance that the interface created for the first few

monolayers is the same as for a much thicker overlayer.

Another method, a dynamical approach, has also been used to study the silicide-silicon and silicide-metal interfaces by XPS[5]. The concept is to monitor the interfacial signal as the interface approaches the surface during the silicide formation. Using this technique, Grunthaner and Mayer have been able to conclude that the metal-silicide interface is richer in metal content while the silicide-silicon interface is richer in silicon content. Interfacial widths of the two interfaces can also be estimated from electron escape depths.

As for in-situ interfacial studies, optical and MeV ion backscattering techniques are most promising for probing the interface. The optical studies generally require detailed information of the dielectric functions over a certain range of optical frequencies. This knowledge is available for most elements or compounds but not for materials of variable composition such as exist in an interfacial region. However, with more optical data becoming available, the optical technique can be very useful for interfacial studies. With ion backscattering, the advantage is that it is a quantitative method because the scattering cross-sections in the Rutherford regime are well characterized. Using normal backscattering techniques with a scattering angle of 170°, the depth resolution is on the order of 200Å. This limit is set at shallow depths (<1000Å) by the energy-resolution

of the solid-state detector (∿16 keV) and at deeper depths by energy straggling in the ion energy loss processes as the particles traverse the solid. The depth resolution near the surface can be improved to ∿50Å by lengthening the effective ion beam path using glancing angle beam incidence (i.e., tilting the sample) or beam exit (i.e., movable detector) geometries. However, the 50Å depth resolution is still inadequate for most interfacial studies because of signal overlapping from the substrate and the overlayer.

We have improved the ion backscattering technique by making use of the channeling effect of MeV ions in crystalline substrates. When the ion beam is aligned along a low index crystallographic direction, a majority of the ions will have insufficient transverse momentum to penetrate the potential barriers formed by the atom rows or planes of the crystals. Consequently, close impact parameter collisions are greatly reduced with a resultant lowering of the scattering yield from the substrate atoms. In addition, the spatial distribution of the channeled ions is strongly enhanced near the center of channels because of the steering force by the atomic potentials. This "flux-peaking" effect can be utilized to probe atoms which have large lateral displacements (∿0.7Å) from the atomic rows of the crystalline matrix. The channeled ions can also be distinguished from the dechanneled ions by their lower energy losses. This difference in energy permits signal separation between the

interfacial non-registered atoms and the crystalline atoms.

Since the channeling phenomenon is best used in single-crystal materials, the technique is applicable only for crystalline substrates if polycrystalline or amorphous over-layers are used, or for crystal-crystal interfaces with an epitaxial layer on top of a crystal.

In this study, we have chosen Si crystals as the substrate and various metals, silicides, and SiO_2 as the overlayer material. The questions we are trying to answer are the interfacial reactivity, overlayer stoichiometry as well as the deviation of the interfacial structure from an "ideal" interface. An "ideal" interface is based on a hypothetical model with the overlayer in direct contact with an abrupt termination of a bulk-like Si surface.

Two types of channeling experiments have been performed in this interfacial study. The first type of measurement is a probe of the interface with the beam first traversing the overlayer and then the Si substrate. As a contrast to the second technique, we shall call it "conventional channeling" because the experiment can be performed on Si substrates of any thickness. Some of the early interfacial studies by channeling using this technique can be found in the work by Bogh[12] on the Ag-Au interface and the work by Chu et al.[13] on the Si-SiO_2 interface. Interpretation of the data at that time was inconclusive because of a lack of understanding on the scattering mechanism due to the first

few surface atoms. With recent interest in the structure of surfaces, the surface peak contribution has been calculated from Monte Carlo methods for a wide range of experimental conditions and the calculated values are in reasonable agreement with experiments[14]. Using the surface studies as a basis, the amount of interfacial disordered Si can be reliably deduced. The disadvantage of conventional channeling is that it is applicable only for thin polycrystalline or amorphous layers (<200Å). Due to multiple scattering in thicker films, a significant portion of the ions can get dechanneled as they enter the Si crystal. The uncertainty in background subtraction becomes the biggest source of error in determining the interfacial disorder.

To circumvent the multiple scattering effect, another channeling technique involves the use of thin Si crystalline substrates with thicknesses less than 1μm (i.e., "thin-crystal channeling"). With the ion beam first traversing the Si crystal in a channeling direction and then the overlayer, the interfacial region can be probed because of the great reduction of the Si substrate signal. The ion beam flux distribution is modified in channeling through such thin crystals so that the beam at the interface scatters primarily from atoms with large displacements from the atomic strings. The scattering spectrum from the exit surface therefore displays a peak which represents only those channeled ions which have been scattered from Si atoms in the overlayer and

from sufficiently displaced atoms in the non-registered layers of the substrate.

The channeling geometries and analytical approach are described in Chapter 2. Applications of the channeling technique are described in the following chapters: Chapter 3 describes the metal-Si interfaces, Chapter 4 the silicide-Si interfaces, and Chapter 5 the SiO_2-Si interface.

References

1. J. L. Freeouf, G. W. Rubloff, P. S. Ho, and T. S. Kuan, Phys. Rev. Lett., 43, 1836 (1979).
2. W. E. Spicer, J. Lindau, P. Skeath, C. Y. Su, and P. Chye, Phys. Rev. Lett., 44, 420 (1980).
3. J. N. Miller, S. A. Schwarz, J. Lindau, W. E. Spicer, B. DeMichelis, J. Abbati, and L. Braicovich, Proceedings of the Seventh Annual Conference on the Physics of Compound Semiconductor Interfaces, Estes Park, Colorado, 1980.
4. L. Braicovich, J. Abbati, G. Ottaviani, J. N. Miller, S. Schwarz, P. R. Skeath, C. Y. Su, C. R. Helms, J. Lindau, and W. E. Spicer, Proceedings of the Seventh Annual Conference on the Physics of Compound Semiconductor Interfaces, Estes Park, Colorado, 1980.
5. P. Grunthaner and J. W. Mayer, Proceedings of the Seventh Annual Conference on the Physics of Compound Semiconductor Interfaces, Estes Park, Colorado, 1980.
6. N. W. Cheung, R. J. Culbertson, L. C. Feldman, P. J. Silverman, K. W. West, and J. W. Mayer, submitted to Phys. Rev. Lett.
7. D. E. Aspnes and J. B. Theeten, Phys. Rev. Lett., 43, 1046 (1979).
8. O. L. Krivanek, D. C. Tsui, T. T. Sheng, and A. Kamgar, in Proceedings of International Conference of the Physics of SiO_2 and its Interfaces, edited by S. T. Pantelides

(Pergamon Press, New York, 1978), p. 356.

9. K. C. R. Chiu, J. M. Poate, L. C. Feldman, and C. J. Doherty, to be published in Appl. Phys. Lett.

10. A. Ishizaka and S. Iwata, Appl. Phys. Lett., 36, 71 (1980).

11. Z. L. Liau, Ph.D. Thesis, California Institute of Technology (1979).

12. E. Bogh, in Channeling-Theory, Observation and Applications, edited by D. V. Morgan (Wiley-Interscience, New York, 1973), p. 435.

13. W. K. Chu, E. Lugujjo, J. W. Mayer, and T. W. Sigmon, Thin Solid Films, 19, 329 (1973).

14. L. C. Feldman, to be published in Surface Science: Recent Progress and Perspectives, CRC Press (1979).

CHAPTER 2

CHANNELING ANALYSIS OF INTERFACES

2.1 The Surface Peak

When a well-collimated beam of MeV light ions is aligned with the major crystallographic axes of a single crystal, it experiences scattering potentials from strings of atoms rather than random scattering centers as in the non-aligned case. If the incident beam flux distribution is uniform, only a few percent of the beam will be deflected by the surface atoms of the crystal by more than 1-2° because the Rutherford scattering mechanism requires an impact parameter of $\lesssim 0.1$Å for such angular deflections. For the majority of the incident ions which have impact parameters larger than 0.1Å, the deflection angle is negligible. As they enter the crystalline matrix, they will be steered into stable orbits by a continuum potential constituted by the parallel strings of atoms. Except for non-ideal effects such as thermal vibrations or crystal defects, the channeled particles will have a low probability of encountering small impact parameter scattering events with the strings of atoms.

The resultant scattering yields of the ions can be reduced to several percent of the random incidence value, depending on details of the crystal structure.

One feature of channeling which has aroused recent interest is the scattering yield contributed by the topmost atoms of the atomic strings as the beam encounters the crystal's surface. The structure of crystal surfaces can be determined by simple geometric arguments using the channeling technique. For the ease of discussion, we will just consider a two-atom model to illustrate the basic concepts. In Fig. 1, the scattering atom is taken to be the topmost atom on the crystal's surface and the second atom is the next nearest neighbor along the atomic string below the surface. The atoms are assumed to be static and the effect of thermal vibrations will be discussed in the later part of this section.

When a uniform beam of ions parallel to the string of atoms encounters the first atom at various impact parameters r, different angular deflections θ will result. For MeV ^4He ions, the scattering potential is roughly Coulombic and for small angular deflections, the scattering angle θ is given by:

$$\theta = \frac{Z_1 Z_2 e^2}{Er} \qquad (1)$$

where Z_1 is the atomic number of the incident ion, Z_2 is the atomic number of the scattering atom, e^2 is the square of the electronic charge (= 14.4 eV-Å), E is the energy of

the incident ion in eV and r is the impact parameter in Å. After the first scattering event, the beam's original direction will be deflected and at the position of the second atom, d, the scattering ions will be at a distance R from the atomic string. The relationship between R and r is given by:

$$R = r + \theta d$$

$$= r + \frac{Z_1 Z_2 e^2 d}{Er} \qquad (2)$$

From equation (2), it is easy to see that R has a minimum value of $R_m = 2(Z_1 Z_2 e^2 d/E)^{1/2}$ for $r = (Z_1 Z_2 e^2 d/E)^{1/2}$. For the cylindrical symmetry of Fig. 1, all the scattered ions will lie outside a cone with a half-angle of $2(Z_1 Z_2 e^2/Ed)^{1/2}$. Using an optical analogy, the second atom is "shadowed" by the first atom of the string from the ion beam and so will be the third, fourth atoms, etc. This phenomenon is generally referred to as the "shadowing effect" in the channeling literature.

To give an order of magnitude for R_m, let us consider the case of 1 MeV ^{4}He ions incident along the <100> axis of Si ($Z_2 = 14$). For a d value of 5.43 Å, R_m is equal to 0.094Å. In contrast, R_m for the <100> axis of W ($Z_2 = 74$ and d = 3.16Å) is equal to 0.164Å. Thus, the shadowing effect strongly favors high Z scattering elements. In the static approximation, the dominant contributions of

scattered ion yield will come from the first atom of each atomic string.

As an application for the analysis of surface structures: if the first atom has a lateral displacement x from the original position, the shadowing of the second atom will no longer be perfect and higher scattering yields of the ions will be measured from experiments. For x larger than R_m, the second atom will lie outside the shadow cone and the extra scattering yield will correspond to one atom/string. Since R_m can be varied by changing the incident beam energy ($R_m \propto 1/\sqrt{E}$), the value of x can be determined accurately from first principles. By combining measurements of normal and off-normal directions, this technique has been used to study the reconstruction and relaxation of Pt (111),[1] W (100),[2] Si (100)[3] and (111)[4] surfaces as well as other absorbate-induced surface structures.[5-7]

In the static approximation, the lattice vibration of the atoms is being ignored and must be properly accounted for in quantitative measurements. For most crystals, the root-mean-square vibrational amplitude, ρ, perpendicular to the atomic rows can be from 0.05Å to 0.2Å and is comparable with the shadow cone radius R_m. This implies the two-atom model described previously has to be modified by a function of the scaling parameter ρ/R_m. Moreover, a more realistic scattering potential is the Thomas-Fermi potential rather

than the pure Coulombic potential. All these complications have made an analytical solution to the surface peak contribution formidable and quantitative results are obtained from Monte Carlo simulations. Results of these calculations on "ideal" surfaces (i.e. the surface treated as an abrupt termination of the bulk) have been published by Stensgaard et al.[8] and details of the method have been outlined in the monograph by Feldman.[9] In their findings, the surface peak intensity can be expressed as a function of one scaling parameter ρ/R_m over a wide range of ion-target combinations. The Monte Carlo results are in good agreement with the experimental results and show the correct energy dependence of the incident ion energy.

As will be discussed in the next section, the concept of the surface peak is intimately related to the channeling study of interfaces with crystalline substrates. Similar to the surface studies, the definition of a "perfect" Si interface is an abrupt termination of the bulk-like Si crystalline matrix and channeling measurements can show the deviation of the interfacial Si atoms from such an idealized structure. In Table 1, we have tabulated the Monte Carlo simulation results for Si along various channeling axes using ^{4}He ions in the 1 to 2 MeV energy range. The ρ/R_m ratio varies between 1.2 to 2, indicating incomplete shadowing. Hence, the surface peak contribution greatly exceeds the value of the perfect shadowing case of 1 atom/row.

As for the experimental determination of the surface peak, the scattering yield due to the first few atomic layers will show up as a peak in the energy spectrum of the backscattering-channeling measurements. Examples of these spectra will be given in the subsequent chapters on various Si interfaces. The number of counts under the peak (Y_{SP}) can be converted to atomic areal density (N_{SP}) by:

$$Y_{SP} = \frac{d\sigma}{d\Omega} \cdot \Delta\Omega \cdot Q \cdot N_{SP} \qquad (3)$$

where $(d\sigma/d\Omega)$ is the differential scattering cross-section of the target, $\Delta\Omega$ is the detector solid-angle and Q is the number of incident ions.

Alternatively, N_{SP} can also be derived by comparing the yield of the surface peak to that of a calibrated standard whose atomic areal density ($N_{Standard}$) is known. For an equal number of incident ions, N_{SP} can be calculated from:

$$\frac{Y_{SP}}{Y_{Standard}} = \frac{(d\sigma/d\Omega)}{(d\sigma/d\Omega)_{Standard}} \cdot \frac{N_{SP}}{N_{Standard}} \qquad (4)$$

2.2 Conventional Channeling - Thin Overlayers

2.2.1 Introduction

The application of channeling to the study of interfaces is a natural extension of the various experiments on absorbate induced surface reconstruction. The experimental quantity being measured is the surface peak (or more

appropriately, the "interface" peak) of the crystalline substrate. The main advantage of ion scattering over other spectroscopic techniques such as Auger, UPS, XPS is that it gives quantitative determination of the number of foreign atoms as well as the number of non-registered substrate atoms, as represented by the interface peak of the channeled spectrum. The origin of the non-registered substrate atoms can be due to substrate reconstruction, formation of non-epitaxial compounds, interfacial mixing or interfacial strain caused by the lattice mismatch between the overlayer and the substrate. Structural information of the interface can be obtained for monolayer and sub-monolayer coverage of foreign atoms by making use of the shadowing effect.[7] For thicker overlayers, details of the interfacial structure can also be studied if it is a high-quality epitaxial layer such as $NiSi_2$ on Si[10] or MBE-grown superlattices.[11] In this section, a method is presented for the study of interfaces with a polycrystalline or amorphous overlayer. These are the most frequently encountered cases in thin-film studies.

In the past, the effect of overlayers on channeling has only been investigated as a function of dechanneling and channeling minimum yields.[12] Information on the interfacial disorder has always been disregarded because of background subtraction problems when solid-state detectors are used. Using an electrostatic energy analyser, Bogh[13]

has studied thin layers of Ag on Au crystals. A background subtraction procedure based on sample tilting (∿0.2°) has also been used by Chu et al.[14] to study the Si-SiO_2 interface. Since the dependence of the surface peak on the angle of beam incidence is still unclear at this point, the latter procedure should be used with caution.

The best method of measuring the surface peak is to place the solid-state detector at a grazing-exit geometry (Fig. 2). By lengthening the outcoming path of the scattered ions, the scattering yields due to atoms underneath the surface can be greatly reduced for a fixed detector energy resolution (∿16 keV). With the reduced background, channeling analysis of the interfacial disorder becomes a relatively easy measurement. In Fig. 2, the dotted area in the energy spectrum represents the surface peak of Si without any overlayer. The shaded area denotes the increase of the interfacial disorder due to the presence of the overlayer X.

One major handicap of conventional channeling is due to the divergence of the beam caused by multiple scattering in the overlayer. This divergence is negligible in interfacial analysis only for overlayers <50Å. The divergence imposes more stringent restrictions on interface analysis for overlayers with high atomic number elements such as Au or Pt.

2.2.2 Multiple Scattering

After the ion beam first traverses the overlayer, the angular divergence can be appreciable when compared with

the channeling half-angle ($\psi_{1/2}$) of the crystalline substrate. The divergent beam will enhance the scattering probability of the first few atoms of the atomic strings because the axis of the shadow cone is no longer collinear with the axis of the atomic strings. In addition, those ions with a divergence angle larger than $\psi_{1/2}$ will be dechanneled and contribute a higher background to signals of the crystalline matrix. These two effects will both contribute to an increase in measured surface peak values. Thus, the magnitude of multiple scattering sets an upper limit on the number of overlayer atoms which can be used with the conventional channeling technique.

The angular distribution of a well-collimated beam after traversing a thin layer of randomly distributed scattering centers has been calculated by L. Meyer,[15] using scattering cross-sections derived from classical collisions. In Meyer's treatment, the angular distributions are characterized by two dimensionless parameters: the reduced thickness τ and the reduced scattering angle $\tilde{\theta}$. The reduced thickness τ is given by:

$$\tau = \pi a^2 N t \tag{5}$$

where a is the Thomas-Fermi screening radius $= 0.46(Z_1^{2/3} + Z_2^{2/3})^{-1/2}$ Å, N is the atomic density of target atoms and t is the thickness of the target layer. Physically, τ represents the total scattering probability of

incident ions traversing the layer of target atoms with thickness t. The reduced scattering angle $\tilde{\theta}$ is the actual scattering angle θ normalized by a characteristic scattering angle $(2Z_1Z_2e^2/Ea)$.

Using successive convolution procedures to keep track of multiple scattering, the angular distribution of the emerging beam $F(\tilde{\theta})$ is given by:

$$F(\tilde{\theta})\ d\omega = \frac{d\omega}{2\pi}\left(\frac{aE}{2Z_1Z_2e^2}\right)^2\left[f_1\left(\tau,\tilde{\theta}\right) - \frac{a^2}{r_o^2}\ f_2\left(\tau,\tilde{\theta}\right)\right] \qquad (6)$$

where $d\omega$ is the differential scattering solid-angle and r_o is half the nearest neighbor distance of target atoms. The f_1 and f_2 functions which determine the angular profile of the emerging beam have been tabulated by Meyer. Since r_o ($\sim$1Å) is much larger than a ($\sim$0.1Å) and f_1 and f_2 are of the same order of magnitude, the f_2 term contribution can usually be dropped in equation (6) for first order approximations. In Fig. 3, we have plotted the angular distribution $F(\tilde{\theta})$ for various τ values with the value of $F(\tilde{\theta} = 0)$ normalized to unity. For τ values between 0.2 to 2, the $F(\tilde{\theta})$ distribution is approximately Gaussian and the angular width can be characterized by $\tilde{\theta}_{1/2}$ which is the $\tilde{\theta}$ value at half the height of $F(\tilde{\theta})$. The dependence of $\tilde{\theta}_{1/2}$ on τ is shown in Fig. 4 and the conversion factors of the reduced thickness τ and reduced scattering angle $\tilde{\theta}$ for some of the elements are listed in Table 2.

To minimize the effect of multiple scattering on the surface peak contribution, it is important to restrict the overlayer thickness such that $\theta_{1/2}$ is less than the beam's original half divergence angle (∿0.03°). Alternatively, if thick overlayers have to be used, the surface peak measurements can be compared with a well-characterized interface which has an overlayer of approximately the same $\theta_{1/2}$. Such an approach has been taken in the study of metal-Si interfaces by using the Ge-Si interface as a reference.

2.3 Thin-Crystal Channeling

2.3.1 Introduction

For ion channeling in thin-crystal experiments 95% of the ions will have a higher energy than the remaining 5% of the beam after they traverse the thin crystal. The higher energy component consists of the channeled ions which experience a lower stopping power $\left(\frac{dE}{dx}\bigg|_C\right)$ because of the absence of close-encounter scattering events. The lower energy component consists of dechanneled ions which have stopping powers equal to the random incidence value $\left(\frac{dE}{dx}\bigg|_R\right)$. The ratios between the channeled and random stopping powers for ^4He ions transmitted through Si thin crystals have been measured by Eisen et al.(16) for various channeling directions. For example, the ratios are equal to 0.55 and 0.7 for 2 MeV ^4He ions along the <110> and <111> channeling axes respectively and the ratios increase slightly for

energies around 1 MeV. There are no data available from Eisen's work on the Si <100> axis; our determination on the Si <100> axis gives a ratio of 0.7 to 0.75 for 2 MeV ^{4}He ions. This value was obtained by depositing a thin layer of Au at the exit surface of a Si (100) thin crystal (∿5000Å) and measuring the energy positions of the Au signal for both channeled and random directions. Since the kinematic factor of Au and the Si thickness are known, the ratio of the two stopping powers can be determined.

The lateral distributions of the channeled and random components are also dissimilar. For the random component, the lateral distribution of the beam is uniform across the crystal channels. In contrast, the channeled ions, which have been steered away from the atomic rows by the continuum potential, are strongly peaked around the middle of the crystal channels. This phenomenon is called "flux-peaking"(17) and is the unique property of channeling that makes the technique useful for locating preferential sites of impurity atoms in crystalline substrates. For a scattering center (i.e. impurity atom or displaced atom of the substrate) located at the middle of the crystal channel, its scattering probability can be 50% higher than the random incidence values. Conversely, if the scattering center has lateral displacements $\lesssim 0.7$Å from the atomic rows, negligible scattering yields can be observed from the channeled ions.

In the thin-crystal channeling experiment, the concept is to establish the flux-peaking effect (which requires the beam to traverse ∿1000Å into the crystal) before the beam interacts with the interfacial region located at the exit side of the thin crystal (Fig. 5). Since the thin crystal has two free surfaces, an interface can be created by transforming one surface into an oxide or silicide layer. Alternatively one can deposit an overlayer of material onto the Si surface.

The number of displaced Si atoms at the interface can be measured by monitoring the interfacial Si yields with the detector in either the backscattering or transmission geometry (Fig. 5). The shaded areas of the Si interfacial signals correspond to the number of displaced Si atoms in the two geometries respectively. Unlike the conventional channeling technique where a surface peak is always observed even for a perfect crystal, the channeled ions (∿95% of the beam) will not see the first atoms of the interfacial crystalline Si because the ions are strongly peaked in the middle of the crystal channels. Consequently, for a "perfect" interface where the interfacial Si atoms are well-ordered, no Si peak will be observed in either of the spectra in Fig. 5.

The choice between the detector geometries is based on various experimental constraints such as differences in kinematic factors between the overlayer and Si and thickness

of the overlayers. Advantages and disadvantages of the two geometries are detailed in the following sections.

2.3.2 Transmission Geometry

One unique feature of the transmission geometry is the good energy separation between the disordered and crystalline signals at the interface. Since the former is contributed by the scattering of channeled ions, the signal is located at a slightly higher energy than the crystalline signal, which is contributed by the dechanneled ions. The energy separation, ΔE, between the two types of Si signals is given by the following equation:

$$\Delta E = K_{Si} t \left(\frac{dE}{dx}\bigg|_R - \frac{dE}{dx}\bigg|_C \right) \tag{7}$$

where K_{Si} is the kinematic factor of Si and t is the thickness of the Si thin crystal.

In Figure 6, the transmission spectrum is shown for a Si (110) crystal (5200Å) with ∿7Å of silicon dioxide at the exit surface. Since the oxide is amorphous, the area under the Si peak will include contributions from the Si atoms in the SiO_2 plus the disordered Si at the Si-SiO_2 interface. The lack of a perfect separation between the disordered and crystalline Si signals is caused by an energy spread in $dE/dx|_C$ associated with various channeling trajectories. The energy spectrum (scaled down by a factor of 40) of a random incidence beam is also included in the figure to

indicate the effect of $dE/dx|_R$. In the random incidence case, the interfacial disorder signal is merged with the signal of the crystalline matrix. The energy positions corresponding to the exit surface of the Si crystals are identical in both channeled and random directions. This verifies that the crystalline Si signal in the channeled spectrum is indeed contributed by the dechanneled component of the beam. By comparing the spectral height of the channeled and random signals, we have deduced that 3% of the beam is dechanneled for this particular case.

To verify the linear dependence of ΔE on the crystal thickness, a series of Si (110) thin crystals with thicknesses ranging from 0.36 to 2.3 microns were measured with the same transmission geometry, using 2 MeV ^{4}He ions. Experimentally, ΔE is defined to be the energy separation between the disorder peak and the mid-point at the rising edge of the crystalline signal (see Fig. 6). The energy separation ΔE is plotted against the crystal thicknesses in Figure 7 and a linear relationship is established. The zero-thickness intercept is ∿10 keV above zero and is below the energy resolution of the solid-state detector (∿16 keV). Thicker Si crystals can be used to achieve greater energy separations between the disordered and crystalline Si signals. In practice, for thin crystals whose thickness exceeds 1 micron, the dechanneling rates due to defects or thermal

vibrations always cause large energy spreads in $dE/dx|_C$ as well as an increase in the channeling minimum yield (χ_{min}) at the exit surface of the thin crystal. For MeV ^4He ions, the optimum thickness in the Si thin-crystal experiments was found to be around 5000Å.

The transmission geometry is usually used with a grazing-exit detector for greater depth resolution and higher mass separation in the scattering energy spectrum. For forward scattering angles ($\theta<90°$), the kinematic factors are less sensitive to differences in various elemental masses than the backscattering case ($\theta>90°$); the sensitivity deteriorates rapidly for smaller scattering angles.[17] This means the energy separation between the metal and Si signals is rather limited. To prevent signal overlap due to energy losses, the thickness of the overlayer has to be limited to <1000Å. The normal technique of preventing signal overlap is by reducing the outcoming path of the scattering ions ($\propto 1/\cos\theta$). This is not applicable here because reducing the scattering angle will also reduce the energy separation of the two signals. This limitation of using thin overlayers makes kinetic studies of silicide interfaces difficult because it is hard to control the silicide reaction such that only part of the thin metal overlayer is consumed.

2.3.3 Backscattering Geometry

The backscattering geometry is mainly used when the overlayer is thick and depth resolution is not of primary

concern. As shown in the schematics of Fig. 5, a grazing-exit detector cannot be used to enhance the depth resolution because the outgoing path of the scattered ions will be in excess of 2 microns. In general, a scattering angle of 170° is used for the detector with a resultant depth resolution of 200Å.

The energy separation argument between the disorder and crystalline Si signals still applies here. However, the energy of the disorder Si signal is at a higher energy in the backscattering geometry and is in the wrong direction for signal separation. In the energy spectrum, the disorder Si signal will be riding on top of the crystalline Si signal which complicates background subtraction procedures. For interfacial disorder signals which are smaller or comparable with the crystalline Si signal, a reliable quantification of the interfacial disorder is impractical.

2.3.4 Transmission versus Backscattering Geometry

For ion-scattering analysis of thin-films, there is a one-to-one correspondence between the detected energy of the scattered ions and the depth of scattering centers below the sample's surface. However, the depth scales of the backscattering and transmission geometries are different because the thickness of the thin film is involved in the calculation of energy losses in transmission geometry.

In Fig. 8, we show schematics of the two detection geometries and their corresponding energy spectra for an

elemental target. For simplicity, the surface energy approximation is used for the stopping power dE/dx and the incident ions are normal to the target's surface. Other variations such as oblique incidence angles and compound targets can also be handled by following the treatment of Chu et al.[18].

For backscattering analysis, the energy E_x of the scattered ion due to a scattering center located at a distance x from surface 1 is given by the well-known formula[18]:

$$E_x = K \left(E_o - x \cdot \left.\frac{dE}{dx}\right|_{E_o}\right) - \frac{x}{|\cos\,\theta|} \cdot \left.\frac{dE}{dx}\right|_{KE_o} \qquad (8)$$

with a corresponding energy loss factor S_{bs} :

$$S_{bs} \equiv - \frac{\Delta E_x}{\Delta x} = K \cdot \left.\frac{dE}{dx}\right|_{E_o} + \frac{1}{|\cos\,\theta|} \cdot \left.\frac{dE}{dx}\right|_{KE_o} \qquad (9)$$

The transmission geometry has a different E_x because the outcoming path for the scattered ion is equal to $(t-x)/|\cos\,\theta|$ instead of $x/|\cos\,\theta|$. Consequently, E_x is given by:

$$E_x = K \left(E_o - x \cdot \left.\frac{dE}{dx}\right|_{E_o}\right) - \frac{(t-x)}{|\cos\,\theta|} \cdot \left.\frac{dE}{dx}\right|_{KE_o} \qquad (10)$$

with the corresponding energy loss factor S_t:

$$S_t \equiv - \frac{\Delta E_x}{\Delta x} = K \cdot \left.\frac{dE}{dx}\right|_{E_o} - \frac{1}{|\cos\,\theta|} \cdot \left.\frac{dE}{dx}\right|_{KE_o} \qquad (11)$$

Since $dE/dx|_{KE_o}$ is larger than $dE/dx|_{E_o}$ for ^{4}He ions in the MeV energy range[19] and both $1/|\cos\theta|$ and K are larger and smaller than unity respectively, S_t will have negative values. This means that the transmission spectrum will have a reversed image to that of the backscattering spectrum as illustrated in Figs. 8(a) and 8(b). Moreover, if K and $1/|\cos\theta|$ have approximately the same values in both geometries such as in the grazing-exit detector case, the depth resolution of the transmission geometry will be inferior to that of the backscattering geometry.

2.3.5 Comparison between Conventional and Thin-Crystal Channeling

The combination of conventional and thin-crystal channeling measurements often gives information on the magnitude of the displacements for the non-registered interfacial atoms. One example will be discussed in the chapter on the Si-SiO_2 interface. As pointed out earlier, the sensitivity of conventional channeling to lateral displacements is ∿0.1 Å and is dictated by the shadow cone radius, R_m. For the thin-crystal channeling case, the flux-peaking effect enhances the ion beam distribution towards the center of the crystal channels and large lateral displacements (∿0.7 Å) are required to give a substantial scattering yield. The sensitivity differences between the two techniques have been calculated by Feldman et al.[20] and Picraux et al.[21]

for the Si <110> channeling direction with 1 MeV ^4He ions. The results are reproduced in Fig. 9. Curve (a) of Fig. 9 corresponds to Monte Carlo calculations of conventional channeling which shows the high sensitivity of the surface peak to small lateral displacements such as surface reconstruction. For displacements of the first surface atom larger than 0.15 Å, the surface peak will increase by an extra atom/row (∿ 2 monolayers for the Si (110) surface). For curve (b) of Fig. 9 which shows the surface peak for thin-crystal channeling, the sensitivity for small lateral displacements (<0.4Å) is rather low and the scattering yields become significant only after the lateral displacements exceed 0.8 Å. Since the shadow cone radius is inversely proportional to the square root of the ion energy while the transverse energy for channeling ($= E\psi^2 + U(r)$)[22] is independent of E for a well-aligned beam (i.e. $\psi=0$), curve (b) will be relatively energy independent whereas curve (a) will be more sensitive to smaller displacements at higher ion energies.

2.4 Lattice Location Experiment of Interfaces by Thin-Crystal Channeling

One important application of ion channeling is the direct determination of impurity locations in crystalline substrates. A concise review on the subject can be found in the paper by Picraux[23]. Briefly, the lattice location

experiment makes use of the flux-peaking effect and the ability to modify the flux distribution within the channels by tilting the crystalline substrate (i.e. angular scan measurements). By monitoring the scattering yields of the ions (or other ion-induced particles such as x-rays or nuclear-reaction products) as a function of the tilt angle, projection of the impurity position along the particular channeling direction can be deduced. To have an unambiguous determination of the lattice site, angular scan measurements along various non-coplanar channeling directions are often required. This procedure is referred to as the "triangulation" process. The main advantage of channeling over normal x-ray or neutron diffraction technique is that the latter gives only the periodicity of the impurity atoms whereas channeling gives the position of the impurities with respect to the crystalline matrix.

Since the establishment of flux-peaking at statistical equilibrium[24] requires the ions to traverse ∿1000 Å into the crystal, application of the lattice location technique for near-surface regions will not be feasible with bulk crystals. To circumvent this problem, a thin-crystal experiment can be devised so that the beam enters the thin crystal via the impurity-free surface, establishes flux-peaking and then impinges on the interfacial region at the exit surface of the thin crystal.

Such an experiment is illustrated in Fig. 10. First, an interfacial region is created on one side of the thin crystal by deposition of foreign atoms or formation of silicides, oxides, etc. With the free Si surface facing the beam, angular scan measurements are taken on both the Si and foreign atom scattering yields. For foreign atoms with zero lateral displacements from the atoms rows, the angular scan curve will follow that of the Si matrix and has the same channeling half-angle , $\psi_{\frac{1}{2}}$ (Fig. 10 (a)). In contrast, for foreign atoms which position themselves at the center of the channels, a sharp peak in the angular scan curve will be observed around the best-channeling direction (Fig. 10 (b)). For inbetween cases, the angular scan curve may exhibit features similar to Fig. 10(a) but with smaller channeling half-angle or with the peaking effect in Fig. 10(b) strongly attenuated. According to the calculations of Alexander et al.[25], multiple peaks can also develop if the site projection is close to but not exactly centered at the middle of the channels. By using the triangulation process, the lattice symmetry as well as the lateral displacements can all be deduced. The advantage of the triangulation technique is the simplicity of the interpretation which is solely based on geometrical considerations.

In Fig. 10, we have assumed the foreign atoms remain on the crystal surface but the technique is equally applicable for intermixed interfaces. The preferential site of the

foreign atoms can still be located. However, the position of the interfacial Si atom can only be inferred from the determined positions of the foreign atoms because angular scan curves of the interfacial Si atoms are limited to tilt angles less than $\psi_{1/2}$. For angular tilts above $\psi_{1/2}$, no energy separation between the crystalline and disordered Si signals can be observed. One conceivable approach to study the structure of the interfacial Si is to measure the amount of disordered Si at various channeling directions. Due to the absence of systematic calculations on the sensitivity of the channeled ions to lateral displacements, this approach was not followed in the present study.

2.5 Effects of Ion Beam Dose and Current on Channeling Analysis

For ion beam analysis of materials using MeV ions, effects such as ion-beam damage and beam heating on the sample have to be carefully evaluated. To ensure that the above two effects are insignificant in the channeling measurements, the Si peak of the Ni-Si interface was investigated as a function of both the ion beam dose and ion beam current. The purpose of the study is to establish the dose dependence of the Si peak so that the beam spot can be moved to a fresh region on the sample after some tolerable dose has been accumulated.

In Fig. 11, we show the scattering yield of the Si peak per micro-coulomb of the analysis beam as a function of the accumulated helium dose for a Si (111) crystal covered with

5.7×10^{16} Ni/cm^2. The ^{4}He ion energy used was 1 MeV and the beam spot area was about 1 mm^2. The measurement was performed at a vacuum of $\sim 4 \times 10^{-10}$ Torr. To accumulate enough yield for counting statistics, the low dosage data points were collected over fresh sample areas with preset dosages until a total of 2 μC was reached. From the curve in Fig. 11, the Si peak value does increase as a function of total ^{4}He dose and a 10% increase is observed after a total ^{4}He dose of 50 μC (i.e., 3.1×10^{16} ions/cm^2). The rate of increase is in reasonable agreement with the value obtained by Feldman on the Si <100> surface peak[26]. For a typical analysis dose of 2 μC, the increase in the Si peak value is 3% and has the same magnitude as the statistical fluctuations of the measurements.

The beam-heating effect was investigated by increasing the analysis beam current from a typical value of 10 nA to 50 nA. For a total dose of 10 μC, no difference in the measured Si peak value was observed between the 10 nA and 50 nA cases. A fresh region about 1 mm from the heavy-current analysis spot was then examined with a current of 10 nA for 2 μC and the data fell on the curve for typical analysis conditions. These observations suggest that the beam-heating effect is not a dominant factor for the Si peak increase.

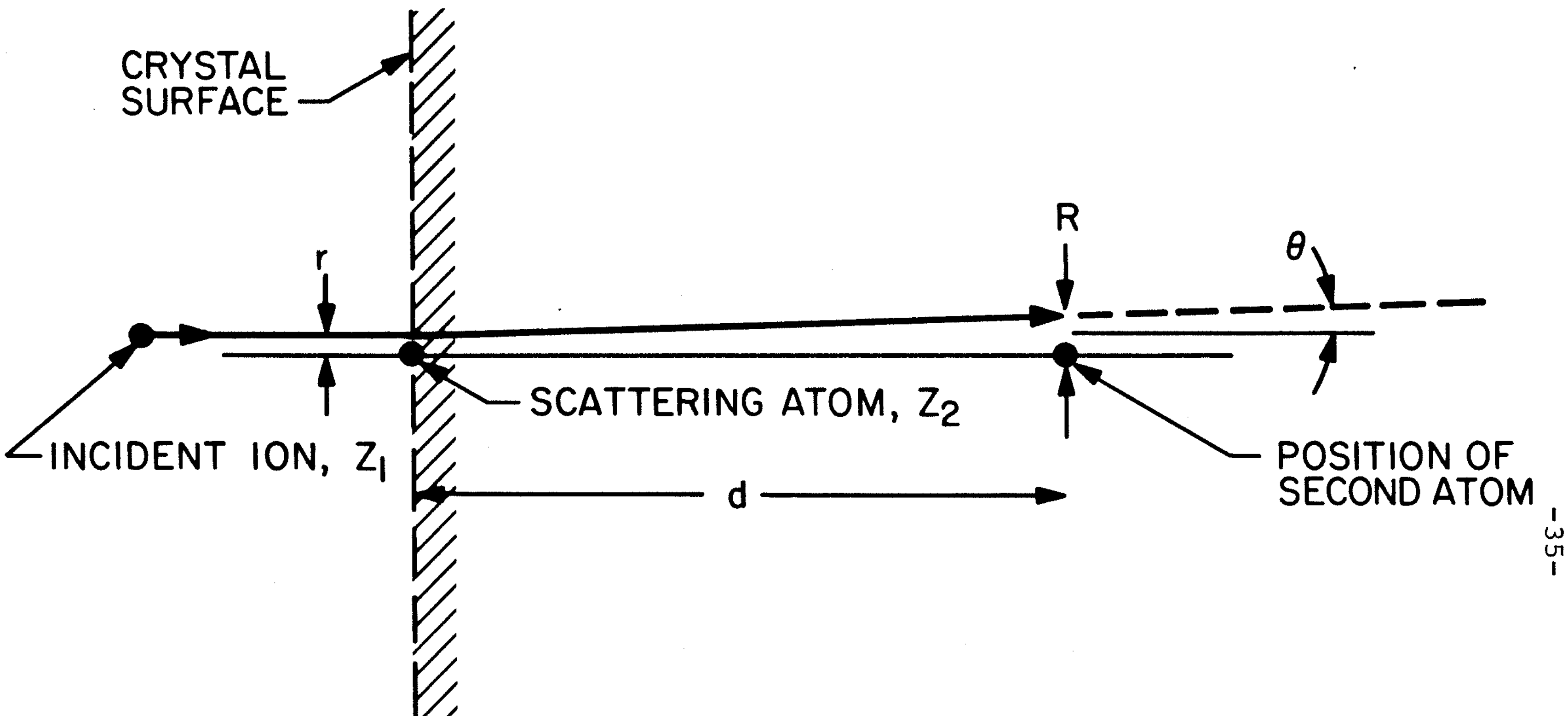

Figure 1 Two-atom surface scattering model to illustrate the shadowing effect. In this figure, the atoms are assumed to be static.

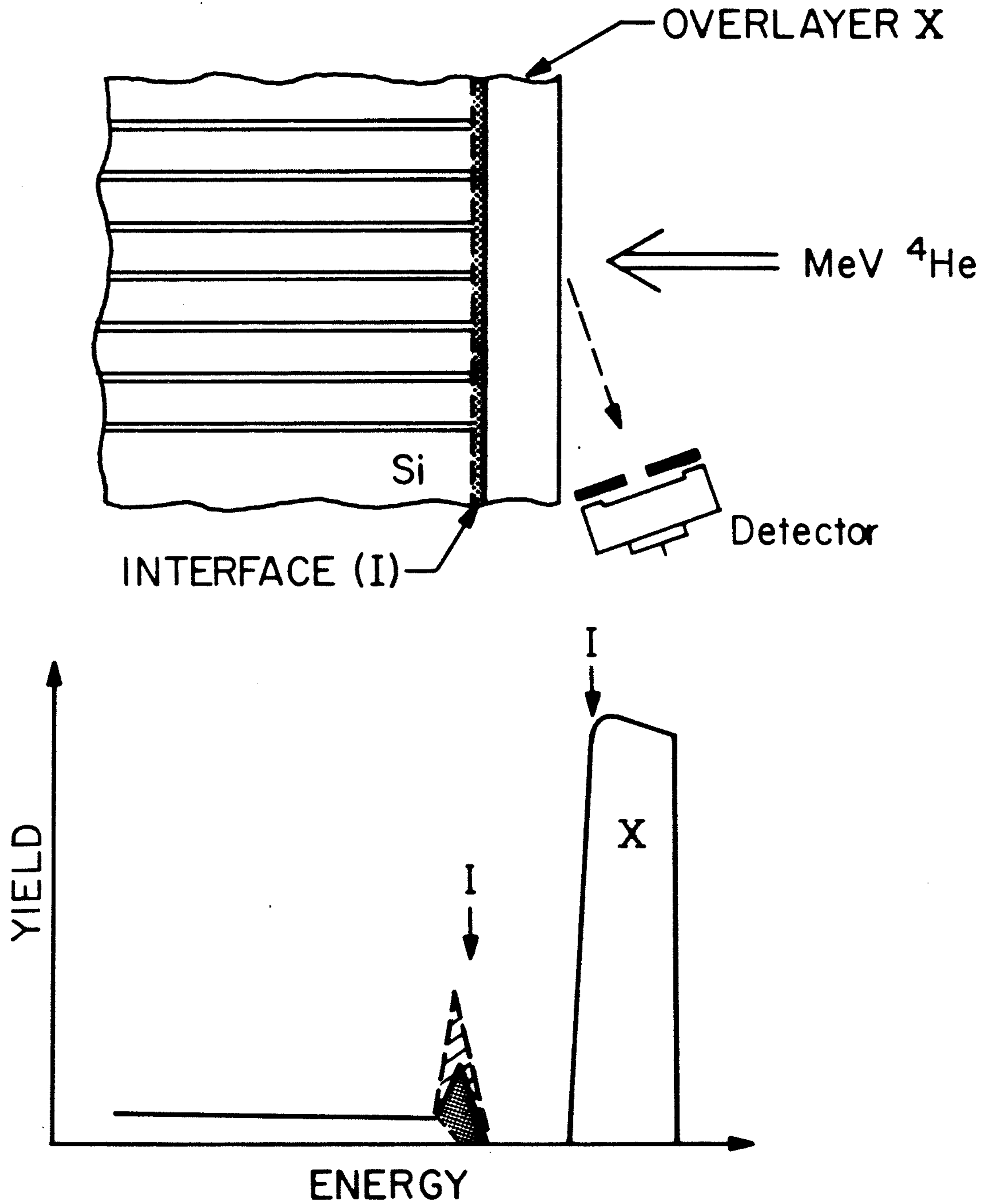

Figure 2 Channeling measurements on Si interfacial disorder. The dotted area represents the intrinsic Si surface peak. The shaded area represents the disordered Si atoms due to the overlayer X.

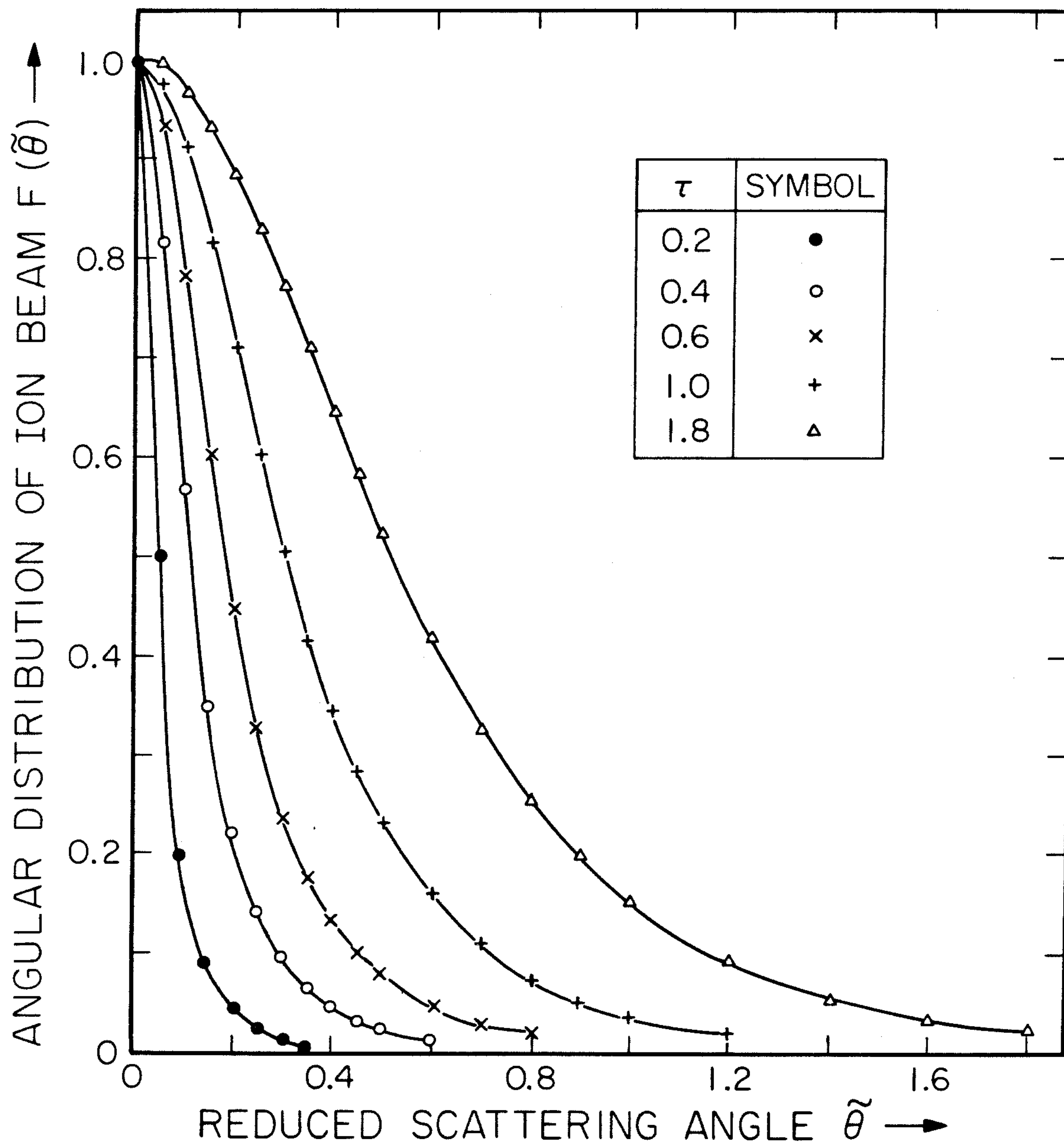

Figure 3 Angular profile of ion beam due to multiple scattering for various reduced thicknesses (τ) [after L. Meyer[15]].

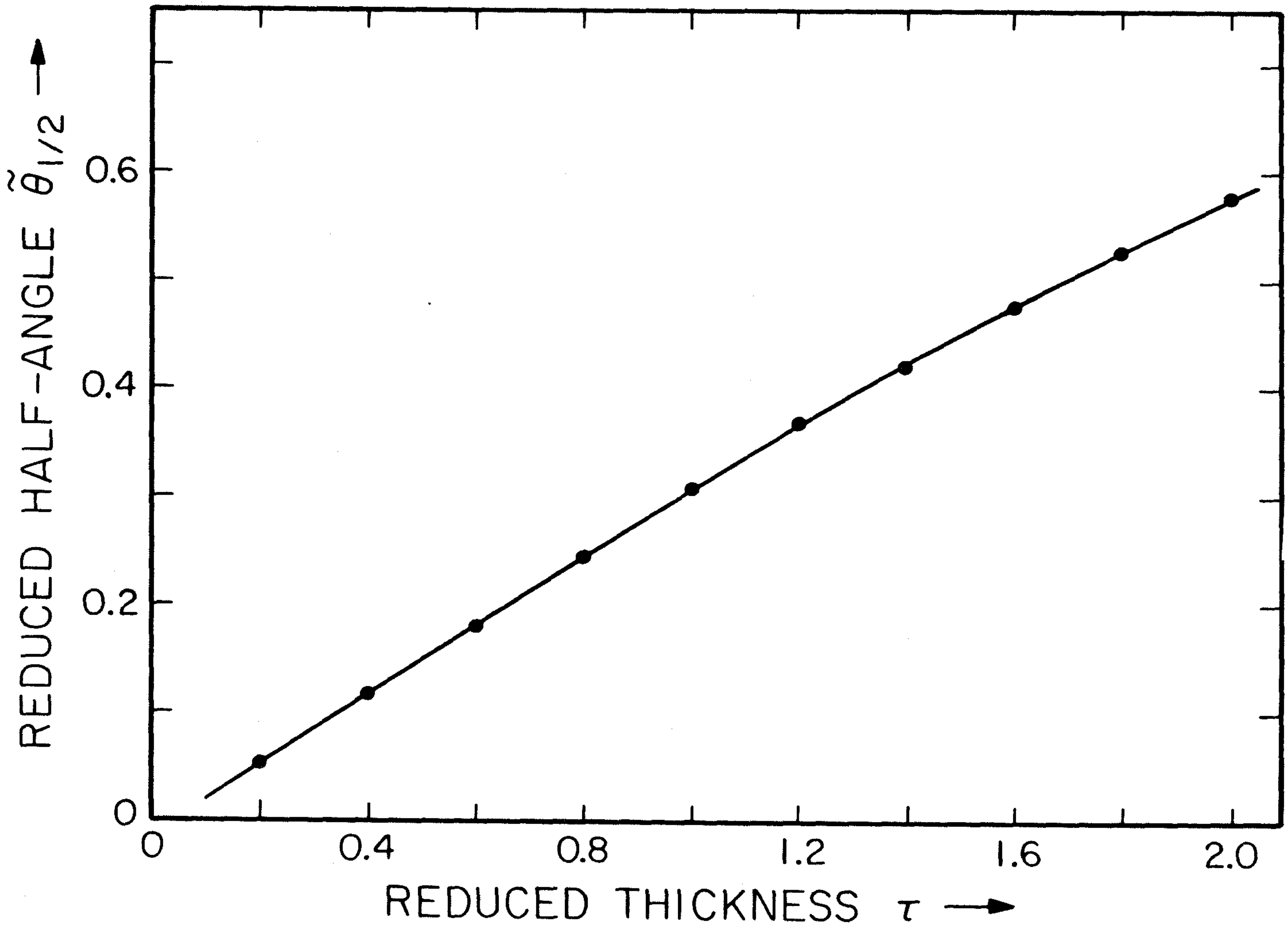

Figure 4 Reduced half-angle ($\tilde{\theta}_{1/2}$) versus the reduced thickness (τ) due to multiple scattering [after L. Meyer [15]]

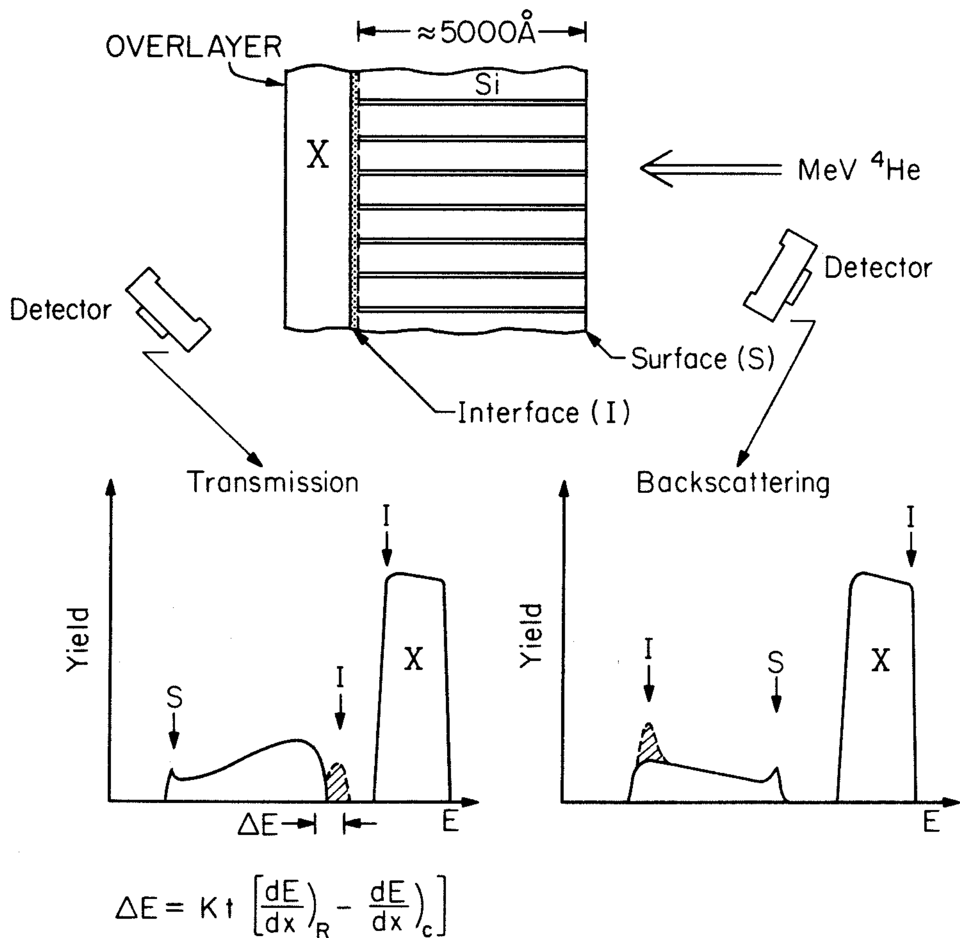

Figure 5 Spectral features of thin-crystal channeling in interfacial studies with backscattering and transmission geometries.

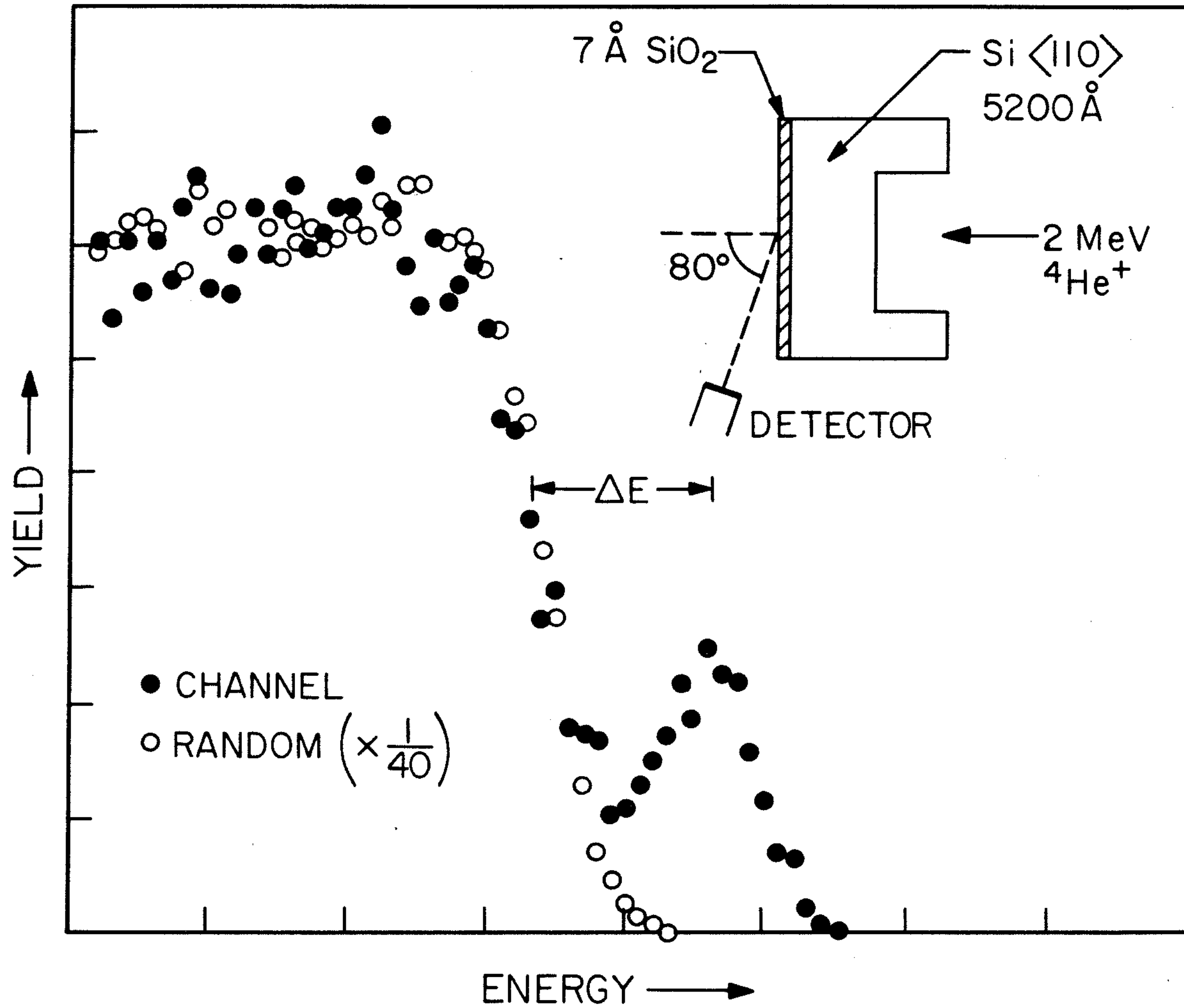

Figure 6 Transmission channeling and random spectra of a 7 Å-thick SiO_2 layer on (110) Si. The energy separation between non-registered and crystalline Si signals is indicated by ΔE.

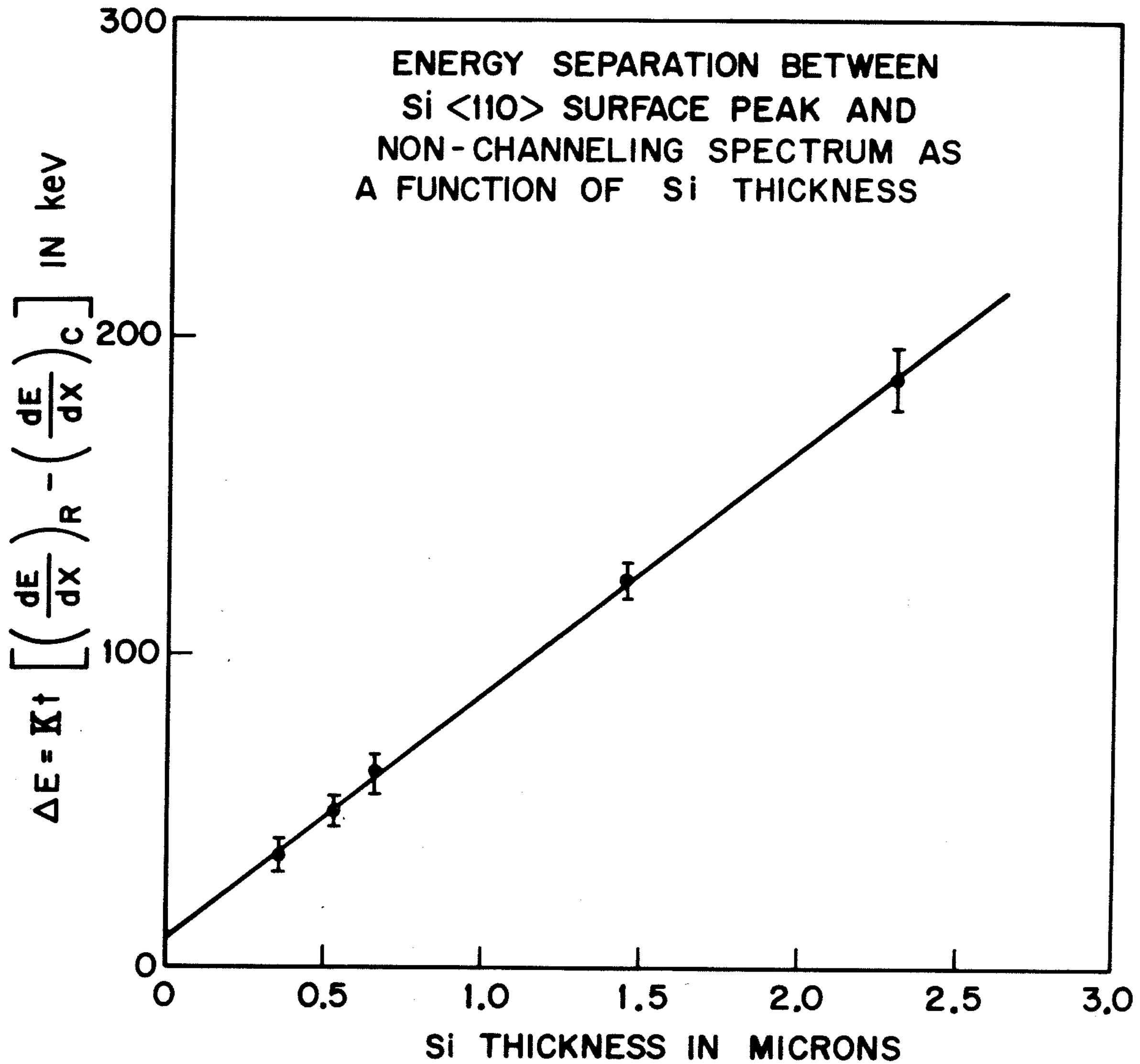

Figure 7 Energy separation, (ΔE), between non-registered and crystalline Si signals in thin-crystal channeling as a function of crystal thickness. The samples are (110) oriented Si thin crystals. The channeling axis is <110>.

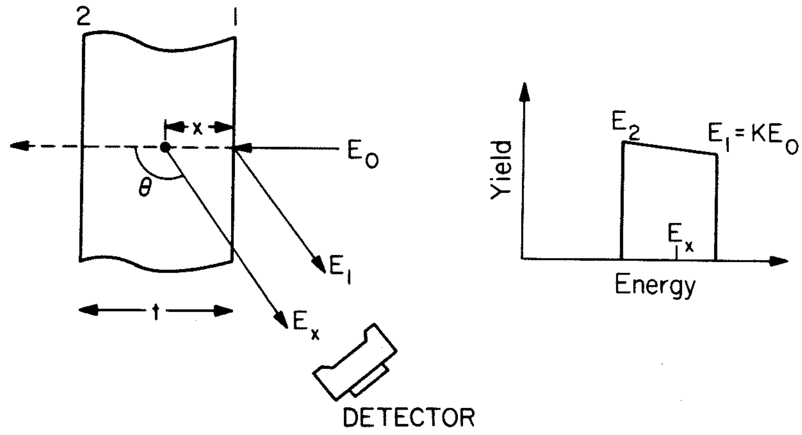

(a) BACKSCATTERING GEOMETRY

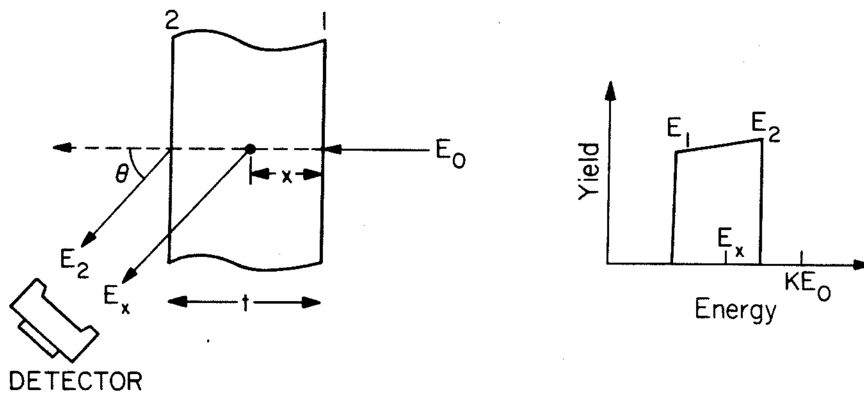

(b) TRANSMISSION GEOMETRY

Figure 8 Energy losses of projectile ions for backscattering (a) and transmission (b) geometries with thin-crystal channeling.

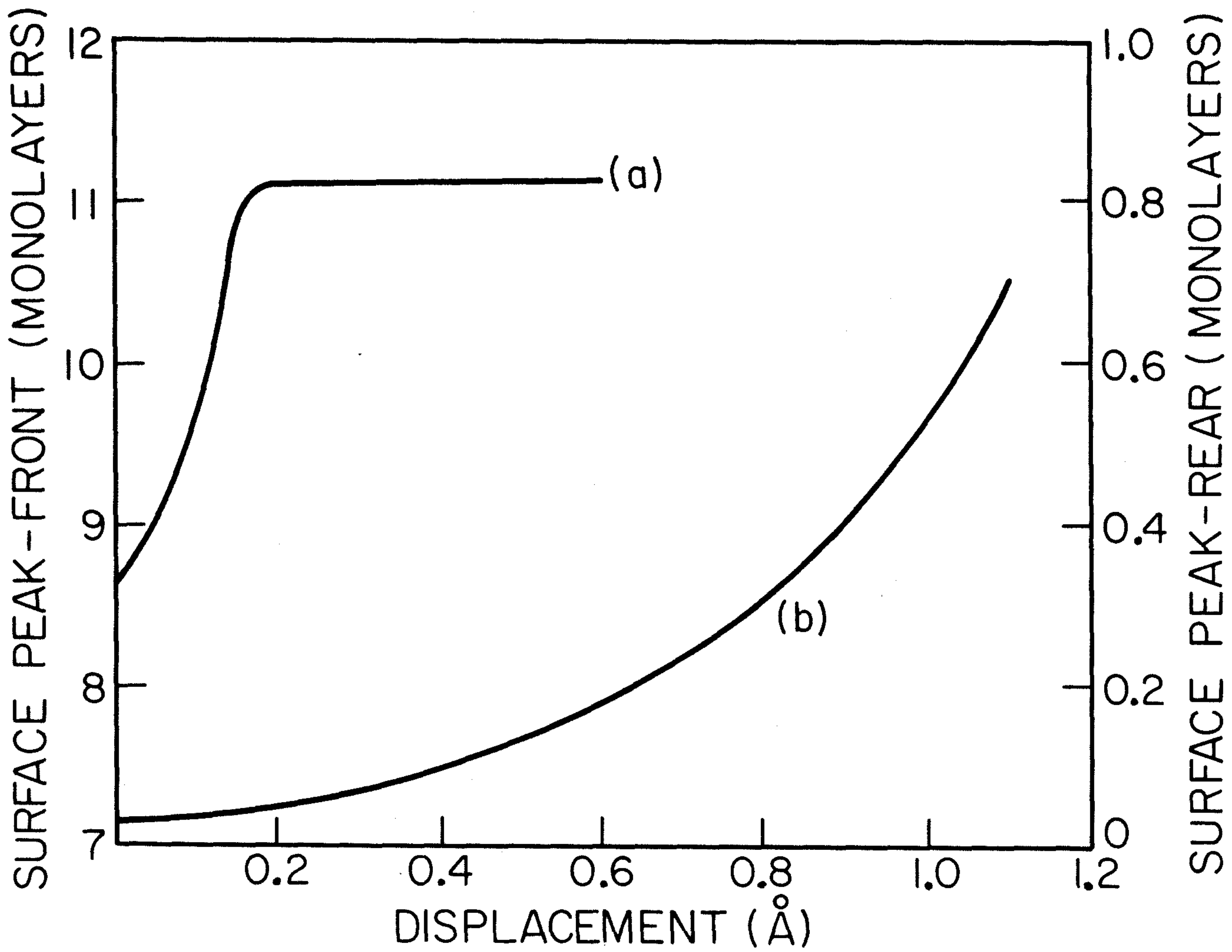

Figure 9 Sensitivity of conventional channeling (a) versus thin-crystal channeling (b) to lateral atomic displacements [after Feldman et al.[20]].

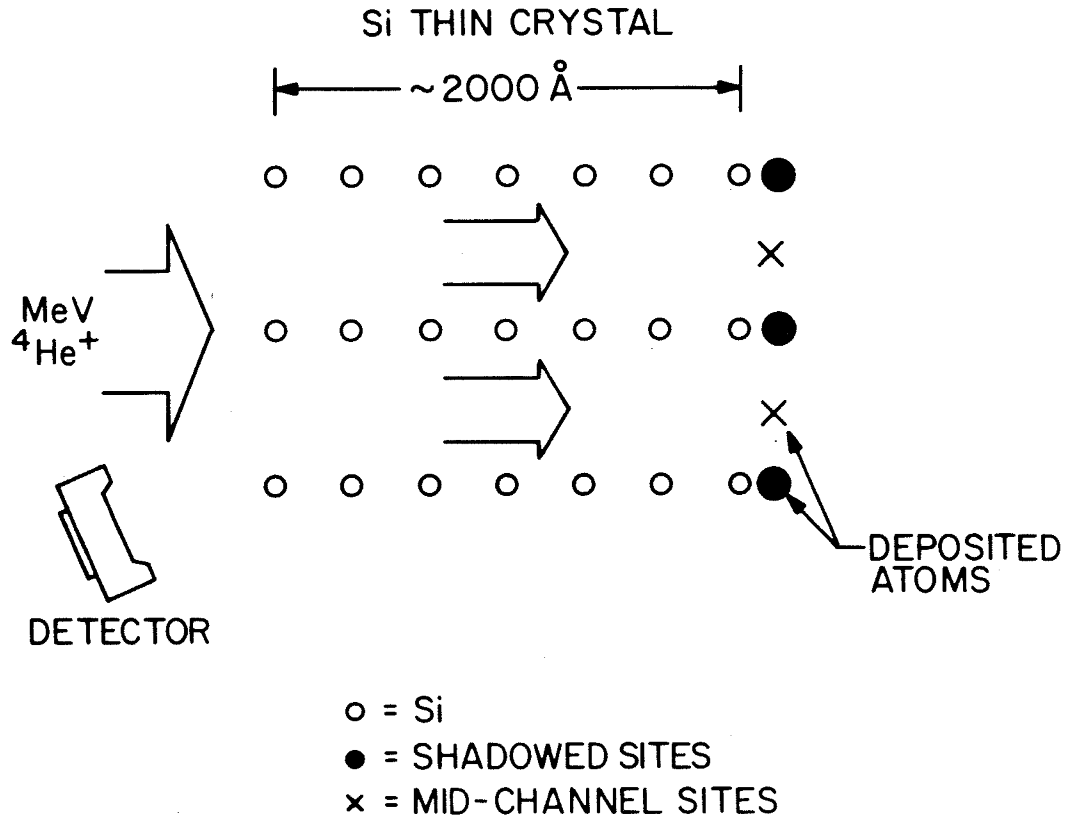

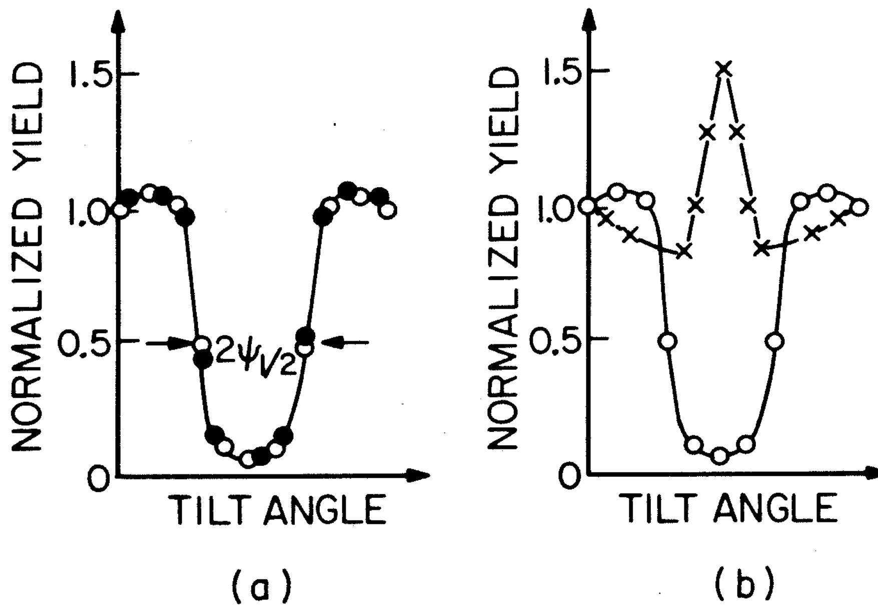

Figure 10 Determination of the lattice location of foreign atoms on Si surface by thin-crystal channeling.

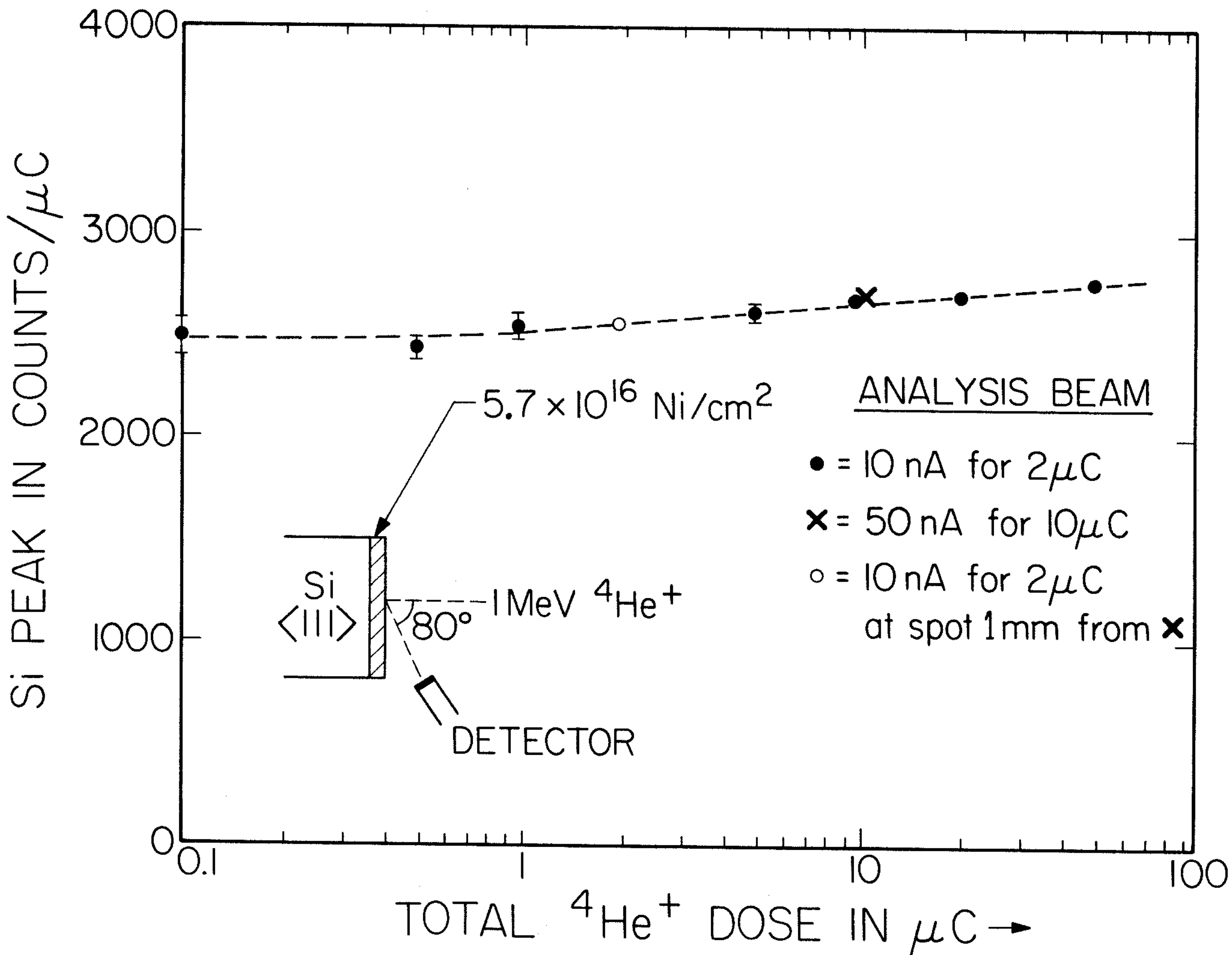

Figure 11 The Si peak as a function of ^4He analysis dose for as-deposited Ni on (111) Si.

TABLE 1 SURFACE PEAK OF "BULK-LIKE" Si SURFACES

		^{4}He Energy in MeV		
		1.0	1.5	2.0
Shadow cone radius R_m in Å	<100>	0.087	0.072	0.063
	<110>	0.074	0.061	0.053
	<111>	0.081	0.067	0.059
Scaling parameter ρ/R_m	<100>	1.22	1.48	1.69
	<110>	1.43	1.73	2.00
	<111>	1.30	1.58	1.82
Surface Peak in atoms/row	<100>	3.1	3.8	4.4
	<110>	3.7	4.5	5.1
	<111>	3.5	4.0	4.6
Surface Peak in 10^{15} atoms/cm^2	<100>	8.4	10.3	11.9
	<110>	7.1	8.6	9.8
	<111>	8.2	9.4	10.8

TABLE 2

CONVERSION FACTORS FOR THE REDUCED THICKNESS τ AND REDUCED SCATTERING ANGLE $\tilde{\theta}$ WITH HELIUM IONS (Z_1=2)

Element	Z_2	a(Å)	τ (a)	$\frac{2Z_1Z_2e^2}{Ea}$ (b)
C	6	0.212	0.141	0.0016
Si	14	0.172	0.093	0.0047
Cr	24	0.149	0.070	0.0093
Ni	28	0.142	0.063	0.0114
Ge	32	0.137	0.059	0.0135
Pd	46	0.123	0.047	0.0215
Au	79	0.105	0.035	0.0433

(a) $\tau = \pi a^2 Nt$ for $Nt = 10^{16}$ atoms/cm^2

(b) $\theta = \tilde{\theta} \cdot \frac{2Z_1Z_2e^2}{Ea}$; value calculated for E = 1 MeV.

References

(1) J. A. Davies, D. P. Jackson, J. B. Mitchell, P. R. Norton and R. L. Tapping, Phys. Lett., 54A, 239 (1975).

(2) L. C. Feldman, R. L. Kaufman, P. J. Silverman, R. A. Zuhr and J. H. Barett, Phys. Rev. Lett., 39, 38 (1977).

(3) L. C. Feldman, P. J. Silverman and J. Stensgaard, to be published in the Proceedings of the 4th International Conference on Ion Beam Analysis, edited by H. H. Andersen, J. Bottiger and H. Knudsen (Aarhus, Denmark, 1979).

(4) R. J. Culbertson, L. C. Feldman and P. J. Silverman, to be published.

(5) I. Stensgaard, L. C. Feldman and P. J. Silverman, Phys. Rev. Lett., 42, 247 (1979).

(6) J. F. Van der Veen, R. M. Tromp, R. G. Smeenk and F. W. Saris, Surf. Sci., 82, 468 (1979).

(7) J. F. Van der Veen, R. G. Smeenk, R. M. Tromp and F. W. Saris, Surf. Sci., 79, 212 (1979).

(8) I. Stensgaard, L. C. Feldman and P. J. Silverman, Surf. Sci., 77, 513 (1978).

(9) L. C. Feldman, to be published in Surface Science: Recent Progress and Perspectives, CRC Press, (1979).

(10) K. C. R. Chiu, J. M. Poate, L. C. Feldman and C. J. Doherty, to be published in Appl. Phy. Lett.

(11) F. W. Saris and W. K. Chu, to be published in Appl. Phy. Lett.

(12) E. Lugujjo and J. W. Mayer, Phys. Rev., B7, 1792 (1973).

(13) E. Bogh, in Channeling-Theory, Observation and Applications, edited by D. V. Morgan (Wiley-Interscience, London, 1973), p. 435.

(14) W. K. Chu, E. Lugujjo, J. W. Mayer and T. W. Sigmon, Thin Solid Films, 19, 329 (1973).

(15) L. Meyer, Phys. Stat. Sol., B44, 253 (1971).

(16) F. H. Eisen, G. J. Clark, J. Bottiger and J. M. Poate. Rad. Eff., 13, 93 (1972).

(17) W. K. Chu, J. W. Mayer and M-A. Nicolet, Backscattering Spectrometry, (Academic Press, New York, 1978), p. 24.

(18) Ibid, p. 54 ff.

(19) J. F. Ziegler, Helium Stopping Powers and Ranges in All Elemental Matter, (Pergamon Press, New York, 1977).

(20) L. C. Feldman, P. J. Silverman, J. S. Williams, T. E. Jackman and I. Stensgaard, Phys. Rev. Lett., 41, 1396 (1972).

(21) S. T. Picraux, W. L. Brown and W. M. Gibson, Phys. Rev., B6, 1382 (1972).

(22) D. Van Vliet, in Channeling-Theory, Observation and Applications, edited by D. V. Morgan (Wiley-Interscience, London, 1973), p. 37.

(23) S. T. Picraux, New Uses of Ion Accelerators, edited by J. F. Ziegler (Plenum Press, New York, 1975), p. 229.

(24) J. Lindhard, Mat. Fys. Medd. Dan. Vid. Selsk., 34, No. 14 (1965).

(25) R. B. Alexander, P. T. Callaghan and J. M. Poate, Phys. Rev., B9, 3022 (1974).

(26) L. C. Feldman, unpublished results.

CHAPTER 3
METAL-SILICON INTERFACES

3.1 The Ni-Si Interface - An UHV Experiment

The UHV experiment was performed at the 3.75 MeV Van de Graaff accelerator facilities of Bell Telephone Laboratories, Murray Hill, New Jersey. The UHV chamber is equipped with ion and titanium sublimation pumps with an operating vacuum in the low 10^{-10} Torr range. A 2.5 meter beamline which houses the collimator slits (1 mm in diameter) is used as a differential pumping buffer between the UHV chamber and the accelerator vacuum. The beamline is always maintained below 10^{-8} Torr by a turbomolecular pump.

The layout of the UHV chamber is shown schematically in Fig. 12. The sample is mounted on a tilt-plus-rotation goniometer equipped with orthogonal linear drives for channeling alignments and positioning of the sample for various operations. The sample temperature can be lowered to below 170°K with liquid nitrogen cooling and heated to 1500°K with electron bombardment from the back of the sample. For low temperature ranges, a thermocouple in proximity with the sample is used to monitor the temperature readings whereas an optical pyrometer is used for high temperatures. The chamber contains LEED optics to examine surface structures. The same LEED unit is also used for retarding field Auger

spectroscopy with a 17 KHz, 5V peak-to-peak modulation voltage. The Auger excitation is provided by a 3 keV glancing incidence electron gun which makes 15° to the sample's surface. For surface cleaning, the sample is sputtered by Ar ions at a partial pressure of $5x10^{-5}$ Torr with a 1 KeV ion sputter gun. A leak valve admits the Ar gas(for sputtering)which can later be pumped out rapidly by the turbomolecular pump of the beamline via an auxiliary exhaust bypass. Evaporation of various materials can be achieved by electron bombardment heating of a Ta furnace which contains the evaporation charge.

For accurate ion beam charge integrations, the sample holder is surrounded by two parallel secondary electron suppressor rings which are biased at -1KV. The movable solid-state detector is mounted on a rotation arm so that scattering geometries between 0-160° can be achieved and is cooled by cold air for improving energy resolution.

The Ni-Si interface is prepared by sequentially depositing Ni atoms onto a clean Si (111) surface in the UHV chamber. Normal pressure during ion-beam analysis is less than $2x10^{-10}$ Torr, and the vacuum is maintained below $1x10^{-9}$ Torr during the Ni deposition. Prior to evaporation, the Si surface is cleaned by sputtering with 1 keV Ar ions and then heated to 1500°K for one minute. The sample is then held at 1175°K for several minutes and finally cooled slowly to room temperature. This procedure consistently produces Si (111)

surfaces with sharp 7x7 LEED patterns. The cleanliness of the sample surface is monitored by Auger electron spectroscopy for low atomic number impurities while heavier impurities are monitored by MeV ion backscattering. For the cleaned Si (111) surface, Auger analysis shows the Si LVV line at 92 eV has a peak-to-peak value of at least a factor of one thousand greater than the carbon KLL line at 272 eV. No other impurities are detected by the Auger technique. Using backscattering with 1 MeV ^4He ions, heavier impurities such as iron are detected with a total concentration less than $2x10^{13}/cm^2$ near the surface. Origins of these impurities are probably due to the sputter-cleaning process which may have sputtered portions of the substrate holder. Typical deposition rates are approximately 0.1 to 0.5 monolayers of Ni per minute. During a nominal room temperature deposition, the substrate remains at a temperature of <325°K, as indicated by a thermocouple in proximity with the sample. The areal densities of the deposited Ni and displaced Si atoms as measured by MeV ion backscattering are calibrated against a "standard" which contains $5.1x10^{15}$ atoms/cm^2 of tellurium implanted into Si.

The backscattering channeling spectra (1.0 MeV ^4He) from a clean Si(111) and a Ni-covered Si(111) surface are shown in Fig. 13. The surface peak of the clean Si surface at room temperature has an areal density of $9.4x10^{15}$ Si/cm^2 which corresponds to 4.0 atoms/row, in close agreement with the theoretical value of 3.5 atoms/row for a Si "bulk-like"

surface.[1] For the first $1.0x10^{15}/cm^2$ of Ni coverage, the 7x7 LEED pattern becomes diffuse and the Si peak increases by $\cong 1.1x10^{15}/cm^2$. The Si peak increases monotonically as a function of the Ni coverage (Fig. 14). At a coverage of $3.5x10^{16}$ Ni/cm^2, the number of non-registered Si atoms involved in the interfacial layer is $1.1x10^{16}/cm^2$. The origin of the non-registered Si can be due to compound formation, Ni-Si interdiffusion, or both.

The low-temperature experiment was performed by holding the substrate temperature at 170°K during Ni deposition and ion beam analysis. Since the intensity of the intrinsic surface peak depends linearly on the lattice vibrations of the Si atoms, it is expected to decrease with temperature. The measured surface peak value for the clean Si (111) surface at 170°K is 3.5 atoms/row ($8.2x10^{15}$ atoms/cm^2).

For the first few monolayers of Ni coverage at 170°K, the Si interface peak increases slowly compared to room temperature deposition. After $1.6x10^{16}$ Ni/cm^2 have been deposited, the sample is allowed to warm up slowly to room temperature. As shown by the first broken arrow in Fig. 14 the Si peak (as measured at room temperature) has increased to $1.5x10^{16}$ Si/cm^2, close to the value for room temperature deposition. The increase over the low temperature value (= $1.0x10^{16}$ Si/cm^2) is much larger than the temperature effects in the intrinsic surface peak. This result was confirmed in a second run by

depositing 2.0×10^{16} Ni/cm^2 at 170°K followed by a slow warming to room temperature, analysis at 300°K, and then analysis at 170°K, as shown in Fig. 14.

The effect of multiple scattering due to the overlayer is not a severe constraint in this experiment because of the low Ni coverages. For the maximum Ni coverage of 3.5×10^{16} atoms/cm^2, the half-angle, $\theta_{1/2}$, due to multiple scattering is equal to the incident beam's angular divergence. Moreover, the low-temperature deposition data on the Si peak values, which increase by $\lesssim 2 \times 10^{15}$ atoms/cm^2 up to a coverage of 2×10^{16} Ni/cm^2, set an upper limit on the amount added to the Si peak by multiple scattering.

The Auger and LEED results as a function of Ni coverage are summarized in Fig. 15. Since the Auger set-up uses a relatively large modulation voltage (5 Volts), it is difficult to deconvolute density of states information from the energy distribution function. However, the various Auger spectra (dN(E)/dE versus E) can still be compared to obtain qualitative information on the Ni-Si interfacial reaction. From one to two monolayers of Ni coverage (1 monolayer = 7.8×10^{14} atoms/cm^2 for the Si (111) surface), the Ni LVV signal is rather prominent in the Auger spectrum while the intensity of the Si LVV line is strongly attenuated. The most curious observation is that the LEED screen still shows a diffused 7x7 pattern. Similar behavior has been observed by Ridgway and Haneman[2] on Ni deposited onto cleaved Si (7x7) surfaces.

One possible explanation is that the Ni atoms form patches over the Si surface with bare Si islands having dimensions larger than the diffraction coherence length. However, Ridgway and Haneman argued that since the spots simply weaken on further Ni deposition without noticeable broadening, negligible Ni clumping takes place and the Ni coverage is uniform. In this study, no I-V measurement has been made on the diffraction spots so that it is not possible to clarify the issue.

With thicker Ni overlayers ($>2\times10^{15}$ Ni/cm^2), no LEED diffraction spots can be observed and the Si LVV signal keeps decreasing but is still visible in the spectrum up to a Ni coverage of 2.8×10^{16} atoms/cm^2. At such thickness, the Ni signal resembles that of bulk samples with LVV peaks at 61 and 102 eV.

At a Ni coverage of 2.8×10^{16} atoms/cm^2 a heating cycle was undertaken with the Ni and Si peaks measured and Auger and LEED patterns observed at various temperatures. At relatively low temperatures ($\sim$575°K) backscattering gave an indication of a partial epitaxial structure ($\chi_{min}\sim0.75$) while the LEED pattern was simply a diffuse background with no visible spot pattern. The non-aligned spectrum indicated a Ni to Si compositional ratio of approximately 3 to 2. Further annealing at a slightly higher temperature ($\sim$625°K) resulted in a loss of epitaxy and a phase with atomic composition

corresponding to NiSi. After a 1090°K anneal the silicide layer itself indicated good channeling ($\chi_{min} \sim 0.05$). The LEED pattern was a sharp 1x1 array with 3-fold symmetry and low background. This final phase undoubtedly corresponds to the epitaxial $NiSi_2$ reported by Chiu et al.[3]

In Fig. 16, we show the Auger spectra of the sample at various stages of heat-treatment. A gradual increase of the Si/Ni intensity ratio can be observed as we proceed towards higher annealing temperatures, following the $Ni_2Si \rightarrow$ "Ni_3Si_2" $\rightarrow NiSi \rightarrow NiSi_2$ phase transformation sequence. It is important to point out that the Auger spectra with monolayer(s) of Ni coverage (Fig. 15) are markedly different from those of the nickel silicides. The difference in electronic structures between as-deposited monolayers of Ni on Si and the nickel silicides has also been observed by XPS measurement.[4] The XPS results indicate that the as-deposited Ni atoms are in a more Si-rich environment than the Ni atoms in the Ni_2Si and NiSi phases.

The Ni-Si interfacial mixing can also be demonstrated qualitatively by Auger spectroscopy. In Fig. 17, we show the Auger spectra of samples with Ni deposition performed at 325°K and 170°K. The Ni coverage is almost identical in the two samples ($\sim 16 \times 10^{15}$ Ni/cm^2). Since the Si intensity will be attenuated exponentially by the escape depth of the Auger electrons through the Ni overlayer

(∿4.3Å[5]), the depth of the Si atoms underneath the Ni surface can be deduced by comparing the Si LVV intensity (92 eV) of the two spectra. It is clear that the Si atoms are much closer to the Ni surface in the 325°K case than the 170°K case. This again confirms the intermixing of the Ni-Si interface at room temperature depositions. However, a quantitative analysis of the Auger spectrum of such a multi-layer structure is formidable because the composition and matrix dependence of the electron escape depths are still not established.

The key issue relating the physical structure of the metal-semiconductor interface and Schottky barrier height (Φ_B) is the structural or stoichiometric variation of phases across the interface. As pointed out by Ottaviani et al.[6] Φ_B is rather insensitive to the metallurgical phase in contact with Si within a particular metal-silicon system. For example, Φ_B lies between 0.68 to 0.72 eV with Ni, Ni_2Si, NiSi or $NiSi_2$ as the contact metal to Si.[7] In view of the different crystal structures and bonding schemes of the metal and its various silicides, ϕ_B is not likely to be controlled by bulk properties but rather by a more general interfacial feature. Since all the silicides are formed by thermal annealing via some type of diffusion mechanism, we believe that this interfacial structure is determined by kinetics. The temperature dependence of the interfacial reactivity

for Ni on Si is just one example which manifests the kinetic nature of such interfaces.

In summary, it has been demonstrated that by depositing Ni in UHV on crystalline Si substrates at ambient temperatures ($\gtrsim 300^{o}K$), an interfacial reaction is initiated and the interfacial width increases monotonically as a function of Ni coverage. For the Ni-Si system, the interfacial reactivity can be strongly suppressed at lower temperatures ($\sim 170°K$). This temperature dependence of the interfacial reactivity strongly suggests the importance of performing Schottky barrier height measurements at low substrate temperatures for meaningful comparison with abrupt metal-semiconductor models.

3.2 Other Metal-Si Interfaces

3.2.1 Conventional Channeling

A series of samples were prepared by depositing 50-200Å of metal layers onto Si wafers with chemically cleaned surfaces. The characterization of such a surface treatment is detailed in Appendix 2. Because the sample preparation and ion-beam analysis were not performed under UHV conditions, the metal overlayers were made relatively thick so as to ensure a complete surface coverage. Otherwise, any exposed bare Si region may form reaction products such as SiO_2 whose contribution to the Si peak cannot be distinguished from that of the metal-silicon interface. Aside from these complications, the interfacial features of these

samples reflect a realistic picture of typical interfaces of actual devices because chemically cleaning procedures are still mainly used in electronic industries.

Prior to evaporation, the Si wafers were organically degreased and dipped into a hydrofluoric acid etch. The residual gas pressure of the evaporation chamber was in the 10^{-8} Torr range and the metals were evaporated by heating with electron bombardment. Deposition rates of the metals varied between 10-30Å per second and the Si substrates were left at ambient temperature during evaporation. The areal density of each metal overlayer was determined by comparing the scattering yields of 1.5 MeV ^{4}He ions from the metal atoms and a Bi-implanted standard with 4.7×10^{15} Bi/cm^2 (8).

As discussed previously in Chapter 2, multiple scattering of the incident beam due to the overlayer atoms is one of the major handicaps for determining the amount of Si interfacial disorder with conventional channeling techniques. Since the effect of multiple scattering on the surface peak has not been calculated or measured in any quantitative fashion, an alternative approach is to establish a baseline for the surface peak value by using a "non-reactive" interface such as evaporated Ge on Si crystals. The Ge-Si sample contains approximately the same number of scattering centers (Ge) as the other metal layers. The interface has been characterized by both conventional and thin-crystal

channeling techniques. In Fig. 18, we show a transmission channeling spectrum of ∿160Å Ge (7.0×10^{16} atoms/cm^2) deposited onto a Si (111) thin crystal. The interfacial disordered Si was measured to be less than 1×10^{15} atoms/cm^2 (∿1 monolayer), as indicated by the shaded area of the Si signal around 1.1 MeV. The absence of interfacial disorder is interpreted as an atomically abrupt Ge-Si interface with no intermixing between the Ge and Si atoms. Results by Hung et al.[9] have shown the Ge-Si interfacial mixing only takes place after high-temperature anneals (>600°C).

In Fig. 19, we show the energy spectrum of the same Ge-Si sample as measured by conventional channeling. The Si peak as represented by the shaded area corresponds to an areal density of 1.6×10^{16} atoms/cm^2 and is 4×10^{15} atoms/cm^2 higher than the surface peak value of a chemically cleaned Si (111) surface (i.e. 1.2×10^{16} atoms/cm^2). The effect of multiple scattering due to the Ge overlayer is quite apparent by measuring channeling minimum yields (χ_{min}) of the crystalline Si signal. For a chemically cleaned Si (111) surface, χ_{min} is equal to 3.5% and the value increases to 11% for the sample covered with ∿160Å of Ge. The enhanced scattering yield is caused by the incident ions making an angle larger than $\psi_{\frac{1}{2}}$ with the Si <111> axis because of multiple scattering. According to the calculation of Meyer (see Chapter 2), the half-angle for multiple scattering, $\theta_{\frac{1}{2}}$, with 160Å of Ge is

0.06° and is about twice the incident beam's divergence half-angle (0.03°). Using the step-function approximation for χ_{min} as proposed by Lugujjo and Mayer[10] (i.e. $\chi_{min} = F(\tilde{\theta}_c)$ of Fig. 3 with $\tilde{\theta}_c = \psi_{\frac{1}{2}} \cdot aE/2Z_1Z_2e^2$), the calculated χ_{min} value is 9% and is in reasonable agreement with the measured value of 11%. Therefore, the χ_{min} value of Si can be used to gauge the amount of multiple scattering caused by the overlayers.

Using the Ge-Si interface as a reference, the Si peak of various metal-Si interfaces such as Ni, Pd, Pt, Cr, V and Au are measured with 1.5 MeV ^{4}He ions. The results are tabulated in Table 3. The calculated values of $\theta_{\frac{1}{2}}$ and the measured χ_{min} values for Si are also presented to indicate the amount of multiple scattering. It is important to point out that the $\theta_{\frac{1}{2}}$ values only include multiple scattering contributions of the metal atoms but not the disordered Si atoms of a reacted interface. Hence, the $\theta_{\frac{1}{2}}$ information is only useful when the interfacial reactivity is low. For highly reactive interfaces such as Pd on Si, no a priori information on the amount of disorder Si can be deduced based on $\theta_{\frac{1}{2}}$ of the metal alone. In such cases, even if the effect of $\theta_{\frac{1}{2}}$ on the surface peak value is well understood, an iterative procedure is still required to solve the amount of disorder interfacial Si self-consistently.

From Table 3, the room temperature reactivity of the various metal-silicon interfaces can be classified into two major categories: (1) the low temperature silicide formation interfaces such as Ni, Pd and Pt which form metal-rich silicide phases (M_2Si) at $\sim$200°C, and (2) the high temperature silicide formation interfaces such as Cr and V which form silicon-rich silicide phases (MSi_2) at $\sim$400°C and the non-silicide formation interfaces such as Au.

For the low temperature silicide formation interfaces, they all show prominent interfacial reactivity even at room temperatures. Out of the three elements, Pd, Ni and Pt, Pd can form the Pd_2Si phase when thin layers ($\sim$100Å) of Pd deposited onto Si crystals have been left in room air for about a month. This effect is closely related to the low activation energy (0.9 eV) required for Pd_2Si formation.[11] For the Pd and Pt data points in Table 3, the Si peak values are probably overestimates of the number of actual displaced Si atoms because the χ_{min} of Si is very high ($\sim$30%) and it is difficult to estimate multiple scattering effects. For the Ni-Si interfaces, χ_{min} values are very close to that of the Ge-Si interface and 1.6×10^{16} atoms/cm^2 is assigned as the "intrinsic" interface peak. From this procedure, the interfacial non-registered Si atoms for the (100) and (111)

substrates are 1.7×10^{16} and 1.3×10^{16} atoms/cm^2 respectively. Similarly, the Cr and V interfaces all show non-registered Si atoms on the order of 5×10^{15} atoms/cm^2.

The room-temperature interfacial reactivity is well-correlated with the dominant diffusion species of the silicide formation mechanism. Using implanted inert gases as diffusion markers,(12) metal elements were found to be dominant moving species for the metal-rich silicides, M_2Si. Conversely, in the case where the disilicide phase is formed, silicon is the moving specie. Since the formation energy of vacancies in metals is much lower than that of semiconductors, the metal-metal bond dissociation mechanism is strongly favored at lower temperatures. Tu(13) has proposed an interstitial diffusion model to explain the low-temperature Si-bond weakening mechanism due to the metal atoms. As will be discussed in Section 3.3, such a mechanism has been verified in the Ni-Si system.

As for the disilicide formation interfaces, the creation of a Si vacancy will require much higher temperatures. Our conjecture is that interstitial diffusion of metal atoms is not the prevalent factor in the formation of disilicides. Nevertheless, the observation of about 5×10^{15} atoms/cm^2 of non-registered Si atoms at the Cr-Si and V-Si interfaces still suggests that an interfacial reaction does take place. Apparently, the interfacial reaction is stopped because

silicide formation is unfavorable. It should be of interest to investigate the structure of these interfaces in future experiments.

The Au-Si interface is singled out in the previous discussions because Au forms epitaxial films on Si (111) surfaces. Using channeling analysis (1.5 MeV ^{4}He), the Au layer itself has a χ_{min} value of 43%, indicating the high-quality of crystallinity. For such a crystal-crystal interface, the $\theta_{1/2}$ and χ_{min}^{Si} arguments for multiple scattering are not expected to be applicable here. The channeling critical angle is greater for Au than Si and the high χ_{min} value for Si may just be caused by the mismatch of $\psi_{1/2}$ across the interface. Such an effect has been demonstrated in a similar case, the $NiSi_2$-Si interface, and will be discussed further in Chapter 4.

One curious property of Au on Si is that although Au-Si does not form a well-defined silicide by thermal annealing, Si atoms can be detected on the Au surface as SiO_2 after heat-treatments in air as low as 150°C.[14] Recently, the room-temperature interfacial mixing of Au and Si has also been studied by Auger spectroscopy,[15] UPS and synchrotron radiation.[16] The photoemission studies indicate that from room temperature to 350°C, no well-defined compound is formed and the interfacial width is $\lesssim$15Å and is in reasonable agreement with our channeling measurements (10-20Å).

3.2.2 Thin-Crystal Channeling

To further elucidate the structure of the non-registered Si at the interface, the highly reactive interfaces such as Ni-Si and Pd-Si have also been studied by thin-crystal channeling with the transmission geometry. As discussed in Chapter 2, the thin-crystal experiments are designed to circumvent multiple scattering problems and the technique is independent of the overlayer thickness. The main differences between thin-crystal and conventional experiments are that (1) no intrinsic surface peak value has to be subtracted from the transmission measurements and (2) transmission channeling is sensitive to disordered atoms with large lateral displacements (∿0.7Å) from the atomic rows.

In Fig. 20, we show the energy spectrum of a Ni-Si sample with the transmission geometry. The disordered Si at the interface is 1.6×10^{16} atoms/cm^2; this is nearly the same as the number of non-registered Si atoms observed by convention channeling. One important conclusion from the transmission results is that it excludes the possibility of having the majority of the displaced Si atoms being strained Si atoms. This is because the transmission measurements only sense large lateral displacements. Since the Si <100> atomic rows are 3.84Å apart, a displacement of 0.7Å will correspond to a strain of 0.18 which is beyond the fracture point of Si.

Similarly, the disordered Si peaks were also observed by transmission channeling with Pd layers on Si (100) and (111)

thin crystals. The measured amounts of disordered Si are 2.2×10^{16} and 1.9×10^{16} atoms/cm^2 respectively (Figs. 21(a) and (b)). These measured values are more reliable than the conventional measurements because no multiple scattering effects have to be considered. However, due to the low activation energy of Pd_2Si formation (0.9 eV), it is quite possible that the number of disordered Si atoms can increase with time even at room temperature because of Pd_2Si formation. The situation will be similar to the kinetic studies of silicide formations.

3.2.3 The Ag-Si Interface

Recent UPS studies by Ottaviani et al.[18] have observed that no change of Si valence band structures can be detected by depositing Ag onto Si surfaces at room temperature and the Ag-Si reaction can only be initiated at >400°C. To investigate the structure of the Ag-Si interface, thin-crystal channeling was employed because of its high sensitivity to interfacial mixing ($\lesssim 1\times10^{15}$ atoms/cm^2). In this experiment, Ag layers of ∿150Å were deposited onto Si (100) and (111) thin crystals (∿5000Å) at ambient temperature. The transmission result on the Ag-Si (100) interface is shown in Fig. 22. No interfacial disorder can be observed and the results are similar to those of a chemically cleaned Si thin crystal surface[19] and the Ge-Si interface. The shaded area around 1.1 MeV denotes the background uncertainty and sets an upper limit of 1×10^{15} atoms/cm^2 for interfacial mixing. Upon a

heat-treatment of 325°C for 30 minutes at a vacuum of $5x10^{-7}$ Torr, no change in the channeling spectrum can be detected. After a heat-treatment of 400°C for 30 minutes, the Si was observed to diffuse outward into the Ag layer as indicated by the shaded area of Fig. 23. The concentration of Si in the Ag layer is ~0.6 atomic percent with a total amount of $5x10^{15}$ Si/cm^2. It is unclear whether the Si goes through the Ag via grain boundary diffusion mechanisms because Si is noted for its low solid solubility in Ag.[20] Since no degradation of the χ_{min} of crystalline Si is observed, this suggests that there is not much Ag inward diffusion into the Si crystal. This behavior is very similar to the Ge-Si interface except the latter requires a much higher temperature (600-700°C) to initiate the interfacial reaction.[9] As of today, Ag is the only example known to be a non-reactive metal-silicon interface. The thin-crystal channeling results of Ag, Ni, and Pd are summarized in Table 4.

3.3 Lattice Location Experiment of the Ni-Si Interface

In the present study, a thin-crystal channeling experiment has been devised to locate the lattice sites of monolayers of Ni atoms deposited onto Si crystalline substrates. Ion-beam channeling has been applied to locate preferential sites of impurities in bulk crystals.[21] By making use of the "flux peaking" effect of ion channeling, the relative position of the impurity atoms with respect to the host's crystalline matrix can be determined by a "triangulation" process, i.e.,

channeling in different crystallographic directions. Since the establishement of flux-peaking requires the beam to traverse ∿1000Å into the crystal, this technique is not applicable for impurities located in the near-surface region of bulk crystals. An alternate method based on the blocking effect has been demonstrated by Van der Veen et al.[22] but the technique is only applicable for monolayer or submonolayer impurity coverages. In the case of the thin-crystal experiment, the Si thin crystal (∿2000Å thick) is made self-supporting and the ion beam can enter the crystal via the metal-free surface and establishes flux-peaking before it encounters the Ni-Si interface at the exit side of the thin crystal.

The experimental set-up is illustrated in Fig. 24(a). The Si(100) crystal used is about 1600Å thick and is ∿1 cm in diameter. It is made self-supporting by a chemical etching technique as described in Appendix 1. Prior to Ni evaporation, the crystal was organically degreased and etched in hydrofluoric acid. The Ni deposition was performed in an electron-beam evaporation system with a residual gas pressure of 4×10^{-8} Torr. Approximately ten monolayers of Ni were deposited onto the Si crystal.

The Si thin crystal was then mounted on a tilt-plus-rotation goniometer with the metal-free surface facing the helium ion beam (1.5 MeV). A carbon substrate with 3.4×10^{16} Au atoms/cm^2 deposited on the surface was placed immediately

behind the thin crystal, separated by a 0.005 inch spacer. The carbon substrate was electrically connected to the thin-crystal and constituted part of the charge collection system.

With the detector placed at a 170° angle, the Au layer was used to serve three purposes: (1) It is a normalization standard such that the total Si and Ni scattering yields are normalized by the total Au scattering yield for every back-scattering spectrum. This effectively eliminates charge integration errors. (2) Since the ion beam impinges upon the Ni and Au layers with virtually identical energies, no correction for the energy dependence of the Rutherford cross-section ($\propto E^{-2}$) is necessary although the energy loss of the ions for traversing the thin-crystal is less for channeling directions than for random directions. (3) With a calibrated amount of Au as the scattering reference, the Ni yield can be converted quantitatively to the areal density along any beam incidence direction. This is particularly valuable for angular scan experiments because energy-loss mechanisms of channeled particles are extremely complicated as a function of angular tilt.

The channeled and random spectra of the Si crystal with a Ni coverage of 9.1×10^{15} atoms/cm^2 are shown in Fig. 24(b). The channeling direction is along the <111> axis. Both the Au and Ni signals appear at slightly higher energies for the channeled spectrum because of the anomalously low energy loss of the channeled particles. During the angular scan experiment,

the Au scattering yield increases gradually by about 2% when changed from the best channeling direction to the random direction; this is in good agreement with the calculated increase of 3%[23]. In Fig. 25, the normalized Si and Ni scattering yields are plotted as a function of the tilt angle around the <100>, <110> and <111> axes. The error bars as indicated in the figure are probable statistical fluctuations. Angular dips of ∿23% of the Ni signal are observed along the <100> and <111> axes. For the <110> axis, two shoulder-like structures are observed for the Ni angular scan curve and the channeled yields are slightly higher than the random yields for tilt angles less than the channeling critical angle. Using this triangulation process, it is evident that preferential sites do exist for the Ni atoms.

The angular dips can be understood as follows: for a well-channeled beam, the flux-peaking effect will steer most of the beam away from the crystal's atomic rows and very few backscattering events (i.e. small impact parameter collisions) can occur if the foreign atoms are "shadowed" by the atomic rows or the foreign atoms take up substitutional sites in the host crystal.

Since angular dips have been observed only in the <100> and <111> but not the <110> channeling directions, the possibility of having the preferential sites being epitaxial Ni on Si or the Ni atoms being in substitutional sites of Si can be

excluded. The magnitude of the dips along the <100> and <111> axes both correspond to an areal density of $\sim 2.1 \times 10^{15}$ Ni atoms/cm^2. For the Si (100) surface, one monolayer of Si atoms corresponds to 6.8×10^{14} atoms/cm^2. Since channeling quantities are measured in terms of projected areal densities, it is necessary to have the Ni atoms occupying the preferential sites below the Si(100) surface and this conclusion is independent of the Si(100) surface being flat or terrained.

Theoretically, angular scans along three non-coplanar channeling directions will be sufficient to determine a particular lattice site in three dimensional space. However, unambiguous determination of the lattice location often requires additional channeling directions and all the results have to be consistent with the presumed lattice position. For this purpose, angular scans along planar channeling directions are particularly informative. In Fig. 26, the normalized Ni and Si scattering yields are plotted as a function of the tilt angle along the (100), (110) and (111) planar channeling directions. For (100) planar channeling, the Ni angular scan curve shows a small dip. An angular dip of $\sim$23% is again observed along the (110) planar channeling direction whereas a peak is observed for the angular scan curve along the (111) planar channeling direction.

From these channeling results, it is important to point out that the preferential sites of the Ni atoms are incompatible

with any of the crystal structures of nickel silicides such as Ni_2Si, Ni_3Si_2, NiSi and $NiSi_2$. Instead, all the results are consistent with $\sim 2.1 \times 10^{15}/cm^2$ of Ni atoms being located at the tetrahedral sites of the Si crystalline matrix. Inside a perfect Si crystal, large interstitial voids are formed by Si cages consisting of ten Si atoms having the "adamantane" structure.[24] Such a cage is illustrated in Fig. 27(a), with six of the Si atoms taking up vertices of an octahedron (B sites) and four Si atoms taking up the vertices of a tetrahedron (A sites). The Si-Si bonds are depicted as tapered arrows in the diagram. With the Ni atom situated at the center of the polyhedron, the projections of the sites along various channeling directions are shown in Fig. 27(b). "Shadowing" of tetrahedral sites by the Si host atoms is found along the <100> and <111> axial, and (100) and (110) planar channeling directions. Along the <100> axial and (111) planar channeling directions, the tetrahedral sites will be exposed to the channeled beam and the channeled scattering yields are expected to be higher than the random scattering yields.

Once the symmetry of the preferential site has been established, detailed features of the angular scan curves can provide extra structural information. For those curves with angular dips, the channeling half angle ($\psi_{\frac{1}{2}}$) of the Ni yield are considerably smaller than those of the Si host

atoms. For axial channeling, the ratio of the channeling half-angles ($\psi_{1/2}^{Ni}/\psi_{1/2}^{Si}$) is about 2/3 and the ratio decreases to 1/2 for planar channeling. As for the angular scan curves with higher than random scattering yields along channeling directions, the flux-peaking effect is less prominent than theoretical predictions.[25] These two observations suggest that the Ni atoms at the tetrahedral sites are not exactly registered with the Si bulk crystalline matrix. Recent channeling studies of the Ni-Si interface[26] have shown that the interfacial layer consists of non-registered Si atoms for monolayers of Ni coverage. From these studies, the angular scan results can be rationalized by having the Ni atoms at the tetrahedral site straining the atoms of the Si cage. The resulting equilibrium positions of the Ni atoms in these distorted cages will no longer be perfectly shadowed by the Si atomic rows or planes of the crystalline matrix. To obtain a rough estimation of the lateral displacements of the Ni atoms, the transverse kinetic energy of the incident beam at $\psi_{1/2}^{Ni}$ is equated to Linhard's continuum potential at a distance r from the Si atomic rows[27],

$$E(\psi_{1/2}^{Ni})^2 = U(r) = \frac{Z_1 Z_2 e^2}{d} \ell n \left\{\left(\frac{\sqrt{3}a}{r}\right)^2 + 1\right\} \qquad (12)$$

From the <100> and <111> angular scan curves, the values of $\psi_{1/2}^{Ni}$ are 0.34° and 0.38°, respectively, and they both give a value of ~0.3 Å for r. The planar channeling results are

consistent with the effects of such displacements by having a smaller dip along the (100) planes (d_p = 1.36 Å) than the (110) planes (d_p = 1.92 Å).

As for the origin of the Ni-Si lattice distortion, we have proposed a simple model based on atomic size effects. With a single Ni atom located at the tetrahedral site, the nearest Si neighbors are those atoms at site A. The Ni-Si distance is 2.35 Å and is identical to that of the Si-Si distance. Using an atomic radius of 1.24 Å for Ni,[28] the hard-sphere model will require a Ni-Si separation of 2.41 Å and is only 0.06 Å larger than the allowed spacing. Therefore the Ni atom can fit snugly inside the Si cage.

The situation is quite different if every tetrahedral site is taken up by Ni atoms. Since the tetrahedral sites also form a diamond lattice with exactly the lattice parameter as Si, the nearest neighbor distance is 2.35 Å. A side-view of the lattice is illustrated in Fig. 28(a) with the appropriate inter-site distances. Let us assume that sites labeled A, B and C in the figure are occupied by Ni atoms. The hard-sphere model will require atom C to be separated from atoms A and B by 2.49 Å but the available inter-site distance is 2.35 Å. Consequently, situations as depicted in Figs. 28(b) and (c) can happen, with atoms A and B displaced relatively by 0.34 Å along the <110> direction or atom C displaced by 0.23 Å along the <100> direction.

Because each Si atom is in intimate contact with four interstitial Ni atoms, the strain will propagate throughout the interfacial layer.

The success of this thin-crystal channeling technique may open up new possibilities for interfacial studies. For example, the atomic structure of the metal-silicon interface has been a matter of controversy for sometime. Based on free energy considerations, a reactive interface such as the Ni-Si system should have a graded interfacial region in composition, structure or probably both. This interfacial region has been observed by channeling and photoemission techniques.[4,26,29] Tu[13] has postulated an interstitial diffusion mechanism at the interface to explain the low-temperature formation of near-noble metal silicides. Walser and Bené[30] have also proposed an interfacial model with the interfacial region being amorphous and with the lowest eutectic composition to explain the first silicide phase being nucleated. For the Ni-Si system, the present channeling results show that the first interfacial layer consists of interstitial Ni atoms inside the Si crystalline matrix. If a structureless interfacial region does exist, it is reasonable to assume that such a region has to occur between the interstitial layer and the metal or silicide layer.

In summary, it has been demonstrated that preferential sites of deposited metal atoms on Si substrates can be located by a thin-crystal channeling experiment. For the

Ni-Si system, $\sim 2.1 \times 10^{15}$ Ni atoms/cm^2 are located at the tetrahedral sites of the Si crystalline matrix.

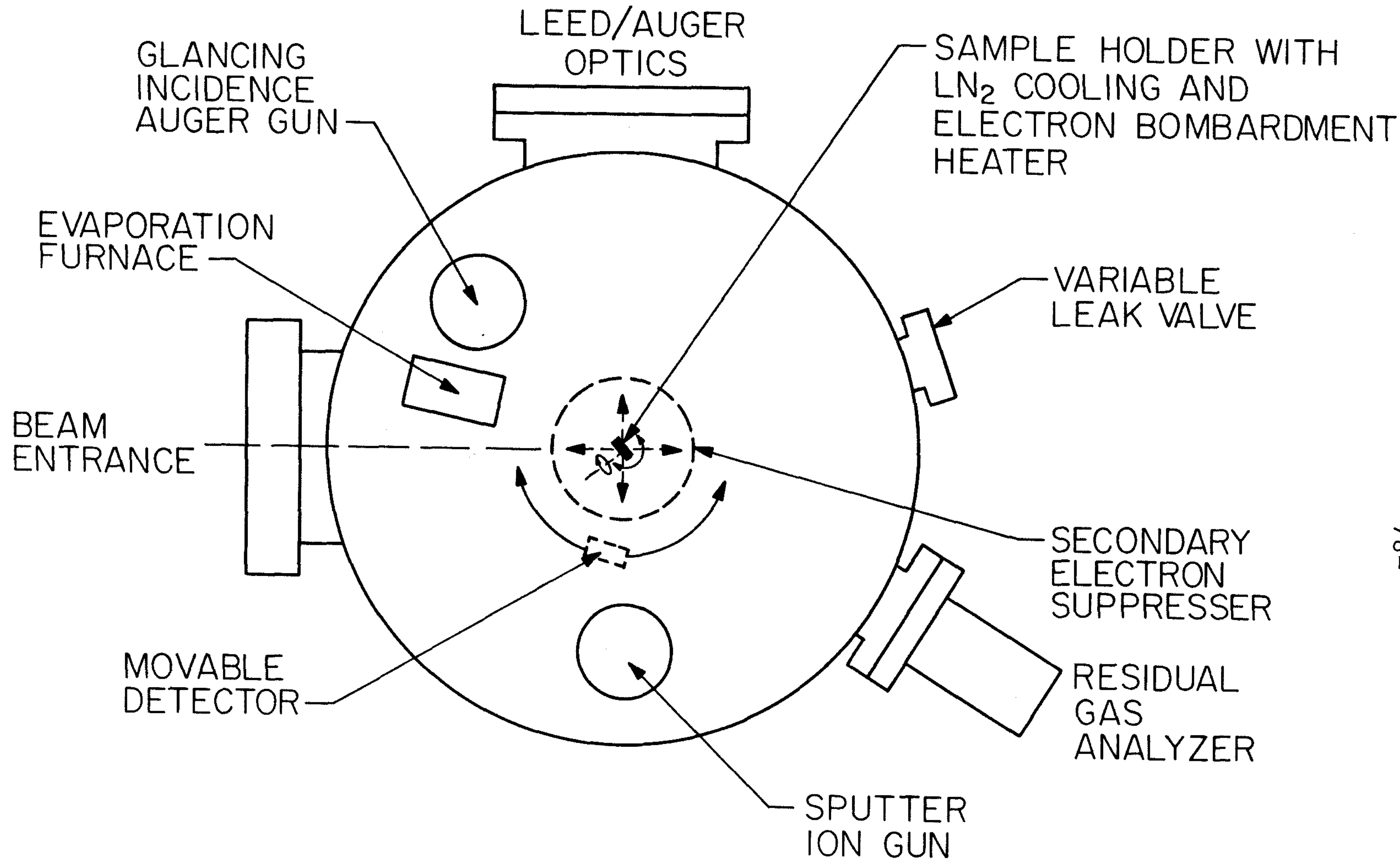

Figure 12 Schematic of UHV chamber designed for channeling studies of surfaces and interfaces

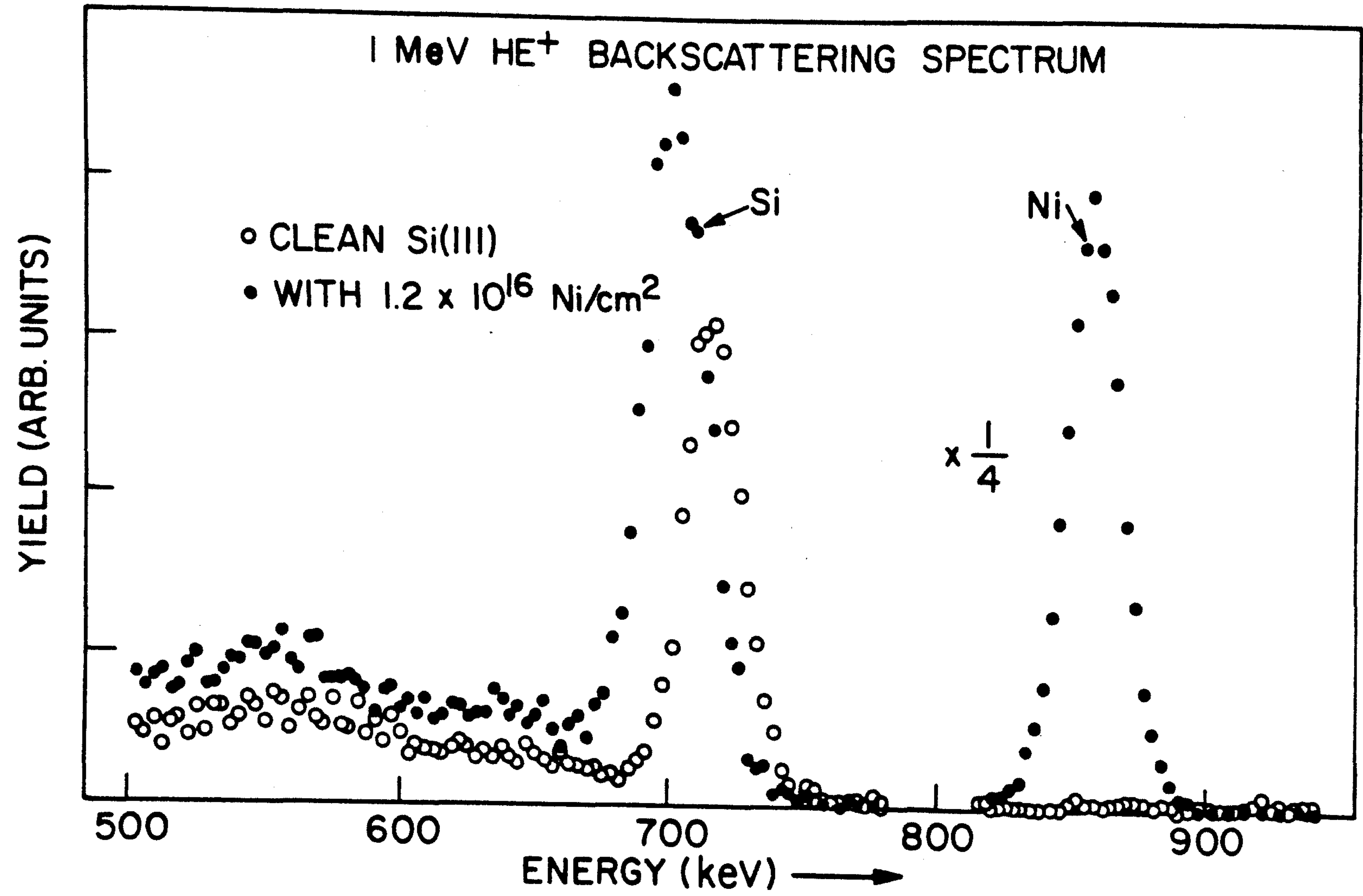

Figure 13 Backscattering spectra for 1.0 MeV ^{4}He incident on a clean Si (111) surface (open circles) and a Si (111) surface covered with 1.2 X 10^{16}Ni/cm^2 (closed circles). The scattering angle is ∿100°.

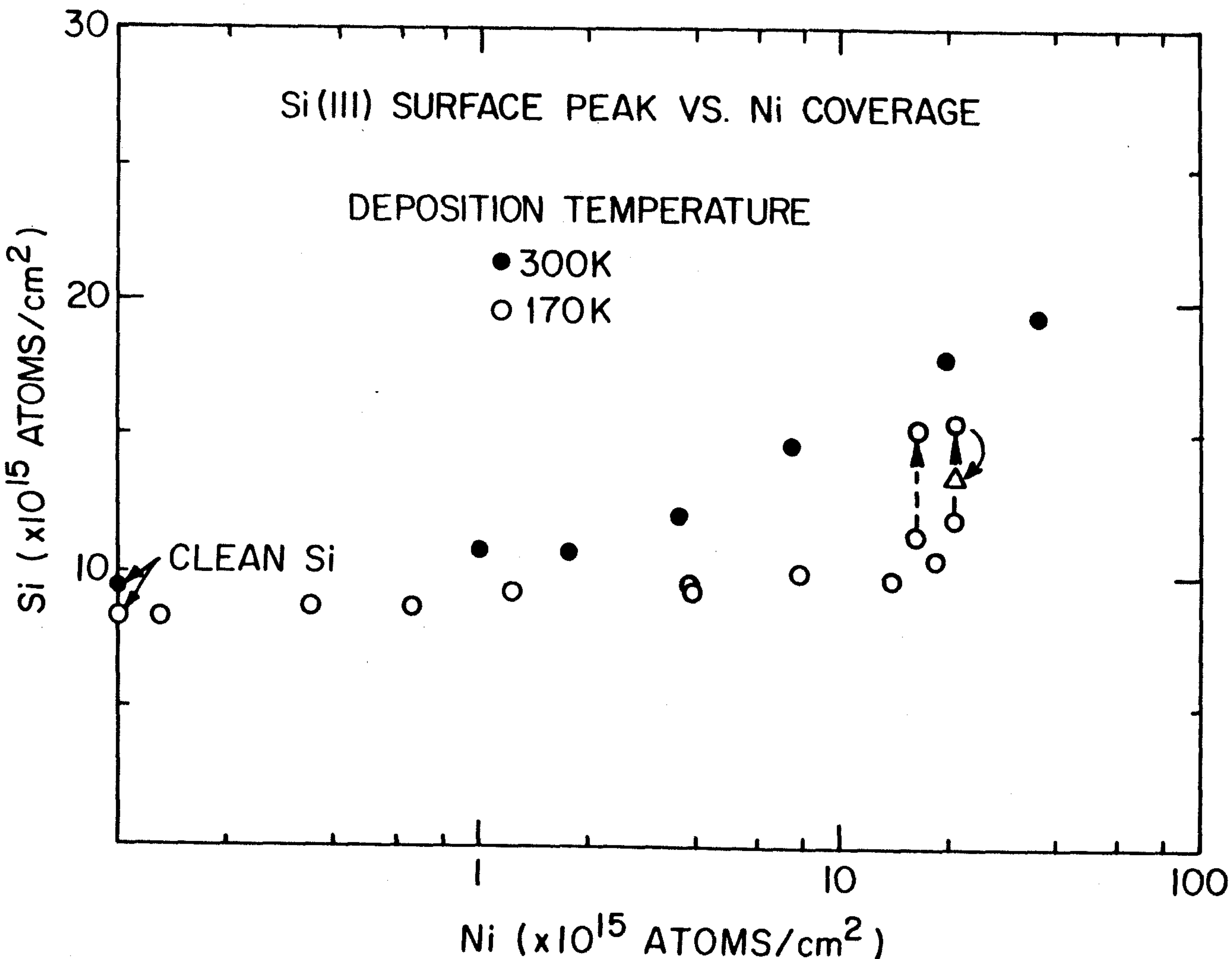

Figure 14 Si interface peak as a function of Ni coverage for deposition at ~ 300°K (full circles) and deposition at ~ 170°K (open circles). The broken arrows indicate the increase of the interface peak which occurs with the slow warming of a 170°K deposition to 300°K. The triangular point indicates analysis at 170°K after warming to 300°K for eight hours.

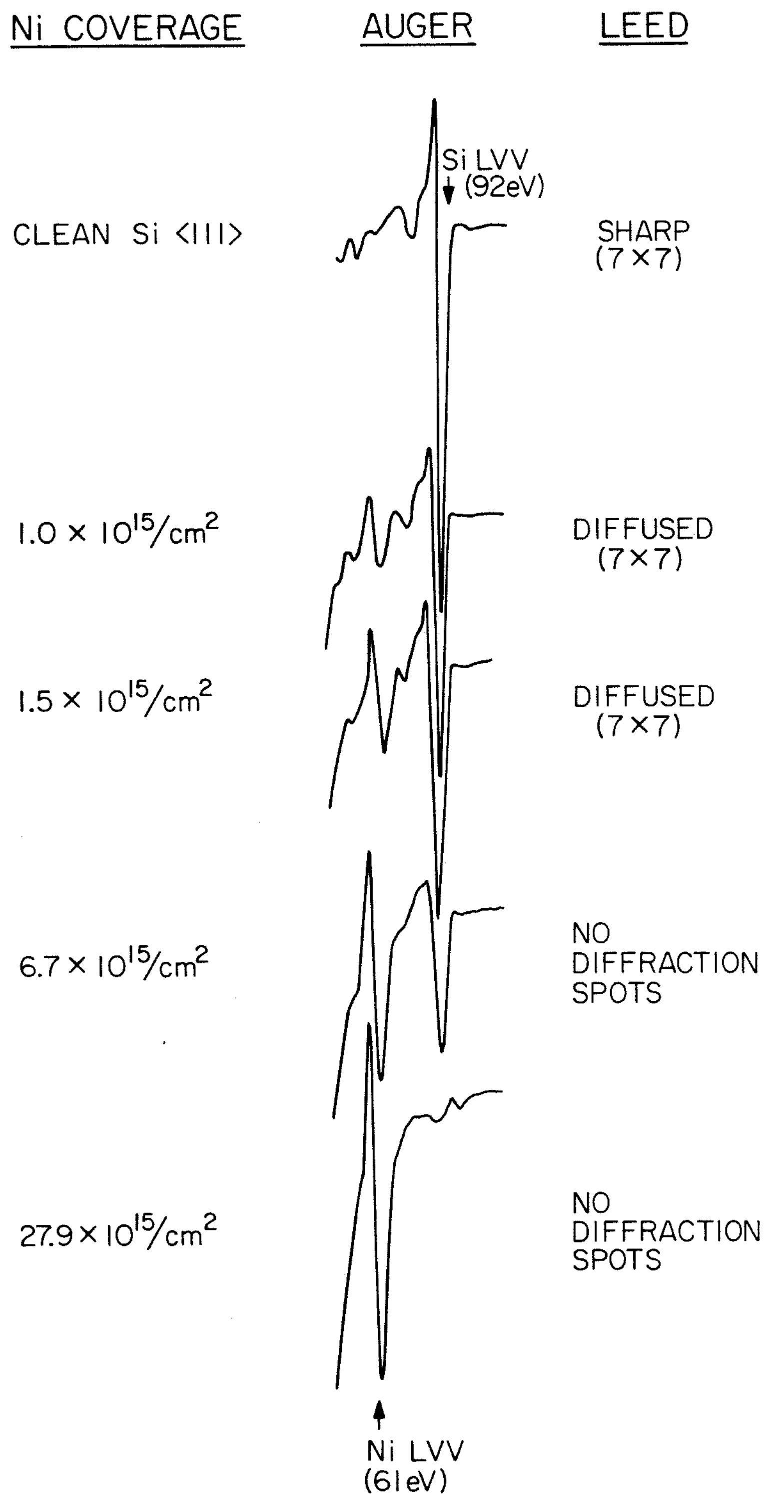

Figure 15 Auger spectra and LEED observations as a function of Ni coverage on a Si (111) surface. The deposition temperature is at 325°K.

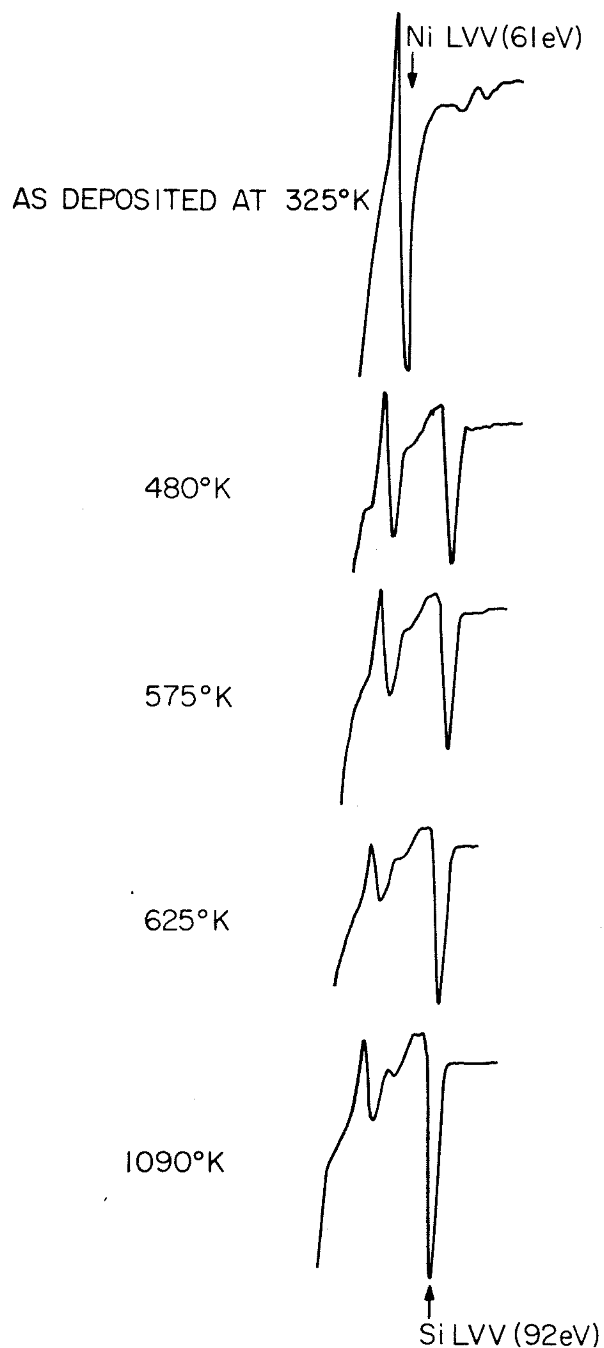

Figure 16 Auger spectra of a Ni-covered Si (111) sample after various heat-treatments.

DEPOSITION TEMPERATURE
AT 325°K
15.7×10^{15} Ni/cm^2

DEPOSITION TEMPERATURE
AT 170°K
16.3×10^{15} Ni/cm^2

Figure 17 Auger spectra of two Ni-covered Si (111) samples. At the higher deposition temperature, the Si LVV signal (92eV) shows a higher intensity; it denotes the Si is closer to the Ni surface.

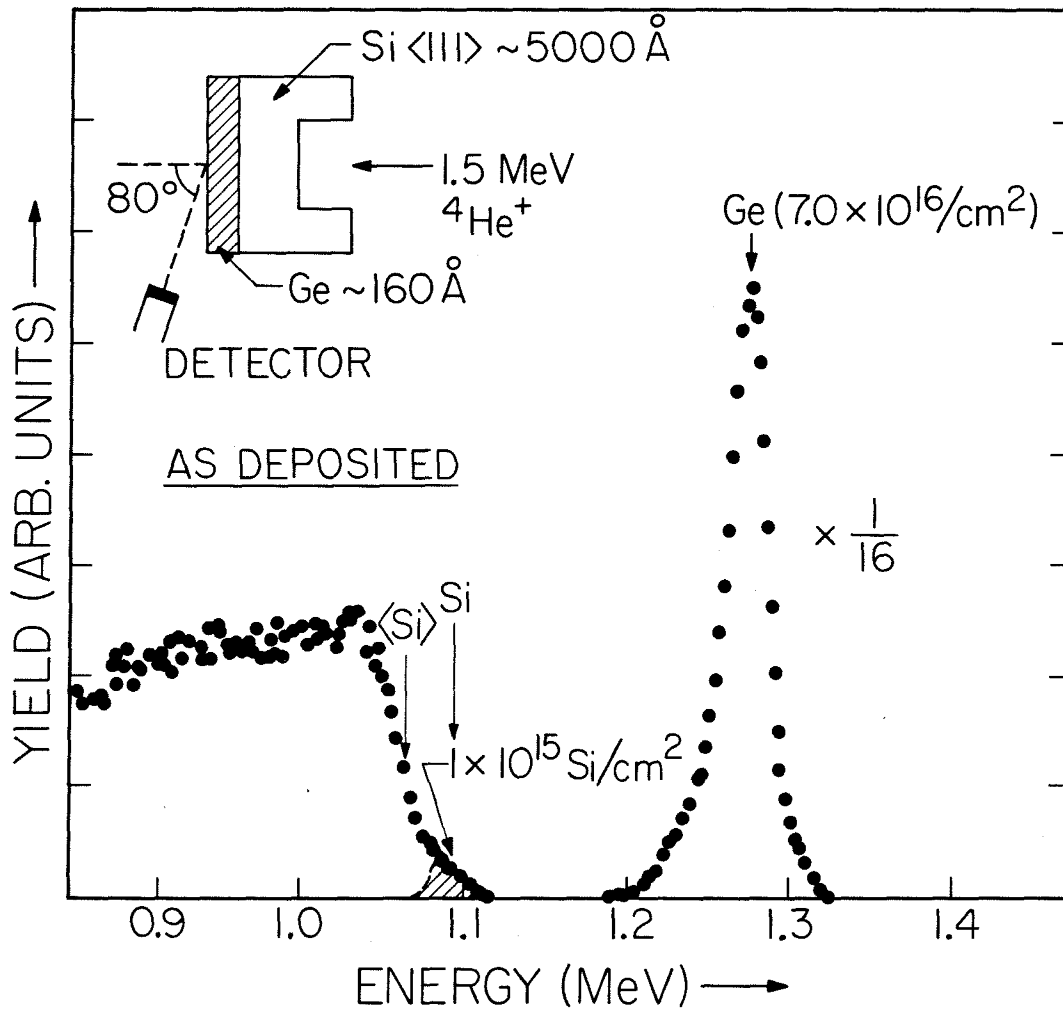

Figure 18 Transmission channeling spectrum of a Ge-covered Si (111) thin crystal. The shaded area represents non-registered Si at the Ge-Si interface.

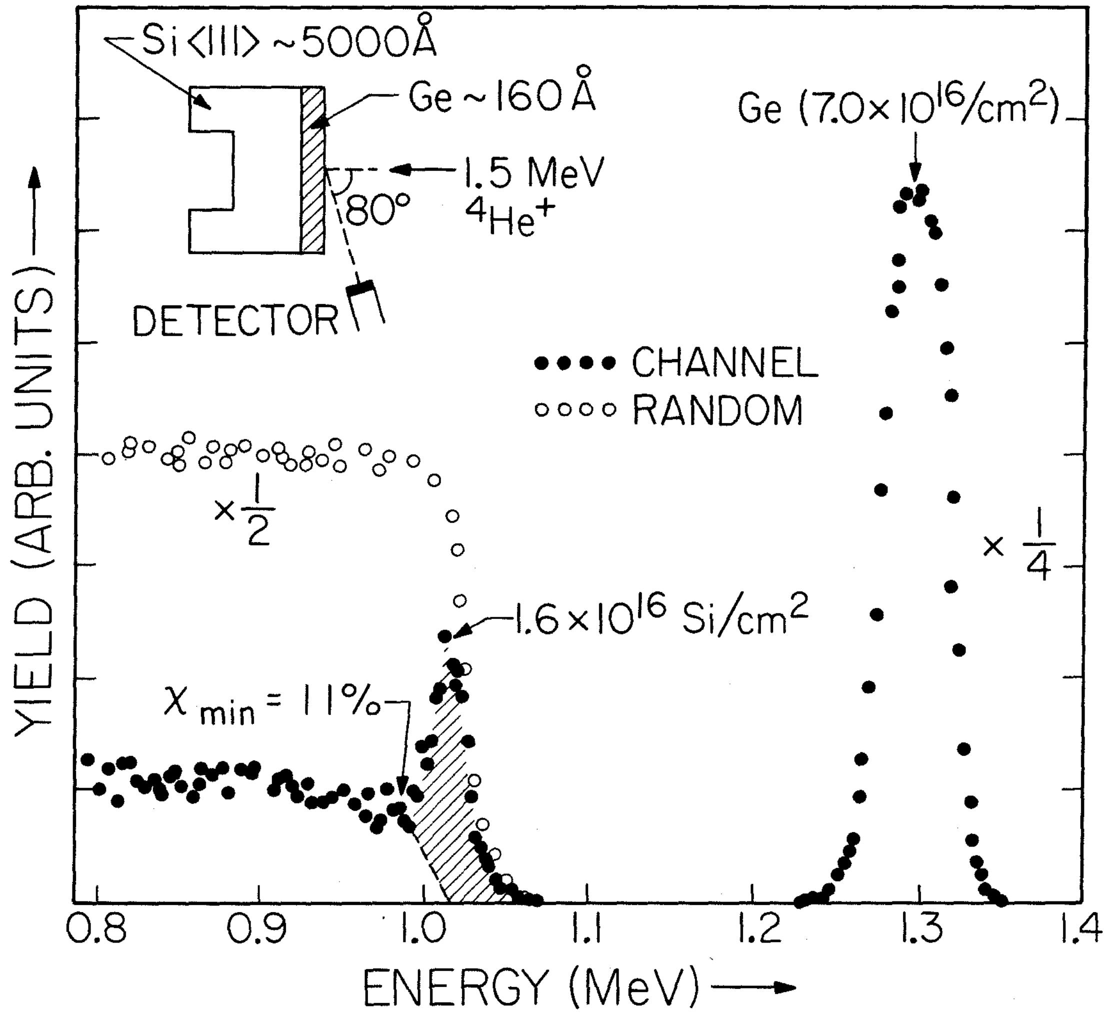

Figure 19 Conventional channeling and random spectra of a Ge-covered Si (111) thin crystal. The shaded area represents the Si interface peak.

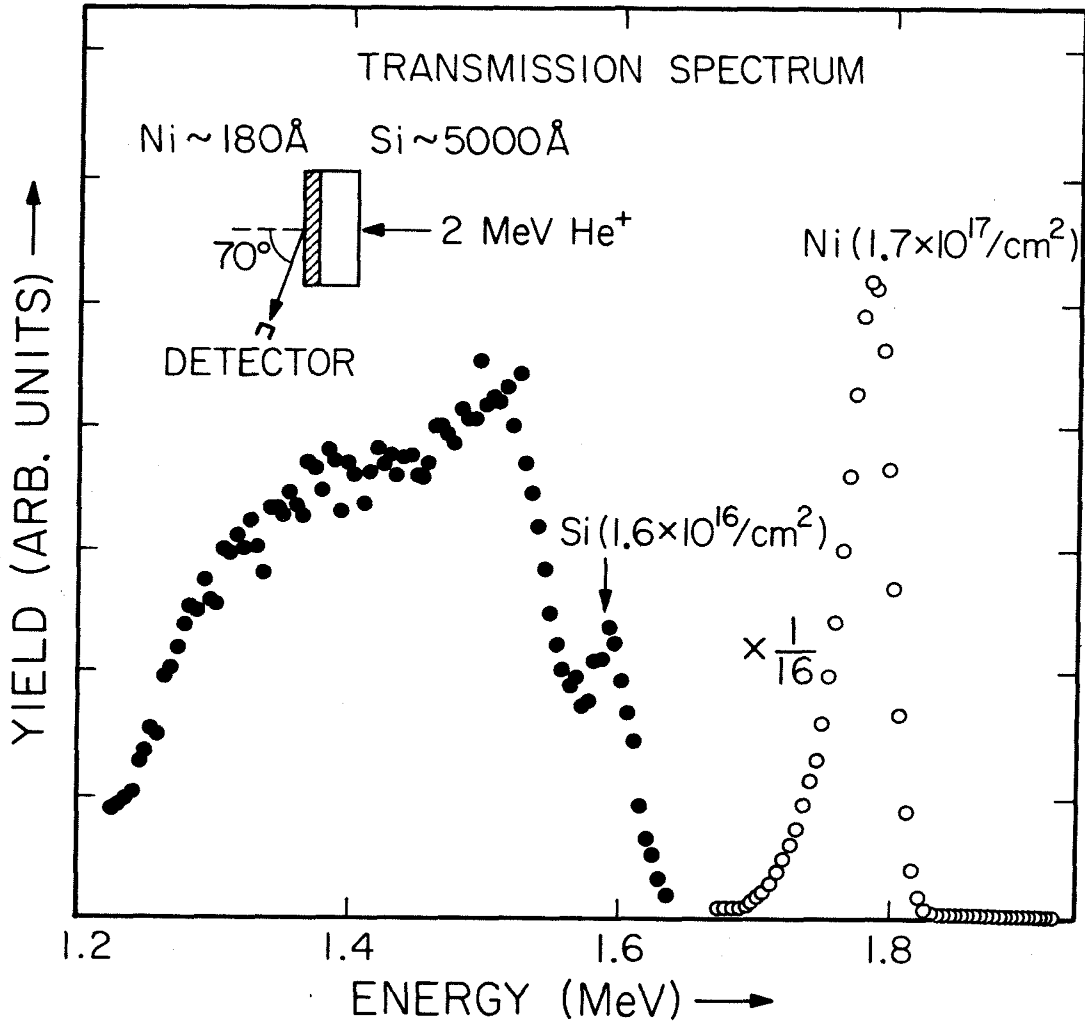

Figure 20 Transmission channeling spectrum of a Ni-covered Si (100) thin crystal with 1.7×10^{17} Ni atoms/cm^2. The open circles indicate the Ni signal and the full circles correspond to scattering from Si. The arrow indicates the "interface peak" associated with scattering from non-registered Si at the Ni-Si interface.

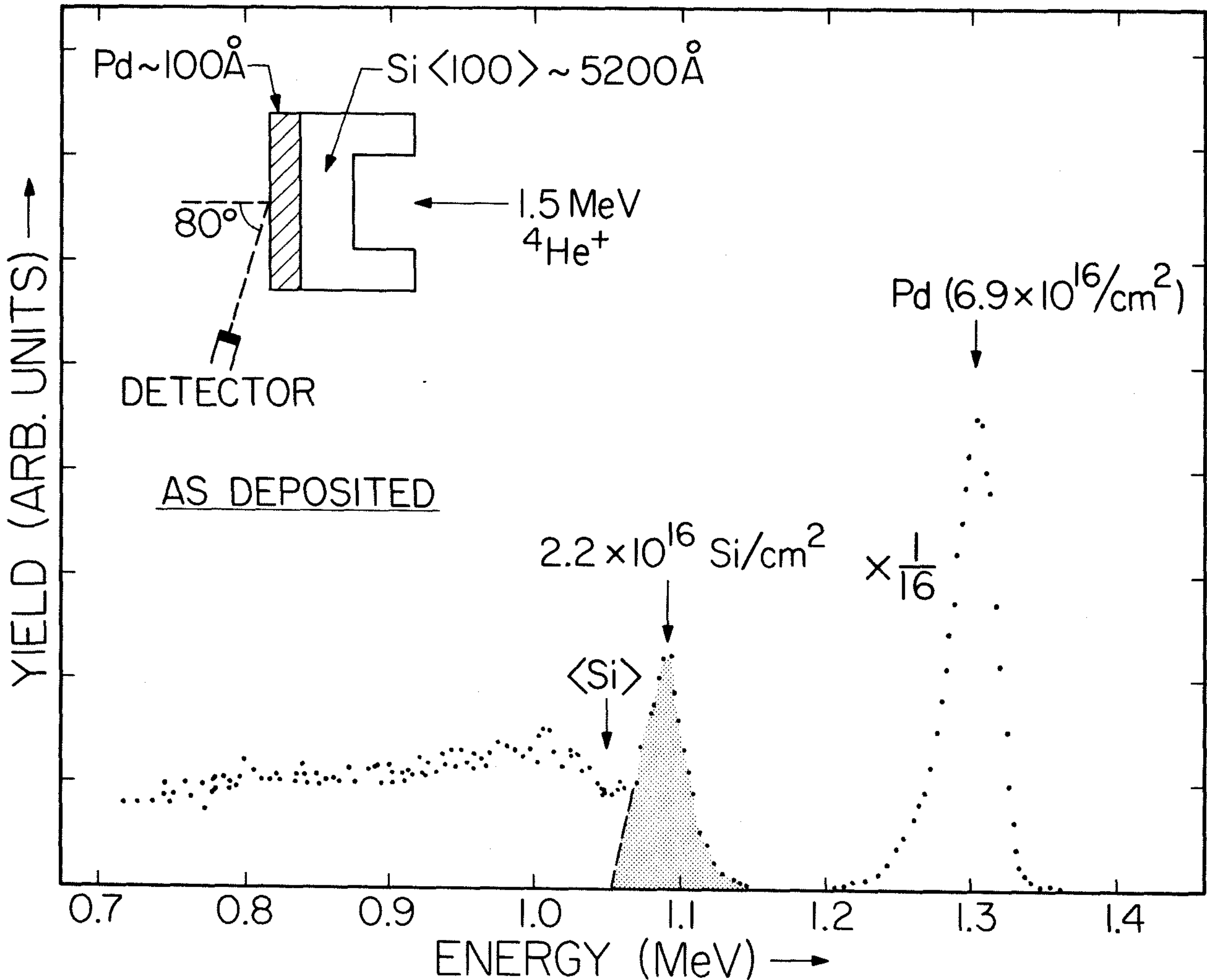

Figure 21(a) Transmission channeling spectrum of a Pd-covered Si (100) thin crystal. The dotted area represents the non-registered Si at the Pd-Si interface.

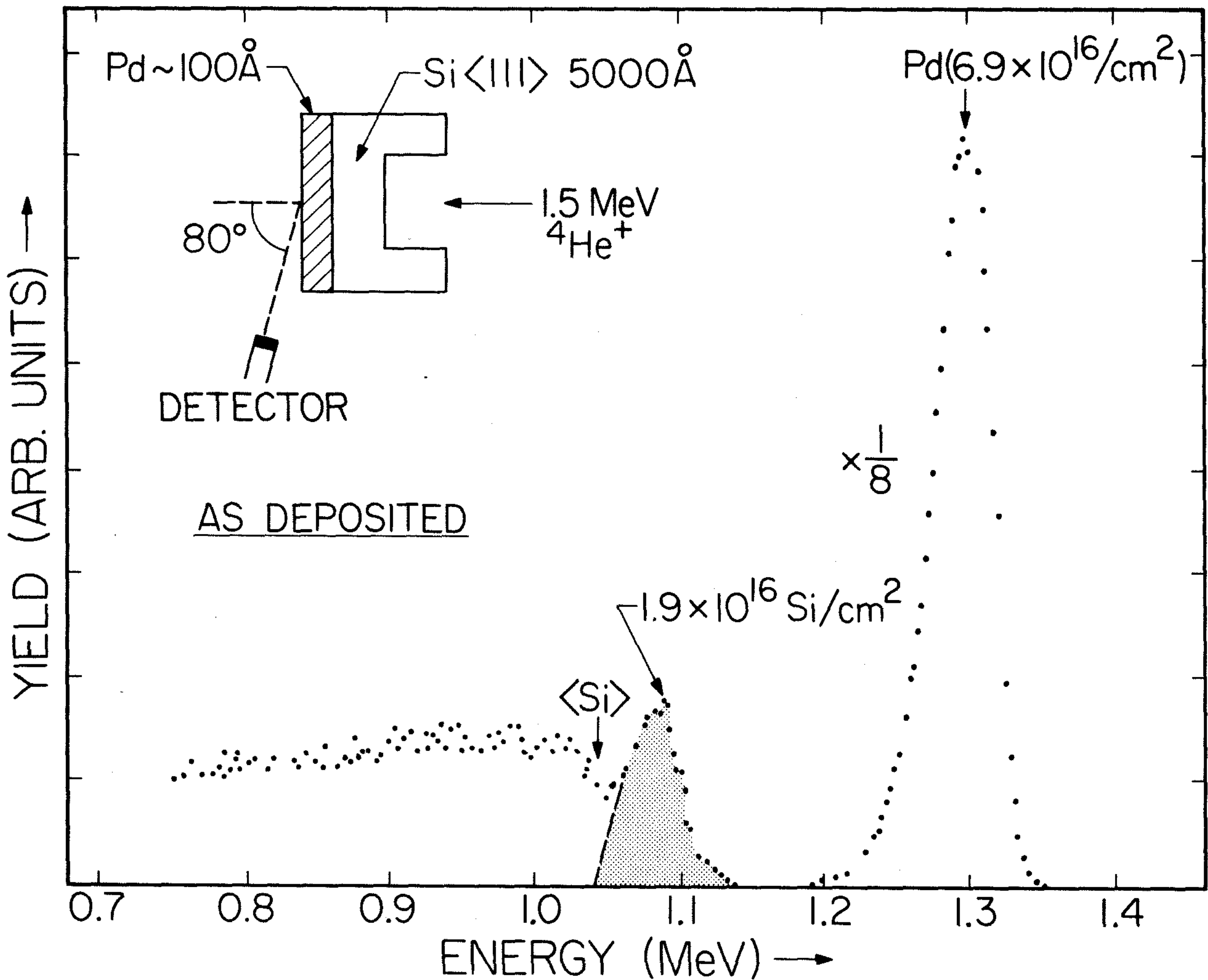

Figure 21(b) Transmission channeling spectrum of a Pd-covered Si (111) thin crystal. The dotted area represents the non-registered Si at the Pd-Si interface.

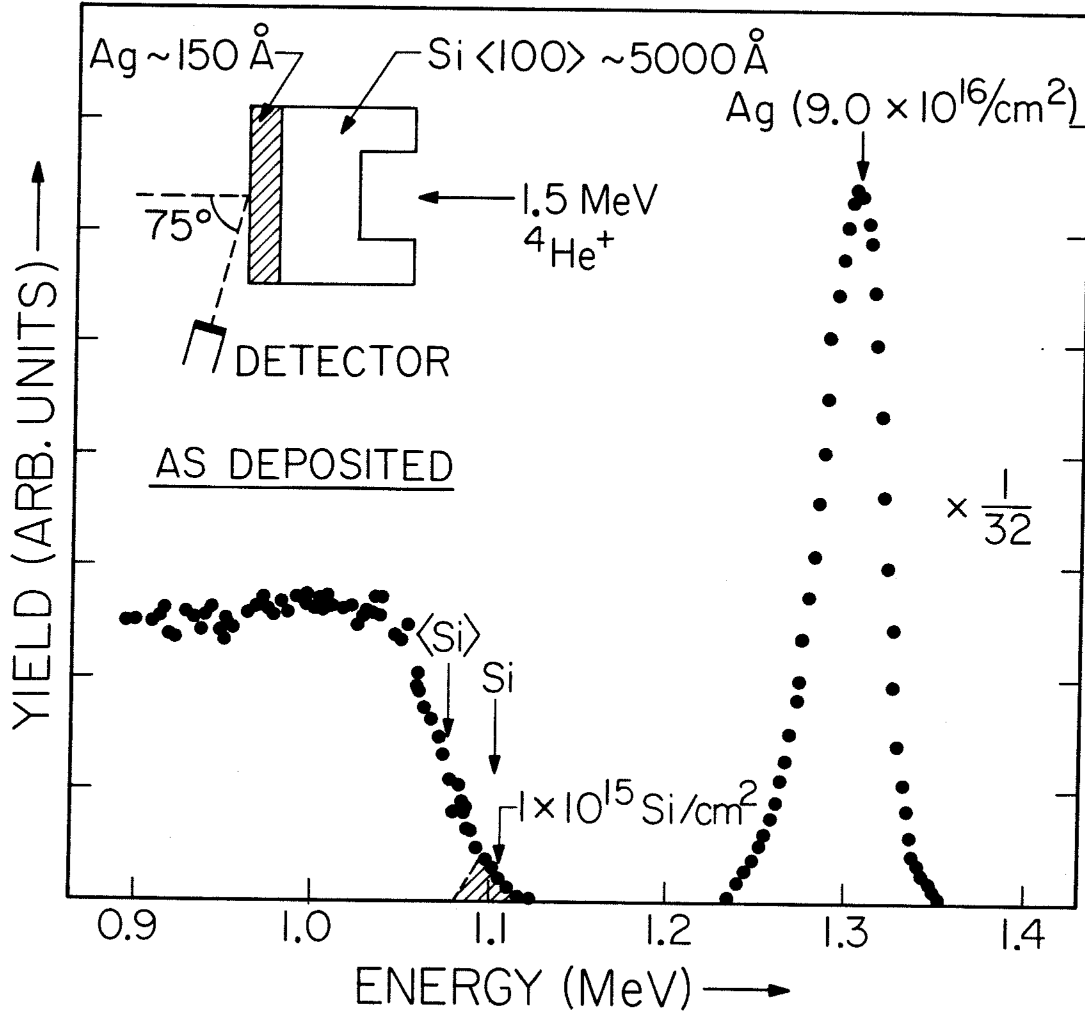

Figure 22 Transmission channeling spectrum of a Ag-covered Si (100) thin crystal. The shaded area represents the non-registered Si at the Ag-Si interface.

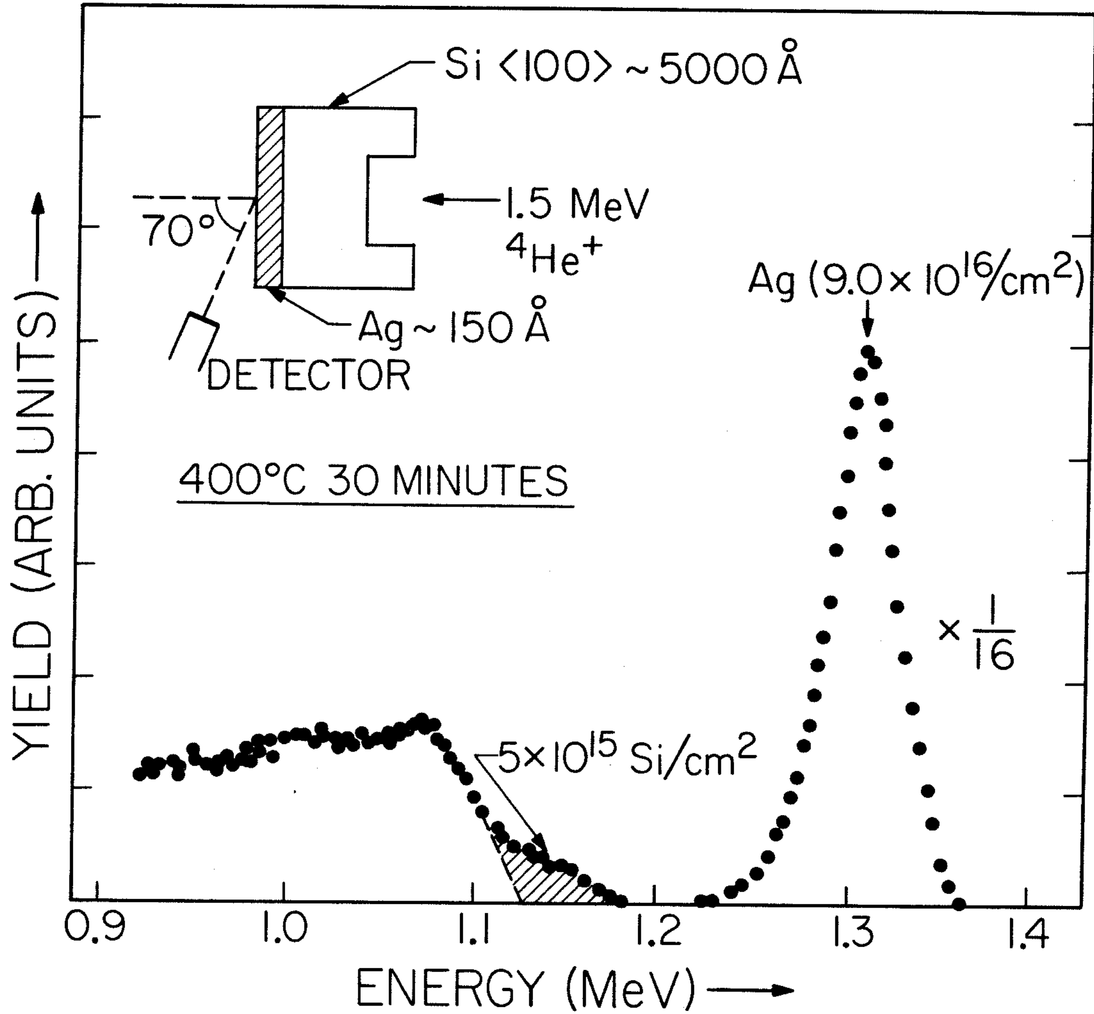

Figure 23 Transmission channeling spectrum of a Ag-covered Si (100) thin crystal after anneal at 400°C for 30 minutes. The shaded area represents the non-registered Si.

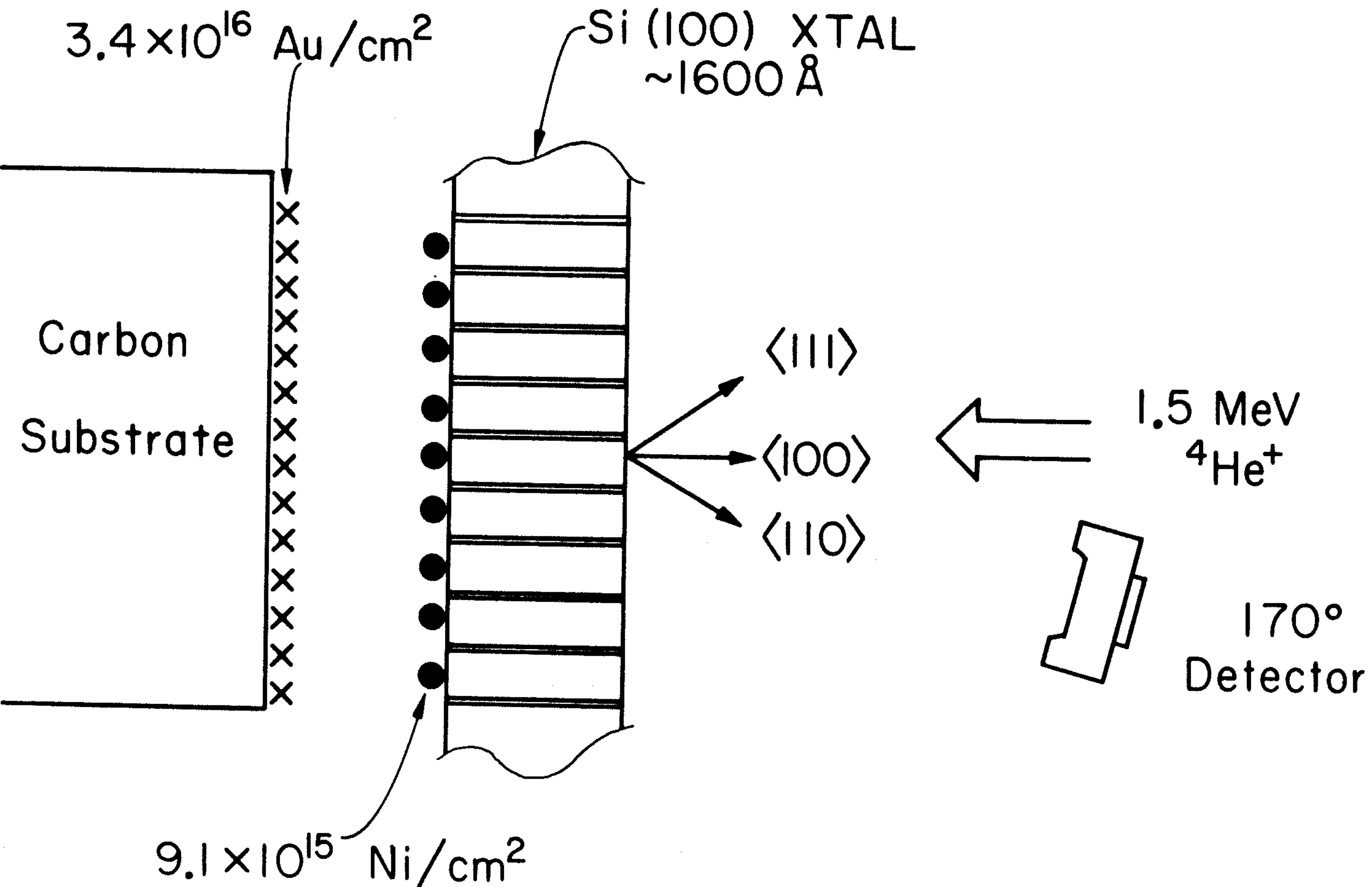

Figure 24(a) Schematic of lattice location experiments by thin-crystal channeling.

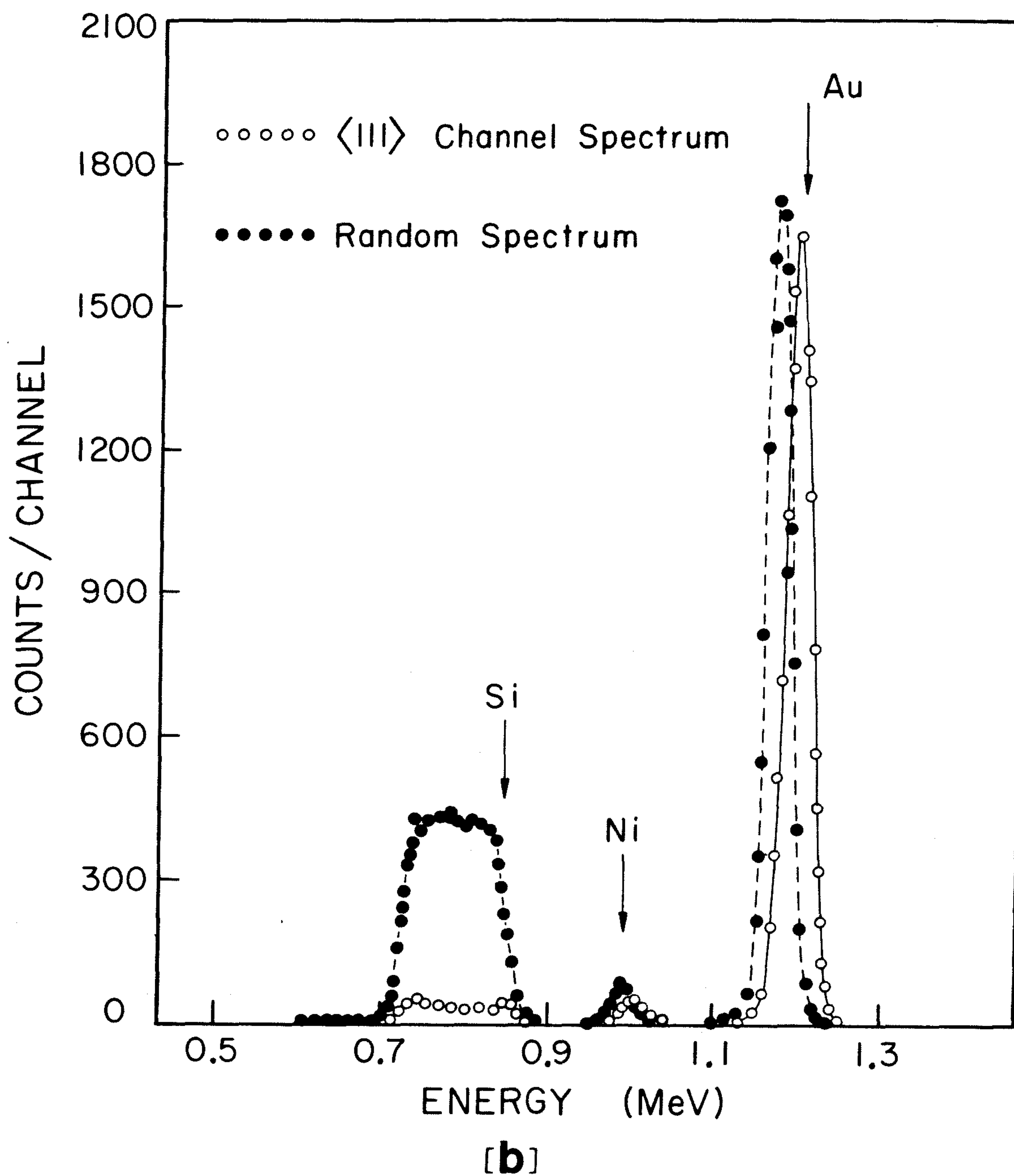

Figure 24(b) Channeled and random backscattering spectra showing energy positions of the Si, Ni and Au signals. The channeling direction is the <111> axis of the Si thin crystal.

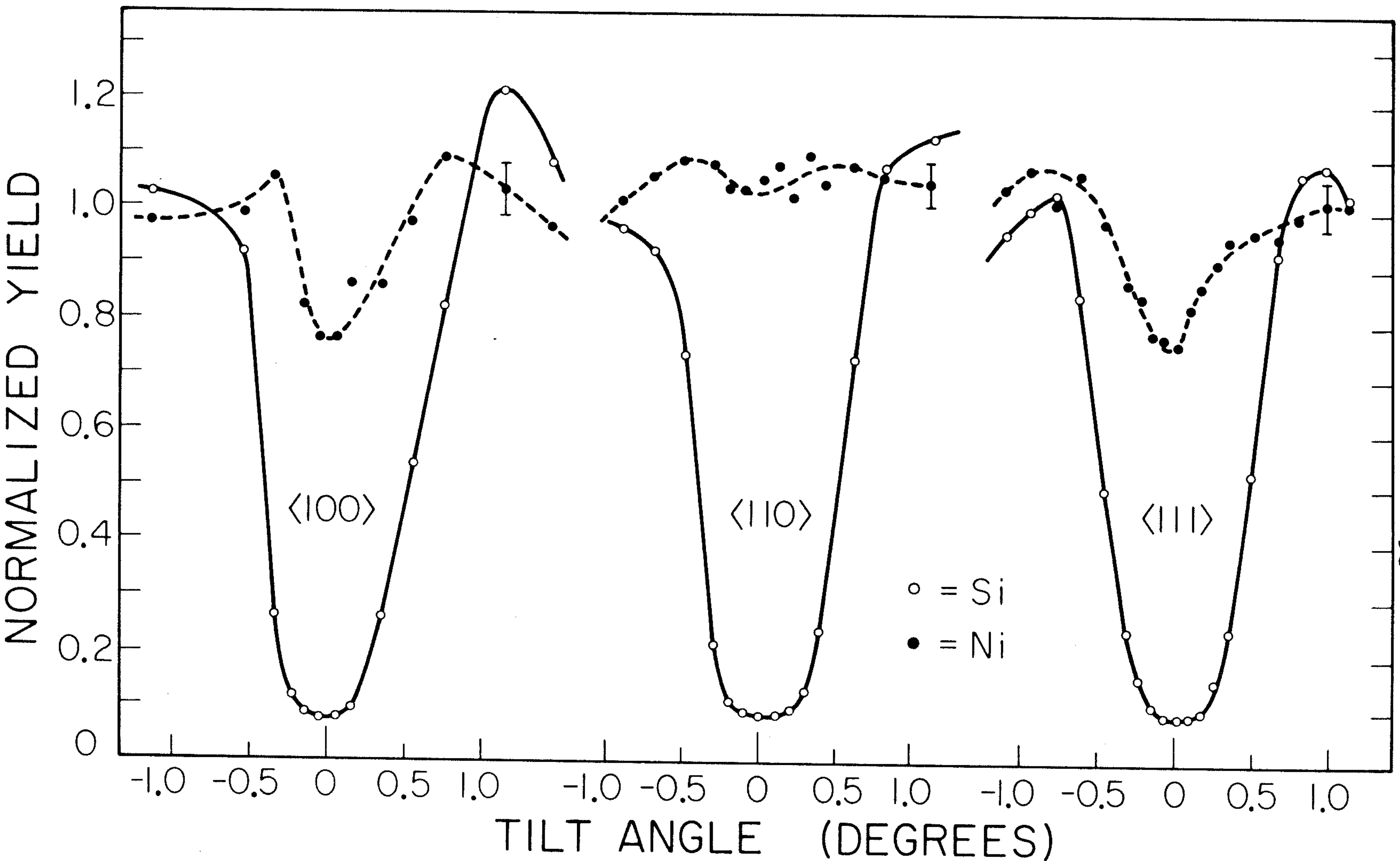

Figure 25 Angular scan curves of the Si(O) and Ni(●) total scattering yields, normalized by the Au yield, along the <100>, <110> and <111> axes. The random yields are defined to be unity.

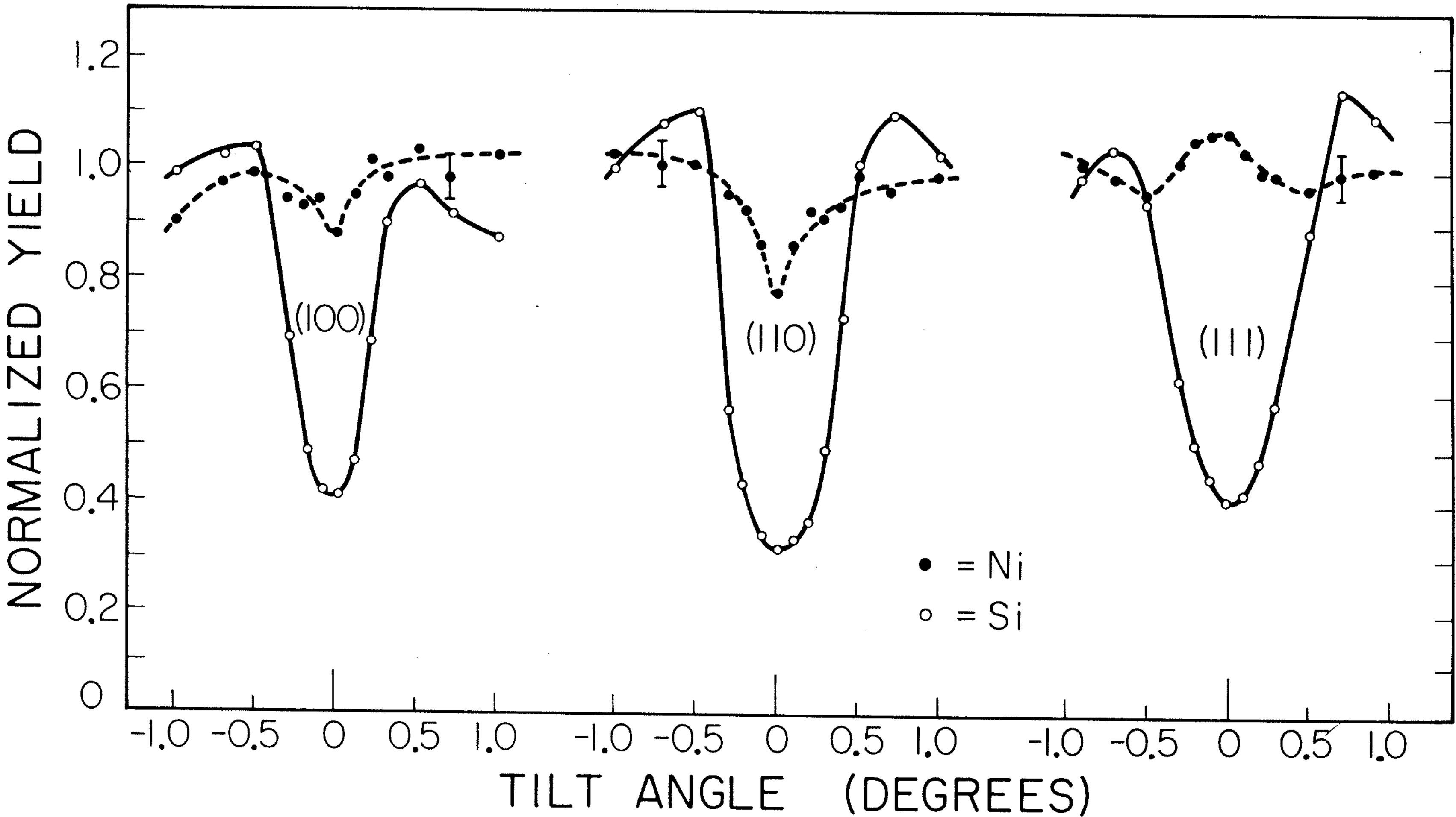

Figure 26 Angular scan curves of the Si(O) and Ni(●) total scattering yields, normalized by the Au yield, along the (100), (110) and (111) planes.

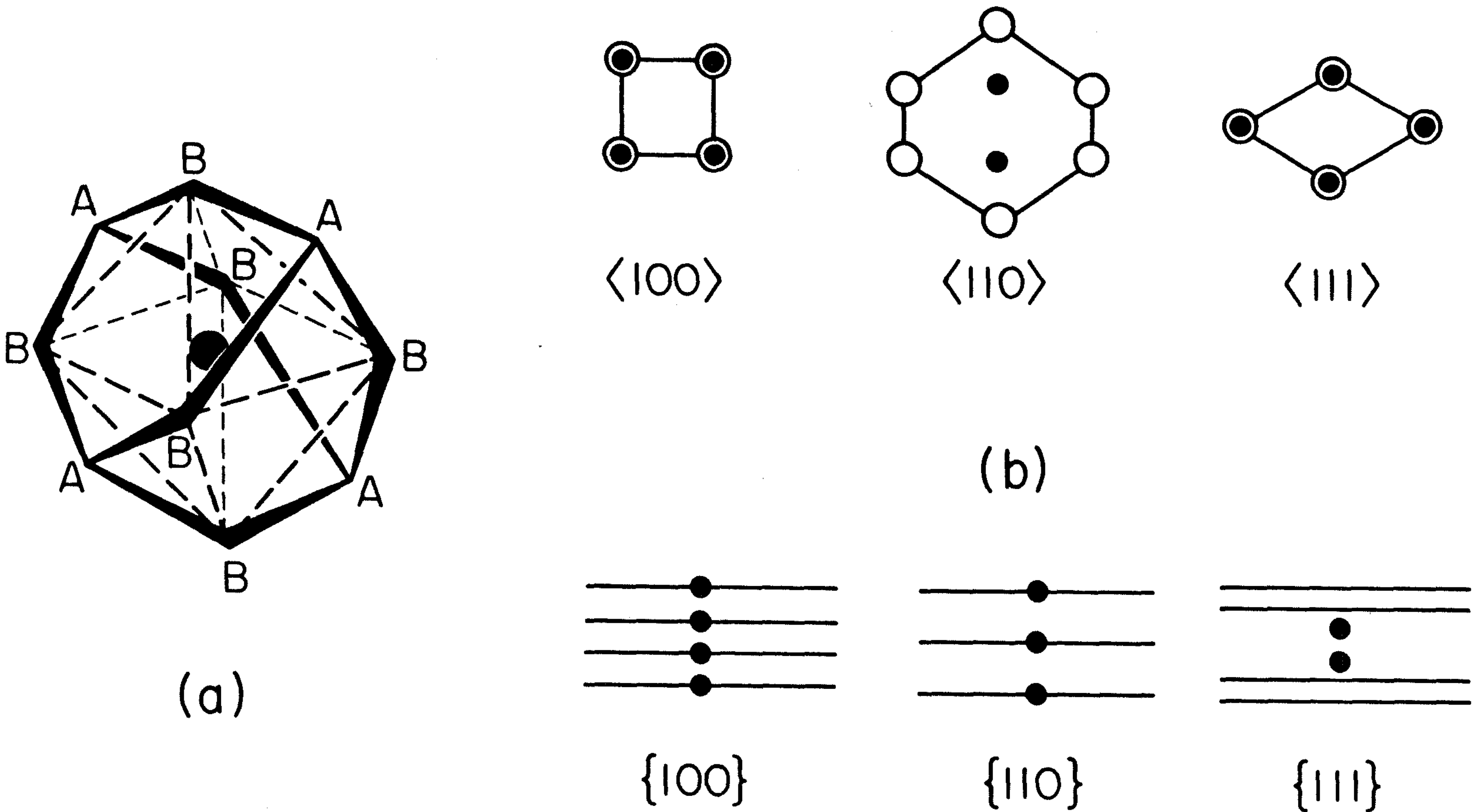

Figure 27 (a) The adamantane structure of the Si cages inside a Si crystal. The tetrahedral site is depicted by the solid circle at the center of the polyhedron.

(b) Projected positions of the tetrahedral sites (●) along the various major channeling directions of a diamond lattice. The Si atomic rows are represented by open circles (O) and the Si atomic planes are represented by full lines ——— .

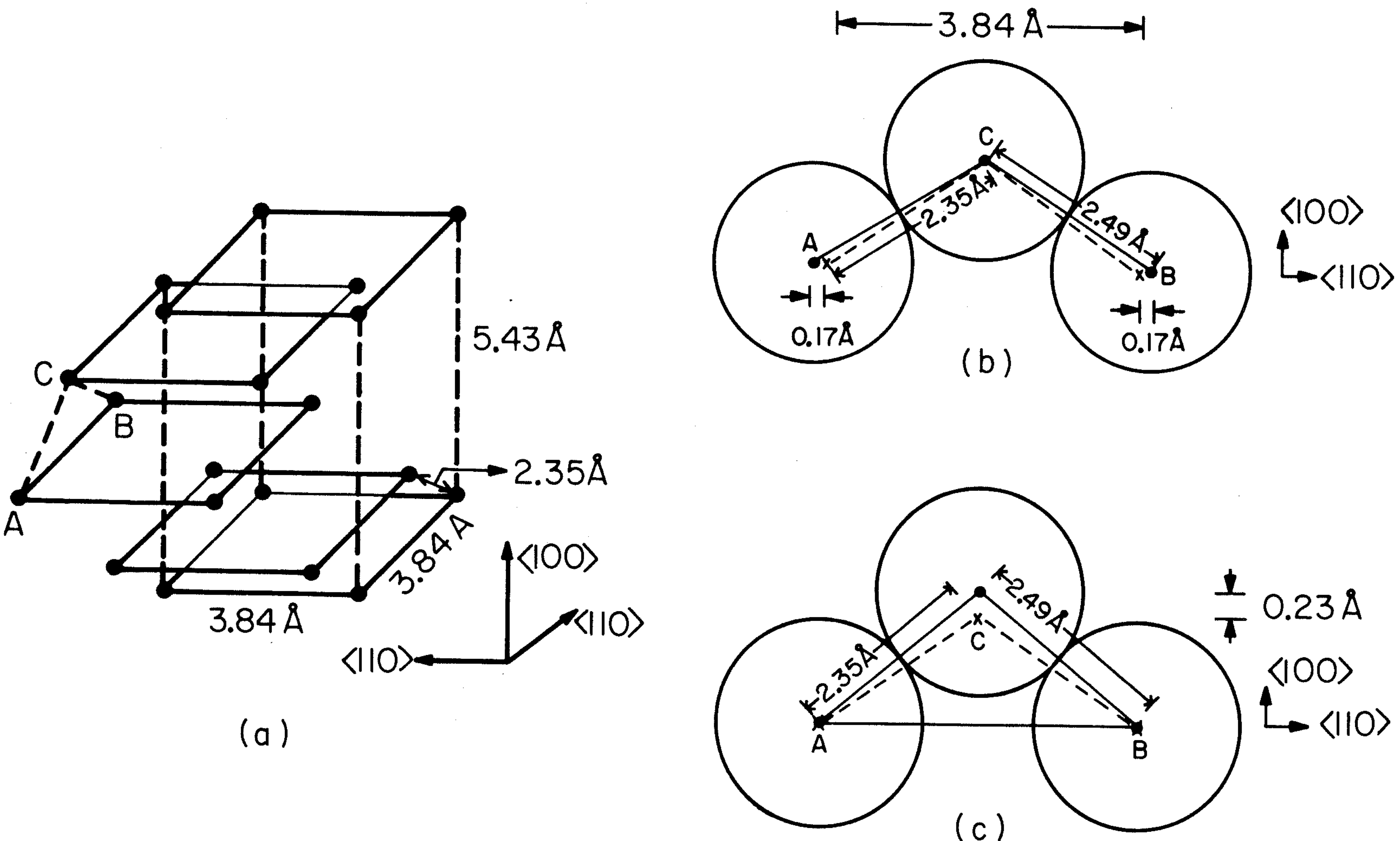

Figure 28 (a) The diamond lattice of the tetrahedral sites of Si. Schematics (b) and (c) show the possible displacements of Ni atoms when occupying the tetrahedral sites of Si.

TABLE 3 SUMMARY OF CONVENTIONAL CHANNELING RESULTS WITH THIN METAL OVERLAYER ON Si CRYSTALS.[(a)]

Metal	Si Substrate	Areal Density of metal in 10^{16} atoms/cm^2	Areal Density of Si Peak in 10^{16} atoms/cm^2	Si χ_{min}	$\theta_{1/2}^{Metal}$	Formation Temperature of First Silicide Phase(17)
Ni	<100>	8.1	3.3	0.12	0.07°	200-350°C (Ni_2Si)
	<111>	7.8	2.9	0.10		
Pd	<100>	5.0	7.9	0.35	0.05°	100-700°C (Pd_2Si)
	<111>	5.0	5.1	0.12		
Pt	<100>	7.8	5.0	0.33	0.23°	200-500°C (Pt_2Si)
Cr	<100>	10.5	2.0	0.15	0.08°	450°C ($CrSi_2$)
	<111>	9.8	2.0	0.10	0.08°	
V	<100>	6.5	2.1	0.09	0.05°	600°C (VSi_2)
Au[(b)]	<111>	6.0	2.1	0.39	-	-
Ge	<111>	7.0	1.6	0.11	0.06°	-

(a) With 1.5 MeV ^4He ions, the intrinsic Si surface peaks are 1.03×10^{16} and 0.94×10^{16} atoms/cm^2 for <100> and <111> axes respectively.

(b) The Au layer is epitaxial on Si (111) (χ_{min} = 43%).

TABLE 4 SUMMARY OF THIN-CRYSTAL CHANNELING RESULTS ON METAL-SILICON INTERFACES

Metal	Si Substrate	Areal Density of metal in 10^{16} atoms/cm^2	Areal Density of Si peak in 10^{16} atoms/cm^2
Pd	<100>	6.9	2.2
	<111>	6.9	1.9
Ni	<100>	16.9	1.6
Ag	<100>	9.0	<0.1
	<111>	9.0	<0.1

References

(1) R. J. Culbertson, L. C. Feldman and P. J. Silverman, to be published.

(2) J. W. T. Ridgway and D. Haneman, Surf. Sci., 26, 683 (1971).

(3) K. C. R. Chiu, J. M. Poate, L. C. Feldman and C. J. Doherty, to be published in Appl. Phys. Lett.

(4) P. Grunthaner and J. W. Mayer, Proceedings of the Seventh Annual Conference on the Physics of Compound Semiconductor Interfaces, Estes Park, Colorado, 1980.

(5) M. P. Seals and W. A. Dench, Surface and Interface Analysis, 1, 1 (1979).

(6) G. Ottaviani, K. N. Tu and J. W. Mayer, Phys. Rev. Lett., 44, 284 (1980).

(7) E. H. Rhoderick, Metal-Semiconductor Contacts, (Clarendon Press, Oxford, 1978), p. 176.

(8) J. L'Ecuyer, J. A. Davies and N. Matsunami, Nucl. Instrum. Meth., 160, 337 (1979).

(9) L. S. Hung, to be published.

(10) E. Lugujjo and J. W. Mayer, Phys. Rev., B7, 1782 (1973).

(11) N. Cheung, S. S. Lau, M-A. Nicolet, J. W. Mayer and T. T. Sheng, to be published in the Proceedings of the Symposium on Thin Film Phenomena - Interfaces and Interactions, The Electrochemical Society Meeting, Los Angeles, California (October 14-19, 1979).

(12) W. K. Chu, S. S. Lau, J. W. Mayer, H. Müller and K. N. Tu, Thin Solid Films, 25, 393 (1975).

(13) K. N. Tu, Appl. Phys. Lett., 27, 221 (1975).

(14) A. Hiraki, E. Lugujjo, M-A. Nicolet and J. W. Mayer, Phys. Stat. Sol., A7, 401 (1971).

(15) A. Hiraki, K. Shuto, S. Kim, W. Kammura and M. Iwami, Appl. Phys. Lett., 31 611 (1977).

(16) J. Abbati, L. Braicovich and A. Franciosi, Solid State Comm., 33, 881 (1980) and L. Braicovich, C. M. Garner, P. R. Skeath, C. Y. Su, P. W. Chye, J. Lindau and W. E. Spicer, to be published in Phys. Rev. B.

(17) K. N. Tu and J. W. Mayer in Thin-Films - Interdiffusion and Reactions, edited by J. M. Poate, K. N. Tu and J. W. Mayer (Wiley-Interscience, New York, 1978), p. 359.

(18) G. Ottaviani, private communication.

(19) L. C. Feldman, P. J. Silverman, J. S. Williams, T. E. Jackman and I. Stensgaard, Phys. Rev. Lett., 41, 1396 (1978).

(20) M. Hansen, Constitution of Binary Alloys, (McGraw-Hill New York, 1958), p. 51.

(21) For example, see S. T. Picraux in New Uses of Ion Accelerators, edited by J. F. Ziegler (Plenum Press, New York, 1975), p. 229.

(22) J. F. Van der Veen, R. M. Tromp, R. G. Smeenk and F. W. Saris, Surf. Sci., 82, 468 (1979).

(23) F. H. Eisen, G. J. Clark, J. Boettiger and J. M. Poate, Rad. Eff., 13, 93 (1972).

(24) F. A. Cotton and G. Wilkinson, Advanced Inorganic Chemistry, (Wiley-Interscience, New York, 1971), p. 35.

(25) S. T. Picraux, W. L. Brown and W. M. Gibson, Phys. Rev., B6, 1382 (1972).

(26) N. W. Cheung, R. J. Culbertson, L. C. Feldman, P. J. Silverman, K. W. West and J. W. Mayer, submitted to Phys. Rev. Lett.

(27) J. A. Davies, in Channeling-Theory, Observations and Applications, edited by D. V. Morgan, (Wiley-Interscience, New York, 1973), p. 391.

(28) L. Pauling, The Nature of The Chemical Bond, (Cornell University Press, Ithaca, 1960), p. 403.

(29) L. Braicovich, J. Abbati, G. Ottaviani, J. N. Miller, S. Schwarz, P. R. Skeath, C. Y. Su, C. R. Helms, J. Lindau and W. E. Spicer, Proceedings of the Seventh Annual Conference on the Physics of Compound Semiconductor Interfaces, Estes Park, Colorado, 1980.

(30) R. M. Walser and R. W. Bené, Appl. Phys. Lett., 28, 629 (1976).

CHAPTER 4

SILICIDE-SILICON INTERFACES

4.1 The Pd_2Si-Si Interface

Palladium silicide, Pd_2Si, is one of the metal silicides that has been extensively studied for its growth kinetics,[1,2] microstructure,[3-6] and electrical properties[7,8]. For Si (100) substrates, Pd_2Si is polycrystalline with the hexagonal c-axis preferentially aligned normal to the surface. Pd_2Si was found to grow epitaxially on Si (111) substrates. The growth kinetics are diffusion-limited and the activation energy was found to be 1.0±0.1 eV for Si(100),(111) and amorphous Si substrates between 190°C and 300°C[9]. The low value of the activation energy together with the grain-size effects on growth rates suggest that grain boundary diffusion is a dominant diffusion mechanism for Pd_2Si formed at low temperatures. One unique feature of the Pd_2Si phase which sets it apart from the other metal-rich silicides (such as Ni_2Si or Pt_2Si) is that the next metallurgical phase, PdSi, does not form until the annealing temperature exceeds 740°C. However, low temperature (300-400°C) formation of the PdSi phase can be obtained by implanting energetic Xe ions through a thin Pd or Pd_2Si film on crystalline Si substrates[10]. This observation suggests that the Pd_2Si-Si interface has a low interfacial free energy.

In this experiment, various thicknesses of Pd films (20 to 200Å) were deposited onto Si (100) and Si (111) thin crystals (∿5000Å thick) by electron-beam evaporation. Prior to evaporation, the thin crystals were organically degreased and etched in hydrofluoric acid. Thermal annealing of the samples was performed in a vacuum of $\sim 5 \times 10^{-7}$ Torr at a temperature of 250°C for 30 minutes. Because of multiple scattering effects, the Pd_2Si-Si interface cannot be analyzed by conventional channeling methods and all the samples were analyzed by thin-crystal channeling with the transmission geometry. The incident ^4He ion energy was 1.5 MeV.

The energy spectrum of a 300Å-thick Pd_2Si sample on Si (100) is shown in Fig. 29. The Pd_2Si layer was found to be polycrystalline by noting that the Pd scattering yields are basically the same for both channeling and random directions (with the proper correction for energy losses). The spectral heights of the Pd and Si signals in the silicide are indicated in the figure as $\overline{Pd}_2Si$ and $Pd_2\overline{Si}$, respectively. The $\overline{Pd}_2Si/Pd_2\overline{Si}$ ratio is determined to be 21.2. The calculated ratio for the stoichiometric compound can be obtained by using[11]:

$$\frac{\overline{Pd}_2Si}{Pd_2\overline{Si}} = \frac{N_{Pd}^{Pd2Si}}{N_{Si}^{Pd2Si}} \cdot \frac{\sigma_{Pd}}{\sigma_{Si}} \cdot \frac{[\varepsilon]_{Si}^{Pd2Si}}{[\varepsilon]_{Pd}^{Pd2Si}} \tag{13}$$

and is equal to 23.3. The [ε] ratio is calculated from equation (11) of Chapter 2 and is equal to 1.08. The 9%

difference between the experimental and calculated values denotes the Pd_2Si is slightly Si rich within the accuracy of Bragg's rule ($\lesssim$5%). The FWHM of the Si signal corresponding to the Si in Pd_2Si is calculated from the [ε] ratio and the FWHM of the Pd signal. The energy position of the Pd_2Si-Si interface is represented by the vertical line in Fig. 29. From the spectrum, a shoulder in the Si signal to the left of the interface is evident and it represents the amount of excessive Si at the Pd_2Si-Si interface. Because the Si signal of the Si in Pd_2Si and the interfacial layer is contributed only by scattering of channeled ions, it is separated from the crystalline Si signal by an energy of $\sim$28 keV (i.e., $\Delta E = Kt\ [dE/dx|_R - dE/dx|_C]$). The rising edge of the crystalline Si signal is indicated by a vertical arrow in the energy spectrum. The presence of the interfacial layer is apparent in the spectrum only for thicker silicide layers. For thinner silicide layers, the interface signal is merged with the silicide signal because of the detector energy resolution and a single Si peak is observed.

To investigate the stoichiometry of Pd_2Si and the Pd_2Si-Si interfacial disorder, the areal density of Si (i.e., Si atoms in both Pd_2Si and interfacial layer) versus the areal density of Pd is plotted in Fig. 30 for various Pd_2Si thicknesses. A straight line with slope equal to 0.54 can be fitted to the data with an intercept of 6×10^{15} Si/cm^2. The dashed line represents the case expected for an ideal Pd_2Si-Si

interface with stoichiometric Pd_2Si in contact with a perfect Si (100) surface. Since transmission channeling is only sensitive to large lateral atomic displacements (>0.7Å), the disordered Si can be due to a Si-rich interfacial silicide layer (not necessarily stoichiometric) or a major lateral displacement of the interfacial Si. The intercept of the curve indicates that approximately 8 monolayers of Si are involved in the interfacial layer.

The slope of the curve (= 0.54) agrees well with the spectral height measurements. It shows Pd_2Si is not perfectly stoichiometric but is ∿8% richer in Si content. Alternatively, we can also explain the data by having more Pd vacancies in the silicide than Si vacancies. Since the areal density measurements make use of Rutherford scattering cross-sections instead of ion stopping powers, the determined stoichiometry is more reliable than the spectral height measurements.

The Pd_2Si on Si (111) thin crystals were found to be epitaxial by channeling experiments after a heat-treatment of 250°C for 30 minutes. Pd_2Si is known to grow epitaxially on Si (111) with only a 2% mismatch in lattice constants[6]. We have found that epitaxial Pd_2Si also grows with a square-root-time dependence and its growth rate is just slightly slower than the non-epitaxial case[9]. Least-squares fitting procedure gives an activation energy of 1.05±0.1 eV for Pd_2Si grown on Si (111) substrates. The χ_{min} value from the Pd signal is ∿80% and is typical for epitaxial Pd_2Si grown at

low temperatures. X-ray diffraction experiments on these films have shown that the epitaxial layers have large mosaic spreads (±3°) along with other polycrystalline grains. The perfection of epitaxial Pd_2Si can be improved by additional annealing at high temperatures (∿700°C) and is probably associated with the grain realignment mechanisms.

The transmission channeling spectrum of a 300Å-thick Pd_2Si sample on Si (111) is shown in Fig. 31. The χ_{min} value of the sample was measured to be 83% from the Pd signal. Following previous procedures, the calculated energy position of the Pd_2Si-Si interface is represented by a vertical line in the channeled spectrum. For a 5000Å-thick Si (111) crystal, the energy separation between crystalline and disordered Si signals is ∿30 keV. The rising edge of the crystalline Si signal is indicated by a vertical arrow in the figure. In contrast to the (100) interface (Fig. 28), less disordered Si is observed at the (111) interface.

For channeling analysis of compound crystals such as Pd_2Si, the dechanneling mechanism is generally quite complicated and depends on the atomic arrangements of the various sublattices. The problem is more severe if the different atomic constituents have large atomic number differences (e.g., UO_2[12], ThO_2[13], and SrF_2[14]). Using ThO_2 as an example (CaF_2 structure), channeled ions along the <110> axis will be steered by alternate rows of pure Th or pure O atoms and each type of atomic rows will have a different continuum

potential. Consequently two distinct channeling profiles are present as indicated by the different $\psi_{\frac{1}{2}}$ and χ_{min} values obtained for Th and O scattering yields. Each channeling component is found to be characteristic of the continuum potential of the particular type of atomic row. When ions are channeled along the <111> axis of ThO_2, no such sublattice effect is observed because every atomic row is identical and each row consists of the same number of mixed atoms. In the continuum potential approximation, average values can be used for both the effective atomic number (Z) and effective atomic spacing ($\bar{d}$).

The situation is very similar to the ThO_2 <110> case when ions are channeled in Pd_2Si along directions parallel to the Si <111> axis. For epitaxial Pd_2Si (hexagonal Fe_2P structure), the hexagonal c-axis is parallel to the Si <111> direction. The continuum potential in the silicide will then be contributed by rows of pure Pd and pure Si atoms. This implies that a detailed calculation of the channeling potential and dechanneling probability is necessary to interpret the scattering yield quantitatively. Since the information is not available at the present time, no spectral height or areal density analysis has been performed on the epitaxial Pd_2Si data. Instead, an estimation is made of the area of the Si spectrum between the Pd_2Si-Si interface and the rising edge of the crystalline Si signal. Using this procedure, we have been able to set an upper limit of $5x10^{15}$ atoms/cm^2 for the

interfacial disordered Si.

4.2 The Ni_2Si-Si Interface

For Ni films vacuum deposited onto Si and annealed between 200°C to 325°C, only the phase Ni_2Si is observed on (100), (111) and polycrystalline Si substrates[15]. However, two phases Ni_2Si and NiSi can form simultaneously in two distinctive layers when amorphous (vacuum-deposited) Si is used as the substrate. Kinetic studies have shown that the formation of Ni_2Si has an activation energy between 1.3 and 1.6 eV[15,16]. During the growth of Ni_2Si, diffusion marker experiments[16] have demonstrated that the mass transport in Ni_2Si is dominated by the inward diffusion of Ni atoms.

In this experiment, the Ni_2Si-Si interface is investigated by thin-crystal channeling. The Ni evaporation and sample preparation procedures are similar to the Pd case and have been described in the previous section. Since the Ni_2Si phase is polycrystalline, the effect of multiple scattering will preclude the possibility of using conventional channeling geometries to extract the amount of Si disorder. In Fig. 32, we show the channeled and random spectra of a Ni_2Si sample using conventional channeling. The silicide was formed at 260°C for 20 minutes and contains 1.6×10^{17} Ni/cm^2. Using 2 MeV ^4He ions, the χ_{min} of crystalline Si is 40%. The spectral heights of Ni and Si signals corresponding to a stoichiometric Ni_2Si layer are indicated as $\overline{Ni}_2Si$ and $Ni_2\overline{Si}$ in the figure. The shaded area in the Si spectrum represents

the areal density of Si atoms corresponding to stoichiometric Ni_2Si ($8x10^{16}$ Si/cm^2). The existence of a large amount of excessive Si is evident from the gigantic interface peak, but quantitative measurements are prohibitive because of the large background signal from crystalline Si.

A transmission channeling spectrum of a 300Å-thick Ni_2Si sample on Si (100) is shown in Fig. 33. In this thin-crystal experiment, the χ_{min} value of the crystalline substrate is only 5% and the energy separation between the non-registered and crystalline Si signals is ∿26 keV. The area of the Si peak represents the total number of Si atoms in the polycrystalline Ni_2Si as well as the interfacial layer. Since the Ni areal density is $1.7x10^{17}$ atoms/cm^2, formation of the stoichiometric phase, Ni_2Si, will only require $8.5x10^{16}$ Si/cm^2. This information suggests that an excess of $4.3x10^{16}$ Si/cm^2 is incorporated either throughout the Ni_2Si phase or near the Ni_2Si-Si interface. We can exclude the former possibility by noting the spectral heights of the silicide surface agree well with that of stoichiometric Ni_2Si. Moreover, the energy position of the prominent interface peak clearly shows a silicon-rich layer (i.e., with Si content higher than Ni_2Si) which is sandwiched between the Ni_2Si and Si substrate. From energy-loss calculations (equation (11) of Chapter 2), the energy position of the Ni_2Si-Si interface is indicated by a vertical line in the spectrum. Using that as a reference, the position of the interface peak shows a majority of the

excessive Si is lying within the silicide layer near the interface.

To investigate the kinetic development of this interfacial layer, thicker Ni films (∿1200Å) were deposited onto Si (100) thin crystals. Thicker Ni films are required so that the Ni_2Si formation can be stopped with sufficient control before all the Ni is consumed. As discussed in Chapter 2, the transmission geometry is no longer possible for such a thick overlayer because the Ni and Si signal will overlap. Instead, the backscattering geometry has to be used with a sacrifice in depth resolution. In Fig. 34, we show the backscattering spectrum of a completely reacted Ni_2Si sample after a heat-treatment of 280°C for 180 minutes. The Ni and Si spectral heights indicate that the silicide composition is uniform as a function of depth and has a Ni to Si composition ratio close to 2. The energy position of the Ni_2Si-Si interface is indicated by the vertical line. A prominent Si interface peak is observed at the silicide-silicon interface. The areal density of the excessive Si is estimated to be $\gtrsim 4.6 \times 10^{16}$ Si/cm^2.

Another sample was heated at 280°C for 80 minutes such that only half of the Ni was consumed to form Ni_2Si. The channeled spectrum is shown in Fig. 35. Since the thin-crystal substrate is thicker (∿7000Å) than the one shown in Fig. 34, the Ni signal is overlapping with part of the crystalline Si spectrum. However, the interfacial Si signal

is interference free. An interface peak is again observed in the Si spectrum with an energy position corresponding to the Ni_2Si-Si interface. This observation is important because it demonstrates the interfacial layer has developed <u>during</u> the growth stage of Ni_2Si.

We propose that the silicon-rich interfacial layer as observed by channeling is initiated by the interstitial diffusion of Ni into the crystalline Si. The presence of interstitial atoms will increase the number of nearest neighbor for Si atoms and weakens the Si bond to create disordered Si. The disordered interfacial Si favors a silicide (not necessarily a stoichiometric phase) which is richer in Si than Ni_2Si. Below the formation temperature of the next stable phase, NiSi, the interfacial disordered Si is consumed by the inward flux of Ni atoms to form Ni_2Si. At the same time, new interfacial disordered Si is generated at the silicide front by the interstitial mechanism. This maintains the Ni_2Si growth process until all the Ni is consumed. The interfacial layer will remain until the annealing temperature reaches 325°C where the formation of NiSi is favored.

4.3 The NiSi-Si Interface

The transformation of Ni_2Si to NiSi occurs around 325°C and ion backscattering studies[16,17] have shown that the NiSi nucleates at the interface between Ni_2Si and Si. NiSi has an orthorhombic crystal structure (MnP) and is the stable

phase in thin-film structures between 350-750°C. On single crystal Si substrates, the NiSi is polycrystalline. With the presence of excess Ni atoms, the NiSi decomposes back to the Ni_2Si phase when annealed at 325°C[18].

The transmission channeling spectrum of a 400Å-thick NiSi layer grown on a Si (100) thin crystal (∿5000Å) is shown in Fig. 36. The silicide was formed by annealing the Ni on Si sample at 350°C for 30 minutes. The spectral heights indicate the silicide has a composition very close to stoichiometric NiSi. In contrast to the Ni_2Si-Si interface, no interface peak can be observed from the Si spectrum. From the channeling point of view, the NiSi-Si interfacial disorder resembles that of the Pd_2Si-Si (111) interface. The areal density under the Si peak corresponds to 1.77×10^{17} Si/cm^2. Assuming a stoichiometric NiSi layer, the excessive Si above a perfect NiSi-Si structure will be 8×10^{15} Si/cm^2. Thus, the areal density of the interfacial disordered Si is definitely less than 8×10^{15} Si/cm^2.

4.4 The $NiSi_2$-Si Interface

The epitaxial nature of nickel disilicide, $NiSi_2$, on single-crystal silicon substrates has been studied extensively[19-23] using MeV ion channeling and reflection electron diffraction. The high crystalline quality of the $NiSi_2$ epitaxial layers is generally attributed to the lattice match between the CaF_2 structure of $NiSi_2$ (a_o = 5.406Å) and the diamond cubic structure of Si (a_o = 5.428Å).

For thin $NiSi_2$ layers ($\lesssim$700Å) grown on Si (111) substrates, the channeling minimum yield (χ_{min}) can be as low as 5% and is close to single-crystal values. The minimum yield, χ_{min}, ($\equiv$ aligned yield/random yield) is the ratio of near-surface backscattering yields when the analyzing beam is aligned along a major crystalline direction to that when the analyzing beam is incident on the sample in a random direction. A smaller χ_{min} value reflects better crystalline perfection. The value of χ_{min} increases approximately linearly with the $NiSi_2$ thickness and is ∿15% for 3500Å thickness $NiSi_2$ layers[22].

Recently, Chiu[24] and Föll[25] have used cross-sectional transmission electron microscopy to study the $NiSi_2$-Si interface. The epitaxial layers grown on (100) substrates are found to be growing in steps of flat terrains. The steps of these terrains (∿1000Å in height) are defined by the (111) and (100) planes of the $NiSi_2$ epitaxial layer. For thin epitaxial layers (<1000Å) grown on (111) substrates, the $NiSi_2$-Si interface is relatively flat and only microsteps (100-200Å in height) can be detected along the $NiSi_2$-Si interface. Such a corrugated interfacial morphology is consistent with the X-ray topography and scanning electron microscopy results of Lau and Cheung[26].

In this study, approximately 150Å of Ni was deposited onto a Si (111) thin crystal (∿6000Å). The sample was heated at 300°C for 30 minutes and then annealed at 800°C for 30 minutes. The annealing vacuum was maintained in the 10^{-8} Torr

range by an ion-pump vacuum system. Because of the high annealing temperature required, a clean vacuum ambient is essential to minimize contamination effects such as oxidation or the build-up of SiC on the sample's surface[27]. For example, similar samples when annealed in a diffusion-pump vacuum system ($\sim 10^{-7}$ Torr) have higher χ_{min} values ($\sim$12%) and sputtering Auger analysis shows the surface layer has high concentrations of C and O atoms.

To characterize the $NiSi_2$ layers, we have performed conventional channeling experiments with the beam directly incident on the silicide along the <111> axis. The channeled and random spectra are shown in Fig. 37. The χ_{min} value from the Ni signal is 6%, indicating the high crystalline quality of the epitaxial silicide. The trailing edge of the Ni random spectrum corresponds to $\sim$90 keV of energy loss and is equivalent to a 250Å thickness variation in the silicide layer.

The Ni and Si peaks near the silicide surface correspond to 4.6×10^{15} Ni/cm^2 and 2.3×10^{16} Si/cm^2, respectively. They do not represent the intrinsic surface peaks of a $NiSi_2$ (111) surface because the Si peak's value is too high. For $NiSi_2$ grown on Si (111) under UHV conditions, which shows a sharp (1x1) LEED pattern, the Ni and Si surface peaks are 3.8×10^{15} and 9.5×10^{15} atoms/cm^2 respectively when measured with 1 MeV ^{4}He ions along the <111> axis. Even if we scale the Si surface peak to 2 MeV values (approximately an increase of 30%), it

is still smaller than the measured value in Fig. 37. As will be shown by the transmission channeling spectrum, the silicide surface contains a silicon-rich layer which is probably a layer of SiO_2 or an oxidized silicide.

From the Ni channeled spectrum alone, it is evident that the number of Ni atoms in any disordered interfacial layer has to be substantially less than $4.6x10^{15}$ Ni/cm^2. Using a much thinner silicide (~360Å) to prevent signal overlapping, Chiu et al.[22] have been able to set an upper limit of $1.5x10^{15}$ Ni/cm^2 for the interfacial disorder. A better limit can be placed if the dechanneling mechanism of the silicide layer is well understood.

Using conventional channeling geometry, the Si channeled spectrum provides no information on the structural perfection of the Si sublattice or the interfacial disordered Si. This is due to a peculiar property of channeling in multi-layered crystals. Since the χ_{min} of $NiSi_2$ from the Ni signal is 6%, we shall expect good channeling in both the $NiSi_2$ and Si crystals but such is not the case. From Fig. 37, the χ_{min} of Si in the silicide is 6% near the surface and it increases gradually to 19% inside the crystalline Si. In contrast, the dechanneling rate of the Ni spectrum is almost negligible. The problem associated with channeling along different rows of pure atoms (e.g., the Pd_2Si-Si (111) case) does not apply here because the <111> axis of $NiSi_2$ consists of rows of mixed Ni and Si atoms.

To resolve this dilemma, we have considered the effect of channeling critical angles ($\psi_{1/2}$) in this problem. For 2 MeV ^{4}He ions, the calculated $\psi_{1/2}$ values of $NiSi_2$ and Si are 0.61° and 0.46° respectively when channeled along the <111> axis. This implies the channeled ions in $NiSi_2$ can have a maximum transverse kinetic energy ($E_\perp = E\psi_{\frac{1}{2}}^2$) of 226 eV. When the channeled ions enter the Si crystal across the $NiSi_2$-Si interface, those ions with $E_\perp$ larger than the Si critical transverse energy (= 129 eV) will be dechanneled and give high scattering yields. The apparent high dechanneling rate within the silicide layer is caused by the lateral non-uniformity of the silicide thickness where the $NiSi_2$-Si interface is at various depths from the silicide's surface.

The transmission channeling and random spectra are shown in Fig. 38. By reversing the channeling sequence through the two crystals, no enhanced dechanneling is observed in the $NiSi_2$ layer because $E_\perp$(Si) is less than $E_\perp(NiSi_2)$. The χ_{min} values for Si in both the Si and $NiSi_2$ crystals are ∿5%. This is reasonable because both Si and $NiSi_2$ have ∿5×10^{22} Si/cm^3. No interface peak corresponding to the interfacial disordered atoms can be observed either from the Si or Ni spectra. Near the silicide surface, the Si content is higher than that of $NiSi_2$ while the Ni content is lower than that of $NiSi_2$. As discussed previously, this is probably due to the presence of a contaminated surface. Seemingly, the contaminated layer does not disrupt the $NiSi_2$ crystal structure

significantly because the Ni signal does not show any appreciable dechanneling. The excess Si near the surface corresponds to an areal density of $6x10^{15}$ Si/cm^2.

To set an upper limit on the number of disordered interfacial Si, we have to consider the total depth scale of the interfacial width (∿250Å) because channeling quantities are given in projected areal densities. In Fig. 38, we have drawn a rectangular box around the $NiSi_2$-Si interface to represent an interfacial disorder of $5x10^{15}$ Si/cm^2 (∿5 monolayers of the Si (111) planes). Since no such step has been observed in the Si spectrum, we are convinced that the interfacial disorder has to be lower than the quoted value. This limit can be lowered if thinner silicide layers and a more grazing exit detector geometry are used.

4.5 Summary

The results of the various silicide-Si interfaces are tabulated in Table 5 together with some relevant silicide formation temperatures. From a thermodynamical point of view, the transformation temperature from Ni_2Si to NiSi is expected to be low because the free energies of silicide formation (ΔH) are almost identical for the Ni_2Si and NiSi phases[28] (i.e., 10.5 and 10.3 Kcal/gm-atom, respectively). However, such an argument does not hold for the Pd_2Si to PdSi transformation although ΔH is 6.9 Kcal/gm-atom for both silicide phases. This suggests that thermodynamic parameters of bulk silicides may not be the dominating factor in thin-film structures.

From Table 5, we have observed a correlation between the interfacial disordered Si and the transformation temperature for the next stable silicide phase. The Ni_2Si phase, which shows the highest interfacial disorder ($4.3 \times 10^{16}/cm^2$), has the lowest transformation temperature. The Pd_2Si-Si and NiSi-Si interfaces are rather similar in terms of interfacial disorder ($<1 \times 10^{16}/cm^2$) and the transformation temperatures are accordingly high. These results indicate that interfacial nucleation is the controlling mechanism for silicide formation on crystalline Si substrates. As a rule of thumb, a more ordered interface will have higher thermal stability against the nucleation of other silicide phases. Recently, Lau et al.[29] have demonstrated that the formation temperature of $NiSi_2$ can be as low as 170°C if ion-beam mixing is used to achieve an amorphous mixture of the $NiSi_2$ composition. The PdSi phase has also been observed to form at 350°C if the Pd_2Si-Si interface is disordered by ion implantation[10]. All these facts suggest that above a certain interfacial Si disorder, the transformation temperature for another silicide phase can be substantially lowered.

Another closely related system is the platinum silicides where the metal-rich silicide (Pt_2Si) forms at ∿200°C[28]. Above 300°C, the PtSi phase starts to grow and it is stable against thermal annealing up to 750°C. Hence, the Pt-Si and Ni-Si are very similar in the growth kinetics data. If our conjecture is correct, the Pt_2Si-Si and Pt-Si interfaces should

be typical of the Ni_2Si-Si and NiSi-Si interfaces, respectively.

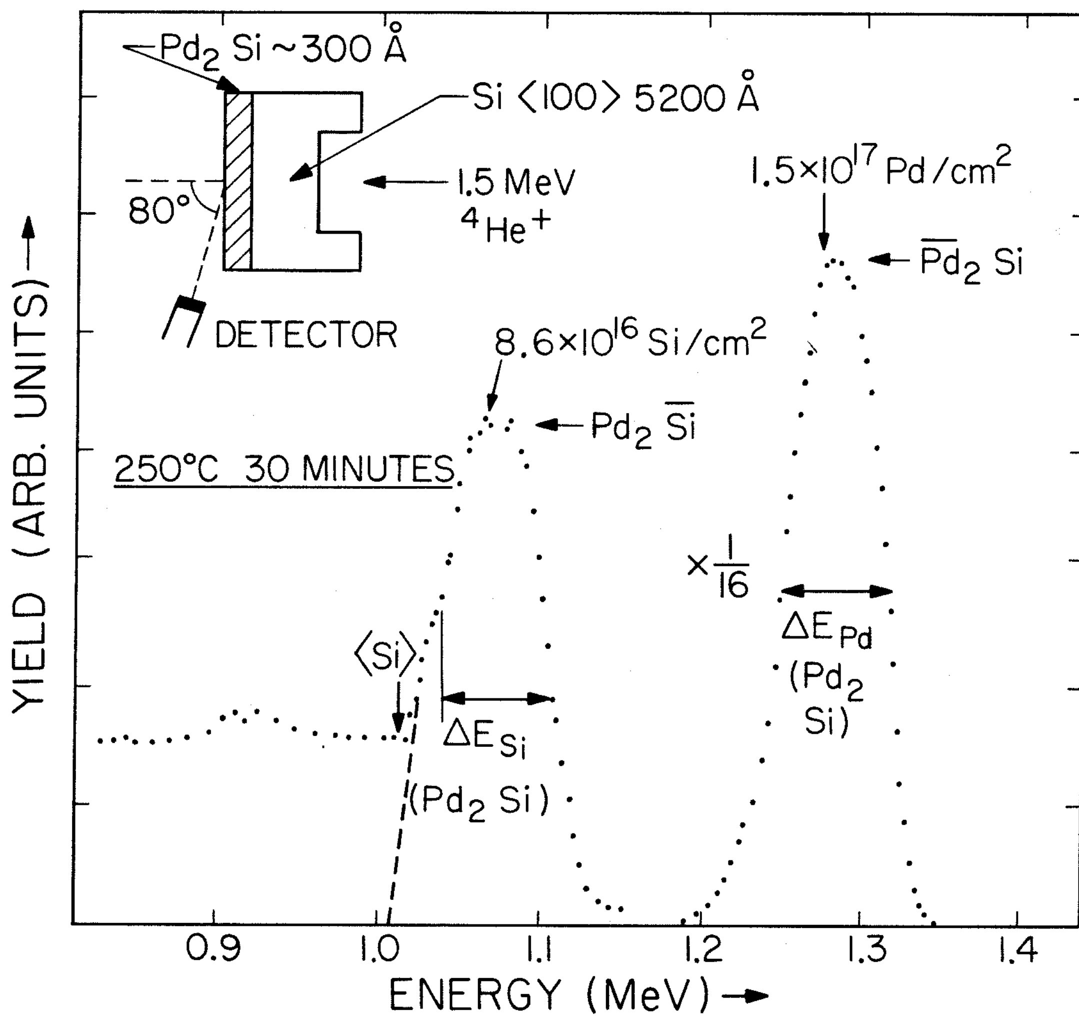

Figure 29 Transmission channeling spectrum of a 300Å-thick Pd_2Si layer on (100) Si. The Pd_2Si layer is polycrystalline.

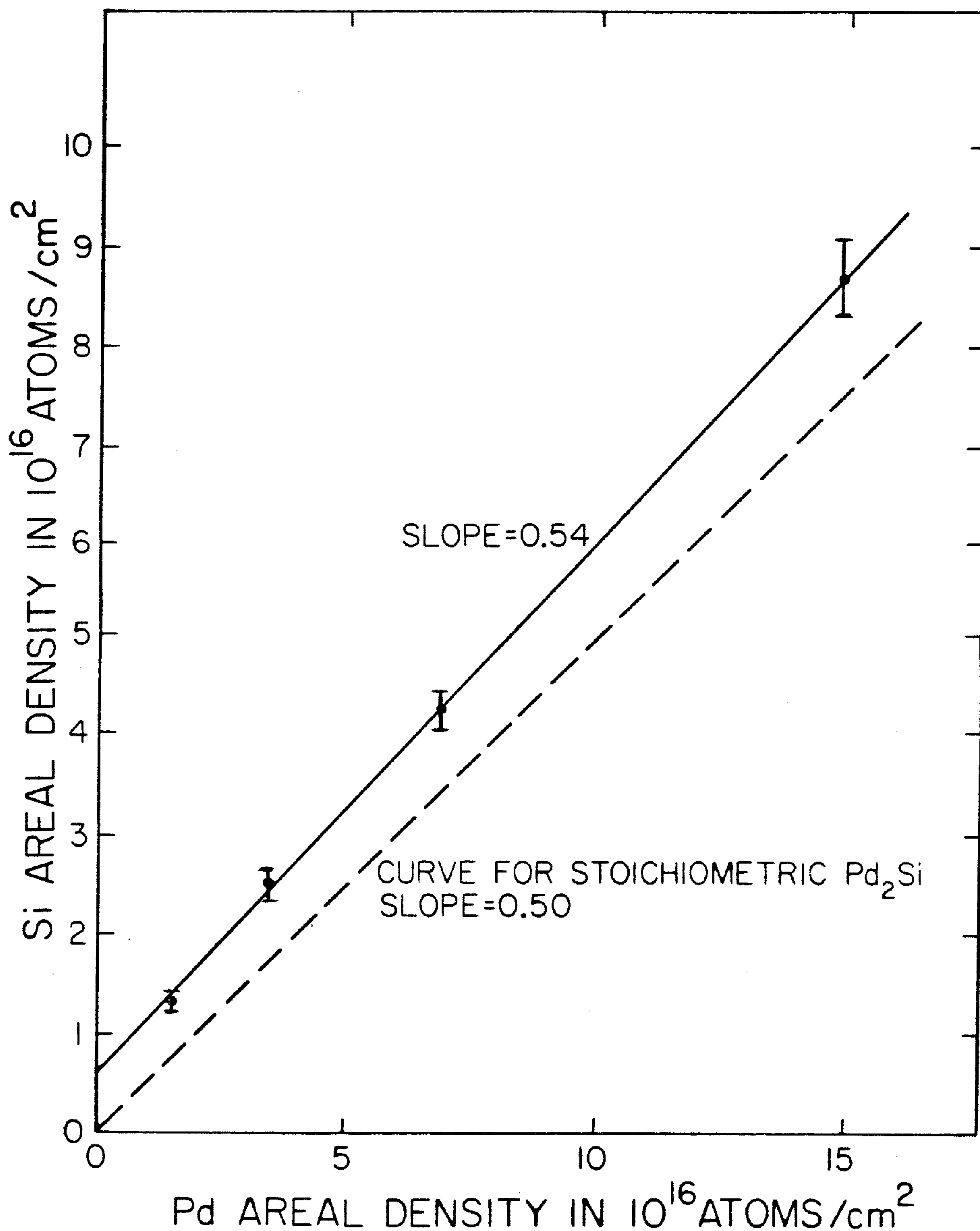

Figure 30 Si areal density versus Pd areal density for Pd_2Si grown at 250°C on Si (100) thin crystals.

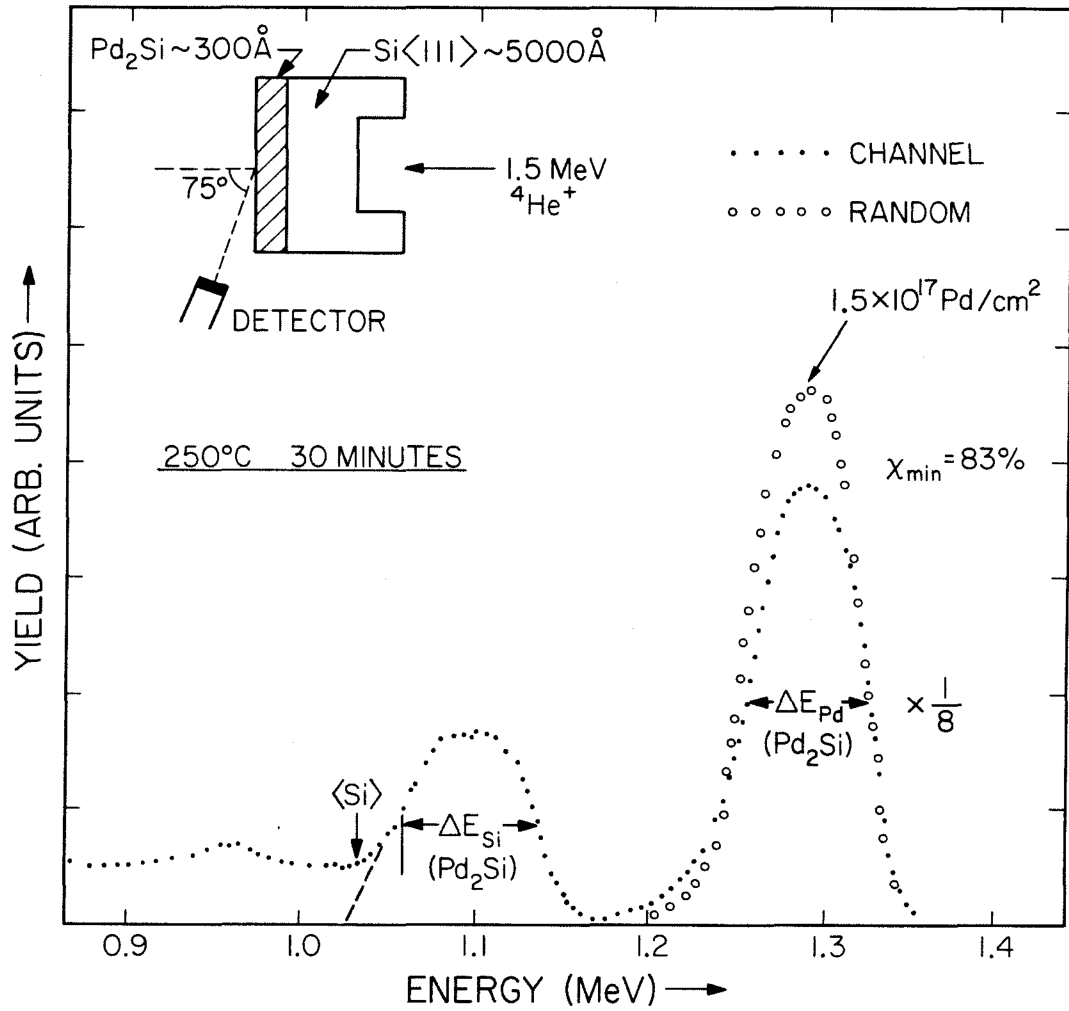

Figure 31 Transmission channeling spectrum of a 300Å – thick Pd_2Si layer on (111) Si. χ_{min} of the epitaxial Pd_2Si is 83%.

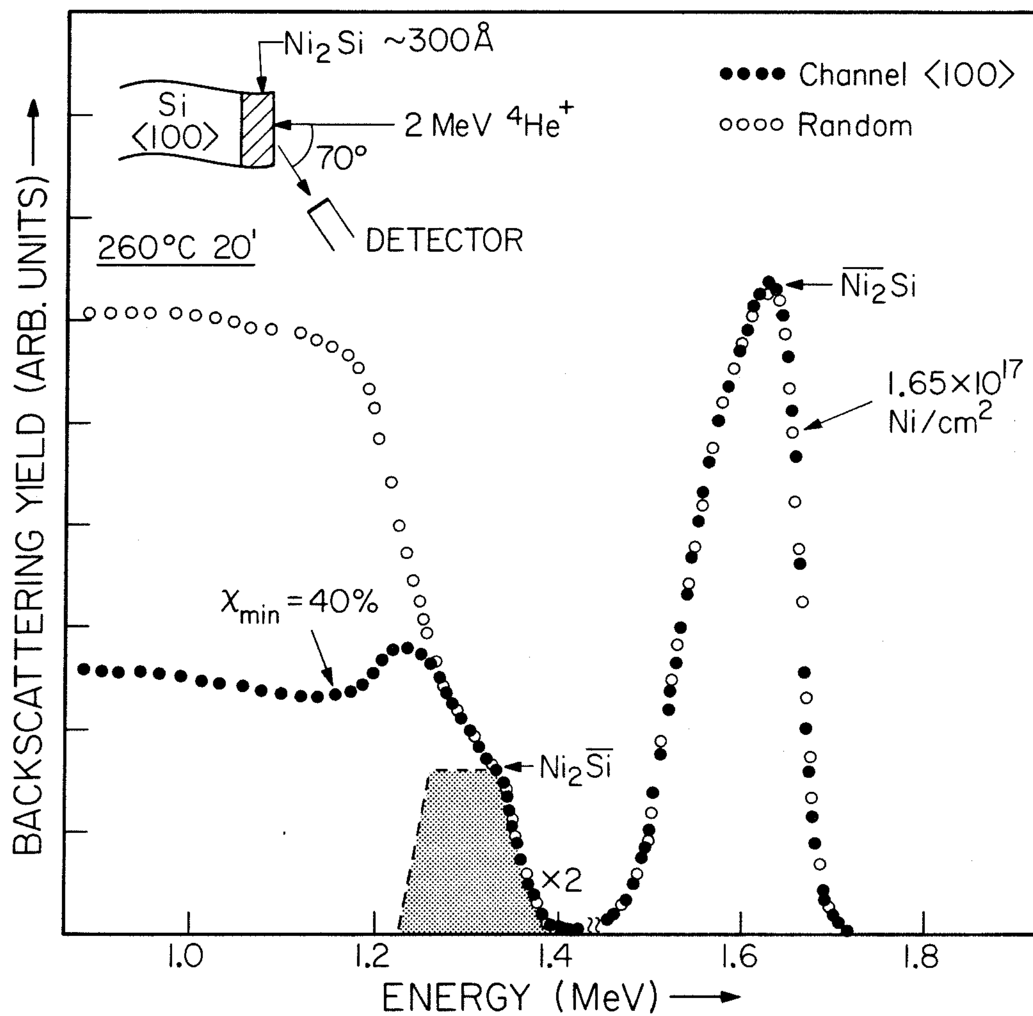

Figure 32 Conventional channeling and random spectra of a 300Å-thick Ni_2Si layer on (100) Si. The dotted area represents the amount of Si required for stoichiometric Ni_2Si.

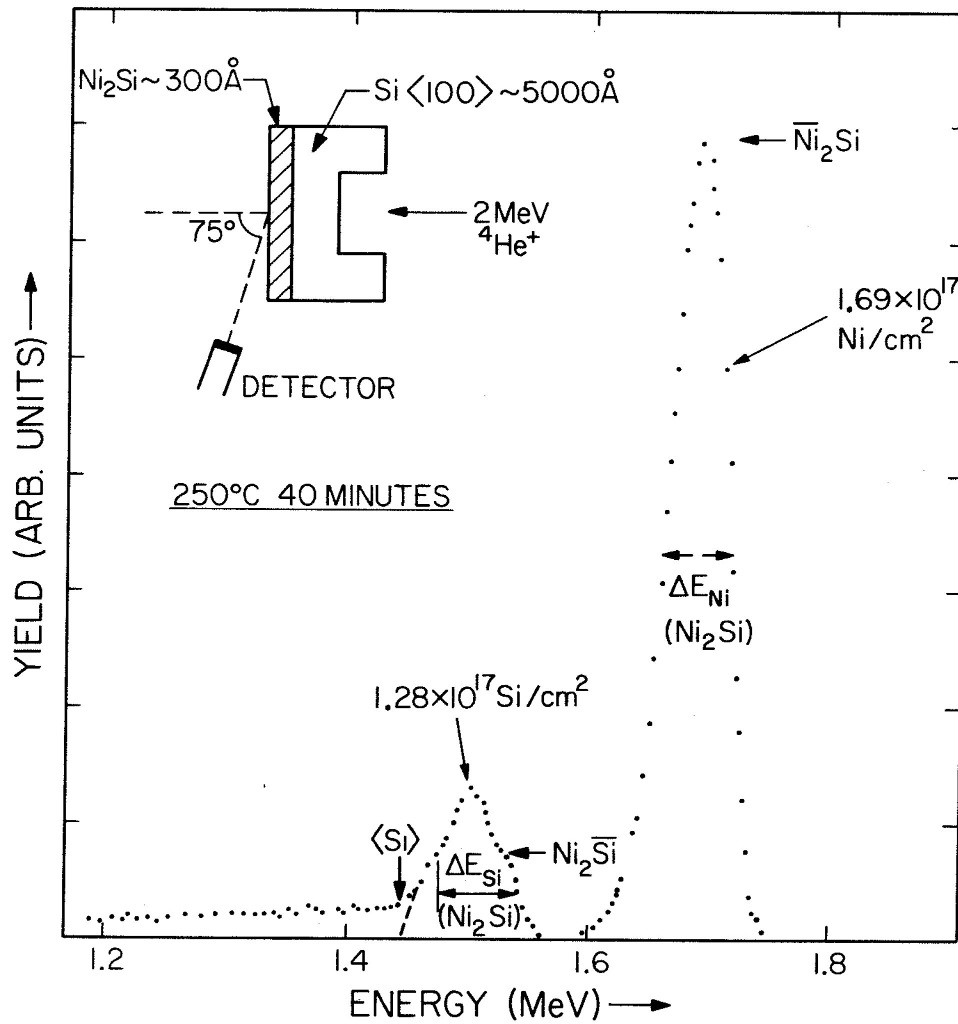

Figure 33 Transmission channeling spectrum of a 300Å-thick Ni_2Si layer on (100) Si.

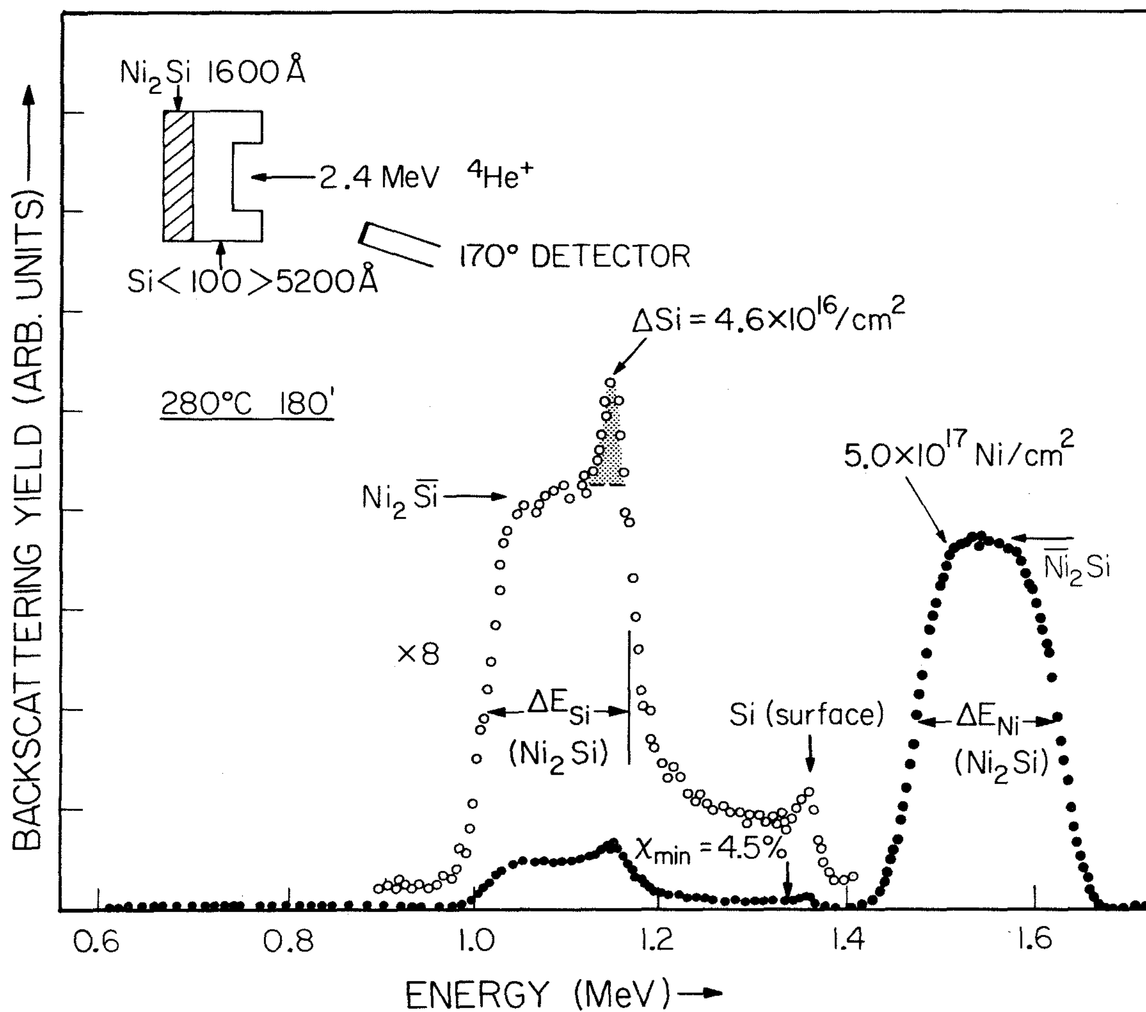

Figure 34 Thin-crystal channeling spectrum (backscattering geometry) of a 1600Å-thick Ni_2Si layer on (100) Si. The dotted area represents the excess Si at the Ni_2Si- Si interface.

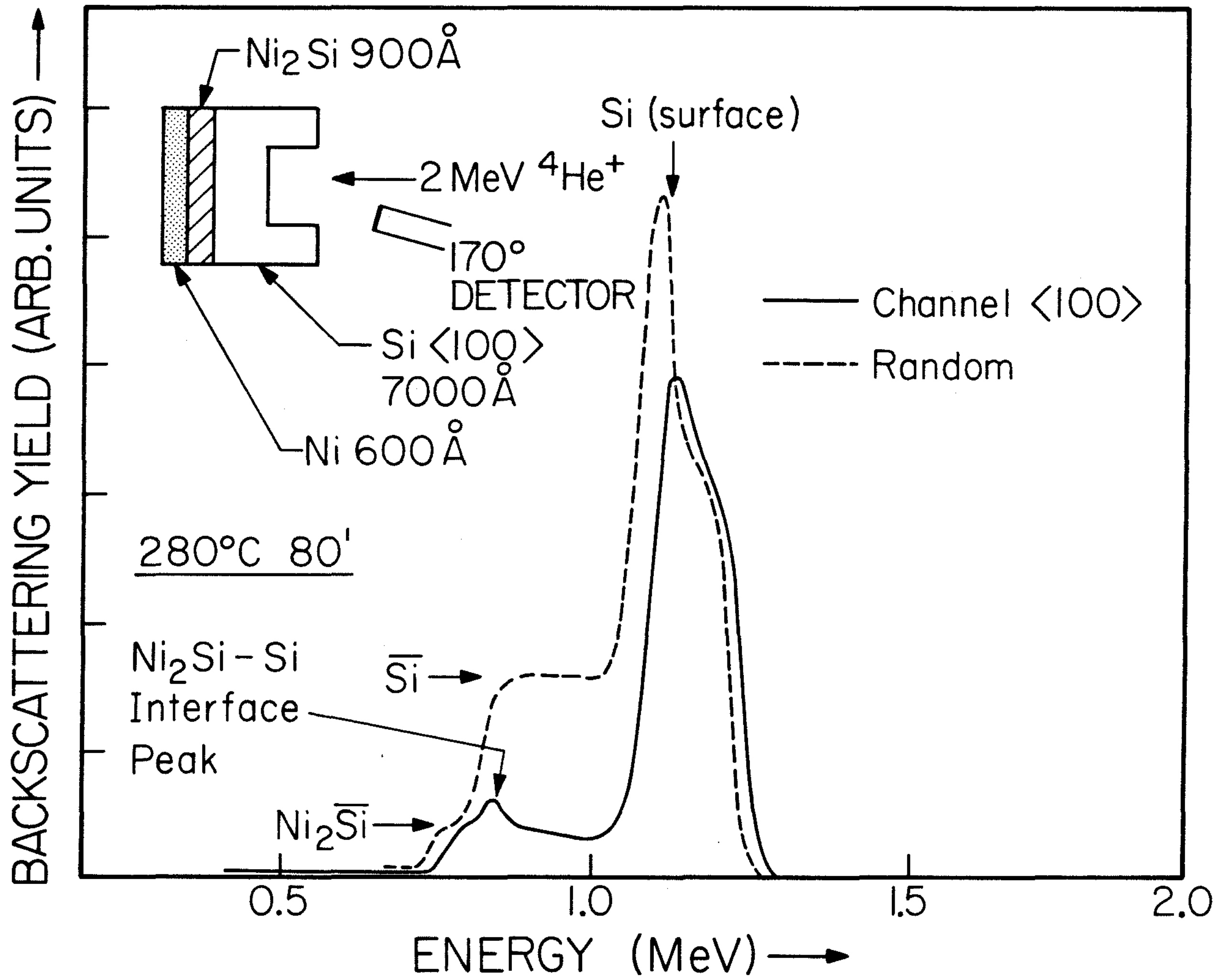

Figure 35 Thin-crystal channeling and random spectra of a Ni-Ni_2Si - (100) Si structure (backscattering geometry).

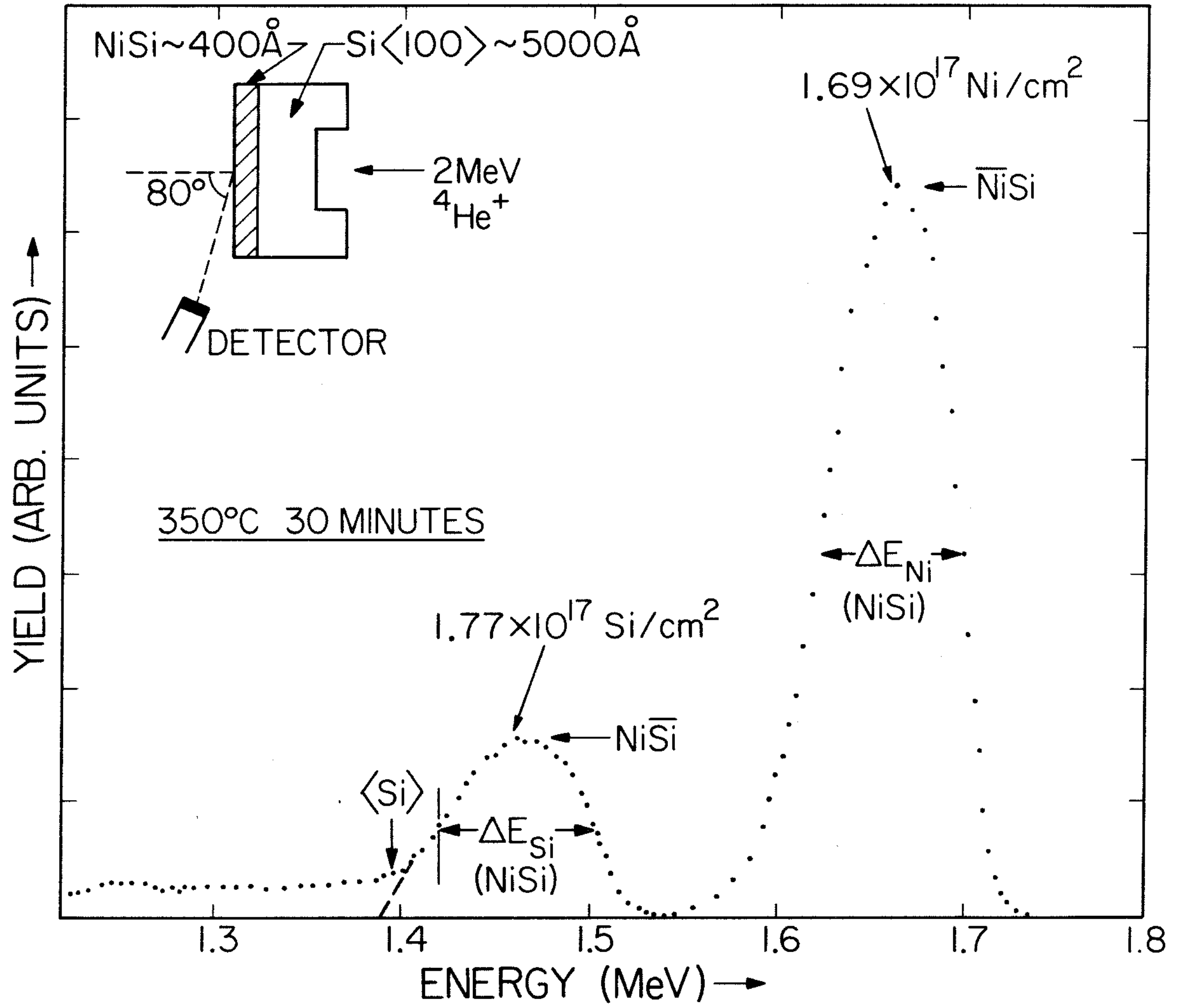

Figure 36 Transmission channeling spectrum of a 400Å- thick NiSi layer on (100) Si.

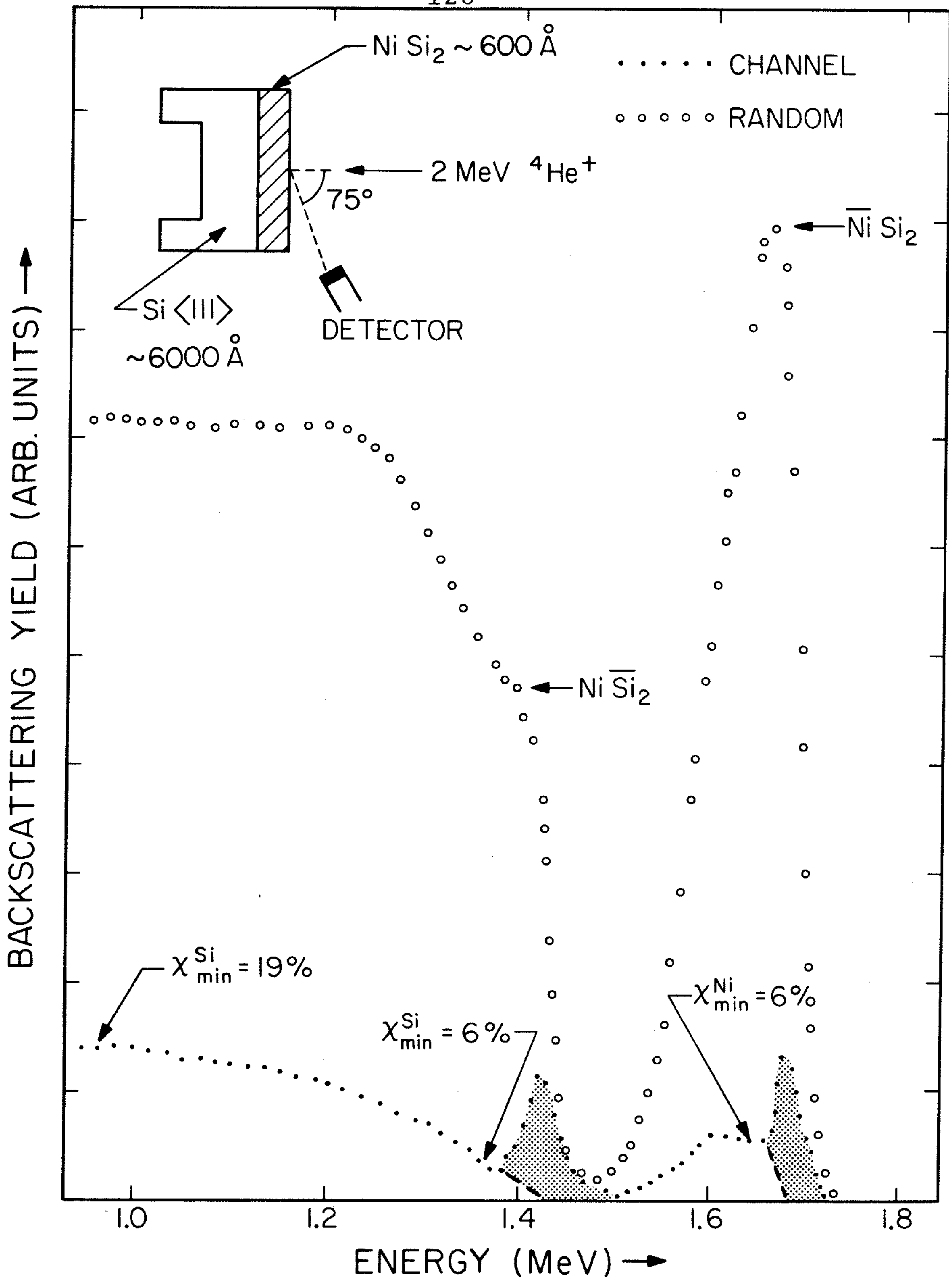

Figure 37 Conventional channeling and random spectra of a 600Å- thick $NiSi_2$ layer on (111) Si.

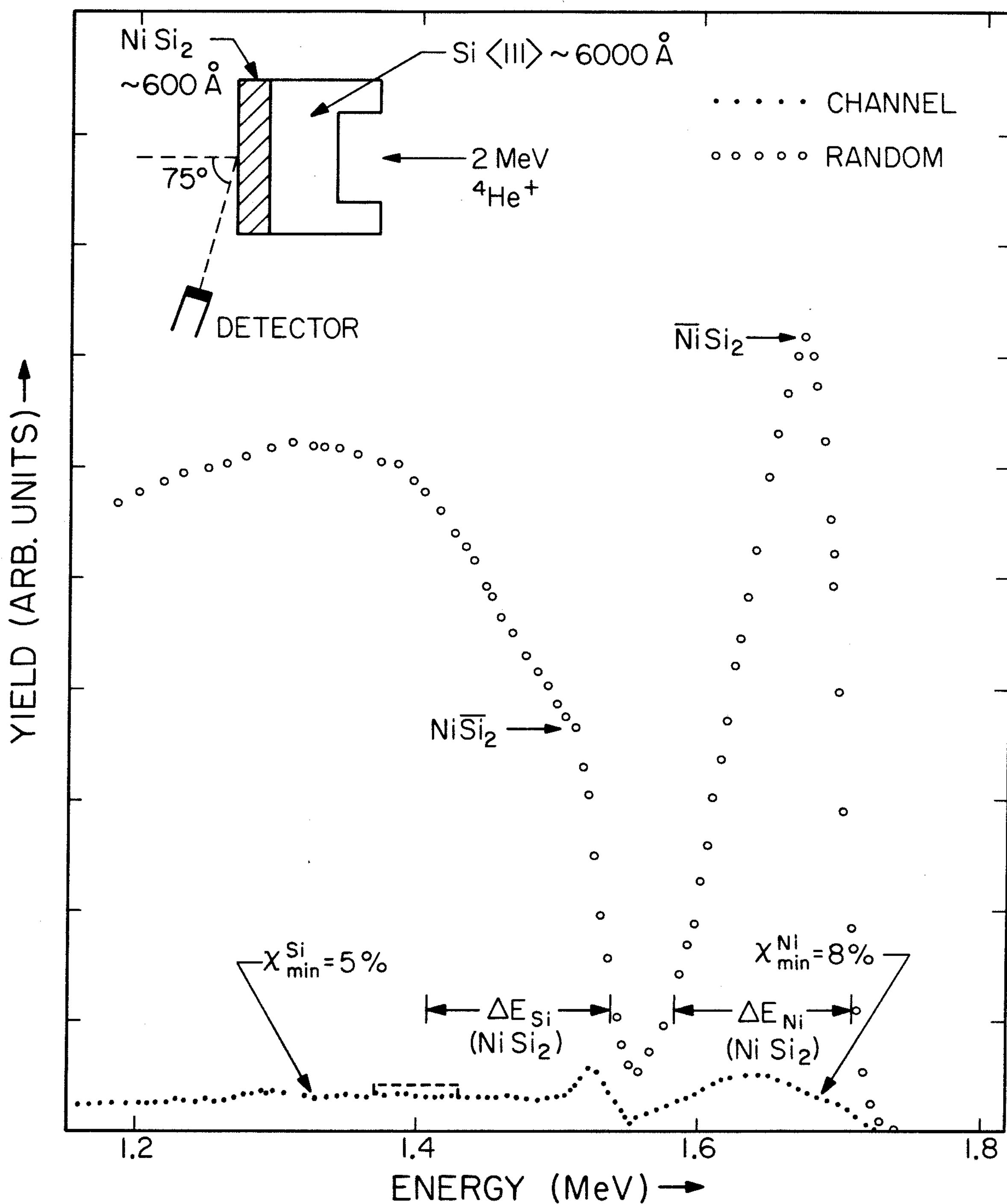

Figure 38 Transmission channeling and random spectra of a 600Å- thick $NiSi_2$ layer on (111) Si.

Table 5 SUMMARY OF SILICIDE-SI INTERFACIAL DISORDER AND SOME RELEVANT SILICIDE FORMATION TEMPERATURES

Silicide	Si Substrate	Interfacial Si disorder	Silicide Formation Temperature	Transformation Temperature to Next Stable Silicide
Ni_2Si	(100)	$4.3 \times 10^{16}/cm^2$	200-325°C	350°C (NiSi)
NiSi	(100)	$<8 \times 10^{15}/cm^2$	350-750°C	800°C ($NiSi_2$)
$NiSi_2$	(111)	$<5 \times 10^{15}/cm^2$	>750°C	-
Pd_2Si	(100)	$6 \times 10^{15}/cm^2$	$\lesssim$200°C	735°C (PdSi)
	(111)	$<5 \times 10^{15}/cm^2$	$\lesssim$200°C	840°C (PdSi)

References

(1) R. W. Bower, D. Sigurd and R. E. Scott, Solid-State Electronics, 16, 1461 (1973).

(2) G. A. Hutchins and A. Shepela, Thin Solid Films, 18, 343 (1973).

(3) S. S. Lau and D. Sigurd, J. Electrochem. Soc., 121, 1538 (1974).

(4) U. Köster, K. N. Tu and P. S. Ho, Appl. Phys. Lett., 31, 634 (1977).

(5) D. H. Lee, R. R. Hart, D. A. Kiewit and O. J. Marsh, Phys. Stat. Sol., A15, 645 (1973).

(6) W. D. Buckley and S. C. Moss, Solid-State Electronics, 15, 1331 (1972).

(7) A. Shepela, Solid-State Electronics, 16, 477 (1973).

(8) M. Wittmer, D. L. Smith, P. W. Lew and M-A. Nicolet, Solid-State Electronics, 21, 573 (1978).

(9) N. Cheung, S. S. Lau, M-A. Nicolet, J. W. Mayer and T. T. Sheng, to be published in the Proceedings of the Symposium on Thin Film Phenomena--Interfaces and Interactions, The Electrochemical Society Meeting, Los Angeles, California (October 14-19, 1979).

(10) B. Y. Tsaur, S. S. Lau and J. W. Mayer, Appl. Phys. Lett., 35, 225 (1979).

(11) G. Foti, J. W. Mayer and E. Rimini, in Ion Beam Handbook for Material Analysis, edited by J. W. Mayer and E. Rimini (Academic Press, New York, 1977), p. 61.

(12) J. A. Davies, L. Eriksson, N. G. E. Johansson and I. V. Mitchell, Phys. Rev., 181, 548 (1969).

(13) F. W. Clinard Jr. and W. M. Sander, J. Appl. Phys., 43, 4937 (1972).

(14) H. Matzke, Phys. Stat. Sol., A8, 99 (1971).

(15) J. O. Olowolafe, M-A. Nicolet and J. W. Mayer, Thin Solid Films, 38, 143 (1976).

(16) K. N. Tu, W. K. Chu and J. W. Mayer, Thin Solid Films, 25, 403 (1975).

(17) D. J. Coe and E. H. Rhoderick, J. Phys., D9, 965 (1976).

(18) G. Ottaviani, G. Majni and C. Canali, Appl. Phys., 8, 285 (1979).

(19) K. N. Tu, E. I. Alessandrini, W. K. Chu, H. Kraütle and J. W. Mayer, Jap. J. Appl. Phys. Suppl. 2, Pt. 1, 669 (1974).

(20) H. Ishiwara, M. Nagatomo and S. Furukawa, Nuc. Instr. Meth., 149, 417 (1978).

(21) H. Ishiwara and S. Furukawa, J. Appl. Phys., 47, 1686 (1976).

(22) K. C. R. Chiu, J. M. Poate, L. C. Feldman and C. J. Doherty, to be published in Appl. Phys. Lett.

(23) N. Cheung, M-A. Nicolet and J. W. Mayer, to be published in the Proceedings of the Symposium on Thin Film Phenomena--Interfaces and Interactions, The Electrochemical Society Meeting, Los Angeles, California (October 14-19, 1979).

(24) K. C. R. Chiu, private communication.

(25) H. Föll, Symposium of Advances in Defect Characterization in Semiconductor Materials and Devices, Materials Research Society Annual Meeting, Cambridge, Massachusetts, (November 26-30, 1979).

(26) S. S. Lau and N. Cheung, to be published in Thin Solid Films.

(27) M. Nagatomo, H. Ishiwara and S. Furukawa, Japan J. Appl. Phys., 18, 765 (1979).

(28) K. N. Tu and J. W. Mayer, in Thin Films--Interdiffusion and Reactions, edited by J. M. Poate, K. N. Tu and J. W. Mayer (Wiley--Interscience, New York, 1978), p. 359.

(29) S. S. Lau, unpublished results.

CHAPTER 5

THE SiO_2-Si INTERFACE

A variety of experimental methods[1] have been used to study the structure of the Si-SiO_2 interface. While the different techniques reveal different aspects of the structure, there is now almost universal agreement that the interface is very sharp (<10Å). Recent backscattering-channeling studies, which make use of improvements in experimental technique and increased understanding of the surface interaction of energetic ions, have demonstrated the sharpness of the interfacial region and suggest that one to two monolayers of underlying Si are not registered with respect to the bulk[2]. This result was derived by observing the scattering intensity of silicon and oxygen from CVD grown oxides of varying thicknesses, i.e., as a function of etching time. The stoichiometry and interfacial reconstruction of native oxides on Si have also been studied by Feldman et al.[3], using a thin-crystal channeling experiment. In this study, conventional and thin crystal scattering geometries are used to study the stoichiometry and interface disorder of a series of thermally grown oxides. The application of both experimental situations to the same samples provides important constraints on the interpretation of the results. Furthermore, the use of oxides thermally grown to varying

thicknesses better defines the interface structure and eliminates potential problems with the etching techniques.

Thin Si crystals (∿5000Å) of (110) orientation were prepared using methods described in Appendix 1. Prior to oxidation, the crystals were organically degreased and dipped into a hydrofluoric acid etch. The oxides, between 4Å to 70Å thick, were grown at 800°C in a dry oxygen ambient.

Channeling experiments have been performed in two different geometries as shown in Figs. 39(a) and 39(b), together with a schematic of the spectral features. Grazing exit angle geometry is used to reduce the background under the Si and O peaks to enhance signal sensitivity and minimize errors in the background subtraction[2]. In the conventional channeling measurements, the Si peak corresponds to scattering from Si atoms in the oxide, reconstructed Si underneath the interface, and an intrinsic surface peak contribution due to the first few monolayers of crystalline Si. Recent calculations based on Monte Carlo methods have been successful in predicting this intrinsic surface peak intensity[4].

The transmission experiment takes advantage of the channeling process, by which ∿97% of the ion beam has a flux distribution sharply peaked at the center of the <110> channels. There is no scattering contribution corresponding to the intrinsic surface peak. At the crystals' back surface, the channeled component will be scattered only by displaced

Si atoms in the amorphous oxide and the reconstructed layers. The anomalously low energy loss of the channeled ions shifts the back surface scattering to higher energy, separating it from the background due to the scattering of non-channeled particles. However, the spread in stopping powers associated with different channeling trajectories prevents a perfect separation.

In both geometries, channeling reduces the continuum background to $\sim$4% of a random spectrum and enhances the sensitivity of the oxygen signal which occurs at a lower energy in the spectrum. By using this technique, we have been able to measure Si and O signals with an oxide layer as thin as $\sim$4Å.

The absolute determination of the areal densities in terms of atoms/cm^2 makes use of a "standard" consisting of 8.4×10^{15} Ag/cm^2 deposited on a Si (110) thin crystal. The absolute uncertainty is smaller than 5% and will enter linearly for both Si and O areal densities.

In Figs. 40(a) and 40(b), we show the energy spectra of two SiO_2 on Si samples with different thicknesses, using conventional channeling. The areal densities of Si and O are determined from the area under the peaks. The lowest energy peak corresponds to carbon which was caused by the build-up of carbonaceous materials <u>on</u> the surface of samples during the ion-beam analysis with the vacuum at $\lesssim 1\times10^{-6}$ Torr. The rate of carbon deposition has been studied in detail by nuclear

resonance techniques and is summarized in Appendix 2. For the interfacial studies, it is clear that the deposited carbon is not at the interface and plays no role in the interfacial properties.

As discussed in Chapter 2, the effect of multiple scattering due to the overlayer has to be evaluated for Si surface peak measurements. For the thickest SiO_2 (∿70Å) used in this study, the total scattering half-angle, $\Theta_{1/2}$, due to the Si and O atoms is 0.01° and is much smaller than the incident beam's divergence half-angle (0.03°). In contrast to the case of metal overlayers, the angular spread due to multiple scattering is small because the low atomic number elements Si and O have weak scattering potentials ($\propto Z_2$).

The transmission spectrum of a sample with a 65Å-thick SiO_2 overlayer is shown in Fig. 41. The Si peak corresponds to the areal density of the Si atoms in the oxide as well as the reconstructed Si interfacial atoms. The peak which has a lower energy than the oxygen signal corresponds to deposited carbon during the ion-beam analysis. Usually, the low atomic number elements such as O and C are difficult to detect in random spectra because the Rutherford scattering cross-section is small ($\sigma_{RBS} \propto Z^2$). Using Fig. 41 as an example, the O and C signals are barely detectable in a non-channeled spectrum because they will be riding on top of a Si signal with approximately thirty times the spectral height

of a channeled Si spectrum.

The areal density of oxygen is plotted versus the areal density of Si for both conventional and transmission experiments in Fig. 42. The dashed lines represent the relation expected for an ideal interface composed of perfect Si single crystal and stoichiometric SiO_2. The difference between the intercepts in the two ideal curves is simply the calculated intrinsic surface peak intensity ($9.8 \times 10^{15}/cm^2$) for 2.0 MeV ^{4}He impinging on Si <110> and using a silicon Debye temperature of 543°K.

Both sets of data can be fit with a straight line of slope one-half, indicating that the oxide is stoichiometric SiO_2. The difference in the Si axis intercepts [$(11.9 \pm .2) \times 10^{15}/cm^2$ and $(.4 \pm .2) \times 10^{15}/cm^2$] of the two experimental curves is primarily due to the intrinsic surface peak and supports the calculated value of this quantity. The difference between the intercept associated with the conventional experiment and the calculated quantity is $(2.1 \pm .2) \times 10^{15}/cm^2$ or two monolayers, in good agreement with the results of Feldman et al.[2]. Qualitatively, this excess can be attributed to either reconstructed Si and/or Si associated with a silicon-rich oxide. In the latter case we would expect an extrapolated intercept for the transmission experiment of $2.1 \times 10^{15}/cm^2$ as well, assuming an amorphous oxide. If the excess Si were entirely due to reconstructed Si, the corresponding intercept in the transmission experiment

would depend on the magnitude of displacements involved. Thus the transmission experiment puts important constraints on the possible interpretations because there is an important difference between the two experimental geometries in sensitivity to displaced Si. In conventional channeling, displacements of ∿.06Å from the equilibrium position of atomic sites are sufficient to make substantial contributions to the measured surface peak. In the transmission experiment, atomic displacements of ∿0.7Å are necessary for significant increases.

In an effort to be more quantitative about the nature of this excess silicon, we have considered some simplified models which allow for a variable number of reconstructed Si layers and/or an interfacial region of variable stoichiometry. The four different models are compared with the experimental data in Fig. 43. For example, if we assume no interfacial reconstruction, an interface layer of $\sim 2 \times 10^{15}$ O/cm^2 with average stoichiometry $SiO_{0.6}$ is required to fit the conventional data as shown by the upper dashed segment in Fig. 43(a). The same model will predict the dashed line for the transmission type of experiment which is inconsistent with the data. Similarly, if one monolayer of the interfacial Si is reconstructed, the $\sim 1 \times 10^{15}/cm^2$ of excess Si will require the interfacial oxide to be $SiO_{0.9}$. Depending on the lateral extent of the displacement in the reconstructed layer, the predicted transmission data will fall <u>between</u> the two dashed lines as shown in Fig. 43(b). The lower dashed line

corresponds to a displacement between 0.1 and 0.4Å while the upper dashed line corresponds to displacements larger than 1.2Å (for reference, see Fig. 9 of Chapter 2). The width of the two dashed lines is equal to one monolayer of the Si (110) surface (9.8×10^{15} atoms/cm^2). Nevertheless, the observed transmission data are still below the predicted values of this model.

Assuming two monolayers of reconstruction, an interfacial layer of average stoichiometry $SiO_{1.9}$ is required to satisfy the conventional data. The corresponding result for the transmission experiment will depend on the lateral displacements and is bordered by the two dashed lines shown in Fig. 43(c) which are two monolayers of Si apart. The transmission data fall between the predicted values. As a last possibility, a model with three monolayers of reconstructed Si is also presented in Fig. 43(d). The conventional data will require the interfacial layer to be 1.6×10^{15} atoms/cm^2 of pure oxygen and this model is precluded because of thermodynamical considerations.

The transmission data also enable us to set some limits on the displacement of the reconstructed Si layers. The calculation of the number of atoms/cm^2 seen by the channeling ions as a function of atomic displacement has been carried out by Picraux et al.[5] Since the channeling ions see $\sim 4 \times 10^{14}$Si/cm^2 at the exit surface, we can have either one monolayer displaced up to 1Å with the other monolayer displaced

between 0.2Å and 0.06Å, or both monolayers displaced up to 0.7Å. The actual situation can be somewhere between these two limits.

The above analysis indicates that in order to fit the data well, an interfacial model with two monolayers of Si single crystal being reconstructed at the interface is required and the interfacial oxide (<4Å) has an average stoichiometry very close to SiO_2 (SiO_x with $x = 1.9 \pm 0.3$). The conclusion is in good agreement with previous channeling results by Feldman et al.[2] and Auger results by Helms et al.[6]. Recent studies by Ishizaka et al.[7] using angular resolved XPS also concluded that the Si-SiO_2 interfacial region is considered to be a first monolayer of Si substrate in contact with the SiO_2 film and no oxygen atoms are contained in the transition region[8]. Computer modeling by Pantelides et al.[1] also supports the idea of an abrupt Si-SiO_2 interface in order to minimize the interfacial elastic strain energy.

Since the Si-SiO_2 interface has been characterized by various analytical techniques, it is appropriate to comment on the meaning of an "interface" as observed by the different probing methods. For spectroscopic methods using electrons (e.g., Auger, UPS, and XPS), the interfacial region is related to the deviation of chemical bonding energies from the pure Si and SiO_2 components. We call this region a "chemical" interface. For example, a chemical shift of 1.6 eV (∿ one half

of energy shift of Si in SiO_2) has been observed for the Si_{2p} line for the interfacial Si atoms by XPS[7] in a transition region (2-3Å) of the Si-SiO_2 interface. The interpretation is that the transition region is considered to be a first monolayer of Si substrate in contact with SiO_2 because the "thickness" of the transition region is of interatomic dimensions. Similarly, interfacial studies using optical spectroscopy are based on refractive index variations across the interface. We call this region an "optical" interface. Results from Aspnes and Theeten[9] show that the Si-SiO_2 interface consists of a (7±2)Å region of chemically mixed Si and O atoms with an average stoichiometry of $SiO_{0.4\pm0.2}$ using a substrate-interface-overlayer-ambient model. The discrepancy of the optical results from others probably lies in the dielectric functions being used. For channeling or TEM observations, it is the structural and compositional deviations from the pure Si and SiO_2 components which distinguish the interfacial region. We call this region the "physical" interface. Depending on our definition, we can either include the reconstructed Si into the interfacial region or include only the non-stoichiometric compounds into the interfacial region.

From the previous discussion, it is clear that the description of an interface may depend on the analytical technique being used. The description of the interface will become more complicated if it is formed from heterogeneous

materials. Here, the atomic composition, atomic structure, and electronic structure are all relevant parameters. From a practical point of view, an interface is well-defined only if the physical positions of all the interfacial atoms have been determined. Then, other interfacial properties can be generated from fundamental principles.

In conclusion, the results of the channeling measurements indicate that thermally grown oxides on Si (110) are stoichiometric SiO_2 at least down to 4Å in thickness. Using a model-fitting procedure, an abrupt Si-SiO_2 interface is deduced with two monolayers of the Si single crystal being reconstructed at the interface. This study does not apply to low oxygen coverages on silicon, but rather it describes the Si-SiO_2 interface with thermal oxides thicker than 4Å. The combination of both conventional and transmission experiments sets upper and lower limits on the number of reconstructed layers and this technique may be the only way to measure reconstruction quantitatively <u>underneath</u> an interface.

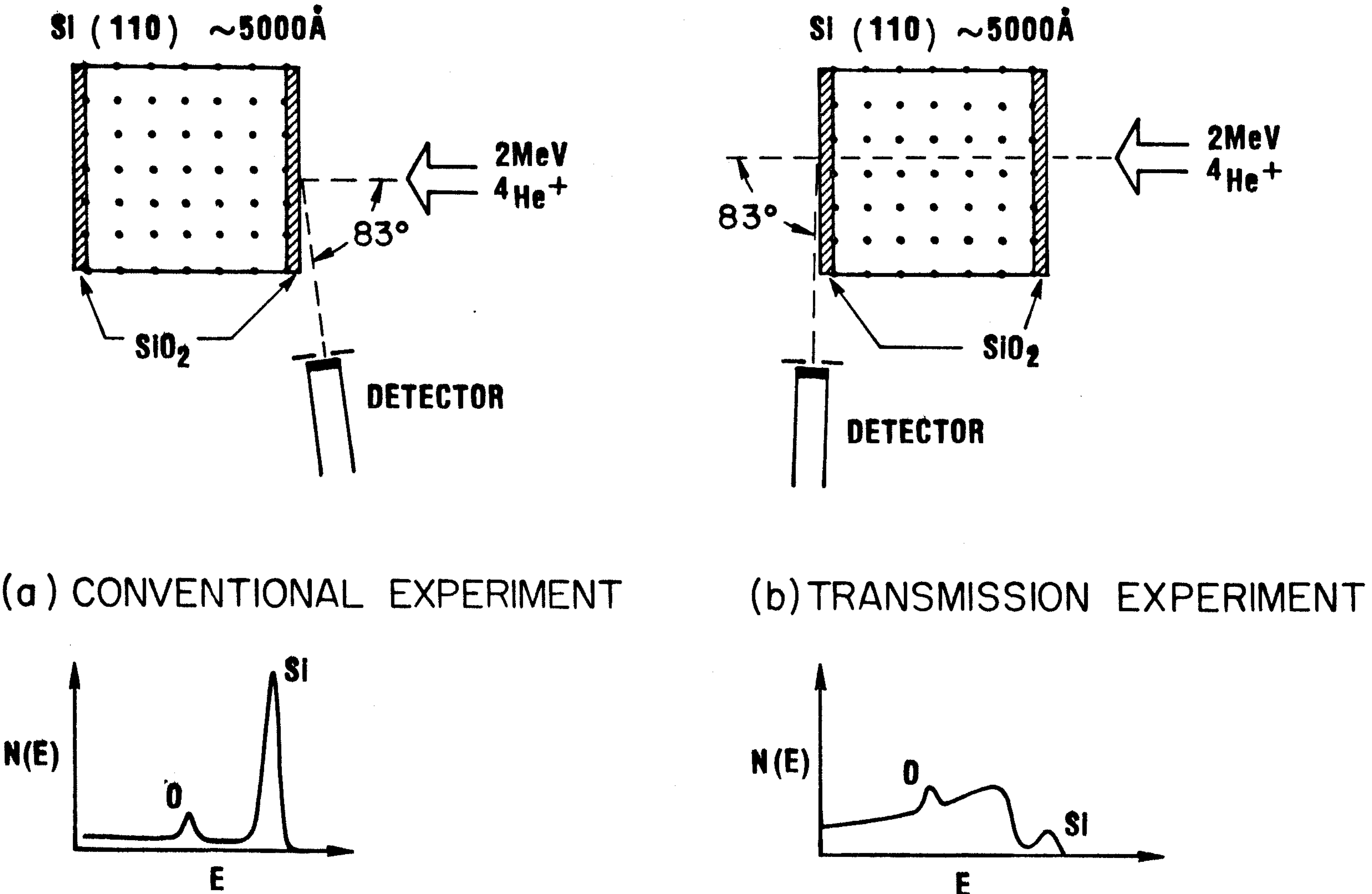

Figure 39 Schematic of the two experimental geometries: (a) conventional and (b) transmission channeling. The two spectra at the bottom illustrate the signals of interest (Si and O) in the two experiments.

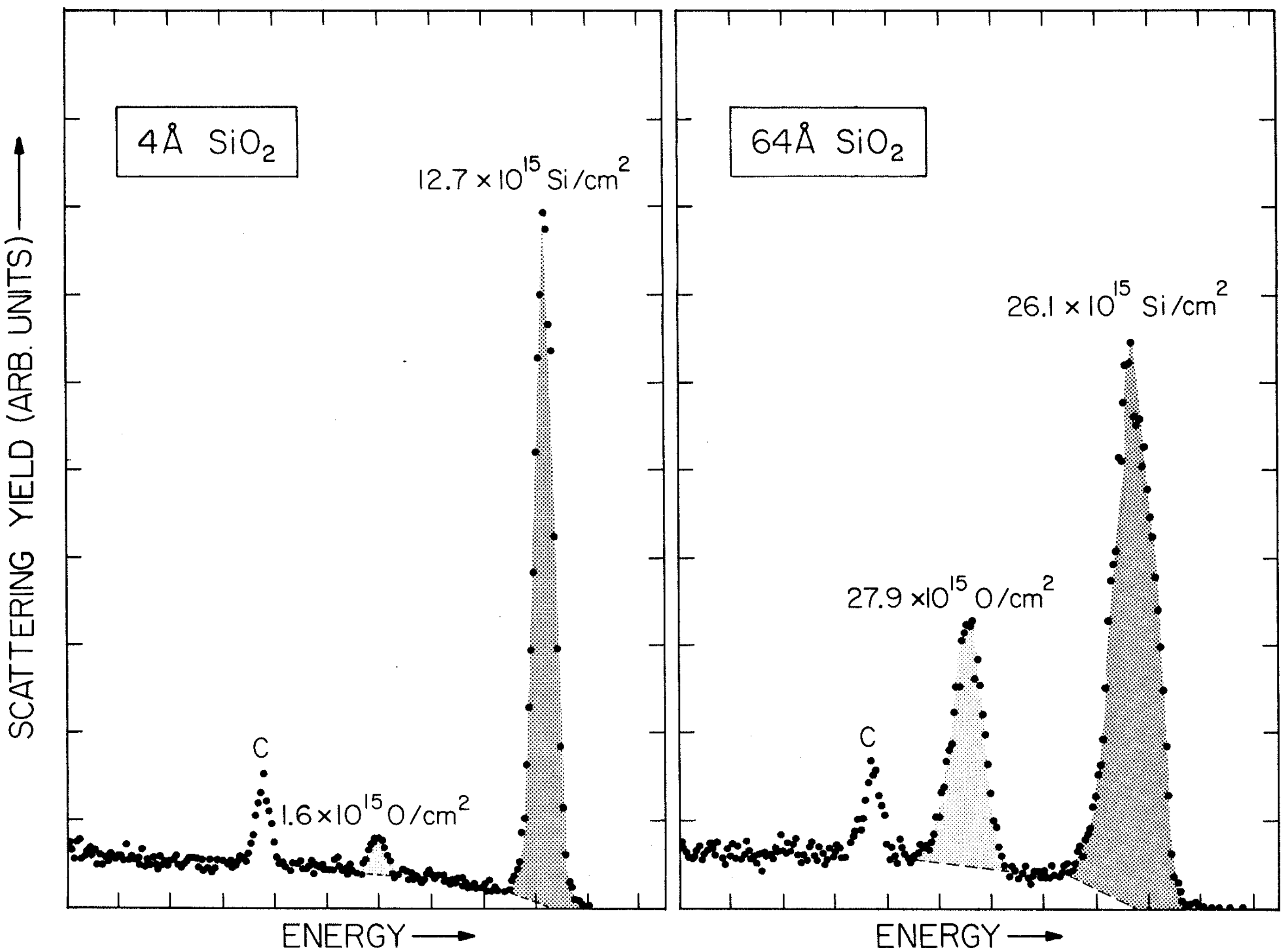

Figure 40 Conventional channeling energy spectra with a thin (4Å) and a thicker (64Å) SiO_2 layer on (110) Si. A grazing-exit detector geometry is used with a scattering angle of 97°.

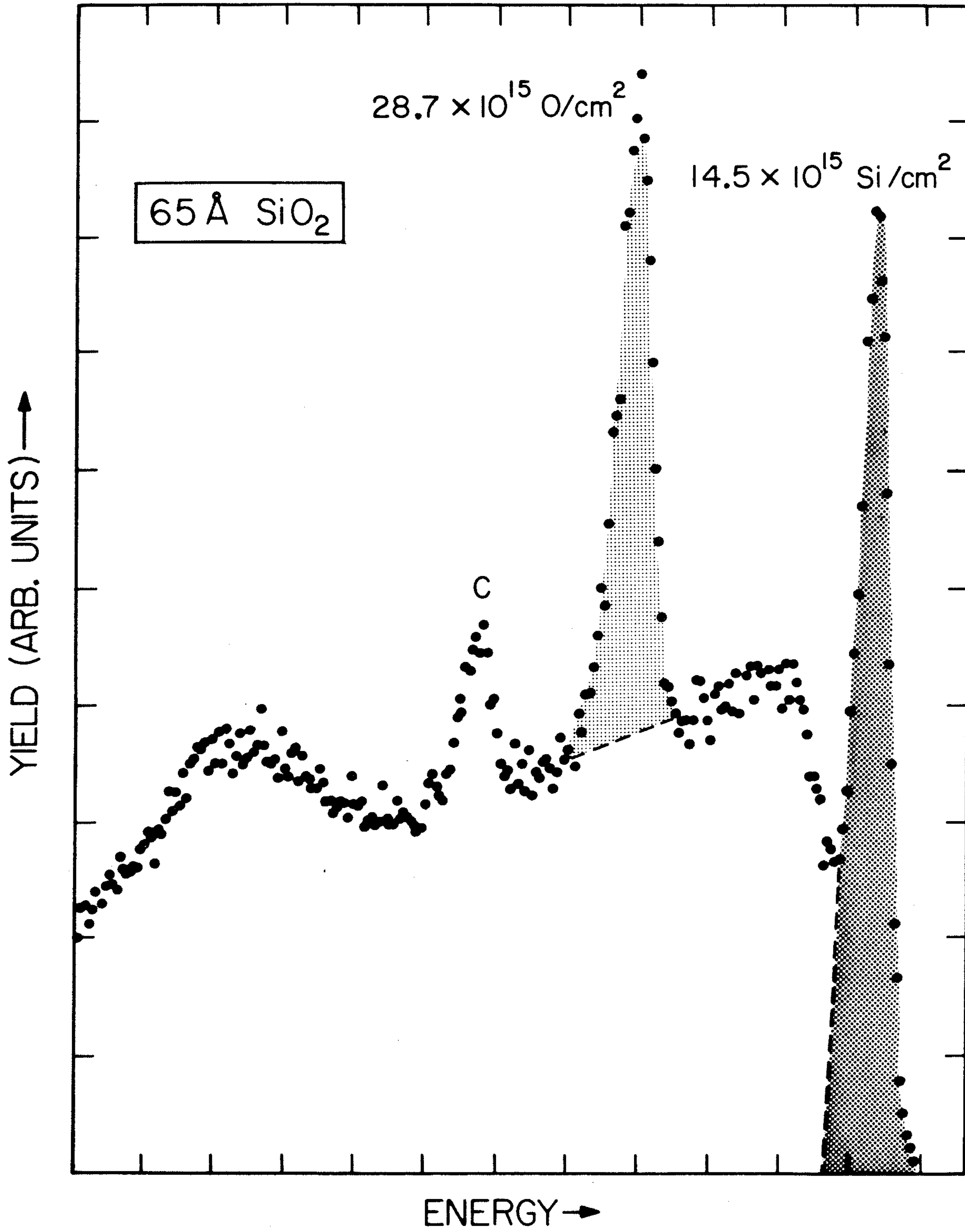

Figure 41 Transmission channeling spectrum of a 65Å- thick SiO_2 on (110) Si.

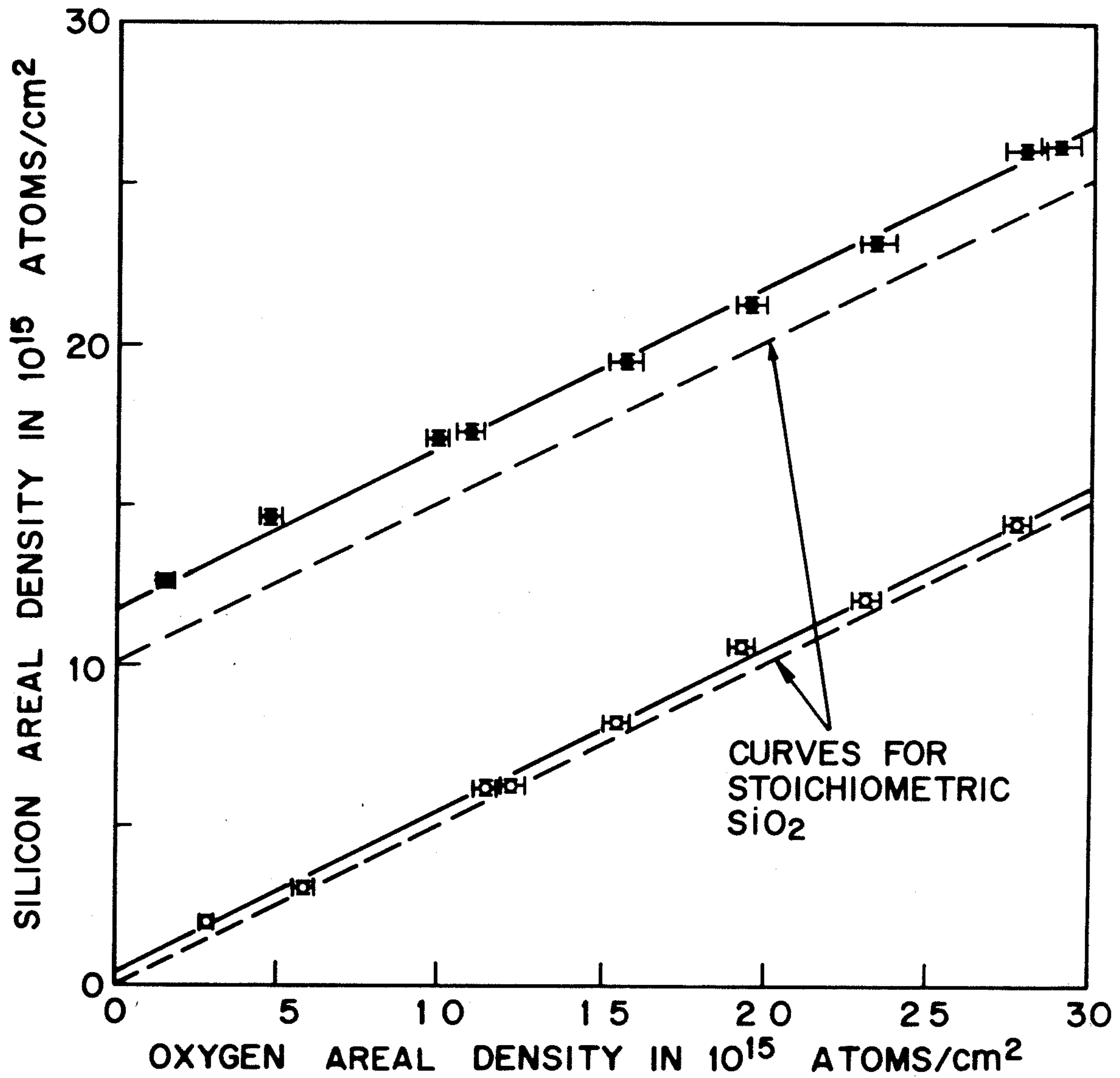

Figure 42 Silicon areal density versus oxygen areal density. Upper set of lines corresponds to the conventional experiment, the lower set to transmission experiment.

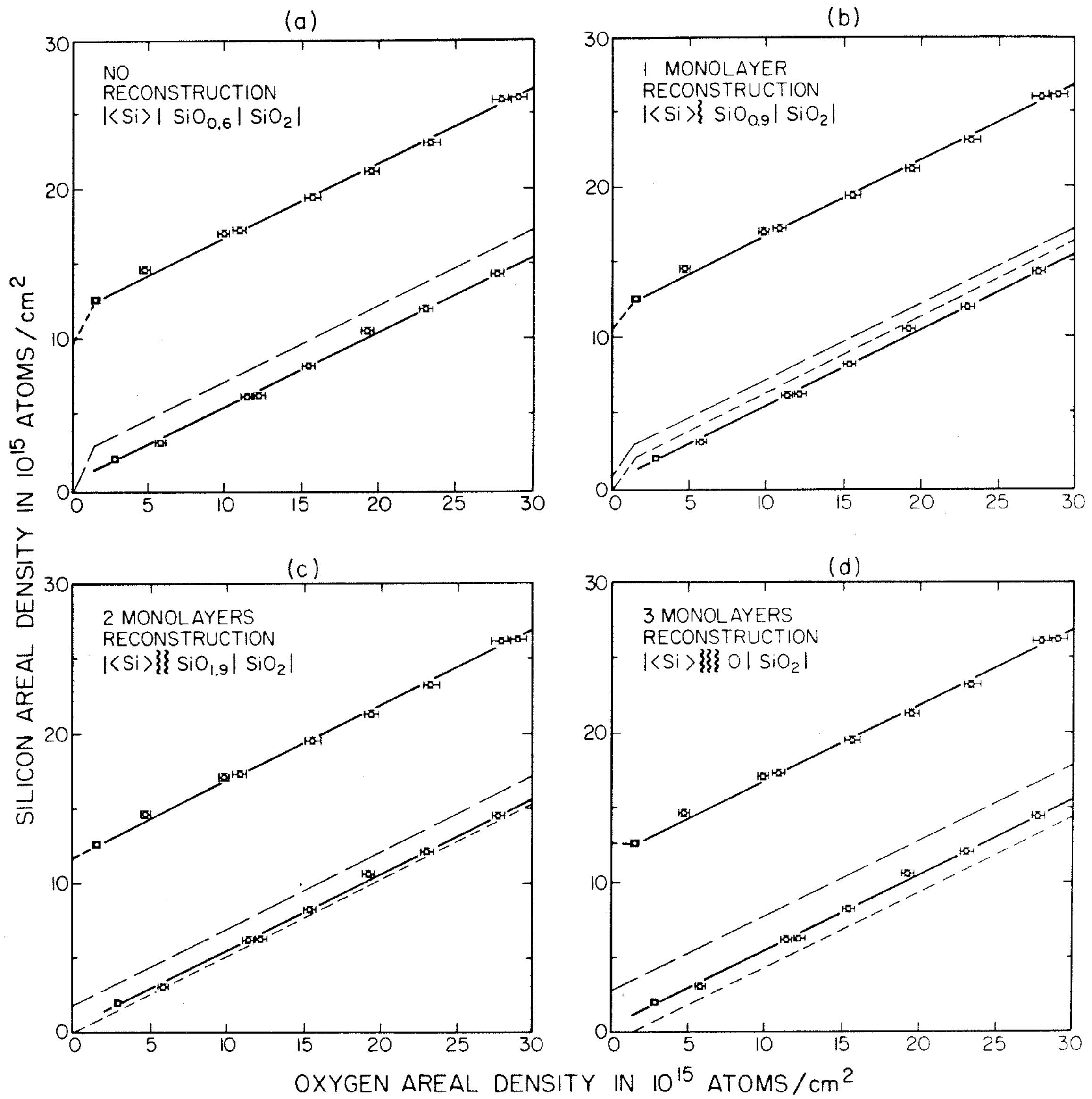

Figure 43 Comparison of experimental data to the predictions based on various numbers of reconstructed Si monolayers.

References

(1) For example, see Proceedings of International Conference of the Physics of SiO_2 and its Interfaces, edited by S. T. Pantelides (Pergamon Press, New York, 1978), p. 339 ff.

(2) L. C. Feldman, I. Stensgaard, P. J. Silverman and T. E. Jackman, Ref. 1, p. 344.

(3) L. C. Feldman, P. J. Silverman, J. S. Williams, T. E. Jackman and I. Stensgaard, Phys. Rev. Lett., 41, 1396 (1978).

(4) I. Stensgaard, P. J. Silverman and L. C. Feldman, Surface Science, 77, 513 (1978).

(5) S. T. Picraux, W. L. Brown and W. M. Gibson, Phys. Rev., B6, 1382 (1972).

(6) C. R. Helms, Y. E. Strausser and W. E. Spicer, Appl. Phys. Lett., 33, 767 (1978).

(7) A. Ishizaka and S. Iwata, Appl. Phys. Lett., 36, 71 (1980).

(8) A. Ishizaka, S. Iwata and Y. Kamigaki, Surf. Sci., 84, 355 (1979).

(9) D. E. Aspnes and J. B. Theeten, Phys. Rev. Lett., 43, 1046 (1979).

APPENDIX 1

PREPARATION OF LARGE-AREA MONOCRYSTALLINE SILICON THIN WINDOWS

A1.1 Introduction

The preparation of self-supporting silicon single-crystals with submicron thicknesses has always been of interest for device applications (e.g., X-ray lithography[1], energy-loss particle detectors[2], Schottky diodes and Josephson junctions[3], ion-beam analysis[4,5], and in-situ transmission electron microscopy studies. Madden and Gibson[2] have used a planar etching method to produce silicon crystals approximately 0.001 inches thick and half an inch in diameter. Meek et al.[4], using an electropolishing technique, have been able to produce 7000Å thick silicon thin windows approximately 2 mm in diameter. Müller and Schröder[6] have used combined processes such as ultrasonic boring, chemical etching, and low-rate ion sputtering to thin silicon crystals down to 1000Å with a window diameter of 40μm. It was after the discovery of the ethylenediamine-pyrocatechol etch (EDP)[7-9], which does not attack silicon when it is sufficiently doped with boron, that preparation of large-area silicon windows became feasible. Based on this selective etch, Schmidt et al.[1] have made silicon windows for X-ray lithography masks up to 4 cm in diameter and 1.3 to 5μm in thicknesses. A sodium hydroxide etch employed by Barycka et al.[10] has also

been able to produce similar results. In this appendix, a relatively simple method is described to prepare large-area silicon thin crystals from 1000Å to 2μm in thicknesses.

A1.2 Experimental

The basic sequence of the procedure is outlined in Fig. 44. A thin p^+ surface layer is formed on the silicon wafer by doping it with boron. With the p^+ layer protected, a window area is etched from the back side down to approximately 1 mil in thickness by using a non-selective etch. The remainder of the undoped silicon inside the window area is finally removed by the EDP etch, leaving a boron-doped layer which is supported by a thick silicon frame.

The starting materials are silicon single-crystal wafers approximately 10 to 20 mils thick with a device-grade surface finish (e.g., Syton polish). The silicon crystals can be p-type or n-type with bulk resistivities between 1 and 10 Ω-cm, and wafers of (100), (110) or (111) orientations can be used.

Although the boron doping can be achieved by either ion implantation or thermal diffusion, the latter has proven to be more convenient for batch processing. A standard boron diffusion technique which ensures uniformity over large wafer areas employs boron nitride as planar diffusion sources and nitrogen as the carrier gas. The diffusion furnace temperature is set at 1050°C and the boron penetration depth, which determines the final thin-crystal thickness, is controlled by the diffusion time. Since the actual boron diffusion profile

depends on the flow rate of the carrier gas and the geometry of the diffusion furnace, some experimentation is needed to determine the optimum diffusion parameters. Roughly speaking, a diffusion time of 15 minutes will give a window thickness of 2000Å to 2500Å; the time increases quadratically with the desired window thicknesses. The boron glass deposited onto the wafer's surfaces is later removed by dipping the wafer in boiling nitric acid and followed by a rinse in hydrofluoric acid. Using this procedure, a p^+ layer will also be created at the unpolished side of the wafer, but it will be removed during the pre-etch step.

After the boron diffusion, the silicon wafer is cleaved into smaller pieces by a diamond scriber. Flat quartz discs about two inches in diameter and 1/8 of an inch in thickness are used as sample mounting substrates for the pre-etch process. An annulus-shaped paraffin dam is built near the perimeter portion of the quartz disc (Fig. 45a). Such a paraffin layer is easily made by cutting "Parafilm" (Dixie/Marathon, Greenwich, Connecticut) into the appropriate shape and melting it on the quartz disc. By placing the silicon wafer with the polished side face-down inside the paraffin dam, a piece of adhesive teflon tape (Connecticut Hard Rubber Company, New Haven, Connecticut) with a circular hole bored in the middle is overlaid on top of the silicon wafer. Rubbing the teflon tape gently will create a tight seal between the wafer and the paraffin. This will effectively prevent

any acid from etching the protected regions of the silicon wafer.

Since the etching rates of EDP for silicon are on the order of microns per hour, it is desirable to remove a major portion of the silicon thickness with a faster etchant. In this study, a mixture of hydrofluoric acid (48% concentration), nitric acid (70.4% concentration) and glacial acetic acid (100% concentration) in the volumetric ratio of 2:5:2 is used. The etching rates for all major silicon crystallographic directions are approximately 25μm per minute and this rate can be adjusted by increasing or decreasing the hydrofluoric acid concentration in the mixture.

For the pre-etch step, the quartz disc with the mounted sample is immersed in a 250 ml teflon or polypropylene beaker containing ∿150 ml of the pre-etch solution (Fig. 45b). The beaker is rotating at 12 RPM and is inclined ∿30° to the horizon. Agitation of the etching solution is provided by feeding pressurized gases such as oxygen or nitrogen via a polypropylene pipette which is lowered into the beaker about 1 cm above the silicon wafer. This rotating plus bubbling motion often gives uniform etching rates over relatively large areas. Without such agitation, the vortex flow pattern due to the rotating beaker will create a concave etching profile in the silicon wafer and the thick edges of the window area will prolong the etching time in EDP by an order of magnitude. The nucleation of gas bubbles on the etching surface is

another problem because they can generate non-uniform etch pits. Introducing the gas jet will disperse these bubbles before they grow in size.

When the silicon wafer is thinned down to ∿1 mil in thickness, the thinned region is transparent to light and will appear reddish when placed on top of a microscope lamp. At this stage, the pre-etch process shall be stopped immediately and the quartz disc assembly is then rinsed thoroughly in water.

Since the thin window is fragile, one should not peel off the teflon tape directly. Instead, a razor blade is used to cut through the tape around the perimeter of the silicon wafer to release it from the quartz disc. The adhesive teflon tape can be detached by soaking the wafer in boiling trichloroethylene for a couple of minutes.

The second thinning step makes use of a selective etch: a mixture of pyrocatechol ($C_6H_4(OH)_2$), ethylenediamine ($NH_2(CH_2)_2NH_2$), and water in the ratio of 3 gm:17 ml:8 ml. This etching solution does not attack silicon if the boron doping level exceeds $7 \times 10^{19}/cm^3$ [9]. The etching rates for (111), (110), and (100) oriented silicon surfaces were found to be 3, 30, and 50μm/hour, respectively[7].

The thinned silicon wafer is put into the EDP etch by leaning it against a glass slide (Fig. 45c). The bath temperature is maintained at 110°C with a hot-plate. To prevent excessive loss of ethylenediamine and water through

evaporation, a reflux system has to be used. A simple way to solve this problem is to cover the pyrex beaker with a small petri dish. Depending on the silicon thickness left by the pre-etch process, the etching time for completion can vary from one to four hours before all the undoped silicon is removed. For good mechanical stability, the boundary between the thick frame and the thin window must be free of burrs. Such a boundary is easily obtained for windows with (100) and (110) orientations. For (111) oriented crystals, the anisotropic etching rates of the EDP etch generally create irregular corners and burry edges. A procedure to minimize these effects will be outlined in the discussion section.

After the EDP etch, the pyrocatechol and ethylenediamine left on the sample's surface can be removed by dipping it into a hot solution of pure ethanol.

A1.3 Characterization of Silicon Thin Crystals

Using this simple procedure, (100), (110), and (111) oriented silicon thin crystals about 1 cm in diameter can be routinely produced with thicknesses ranging between 1400Å to 2μm. With some precautions, silicon windows as large as 2 cm in diameter and 2000Å in thickness can also be prepared (Fig. 46).

Due to the selective etching properties of the EDP solution, lateral uniformity of the thin crystals is primarily determined by the boron diffusion process. The physical thickness of the samples was measured with MeV ion back-

scattering spectrometry[11], using tabulated values of the energy-loss stopping powers. The thickness variation of a 1700Å thick Si (100) crystal about 0.9 cm in diameter is shown in Fig. 47. The helium ion energy used was 1.5 MeV. To enhance the depth resolution, the solid-state detector was placed at an angle of 20° to the window's surface. The sampling beam spot was about 1/2 mm x 1/2 mm and thickness measurements across the window area were taken at distance increments of 1 mm apart. Care was taken to avoid any ion-beam channeling effect because it will lower the energy-loss stopping powers. Results of the scanning thickness measurements show that, except for regions near the edge area, uniformity of the sample varies only by ±60Å across the whole window.

It is well known that boron can occupy substitutional positions in the silicon lattice up to concentrations of 0.3 at.%[12] ($1.5 \times 10^{20}/cm^3$). Nevertheless, boron segregation or formation of defects can still occur depending on the doping method and the thermal history of the sample. To investigate the crystalline perfection of these silicon thin crystals, TEM studies are particularly suitable because the windows are transparent to keV electron beams without further sample thinning.

A convenient way to transfer the thin window to the TEM sample stage is by gluing a ring-shaped sample holder to the thin crystal using epoxy and cracking the silicon window

outside the ring area. TEM micrographs of two Si (110) thin crystals with thicknesses of 3000Å and 7500Å are shown in Fig. 48 as samples A and B, respectively. For the 3000Å-thick sample (i.e., shallow boron diffusion) no defects such as dislocation lines or stacking faults can be observed. For the thicker sample with a longer boron diffusion time, the dominant defects are dislocation loops along with some stacking faults.

The channeling properties of ion beams in single-crystals can be very informative on characterizing the depth distribution of defects[13]. For monocyrstalline materials, the backscattering yield of MeV ions due to the crystalline matrix will be reduced by more than an order of magnitude when the ion beam is aligned along major crystallographic directions. One useful parameter to characterize the crystalline quality of the matrix is the channeling minimum yield (χ_{min}), which is defined by the ratio of the scattering yields between channeling and random incident directions. For all the (100), (110), and (111) oriented silicon thin crystals prepared by this method, the χ_{min} values near the surface region are between 3 to 5% and the values are comparable with those of the starting silicon wafers. The channeled and random spectra of a 4300Å-thick Si (110) crystal is shown in Fig. 49. The χ_{min} value is 3.5% near the surface region, and it increases to 4% at the rear end of the crystal. This indicates there is not much dechanneling

due to defects. For a sample which is heavily doped with boron (e.g., sample B as indicated in Fig. 48), the χ_{min} value can be as high as 8% at the rear end of the crystal. This increase in χ_{min} is partly due to the increased thickness of the crystal and partly due to the presence of defects.

A1.4 Discussion

The preparation of (111) oriented silicon thin crystals deserves some special attention because the EDP etch has very low etching rate on silicon (111) surfaces. Consequently, the etching mechanism progresses much faster laterally on other crystallographic planes which intersect the (111) surface than the (111) surface itself. This often results in windows of irregular shapes and sharp corners such as shown in sample A of Fig. 50. To minimize such effects, a slightly thinner area is created around the center of the window area during the pre-etch process. This can be achieved by lowering the gas flow rate so as to produce less bubbling agitation. When dipped into the EDP etch, the thin window will first start at the thinnest central area and expand laterally. The EDP etching process will be stopped before the thin window area expands to the edge of the thick silicon frame. Sample B of Fig. 50 illustrates the smooth window contour which can be obtained by following such a procedure. The oval-shaped thin window has proven to be far superior in mechanical stability than those with sharp corners.

Making the silicon single crystals self-supporting also

raises new possibilities of designing interesting device structures such as transducers, electronic devices, or a hybrid of both. However, the boron concentration has to be lowered to $\sim 10^{16}/cm^3$ in order to make them useful for active devices. This can be done by a thermal drive-out process in a nitrogen ambient, as described by Huang and van Duzer[3]. Alternatively, these thin crystals can be used as a seed to grow epitaxial silicon layers on top and/or bottom by processes such as chemical vapor deposition. The feasibility of the latter concept has yet to be demonstrated.

During the course of this study, it has been found that the silicon thin crystal can be made amorphous by ion implantation up to 1/3 of its original thickness or can be heated to 1000°C without breaking. Layers of SiO_2 and metal silicides can also be grown on these thin crystals by thermal annealing up to 850°C.

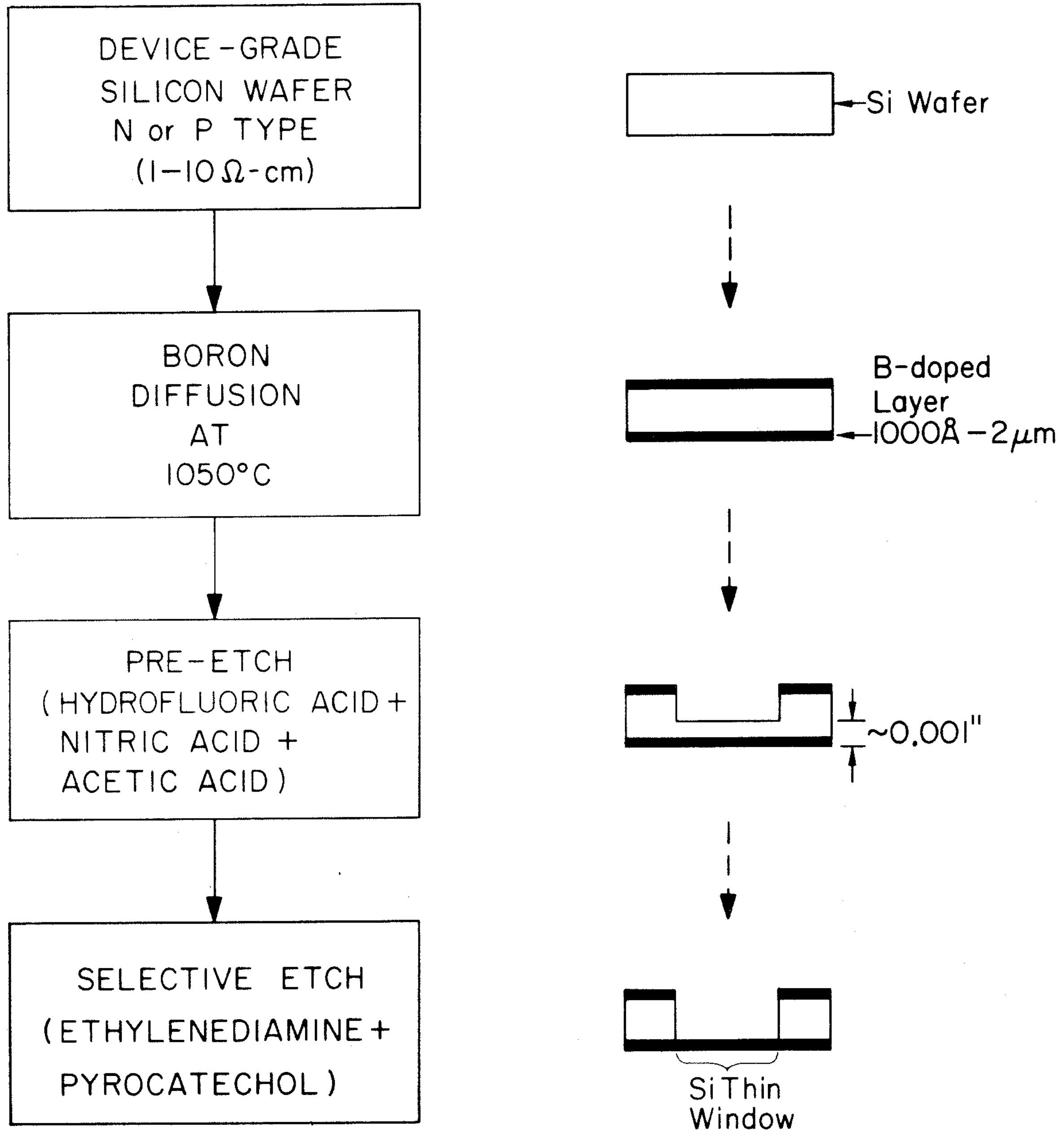

Figure 44 Flow chart of processes used to prepare silicon thin windows.

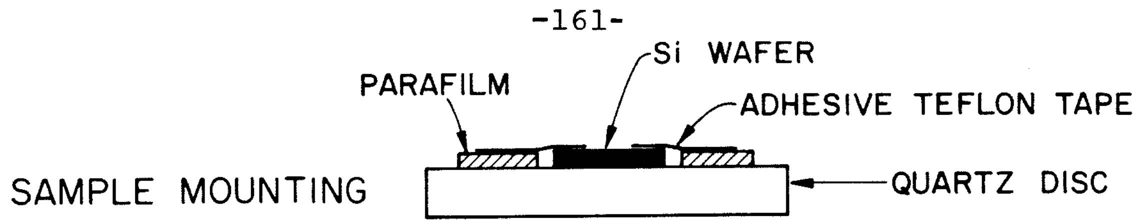

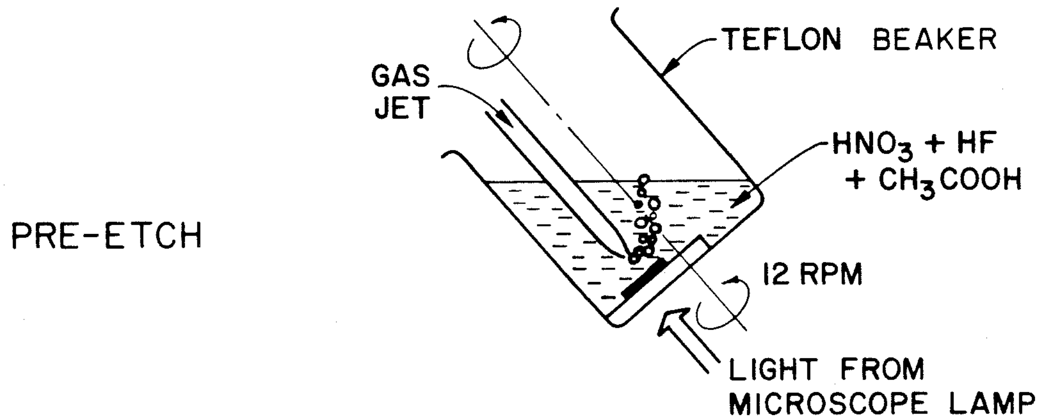

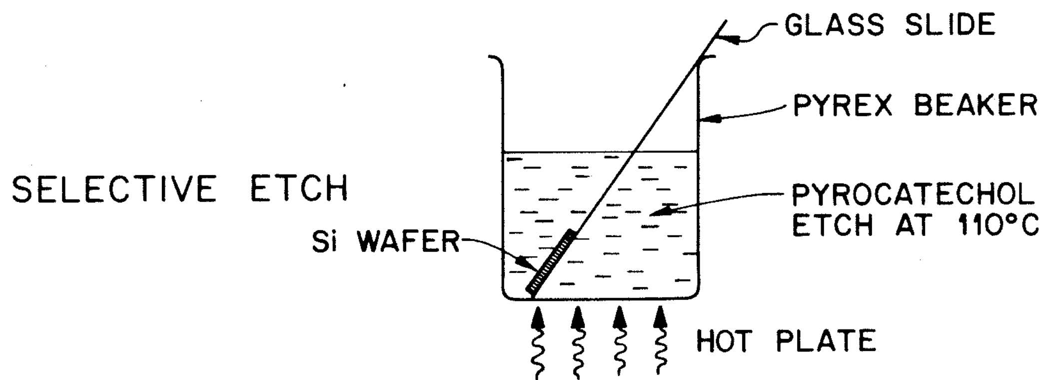

Figure 45   Experimental set-up for the etching processes.

Si <100>
2000 Å

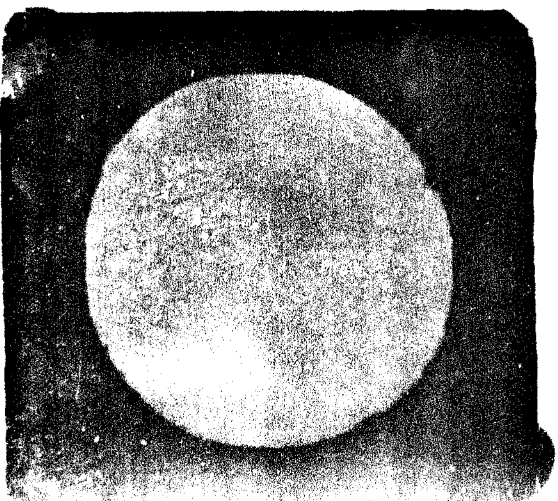

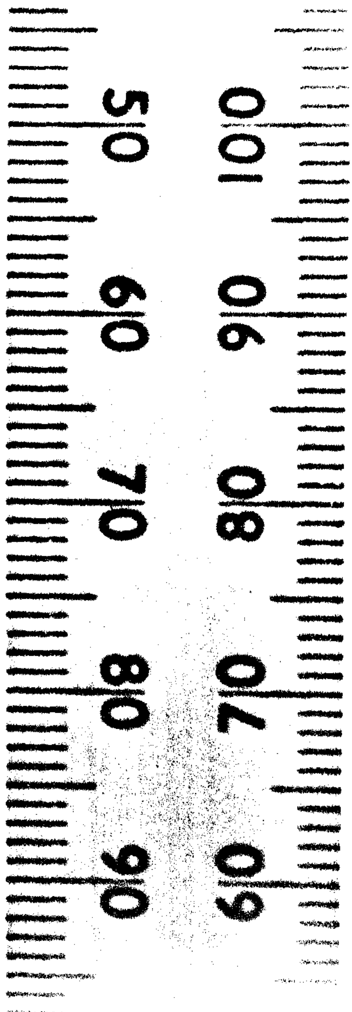

Figure 46 Photograph of a 2000 Å thick, self-supporting Si(100) crystal. The diameter of the window area is 2 cm.

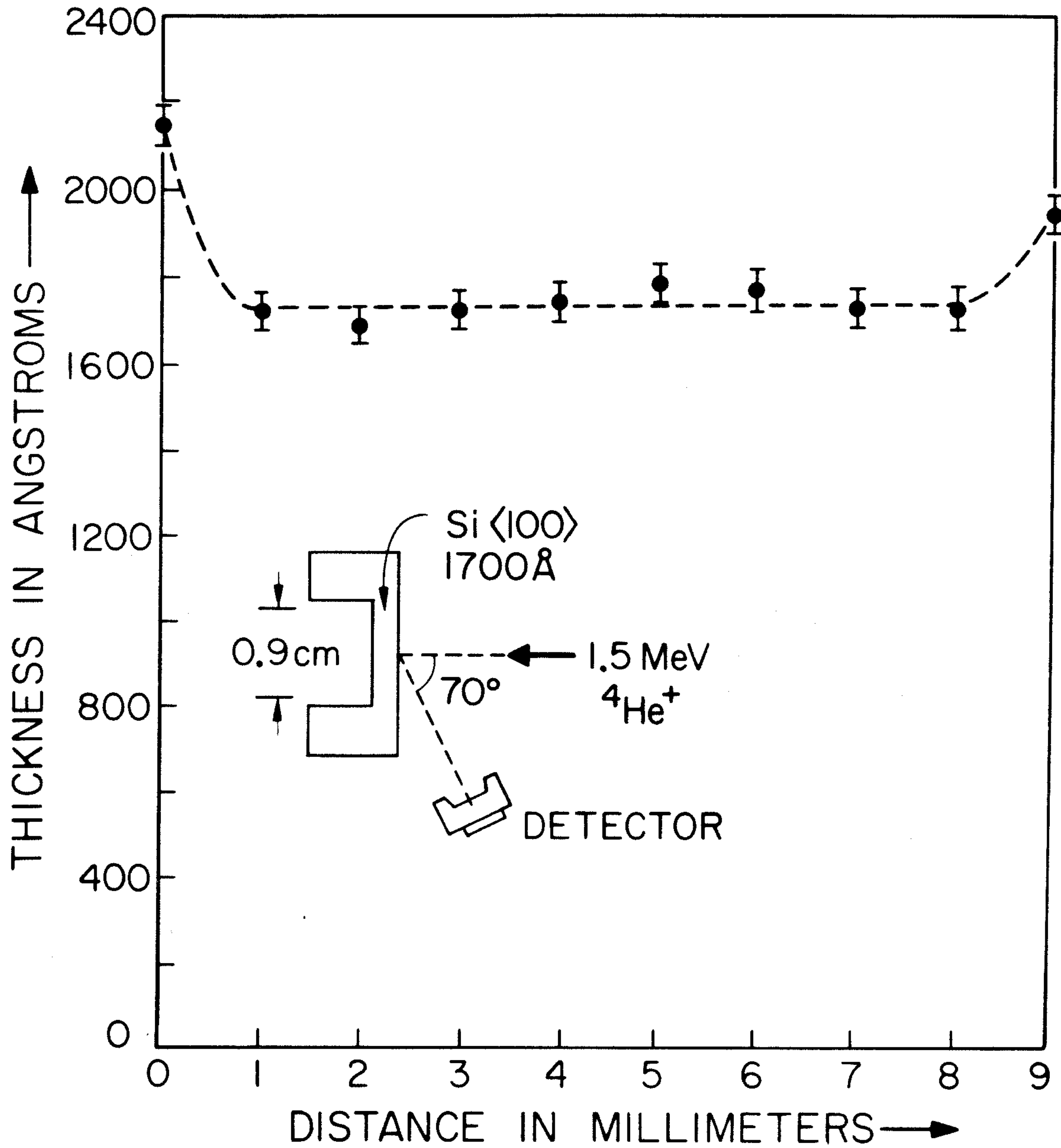

Figure 47 Results of thickness measurements across a 1700 Å-thick (100) Si crystal using backscattering spectrometry.

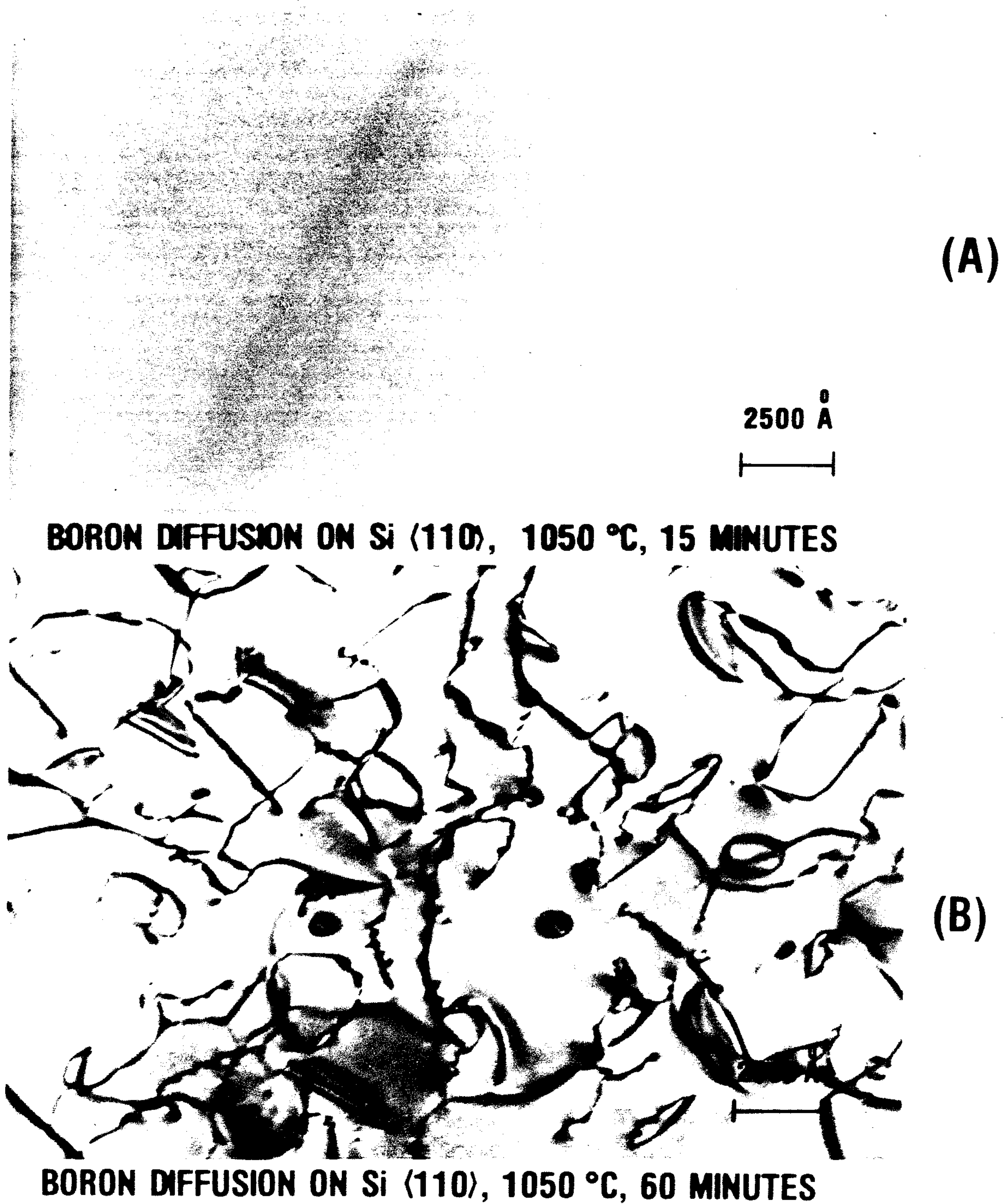

Figure 48 TEM micrographs of a 2500 Å-thick (A) and a 7500 Å-thick (B) Si(110) crystals prepared by using different boron diffusion times.

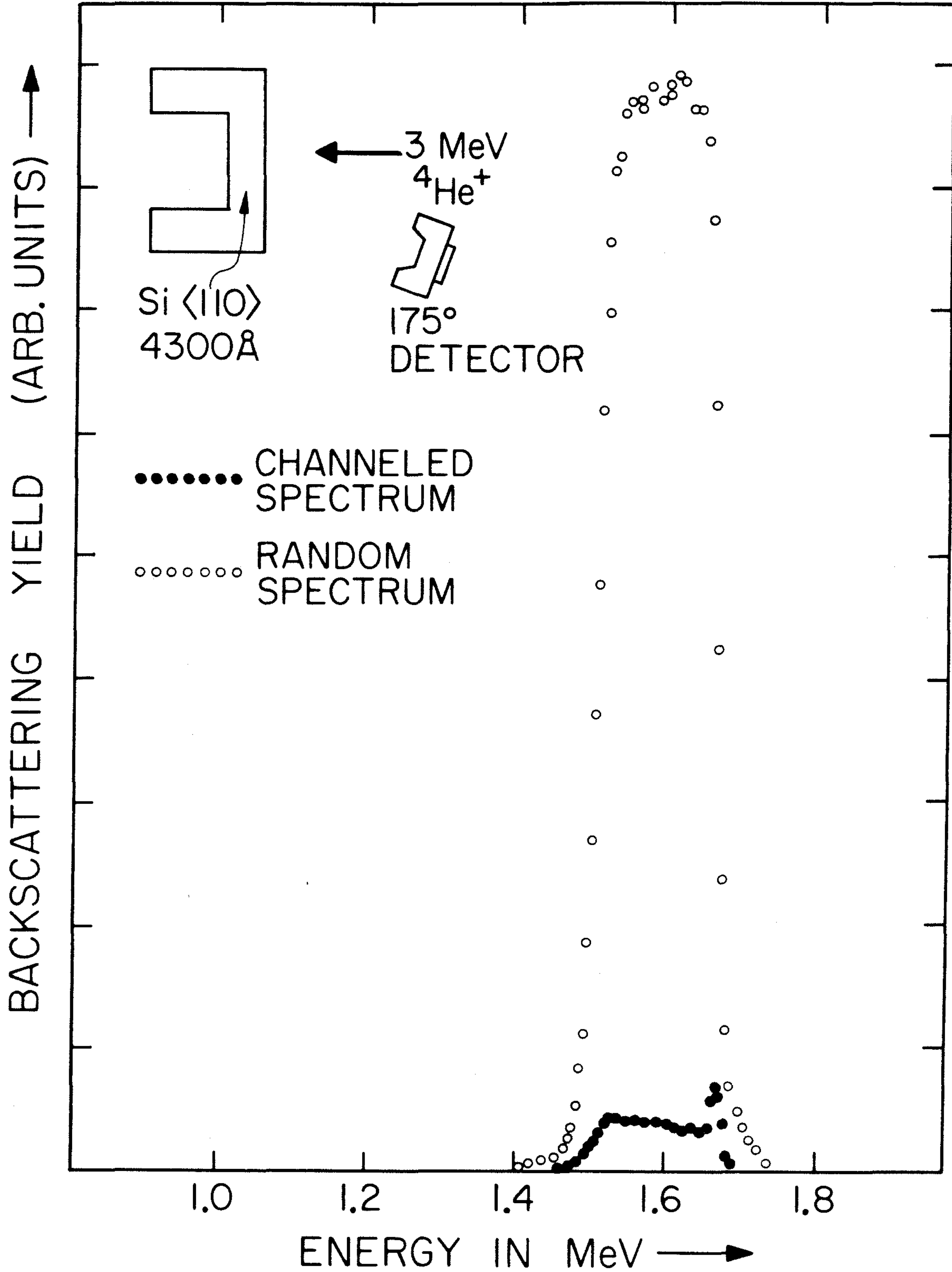

Figure 49 Channeled and random spectra of a 4300 Å-thick Si(110) crystal. The channeling axis is <110>.

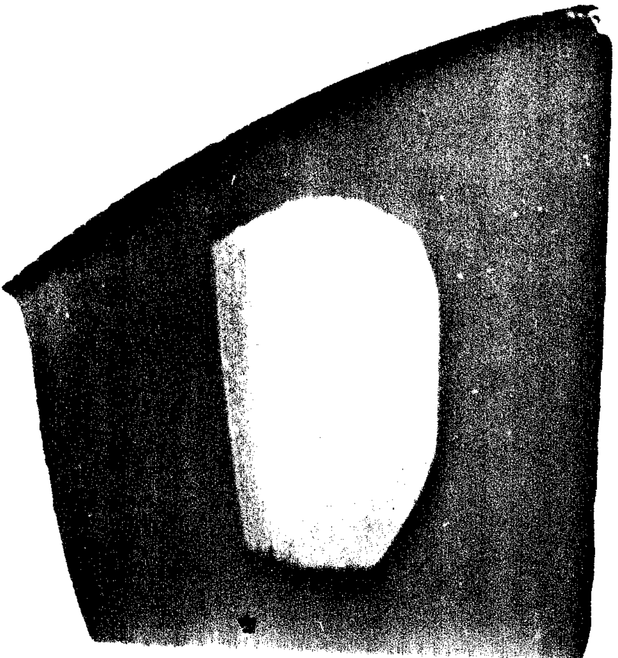

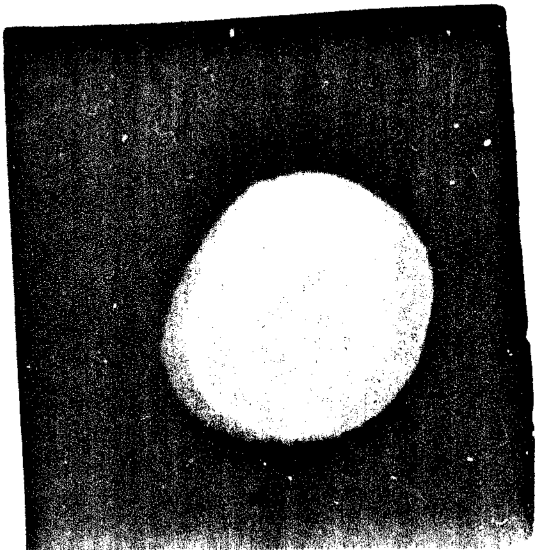

Figure 50 Photograph showing the sharp corners of (111) oriented silicon thin windows (A) and the improvement by modifying the pre-etch etching profile (B).

References

(1) C. J. Schmidt, P. V. Lenzo and E. G. Spencer, J. Appl. Phys., 46, 4080 (1975).

(2) T. C. Madden and W. M. Gibson, IEEE Trans. Nucl Sci., NS-11, 254 (1964).

(3) C. L. Huang and T. van Duzer, IEEE Trans. Electron Devices, ED-23, 579 (1976).

(4) R. L. Meek, W. M. Gibson and R. H. Braun, Nucl. Instrum. Meth., 94, 435 (1971).

(5) L. C. Feldman, P. J. Silverman, I. Stensgaard and T. Jackman, Phys. Rev. Lett., 41, 1396 (1978).

(6) H. W. Müller and B. Schröder, J. Appl. Phys., 49, 3595 (1978).

(7) R. M. Finne and D. L. Klein, J. Electrochem. Soc., 114, 965 (1967).

(8) J. C. Greenwood, J. Electrochem. Soc., 116, 1325 (1969).

(9) A. Bohg, J. Electrochem. Soc., 118, 401 (1971).

(10) I. Barycka, H. Teterycz and Znamirowski, J. Electrochem. Soc., 126, 345 (1979).

(11) W. K. Chu, J. W. Mayer and M-A. Nicolet, Backscattering Spectrometry (Academic Press, New York, 1978).

(12) F. H. Horn, Phys. Rev., 97, 1521 (1955).

(13) D. S. Gemmell, Rev. Mod. Phys., 46, 129 (1974).

APPENDIX 2

CHARACTERIZATION OF Si SURFACES CLEANED BY HYDROFLUORIC ACID

A2.1 Introduction

In device fabrications, one of the final procedures to clean Si wafers involves a hydrofluoric acid etch which removes the oxides on Si surfaces. Depending on the laboratory conditions, monolayers or submonolayers of contaminants such as O and C may still be left on the surface and can be detected easily by techniques such as Auger or X-ray photoemission spectroscopy. It is conceivable that these surface impurities may play a role in the interfacial reactions after a layer of material is deposited on top. A detailed characterization of the as-cleaned Si surfaces should be considered as an integral part of the interfacial studies.

For all the Si crystals used in this research, the Si was first organically degreased and then dipped into an aqueous solution of hydrofluoric acid (48% concentration) prior to the metal evaporations. The goal of the present study is to identify the contamination species as well as to determine the contamination levels of such a surface preparation procedure. First, nuclear resonance techniques were used to determine quantitatively the amount of O and C because of their known scattering cross-sections. X-ray photoemission spectroscopy (XPS) was then used to determine the various contamination species, the chemical states of the contaminants and the

relative abundance of these contaminants. Since XPS needs a "standard" to convert the various measured intensities into absolute quantities, the O_{1s} line will be used as an internal standard whose atomic areal density is determined independently by nuclear resonance techniques.

A2.2 Nuclear Resonance Techniques

For ion-beam scattering analysis, the scattering cross-sections in the Rutherford regime have been well characterized and tabulated(1). For low atomic number (Z) elements, the scattering cross-sections are low and the signals of interest are usually obscured by substrate scattering signals. To minimize the background levels, Feldman et al.(2) have used the channeling technique with a grazing exit detector geometry to determine oxygen coverages on Si crystals in the range of 1×10^{15} atoms/cm^2. A more sensitive technique to detect submonolayer coverages of oxygen is to make use of the $^{16}O(\alpha,\alpha)^{16}O$ nuclear reaction(3) with ^4He ions at 3.054 MeV. The resonance has a differential scattering cross-section ($d\sigma/d\Omega$) of $\sim$1 barn per steradian and a FWHM resonance width of 13 keV . Since $\sigma_{resonance}/\sigma_{RBS}$ is strongly peaked towards the back-scattered direction, the solid-state detector is placed at a scattering angle of 175°

To illustrate the sensitivity of the technique, the backscattering-channeling spectrum of a 2500Å-thick Si (100) crystal, which was cleaned by dipping in hydrofluoric acid,

is shown in Fig. 51. The amount of oxygen at the front surface was measured to be 7.5×10^{14} atoms/cm^2. This areal density is determined by comparing the resonance scattering yields between the sample and a reference which has ∿20Å of SiO_2 on a Si crystal. The latter's high oxygen concentration can be easily quantified by normal backscattering-channeling techniques at energy regimes where the Rutherford cross-sections are applicable. The marked difference between nuclear resonance and Rutherford cross-sections can be appreciated by noting the absence of any scattering signal from the oxygen atoms at the back side of the thin crystal. After the beam has traversed the thin crystal, the ion energy is decreased by about 50 keV and the energy shift falls outside the resonance energy width of the $^{16}O(\alpha,\alpha)^{16}O$ reaction. By rotating the crystal such that the back surface was facing the incident beam, the oxygen concentration at the back surface was determined to be 7.0×10^{14} atoms/cm^2.

In the thin-crystal case, there is no signal interference from the Si substrate and detection sensitivity on the order of 1×10^{14} O/cm^2 can be easily achieved. With thick crystalline substrates, the Si scattering yield will extend all the way below the Si edge and channeling will be required to suppress the background level by a factor of ∿20. Based on the Si channeled yield of Fig. 51, a detection sensitivity of 2×10^{14} atoms/cm^2 for oxygen can be assumed by using this technique.

For all the Si samples cleaned by hydrofluoric acid, the oxygen areal density on the surface always fell between $7 \times 10^{14}/cm^2$ to $1 \times 10^{15}/cm^2$. A more detailed discussion on the chemical nature of these oxygen atoms will be given in the XPS section.

The amount of carbon on the as-cleaned Si surfaces was measured by the $^{12}C\ (\alpha,\alpha)\ ^{12}C$ nuclear reaction(4) around 3.2 MeV, using ^4He as the projectile ion. The differential scattering cross-section is 0.1 barn/steradian at a scattering angle of 170°. Unlike the $^{16}O(\alpha,\alpha)\ ^{16}O$ reaction, $d\sigma/d\Omega$ varies by less than 10% for a 50 keV change in ^4He energy. The carbon areal density was determined by the following equation:

$$\text{Carbon atoms/cm}^2 = \frac{\text{Scattering Yield}}{\left(\frac{d\sigma}{d\Omega} \cdot \Delta\Omega \cdot Q\right)} \qquad (14)$$

where Q is number of incident ^4He ions and $\Delta\Omega$ is the detector solid-angle (= 2.9×10^{-2} steradian). After an analysis dose of 10μC (i.e. 6.25×10^{13} ions), the carbon concentration was measured to be $\sim 1 \times 10^{15}$ atoms/cm^2 on both surfaces of the as-cleaned Si thin crystal and the value kept increasing as a function of the accumulated ^4He dose (Figure 52). By extrapolating to zero ion dose, the carbon contamination on the as-cleaned Si surface was estimated to be between 3×10^{14} and 5×10^{14} atoms/cm^2.

The build-up of carbon on sample surfaces has always been a problem for ion implantation and ion-beam analysis unless the experiment is performed under ultra high vacuum conditions. This thin-crystal experiment clearly demonstrated that the carbon build-up is not due to particles carried along with the beam because the carbon levels increased at the same rate at both front and back surfaces of the thin crystal. Instead, the carbon build-up is probably caused by the ion-beam decomposition of hydrocarbon molecules in the vacuum chamber.

A2.3 X-ray Photoemission Spectroscopy

The XPS analysis on the as-cleaned Si surfaces was performed at a vacuum of $\lesssim 1 \times 10^{-9}$ Torr, using AlKα radiation (photon energy = 1486 eV). A photoemission spectrum corresponding to electronic binding energies between 0 to 1250 eV is shown in Fig. 53(a). The major contaminants were identified to be carbon, oxygen and fluorine from the C_{1s}(284eV), O_{1s}(532eV) and F_{1s}(685eV) photoelectrons. Using the tabulated values of photoelectric cross-sections of various elements relative to the C_{1s} level,[5] their relative concentrations can be determined by measuring the integrated intensities of the various peaks (Figs. 53(c), 53(d) and 53(e)). This procedure is justified as long as the impurities are located at the near-surface region shallower than the escape depth of the photoelectrons (10-20Å). For example, the cross-sections of C_{1s}, O_{1s} and F_{1s} lines are 1, 2.93 and 4.43 respectively. With a

measured O/C intensity ratio of 0.96, the carbon concentration will be 2.3×10^{14} atoms/cm^2 if the oxygen concentration is taken to be 7×10^{14} atoms/cm^2. This value for C agrees well with the nuclear resonance measurements. Similarly, the F/C intensity ratio was found to be 1.5 and this corresponds to a fluorine concentration of 7×10^{14} atoms/cm^2. Between different runs, the fluorine contamination can vary between 2×10^{14} to 7×10^{14} atoms/cm^2 and this may be related to the outgasing conditions during the pump-down procedure.

One noticeable feature of the Si_{2p} line is the absence of any Si_{2p} signal corresponding to SiO_2 (+4 oxidation state) and SiO (+2 oxidation state) in Figure 53(b). This implies the oxygen atoms are either chemically bonded as part of a silicon-fluorine complex or possibly as a monolayer of water on the Si surface.

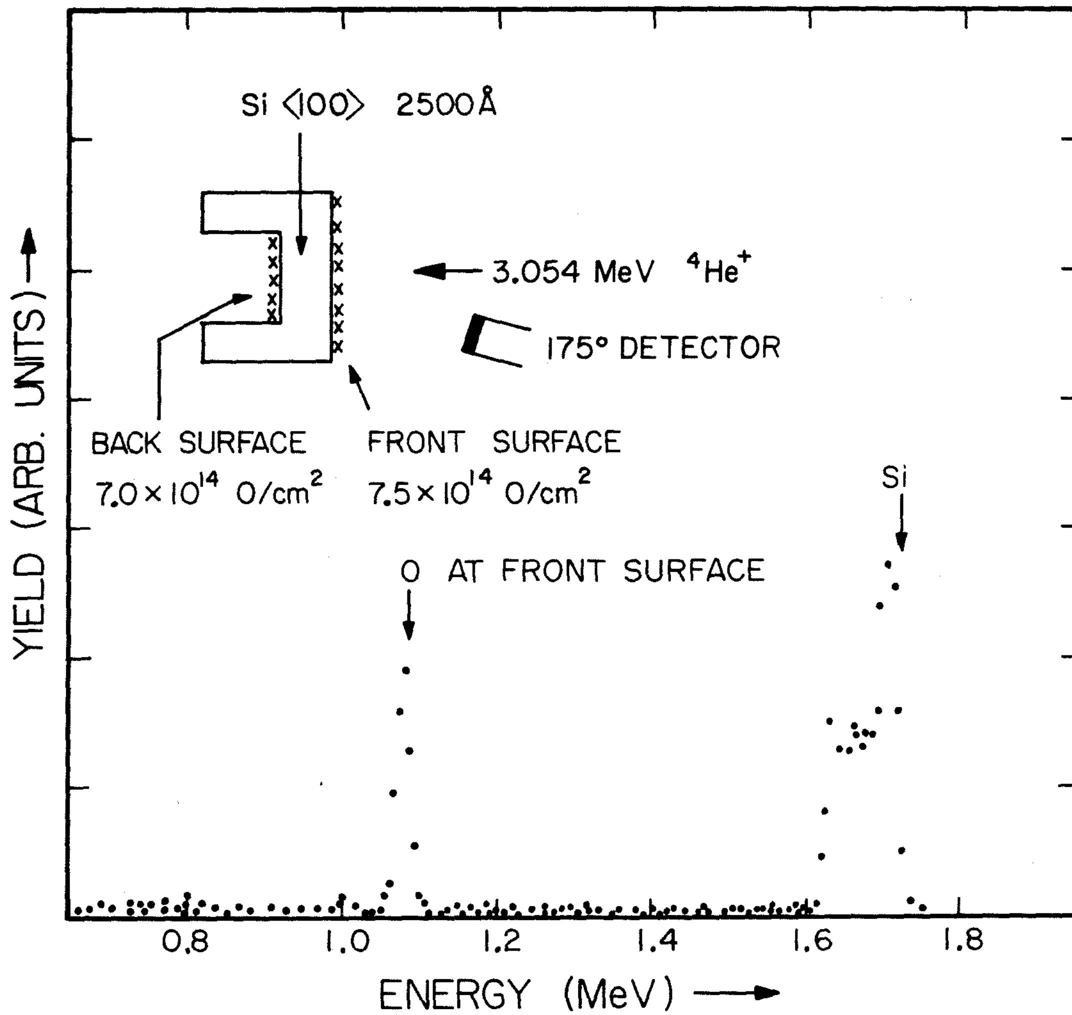

Figure 51 Backscattering - channeling spectrum of a chemically cleaned Si (100) thin crystal. 3.054 MeV ^{4}He ions are used to induce the $^{16}O(\alpha,\alpha)^{16}O$ nuclear resonance.

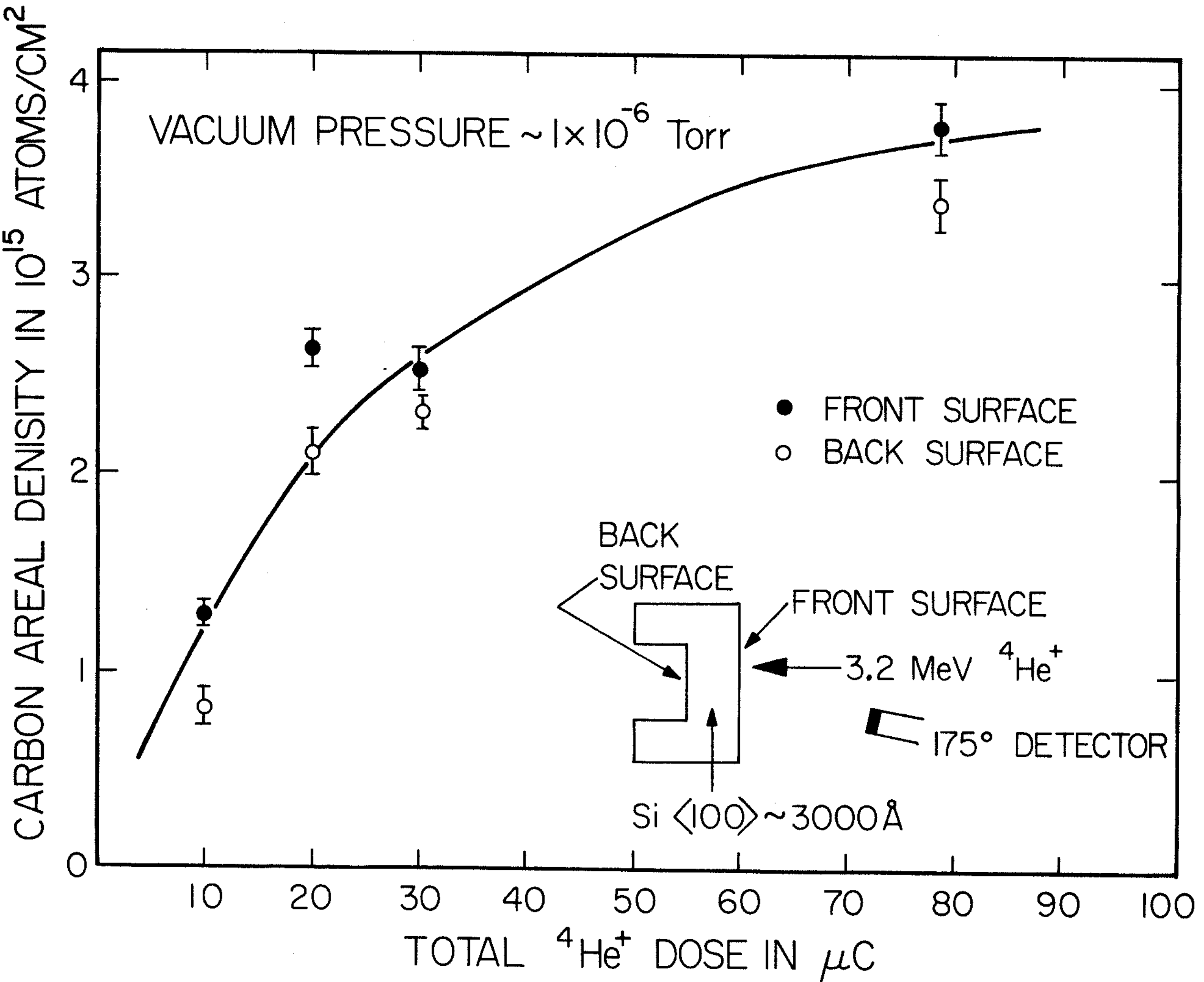

Figure 52 The build-up of carbon on sample surfaces as a function of ^4He dose. The C areal densities are measured by the $^{12}C(\alpha,\alpha)^{12}C$ nuclear resonance.

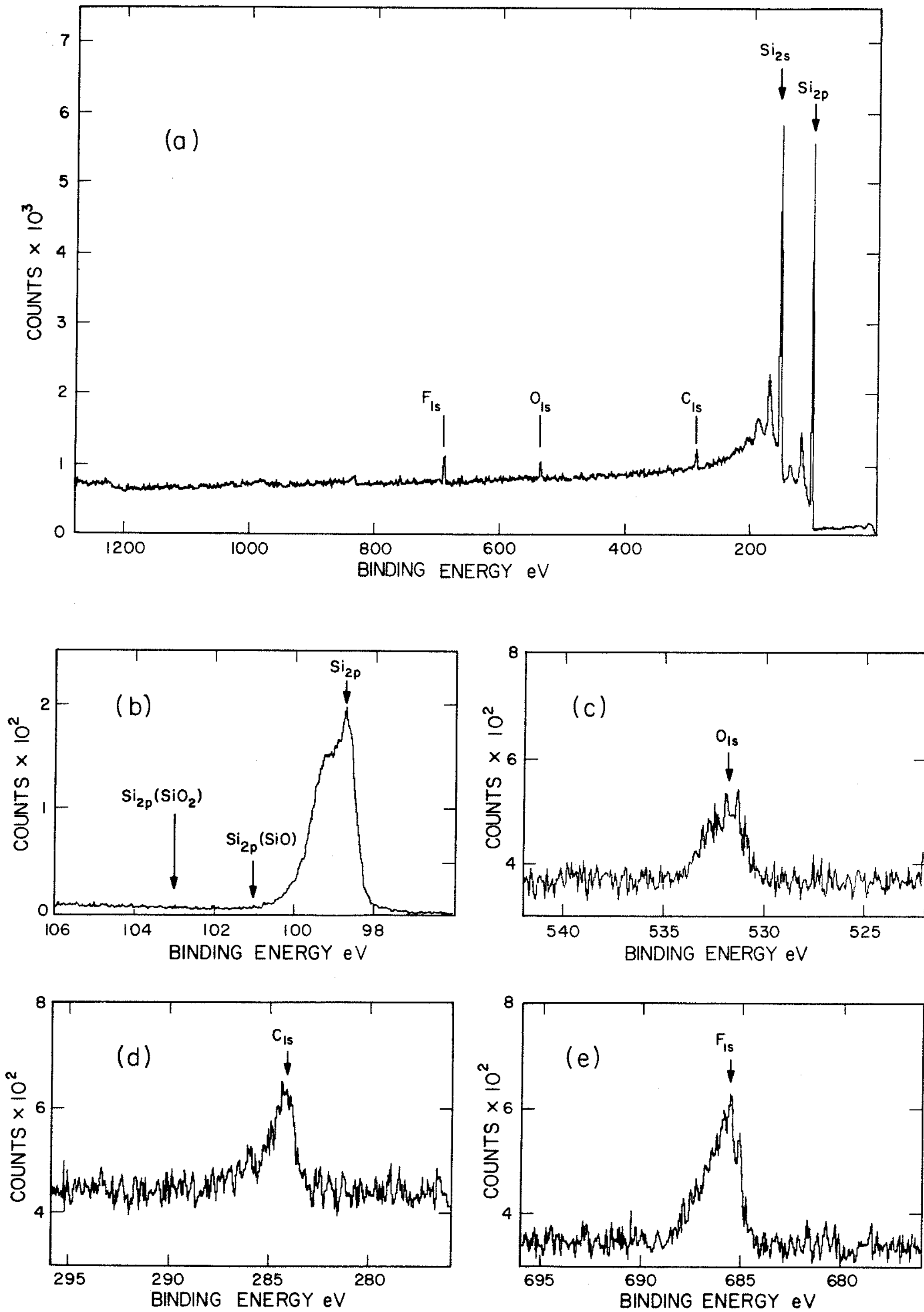

Figure 53 XPS spectra of a chemically cleaned Si surface. The excitation photons are AlKα radiation (1486 eV).

References

(1) Ion Beam Handbook For Material Analysis, edited by J. W. Mayer and E. Rimini, (Academic Press, New York, 1977).

(2) L. C. Feldman, P. J. Silverman, J. S. Williams, T. E. Jackman and I. Stensgaard, Phys. Rev. Lett., 41, 1396 (1978).

(3) J. R. Cameron, Phys. Rev., 90, 839 (1953).

(4) R. W. Hill, Phys. Rev., 90, 845 (1953).

(5) J. H. Scofield, J. Electron Spectrosc. Rel. Phen., 8, 129 (1976).

PART II

DIFFUSION BARRIER PROPERTIES OF TITANIUM NITRIDE

CHAPTER 1

INTRODUCTION

Diffusion processes in metallic thin films have a major impact on the design of microelectronic structures. Metallic contacts, besides being an integral part of active elements, such as Schottky diodes and MOS devices, also serve as interconnecting paths between devices. Some common problems associated with metallization schemes on semiconductor devices are the formation of intermetallic compounds between the metal layers and the diffusion of metallic elements into Si in the vicinity of active junction areas. These reactions can occur during processing steps at temperatures as low as a few hundred degrees Celsius. The formation of intermetallics can cause problems such as loss of adhesion, loss of solderability, and an increase of sheet resistivity(1). The presence of metallic impurities at the active junction areas will lower the carrier lifetimes and create leakage currents. In some severe cases, alloy penetration pits can occur with metallic spikes shorting out the junction or causing diode breakdown(2).

One approach to solve the diffusion problem is to interpose a barrier material between the reactive interfaces to minimize the interdiffusion. This barrier material has to be highly conductive for low series resistance. In

addition, a good adherence of the barrier material to the adjacent layers is required. Depending on the processing steps involved and the device specifications, several metal layers are usually incorporated into the metallization scheme to fulfill all the requirements.

With the demand for higher operational speeds and device packaging densities, the use of shallow-junction active elements is indicated. Consequently, metallization schemes which have been proven successful in the past should be re-examined. With the reduced dimensions of devices, it is clear that a more effective barrier material to diffusion has to be provided between the reactive layers.

A recent review[3] has listed various considerations for an effective diffusion barrier in metallization schemes. Elemental metallic films as the barrier material are inherently unstable because they can form alloys or intermetallic compounds with the adjoining metals at elevated temperatures. From thermodynamical arguments, a positive free energy of formation between the barrier and the metals is a prerequisite for thermal stability. Chemical compounds such as oxides, nitrides, carbides, and borides usually satisfy this criterion. Among this class of materials, the nitrides, carbides, and borides of the transition metals are of particular interest because their bulk electrical resistivities, 30 to 200 $\mu\Omega$-cm, are comparable with those of the pure metals. These compounds are inert with respect

to many other high conductivity metals such as gold, silver, platinum, and copper[4] and are potential candidates for thin-film diffusion barriers.

Many of these compounds have been studied by Hägg[5] and a systematic survey of the physical properties and underlying principles can be found in the work by Goldschmidt[6]. According to Hägg, the structure and properties of compounds of boron, carbon, hydrogen, and nitrogen (the metalloids, X) and the transition metals (M) are determined by the radius ratio r_X/r_M. If the ratio is less than 0.59, very simple structures arise in which the metalloid atoms are located at the interstitial voids of the metal atom lattice. The co-ordination number of the metal atoms remains the same, 12 or 8, as in the pure metals. For example, the mono-nitrides and monocarbides of the Group IVB and Group VB elements all have the rocksalt structure. The sublattice of the metallic elements is face-centered cubic (f.c.c.) with a co-ordination number of 12. As pointed out by Hume-Rothery[7], the f.c.c. metal lattice is adopted because this permits the metal atom to have mutually perpendicular bonds to its six metalloid neighbors, so that they satisfy the mutually perpendicular bonds of nitrogen (the three p-orbitals) and carbon (one hybrid sp-orbital and two p-orbitals). With the rocksalt structure, the metalloid atoms will be situated at the octahedral voids[8] of the metal lattice and the metal-metal atomic distance is

determined by the atomic radii of the interstitial atoms. It is evident that one of the necessary conditions for metallic bonds to be formed is that the metal atoms should not be too far apart; a condition which is satisfied by the mononitrides and monocarbides with the rocksalt structure.

Associated with the interstitial nature of the metalloid atoms is the wide composition range of the interstitial compounds. For a metalloid deficiency, vacancies are formed at the interstitial voids. A metalloid excess has been reported for the Group IVB and VB mononitrides but not the monocarbides[9-11]. The extent to which the excess nitrogen phase can exist is still ill-defined and has been considered as an adsorption of free gas[9], metal vacancies[10], and interstitial nitrogen at the tetrahedral voids[11].

In this diffusion barrier study, we have singled out titanium mononitride (TiN) as the barrier material because of its low electrical resistivity (22 μΩ-cm in bulk samples). This resistivity value is even lower than that of pure Ti (48 μΩ-cm)[12]. Moreover, the heat of formation of TiN (80.3 Kcal/gm-atom)[13] is much larger than those of the titanium silicides: Ti_5Si_3 (17.3 Kcal/gm-atom), TiSi (15.5 Kcal/gm-atom), and $TiSi_2$ (10.7 Kcal/gm-atom)[14]. This indicates that TiN will be metallurgically stable with respect to silicon substrates. From the Ti-N phase diagram[15] and heat of formation of other transition metal

nitrides[16], we expect TiN to be miscible with Ti, Zr, Hf, and Ta.

The preparation of TiN thin films has been investigated by previous workers. Methods such as reactive sputtering[17-19], reactive evaporation[10, 20 ,21], ion implantation[22], reactive ion plating[23-25], and chemical vapor deposition[26, 27] have been used. The properties of a titanium nitride film depend on the nitrogen/titanium ratio, impurities and imperfections in the film. Consequently, the properties of TiN films are process-dependent. In this study, reactive sputtering was chosen for the deposition method because it is well established and compatible with semiconductor manufacturing. In addition, only two elements (i.e., Ti and nitrogen) are needed. We have investigated electrical properties, chemical composition, phase, and microstructure of reactively sputtered TiN films as a function of the RF power and the gas pressure during deposition. The aim was to find out the optimum conditions to get highly conductive films. Results of the TiN preparation and characterization will be presented in Chapter 2.

In Chapter 3, we have investigated the potential of TiN as a diffusion barrier in various metallization schemes for Si substrates. The temperature range of interest is from 400°C to 700°C. The reaction of Ti on Si substrates was also studied because Ti is widely used as a first-contact metal for Si. Various metals of high electrical

conductivity (Au, Ag, Al, Cu, and Pd) are used as the top metal layer.

Titanium nitride has already been successfully incorporated into metallization schemes on actual devices. Fournier[28] has applied a layer of TiN between Ti and Pt layers in the metallization scheme for insulated-gate field-effect transistors. His results demonstrate that the diffusion of Pt into Ti is blocked effectively during a heat-treatment of 30 minutes at 450°C. In the Au-Pt-Ti scheme for beam-lead devices, Garceau et al.[29] have also reported that the incorporation of a 100Å-thick TiN layer between Ti and Pt can inhibit the formation of the intermetallic, TiPt. In Chapter 4, we have applied titanium nitride to solve a packaging problem for Si solar cells. Using the TiN-Ti-Ag metallization scheme, no degradation of the cells' I-V performance can be detected after a 600°C anneal for 10 minutes. To our knowledge, this is the first time a high temperature diffusion barrier has been demonstrated on a shallow-junction (∿2000Å) device.

References

(1) P. M. Hall and J. M. Morabito, Thin Solid Films, 53, 175 (1978).

(2) R. Rosenberg, M. J. Sullivan and J. K. Howard, in Thin Films - Interdiffusion and Reactions, edited by J. M. Poate, K. N. Tu and J. W. Mayer (Wiley-Interscience, New York, 1978), p. 13.

(3) M-A. Nicolet, Thin Solid Films, 52, 415 (1978).

(4) C. W. Nelson, in Proceedings of International Symposium on Hybrid Microelectronics, International Society of Hybrid Microelectronics, Dallas, Texas (September 29-October 2, 1969), p. 413.

(5) G. Hägg, Z. Phys. Chem., B6, 221 (1930) and Z. Phys. Chem., B12, 33 (1931).

(6) H. J. Goldschmidt, Interstitial Alloys (Plenum Press, New York, 1967).

(7) W. Hume-Rothery, Phil. Mag., 44, 1154 (1953).

(8) C. S. Barrett and T. B. Massalski, Structure of Metals (McGraw-Hill, New York, 1966), p. 236.

(9) Ref. (6), p. 216.

(10) P. J. P. De Maayer and J. D. Mackenzie, Z. Naturforsch., 30A, 1661 (1975).

(11) M. Mäenpää, H. von Seefeld, N. Cheung, M-A. Nicolet and A. G. Cullis, to be published in the Proceedings of the Symposium on Thin Film Phenomena - Interfaces and Interactions, The Electrochemical Society Meeting,

Los Angeles, California (October 4-19, 1979).

(12) S. N. Lvov, V. F. Nemchenko, and G. V. Samsonov, Sov. Phys. Dokl., 5, 334 (1961).

(13) G. V. Samsonov, Plenum Press Handbooks of High Temperature Materials, No. 1 (Plenum Press, New York, 1964), p. 294.

(14) K. N. Tu and J. W. Mayer, in Thin Films - Interdiffusion and Reactions, edited by J. M. Poate, K. N. Tu and J. W. Mayer (Wiley-Interscience, New York, 1978), p. 398.

(15) M. Hansen, Constitution of Binary Alloys (McGraw-Hill, New York, 1958), p. 989.

(16) G. V. Samsonov, Plenum Press Handbooks of High Temperature Materials, No. 2 (Plenum Press, New York, 1964), p. 87.

(17) T. Abe and T. Yamashina, Shinku, 18, 375 (1975).

(18) D. Gerstenberg, Annalen der Physik, 11, 354 (1963).

(19) H. Mitsuhashi, Y. Igasaki and M. Kaneko, J. Crystal Growth, 45, 350 (1978).

(20) Y. Igasaki, H. Mitsuhashi and K. Azuma, Japan. J. Appl. Phys., 17, 85 (1978).

(21) G. Beensh-Marchwicka, S. Dembicka-Jellonkowa and L. Krol-Stepniewska, Thin Solid Films, 36, 361 (1976).

(22) I. M. Belii, F. F. Komarov, V. S. Tishkov and V. M. Yankovskii, Phys. Stat. Sol., 45A, 343 (1978).

(23) T. Sato, M. Tada, Y. C. Huang and H. Takei, Thin

Solid Films, 54, 61 (1978).

(24) Y. Murayama, J. Vac. Sci. Technol., 12, 818 (1975).

(25) M. Kobayashi and Y. Doi, Thin Solid Films, 54, 67 (1978).

(26) T. Takahashi and H. Itoh, J. Electrochem. Soc., 124, 797 (1977).

(27) W. Schintlmeister, O. Pacher, K. Pfaffinger, and T. Raine, J. Electrochem. Soc., 123, 924 (1976).

(28) U. S. Patent 3,879,746 (1975), to P. R. Fournier.

(29) W. J. Garceau, P. R. Fournier and G. K. Herb, Thin Solid Films, 60, 237 (1979).

CHAPTER 2

PREPARATION AND CHARACTERIZATION OF TITANIUM NITRIDE FILMS

2.1 Experimental

The sputtering process was carried out in a RF powered (f = 13.56 MHz) diode sputtering chamber with planar magnetron cathodes and grounded substrate (anode). A pure nitrogen plasma and a titanium target were used. The quoted purity of N_2 and Ti was 99.999% and 99.99%, respectively. The distance between the target and the substrate was 7 cm. Before sputter-deposition, the system was evacuated to $<10^{-6}$ Torr. Then nitrogen gas was introduced into the chamber through a variable leak. Gas pressures between 3 mT and 100 mT were used and RF power was varied from 500 W to 1500 W. The substrate temperature was estimated to be 150°C. Because the sputtering rate depends on the deposition conditions, the sputtering time was adjusted to keep the film thickness around 1000Å in all cases.

For each deposition, the TiN layer was deposited onto three different kinds of substrates (vitreous carbon, quartz, and Si (100) wafer). The chemical composition and film thickness were determined by MeV ^{4}He backscattering spectrometry with samples deposited on vitreous carbon substrates. The electrical measurements were performed on the TiN layers deposited on the quartz or Si substrates.

Since the Si wafers have a high electrical resistivity (1 to 10 Ω-cm), no difference in the electrical parameters can be detected by comparing the values obtained on either the quartz or Si substrates.

The electrical investigations were carried out by means of the van der Pauw method[1] and the four-point probe measurements. The sheet resistivity was determined by both methods and the sheet carrier concentration and the Hall mobility by the van der Pauw measurements. A dc system was used to measure the Hall effect, with direct current in a dc magnetic field (4 kilogauss). The corresponding "bulk" values were determined using the film thickness values obtained by backscattering measurements.

The crystal structure of the TiN layers were identified by both electron and X-ray diffraction methods. Micrographs from transmission electron microscopy (TEM) provided additional information on the grain sizes and crystal defects of the TiN layers.

At the initial stage of this study, titanium nitride films were also prepared by direct sputtering of a sintered TiN (99.9% nominal purity) target with Ar (99.99% pure) as the sputtering gas. Typical sputtering RF power and Ar pressure were 700 watts and 3 mT, respectively. For the directly sputtered TiN films, oxygen is always present with a concentration of ∿20 at. %. Moreover, Zr at a concentration of a couple of atomic percent can also be detected by back-

scattering. Since no Zr contamination has been observed from the sputtering of other target materials, we have concluded that the Zr is incorporated in the sintered TiN target. The electrical resistivity of these TiN films is ∿130 μΩ-cm. Because of the Zr contamination, no systematic study has been pursued to characterize the directly sputtered TiN films.

2.2 Results and Discussion

For backscattering analysis, the titanium nitride was deposited onto a carbon substrate in order to enhance the signal sensitivity of low Z elements such as N and O in the spectrum. The actual film thickness was found to vary from 700Å to 1300Å. For the calculations, a stoichiometric rock-salt structure of TiN with a lattice parameter of $a_o = 4.24$Å was assumed. In Fig. 1 the nitrogen/titanium ratio is shown as a function of sputtering parameters, i.e., RF power and gas pressure. The atomic composition of the nitride films is close to stoichiometric TiN. However, the N/Ti ratio varies from 0.92:1 to 1.32:1 with a slight tendency to have more nitrogen when the RF power is low and when the gas pressure is high. Backscattering measurements showed that oxygen is often present in the film and its concentration is strongly dependent on sputtering conditions (Fig. 2). With a RF power of 1200-1500 W and a gas pressure of 3-10 mT, the oxygen concentration is below the detection limit, which is about 5 at. % for the backscattering technique. The oxygen

concentration (oxygen/titanium ratio in Fig. 2) increases with decreasing RF power and increasing gas pressure up to an O/Ti ratio of about 0.5 when the RF power and the gas pressure have the values of 500 W and 100 mT, respectively. The deposition rate decreases from 600Å/min to 120Å/min when the RF power decreases from 1500 W to 500 W, but for a fixed RF power it stays more or less constant as a function of gas pressure.

The origin of oxygen in the sputtered TiN is probably due to the presence of water vapor in the sputtering chamber. We have observed that when the nitrogen pressure is high, the spatial extent of the nitrogen plasma reaches the walls of the sputtering chamber. It is likely that the nitrogen ions have sputtered the water molecules sticking on the walls and dissociated them into oxygen and hydrogen ions. We believe that the oxygen contamination can be reduced either by performing the sputter deposition in a bakeable vacuum chamber or by minimizing the exposure of the sputtering chamber to air during sample loading and unloading.

In Fig. 3, the resistivity is shown as a function of the sputtering parameters. The resistivity has the lowest value of 170 μΩ-cm when a high RF power and a low gas pressure are used. An increase of one order of magnitude in the resistivity is observed by decreasing power and increasing pressure. The resistivity shows a linear dependence on the oxygen concentration in the films. This can clearly be seen

in the topmost part of Fig. 4, where the resistivity versus O/Ti ratio has been plotted. The corresponding carrier concentrations and Hall mobilities are shown in the same figure. According to the Hall measurements, the free carriers are electrons and their concentration has a constant value of $\approx 4 \cdot 10^{22} cm^{-3}$ over the measured range. Conversely, the Hall mobility decreases from 1 cm^2/Vs to 0.1 cm^2/Vs with increasing O/T ratio.

The results from the van der Pauw and four-point probe measurements are in good agreement. Although our investigation was concentrated on film thicknesses of around 1000Å, random checks showed no thickness dependence of the resistivity for films between 200Å and 2000Å.

An electron diffraction pattern and a bright field micrograph of a typical TiN film deposited on the Si(100) substrate are shown in Fig. 5. The N/O/Ti ratio in this film is 1:0.25:1. The film has a fcc-structure and it is polycrystalline with a grain size distribution in the region of 100-200Å. Crystal defects such as dislocation lines are also observed within the grains. The rocksalt structure of TiN was identified by the relative intensities of X-ray diffraction lines. The X-ray diffraction pattern of a 1000Å-thick TiN sample deposited on a Si (100) substrate is shown in Fig. 6. From reported powder patterns[(2)], the relative intensities of TiN's (111), (200), and (220) diffraction lines are 77, 100, and 56, respectively. They are

in qualitative agreement with our results. Using least-squares fitting procedures, the lattice constant (a_o) of the sputtered TiN films is determined to be 4.24±0.02Å.

The Hall measurements show that a reduction of the electron mobility is responsible for the resistivity increase of TiN films. This reduction is correlated to the amount of oxygen in the film. There are several possibilities to explain the influence of oxygen atoms on the transport mechanism. We can speculate that oxygen atoms are located in grain boundaries forming an interconnected network of higher resistivity. Alternatively, the lowering of electron mobility can be explained by an enhanced scattering mechanism such as Ti vacancies or interstitial impurities. Assuming a Fermi velocity of $\sim 10^8$cm/sec for the electrons, the mean free path is estimated to be ∿5Å from the resistivity and electron concentration values[3]. This is much smaller than the average grain size. Thus, grain boundary scattering is not a dominant factor in determining the conduction mechanism.

For the samples with a high content of nitrogen and oxygen (i.e., when the RF power is low and nitrogen pressure is high), it is unlikely to explain the Ti deficiency (∿30 % from stoichiometric TiN) by Ti vacancies. We propose that the excess nitrogen and oxygen atoms are incorporated interstitially at the tetrahedral voids of TiN's rocksalt structure[4]. Since there are eight tetrahedral voids per unit cell as compared with four Ti atoms per unit cell, an

ample amount of interstitial atoms which have small atomic radii can be accommodated in these voids before they distort the crystal structure. Once positioned at the tetrahedral voids, the interstitial atoms (nitrogen and oxygen in this case) will act as scattering centers for the conduction mechanism.

2.3 Summary

Titanium nitride film reactively sputtered with a RF power in the range of 500-1500 W and a gas pressure range of 3-100 mT grows in the rocksalt structure. This is typical for TiN films containing more than 30-40 at. % nitrogen[5,6]. The film has a metal-like electrical resistivity which is lowest (170 $\mu\Omega$-cm) when a high RF power and a low gas pressure are used. Increasing the oxygen concentration in the film will increase the electrical resistivity by lowering the electron mobility. Hence, it is important to minimize the presence of oxygen during sputter-deposition to produce highly conductive TiN films.

The resistivity of titanium nitride films attained in this study is higher than the reported bulk value of 22 $\mu\Omega$-cm[7]. Values of 50 $\mu\Omega$-cm have been reported for stoichiometric sputtered layers[8]. Similar resistivity values have also been achieved by applying a negative bias voltage to the substrate during deposition[9].

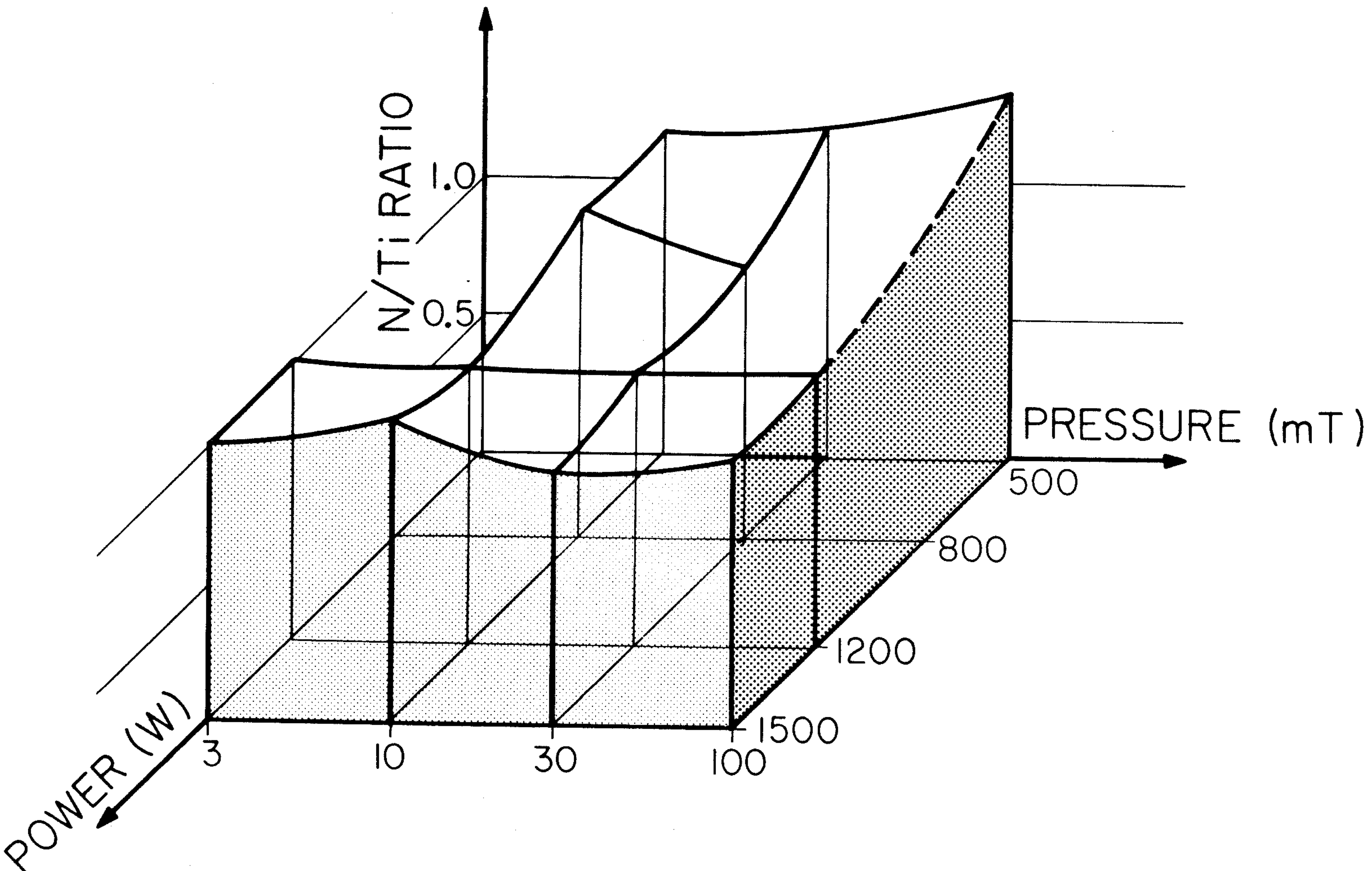

Figure 1 Nitrogen/Titanium ratio of TiN films versus sputtering parameters.

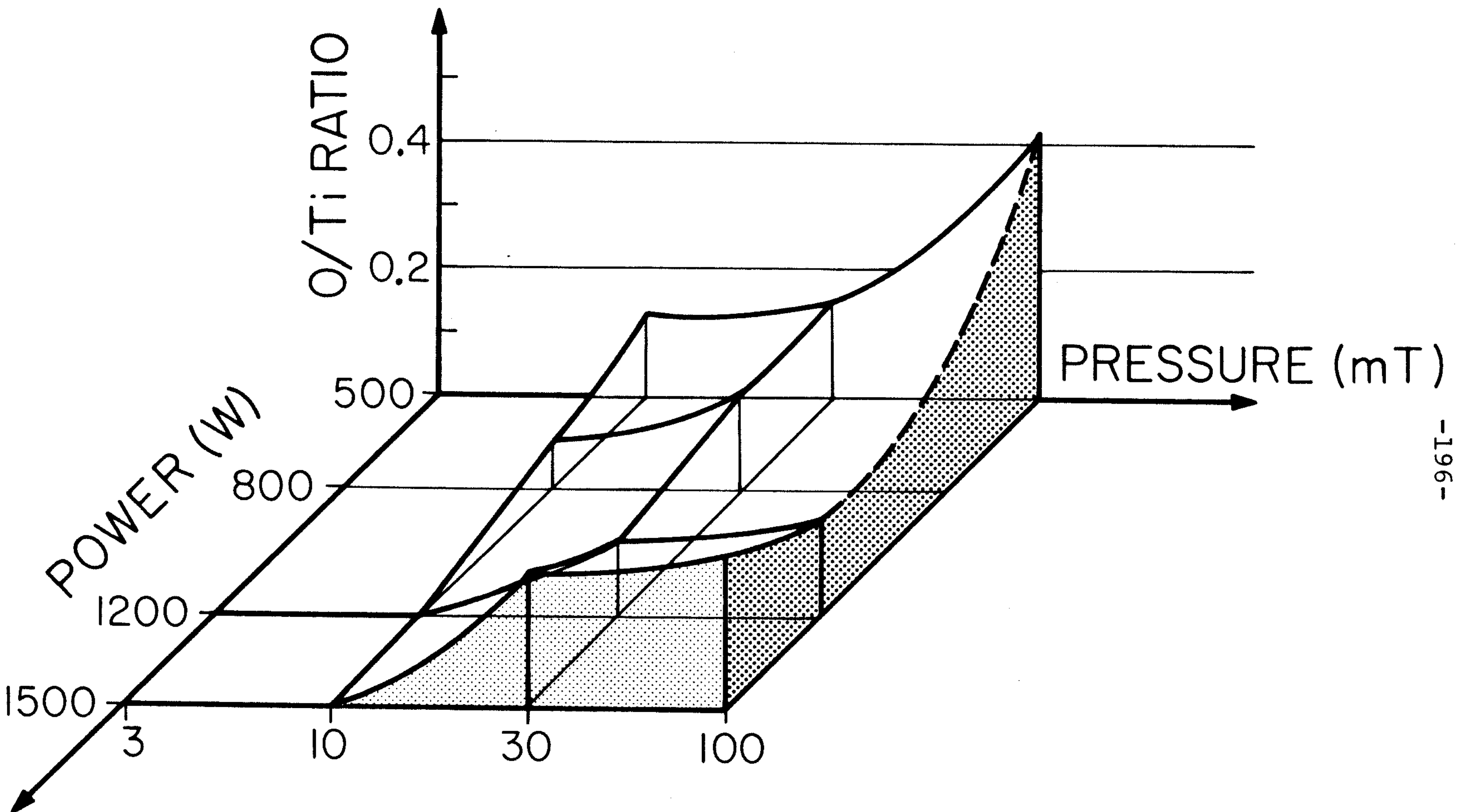

Figure 2 Oxygen/Titanium ratio of TiN films versus sputtering parameters.

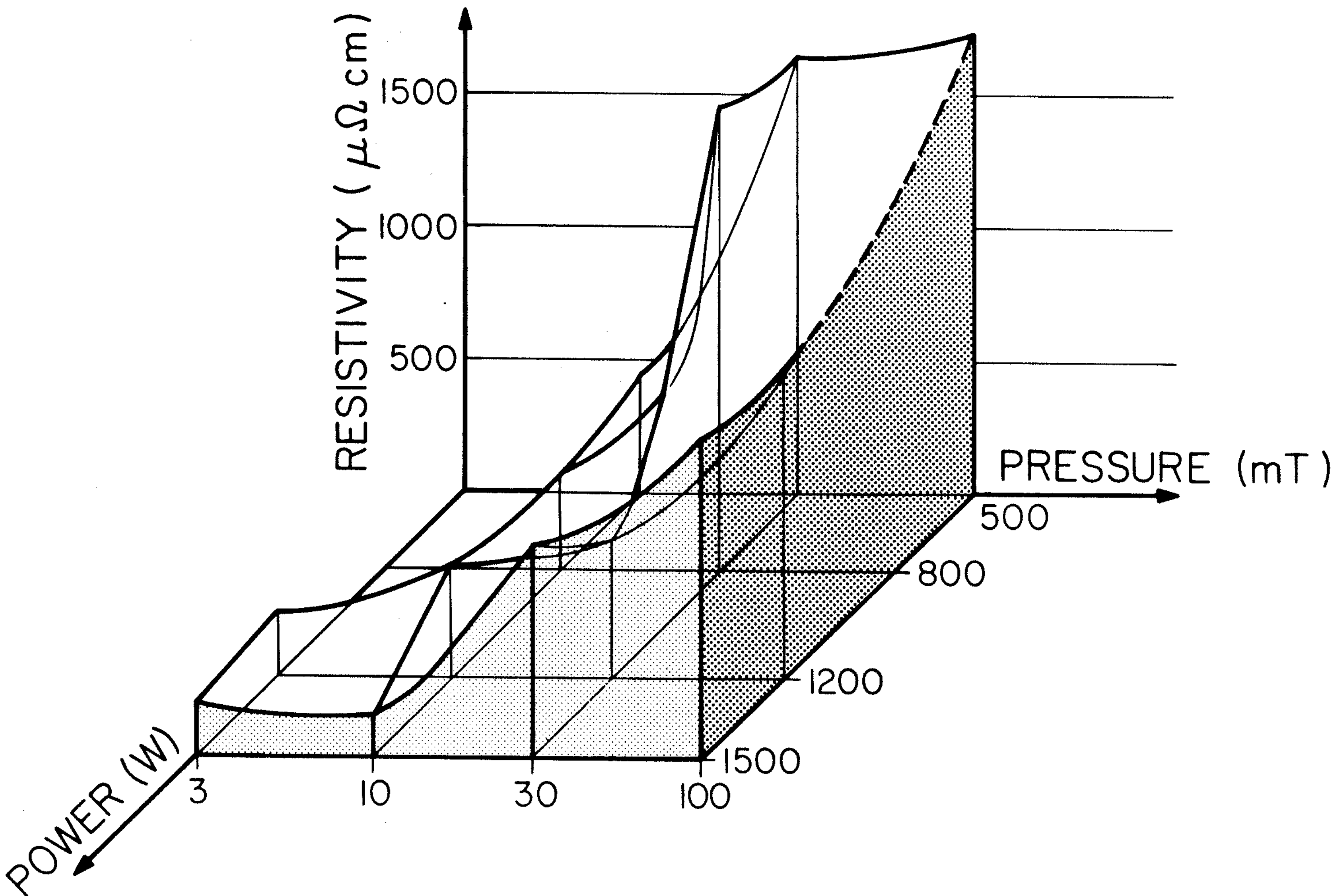

Figure 3 Electrical resistivity of TiN films versus sputtering parameters.

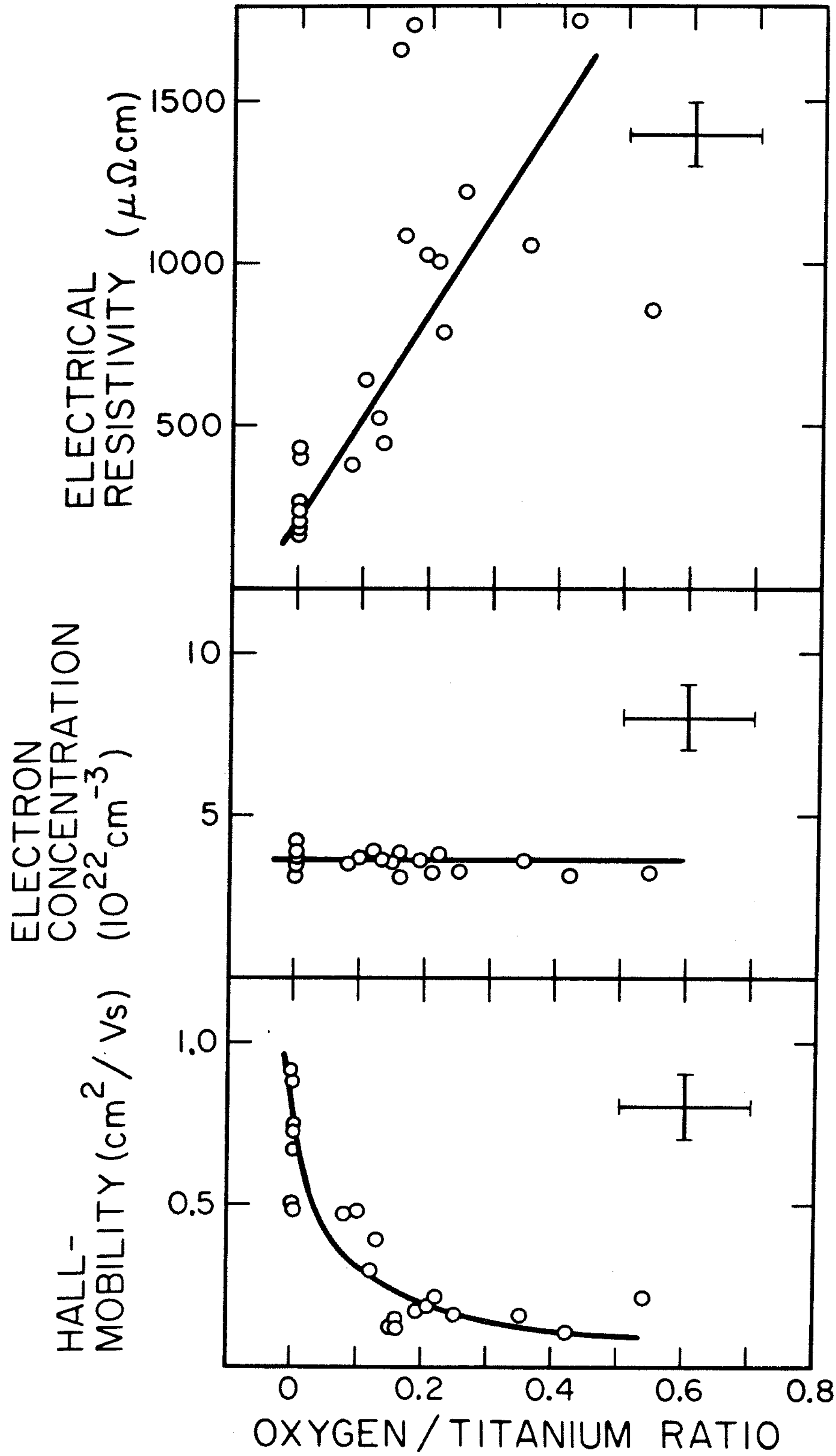

Figure 4 Electrical resistivity, electron concentration and Hall mobility of TiN layers as a function of the oxygen/titanium ratio.

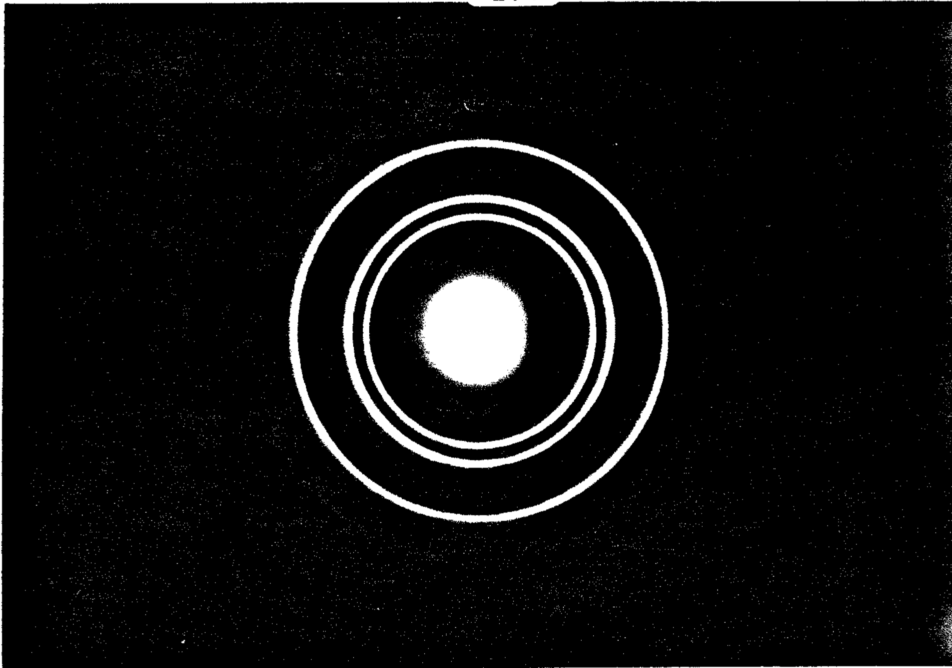

A

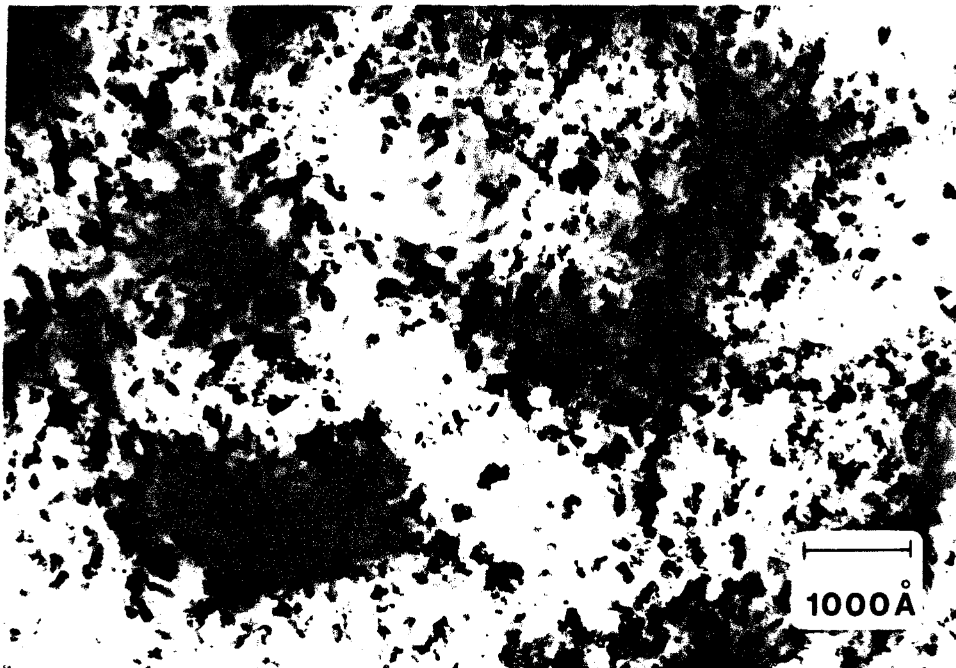

B

Figure 5 TEM diffraction pattern (A) and bright-field micrograph (B) of a reactively sputtered TiN film.

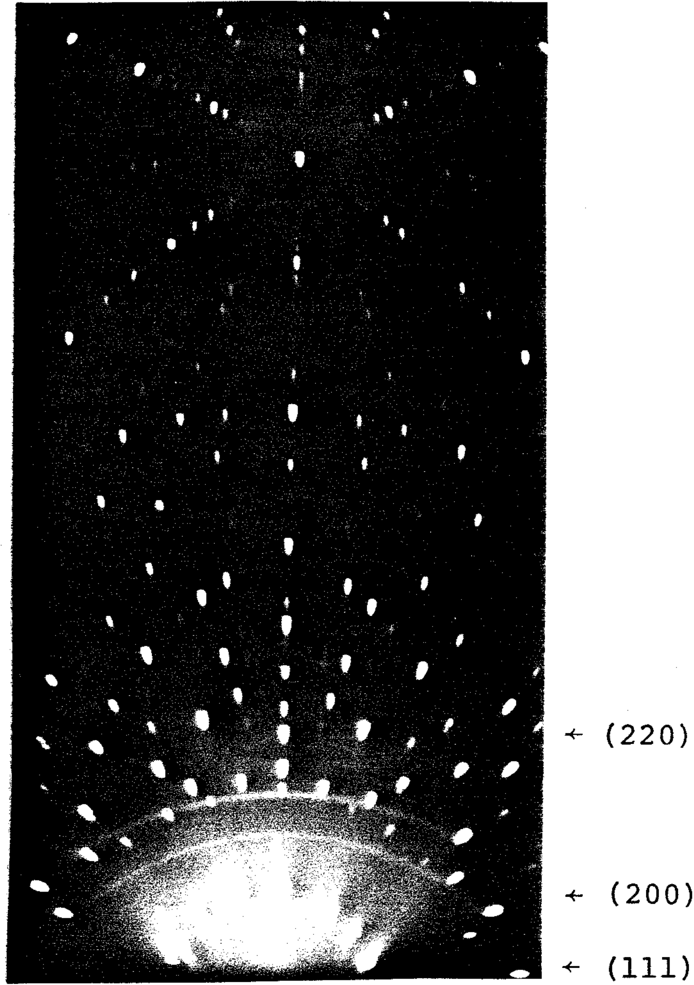

Figure 6 X-ray diffraction pattern of a TiN layer (~1000Å) on (100) Si.

References

1. P. F. Kane and G. B. Larrabee, Characterization of Semiconductor Materials (McGraw-Hill, New York, 1970), p. 96.
2. ASTM Card No. 6-0642.
3. C. Kittel, Introduction to Solid State Physics (John Wiley, New York, 1976), p. 169.
4. C. S. Barrett and T. B. Massalski, Structure of Metals (McGraw-Hill, New York, 1966), p. 236.
5. D. Gerstenberg, Annalen der Physik, 11, 354 (1963).
6. Y. Igasaki, H. Mitsuhashi, K. Azuma and T. Muto, Japan. J. Appl. Phys., 17, 85 (1978).
7. M-A. Nicolet, Thin Solid Films, 52, 415 (1978).
8. W. J. Garceau, P. R. Fournier and G. K. Herb, Thin Solid Films, 60, 237 (1979).
9. R. S. Nowicki, private communication.

CHAPTER 3

TITANIUM NITRIDE AS A DIFFUSION BARRIER IN METALLIZATION SCHEMES FOR SILICON

3.1 Sample Preparation and Analytical Techniques

In this study, we have investigated the potential of TiN as a diffusion barrier in various metallization schemes for Si. The temperature range of interest is from 400°C to 700°C. Various metals of high electrical conductivity such as Au, Ag, Al, Cu, Pd are used as the top metal layer. The effectiveness of TiN to block the metal-substrate reaction is tested against a thin film of Ti on a single-crystal Si substrate or against a plain single-crystal Si substrate.

The sample configurations used in this study are summarized in Fig. 7. The TiN layer (∿1000Å) is interposed between the top metal layer (Au, Al, Ag, Cu, or Pd) and the substrate. The substrate material can either be: (A) a 2000Å Ti film on Si (100) wafer or (B) a Si (100) wafer. Case (A) is emphasized because Ti is a widely used first-contact metal with Si, and case (B) is tested because of the simplicity of the scheme. Since metallic thin-film inter-diffusion studies have been well documented[1], the corresponding samples without the TiN layer (cases (a) and (b)) are only used as reference samples and results will only be presented for some cases.

The TiN thin films were prepared in a RF sputtering deposition chamber equipped with 7.5-cm diameter planar magnetron sputtering targets. The target to substrate distance was 7 cm and a RF generator with a frequency of 13.56 MHz was used. The substrate temperature during deposition was estimated to be around 150°C. Two sputtering modes were employed in this experiment to prepare the TiN films. The first method was to synthesize TiN reactively by sputtering a 99.9% pure Ti target with 99.99% pure nitrogen as the sputtering gas. During sputtering, a nitrogen pressure of 20 mT and a RF power of 1500 watts were used. The second method was to directly sputter a sintered TiN (99.9% pure) target with Ar (99.99% pure) as the sputtering gas. The Ar pressure was 3 mT and a RF power of 700 watts was used. Transmission electron microscopy has identified that TiN films prepared by both methods have the same fcc-crystal structure and both films are polycrystalline with grain sizes between 100Å to 200Å. Details of the films' composition and electrical characteristics versus sputtering conditions are discussed in Chapter 2. In the present study, the reactively sputtered TiN film has a N:Ti ratio of approximately 1:1 and an oxygen contamination of less than 5 at. %. The bulk electrical resistivity of these films is approximately 170 μΩ-cm as determined by four-point probe measurements. For the directly sputtered TiN films, the oxygen concentration is about 20 at. % and the electrical resistivity is about

130 $\mu\Omega$-cm. From our diffusion studies, both types of TiN films behave very similarly as diffusion barriers. Hence, only data from the reactively sputtered TiN layers will be presented.

To avoid the complication of various contaminants which may be present in sputtered-deposited metal films, all the metallic films were deposited by electron-beam evaporation in an ion pump vacuum system. Typical residual gas pressure before evaporation is in the 10^{-8} Torr range. Evaporation rates for the metallic films are between 20Å and 50Å per second.

After the metal depositions, the samples were cleaved into smaller pieces and placed in a quartz boat. The heat-treatment was performed in a vacuum furnace with a vacuum better than 2×10^{-6} Torr.

We have used MeV helium ion backscattering spectrometry[2] (BS) to measure the thickness of the films and the diffusion profiles of the multi-layers. The detector angle was 170° for all measurements. This technique has the advantage that it is practically nondestructive and gives atomic concentrations at various depths from the surface.

SEM micrographs of the samples' surfaces were taken with a JOEL Super II scanning electron microscope which is equipped with an energy dispersive analysis by X-rays (EDAX) system for elemental analysis. The electron beam's excitation energy used was 25 keV.

Metallurgical phases formed after various thermal treatments were identified with a Read camera using CuKα radiation.

3.2 Results

3.2.1 Silver

The Ag-Ti reaction was observed to be prominent at annealing temperatures around 500°C. In Fig. 8, we show the atomic profiles of a Si-Ti-Ag metallization scheme after 600°C thermal treatments. Significant interdiffusion between the Ag and Ti layers is detected after 10 min. With time, a substantial amount of Ti is observed at the sample's surface after 40 min. Simultaneously, the Ag concentration extends toward the Ti-Si interface. The Ag:Ti concentration ratio is not uniform as a function of depth, indicating that the reaction is probably not a layer-by-layer growth mechanism. X-ray diffraction lines corresponding to the intermetallic compounds TiAg and Ti_3Ag are identified for the heat-treated samples, but not for the as-deposited sample. Broadening of the Ti and Si signals at the Ti-Si interface denotes the onset of $TiSi_2$ formation which becomes prominent for annealing temperatures above 600°C. In this system, the Ag-Ti reaction is not affected by the presence of the silicon substrate because similar results can be observed by replacing the Si substrates with SiO_2 substrates.

To investigate whether the TiN can act as a diffusion barrier between the Ag and Ti layers, we have interposed a

1000Å-thick TiN layer. BS analysis (Fig. 9) shows that the Ag-Ti reaction is reduced drastically. After a 600°C, 10 min anneal, no interdiffusion between the Ag and Ti layers is observable by backscattering spectrometry. Prolonged annealing up to 80 min shows a Ti peak at the sample's surface and the beginning of the Ti-Si reaction at the Si interface, while the Ag layer remains basically intact.

SEM micrographs of the as-deposited Ag surface and the annealed surface (600°C, 80 minutes) of the Si-Ti-TiN-Ag system are presented in Fig. 10. The as-deposited Ag films have grains ranging from 4000Å to 1μm. After the 600°C heat-treatment, the surface topography turned rough with poor intergranular contacts. Porous cavities on the order of 4000Å in diameter were observed everywhere on the sample's surface.

On a plain single-crystal silicon substrate, a layer of Ag reacts completely with Si after 10 min at 500°C (Fig. 11). By interposing a TiN layer of 700Å thickness between the Ag and Si, no Ag-Si interdiffusion can be observed with backscattering spectrometry after a 600°C annealing of 80 min (Fig. 12).

3.2.2 Gold

Previous experiments by Poate et al.[3] have shown that Au and Ti layers react around 350°C to form the intermetallics $TiAu_4$ and $TiAu_2$. For our studies with Ti on Si as the substrate, interposing a TiN layer of 850Å thickness

between the Au and the Ti layers can inhibit the Au-Ti reaction during a 350°C, 48 min annealing (see Fig. 13). However, the metallization system fails completely after a 450°C, 60 min annealing, as indicated by the BS spectrum (Fig. 13). High concentrations of Au are located at distances beyond the original TiN thickness from the surface.

To catch the earlier stage of this failure mechanism, we have given the sample a short-time anneal at 400°C for 10 min. After such heat-treatment, localized failures show up as isolated patches over the sample's surface. Prolonged annealing cause the patches to expand laterally until all the Au is consumed. SEM micrographs of one of the isolated patches are presented in Fig. 14. The surface consists of islands approximately 500 microns in diameter. The islands are separated by cracks which are partially filled with a resolidified material. This material has been identified by EDAX to be an Au-Ti-Si mixture which has a greater Au concentration than the island material. The surface cracking is similar to the failure pattern of the Si-TiW-Au metallization scheme when heated to 400°C[4]. Droplets of Au-Si alloy about 5 microns in diameter have balled up on the islands' surfaces and no Ti can be detected in these droplets by the EDAX technique. Along the cracks where the Au-Ti-Si mixture has flaked off, the bottom material was identified to be pure Si and the bottom area has a rough topography indicative of a fracture mechanism.

For thin films of Au evaporated on single-crystal Si substrates, the migration of Si atoms at low temperatures (∿200°C) through the Au film to the surface has been reported by Hiraki et al.[5]. With a thin layer of TiN as the diffusion barrier, no Au-Si interdiffusion is observable by BS when the annealing temperature is 350°C (Fig. 15). At 450°C, the Au layer is basically intact, but traces of Au can be detected penetrating the TiN layer. No localized failures similar to the case of the Si-Ti-TiN-Au system are observed up to a 450°C, 60 min annealing. At 500°C, the Si-TiN-Au system fails completely (Fig. 16) after 10 min; resolidified Au droplets several microns in size are balling up on the sample's surface. Unlike the Si-Ti-TiN-Au system, no surface cracking phenomenon is observed by SEM.

3.2.3 Aluminum

The Ti-Al reaction has been studied by Bower [6] and Howard et al.[7]. The intermetallic phase, $TiAl_3$, forms around an annealing temperature of 325°C. For the Si-Ti-TiN-Al system, no Ti-Al interdiffusion is observed by BS below 500°C. For a 500°C, 40 min annealing, the BS spectrum (Fig. 17) shows a small penetration of the Al by Ti but no detectable movement of the Al or Si.

The SEM micrograph of a sample subjected to a 550°C, 10 min annealing shows "blisters" over the sample's surface, approximately 30 microns apart (Fig. 18a). Some blisters have developed a volcano-like structure (Fig. 18b) where the

Al film nearby has segregated into discrete patches. A spot analysis by EDAX confirms that only small amounts of Al are present between these patches. At 600°C, the metallization scheme fails completely after 20 min, and the Al film balls up into irregular patterns on the TiN surface.

The reaction of Al films on single-crystal Si has been well studied[8]. Aluminum spikes are observed extending into the Si after 400°C annealing. In this diffusion barrier study, the Si-TiN-Al system is observed to behave like the Si-Ti-TiN-Al system, with a similar failure pattern starting at 500°C.

3.2.4 Copper

For the reference sample of Cu on Ti (case (a) of Fig. 7), BS shows a reaction after a 500°C annealing for 40 min. More than one of the Ti-Cu intermetallic compounds are detected by X-ray diffraction. For the Si-Ti-TiN-Cu system, no interdiffusion between Cu and Ti is observed for thermal annealing at 600°C up to 80 min. After 30 min at 700°C, the Ti has reacted completely with Si to form $TiSi_2$ (Fig. 19), but the Cu and TiN layers show no degradation by both BS and optical microscopy.

For the Si-TiN-Cu system, no Cu-Si interdiffusion can be observed at 600°C. At 700°C, a slight interdiffusion takes place at the Cu-TiN interface (Fig. 20).

3.2.5 Palladium

Poate et al.[3], using backscattering spectrometry,

have measured substantial Ti-Pd interdiffusion for vacuum annealing around 312°C. Ti was reported to distribute uniformly through the Pd at 10 at. % levels at these temperatures. With the Si-Ti-TiN-Pd metallization system, no Ti-Pd interdiffusion is observed after annealing at 600°C up to 80 min.

The Pd-Si system forms the silicide, Pd_2Si, at temperatures ranging from 200°C to 600°C[9]. The reaction rates are fast because of the low activation energies for diffusion (∿1 eV). Using the TiN layer as a diffusion barrier, no Pd-Si reaction is observed after a 600°C, 80 min annealing.

3.3 Discussion

For the five metals (Au, Al, Ag, Cu, and Pd) being investigated, we have demonstrated that the presence of a thin layer of TiN (∿1000Å) effectively raises the failure temperature at which significant metal-substrate interdiffusion occurs. In Table 1, we have listed some relevant temperatures such as the melting points of the metals, the failure temperatures of TiN as a diffusion barrier against both Ti on Si and pure Si substrates, and the lowest eutectic temperature between metals and substrates.

The first observation is that the failure temperature of TiN as a diffusion barrier is not related to the melting points of the metals. Although we have observed melting processes in the cases of Au and Al, the conspicuously low failure temperature for Au (400°C) when compared with its

melting point (1063°C) proves that the melting process is due to an alloying effect. Indeed, despite their similar melting points, Au and Cu behave as opposite extremes in our diffusion studies.

Comparison of the failure temperatures for Ti on Si substrates and pure Si substrates shows only minor differences. For the purpose of subsequent discussions, no distinction will be made between the two types of substrates. However, it is nevertheless true that the presence of a Ti layer on the Si substrate can influence the TiN's barrier properties. Since the presence of Ti does not materially improve the failure temperatures of TiN as a diffusion barrier, the simpler Si-TiN-metal metallization scheme appears to be preferable, provided the Si-TiN contact has acceptable adhesion and electrical properties.

The correspondence between the failure temperatures of TiN and the lowest metal-silicon eutectic temperature is another important observation. The three metals, Au, Al, and Ag, form simple eutectics with silicon, with eutectic temperatures at 370°C, 577°C, and 830°C, respectively. It is not pure coincidence that we observed melting phenomena for Au and Al around such annealing temperatures. In the Au case, the presence of Si in the molten Au-Si droplets indicates that there has been an outward flux of Si atoms from the Si substrate. A similar migration of Si atoms through metal films toward the free surface has been reported

by Hiraki et al.[5]. Silver, Cu, and Pd have their lowest eutectic temperature with Si or Ti ranging between 720°C and 850°C. Indeed, no metal-substrate reaction is observed when the samples are annealed within the 600°C-700°C temperature range(except in the Si-Ti-TiN-Ag case at 600°C). For the Si-Ti-TiN-Ag system,an isolated Ti signal is observed at the sample's surface although the Ag layer remains basically intact. This is probably due to the instability of Ag against oxidation at high temperatures. From the SEM micrographs (Fig. 10), we have learned that the intergranular contact between the Ag grains is poor after the 600°C anneal. The existence of a continuous network of microcracks between the grains is highly probable. Therefore, the presence of a partial pressure of oxygen in the annealing ambient may act like a sink for the outward migration of Ti through the TiN layer because the formation of TiO_2 is favorable at such elevated temperatures.

Since the initial phase of the eutectic failures is laterally non-uniform, we believe that the metal or Si diffusion is through grain boundaries or defects such as pinholes. Whether the TiN layer behaves as a stuffed barrier where the intergranular impurities provide the barrier action is an issue for future investigations.

The Si-Ti-TiN-Cu metallization scheme is of particular interest. It clearly demonstrates the effectiveness of TiN as a diffusion barrier to block a thermodynamically favorable

reaction (i.e., the Cu-Ti reaction) while another thermodynamically less favorable reaction is taking place (i.e., the Ti-Si reaction). Variations based on this metallization scheme can produce numerous metal-silicide-silicon combinations from one-step thermal anneals.

In summary, thin TiN layers prepared by RF sputtering deposition can act as a diffusion barrier for the various metallization schemes we have studied. The failure temperature of these TiN layers as a diffusion barrier is related to the metal-silicon eutectic temperature. The failure mechanism is believed to be initiated by grain boundary diffusion or transport through defects such as pinholes. We have also demonstrated that a thin TiN layer can block a thermodynamically favorable reaction, while another less favorable reaction is taking place.

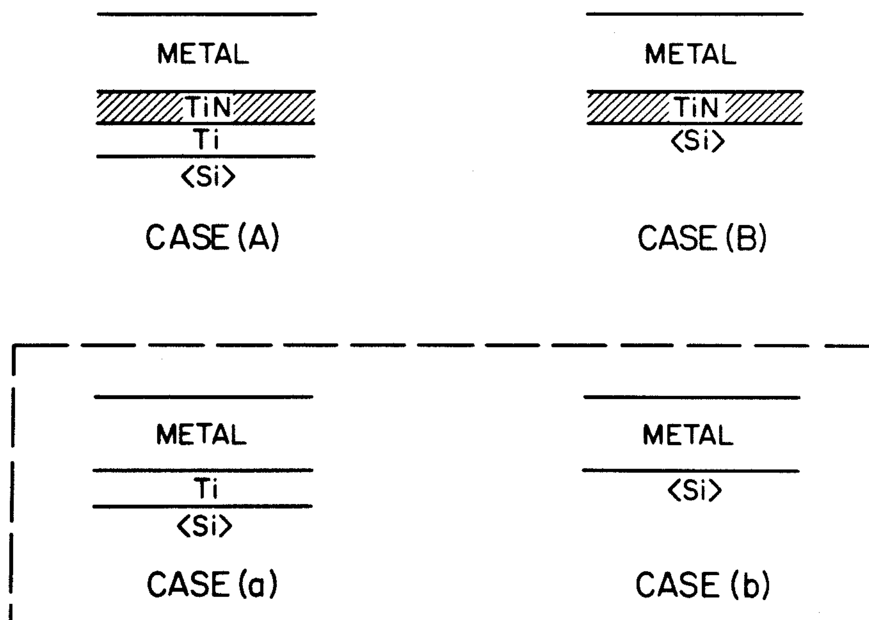

* METAL = Au, Al, Ag, Pd, Cu

† TiN PREPARED BY: (1) REACTIVE SPUTTERING OF Ti WITH N_2
(2) DIRECT SPUTTERING OF TiN WITH Ar

Figure 7 Sample configurations of various metallization schemes on Si:
(A) Si-Ti-TiN-Metal
(a) Si-Ti-Metal
(B) Si-TiN-Metal
(b) Si-Metal.

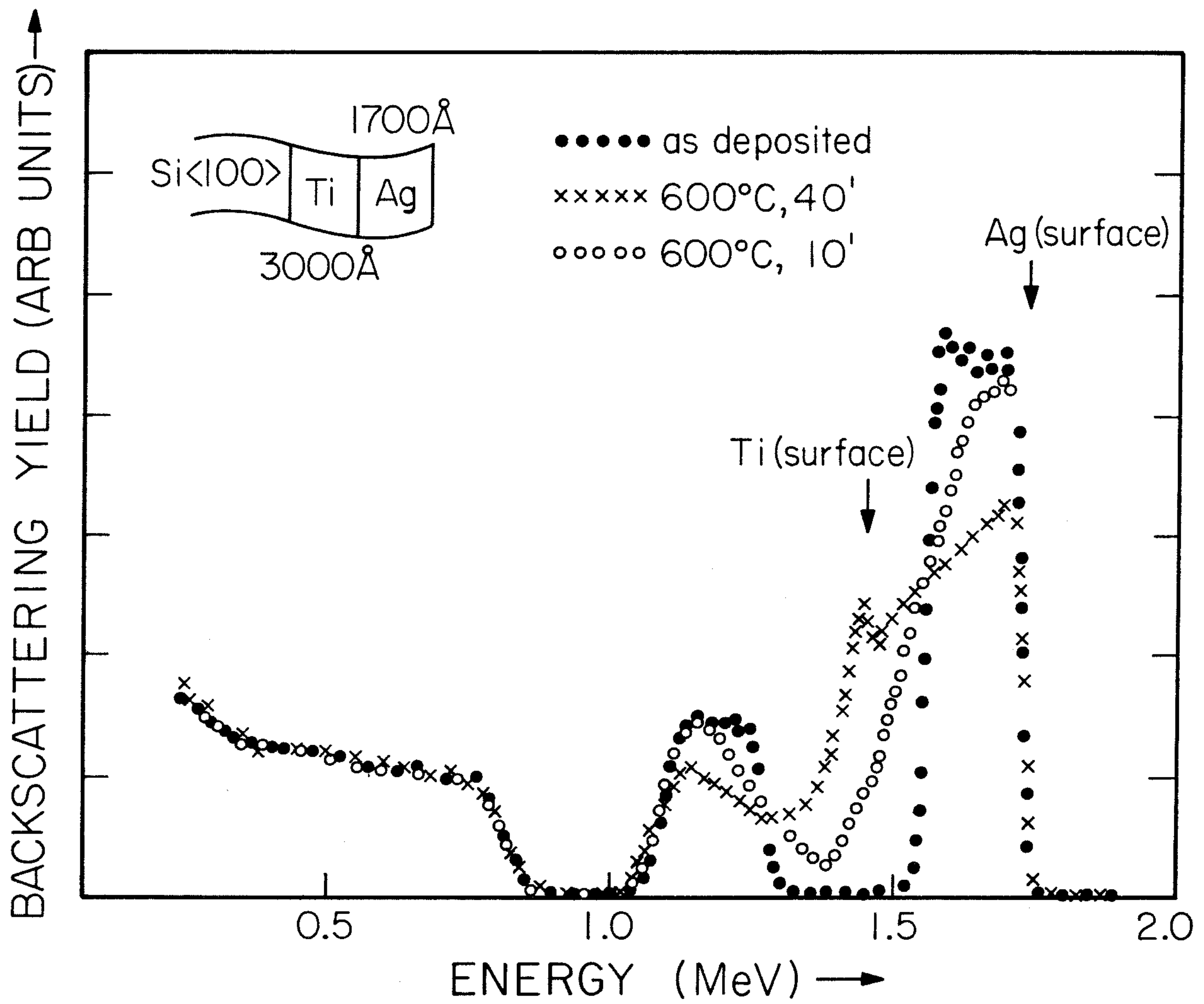

Figure 8 Backscattering spectra of the Si-Ti-Ag system. The incident ^4He energy is 2 MeV.

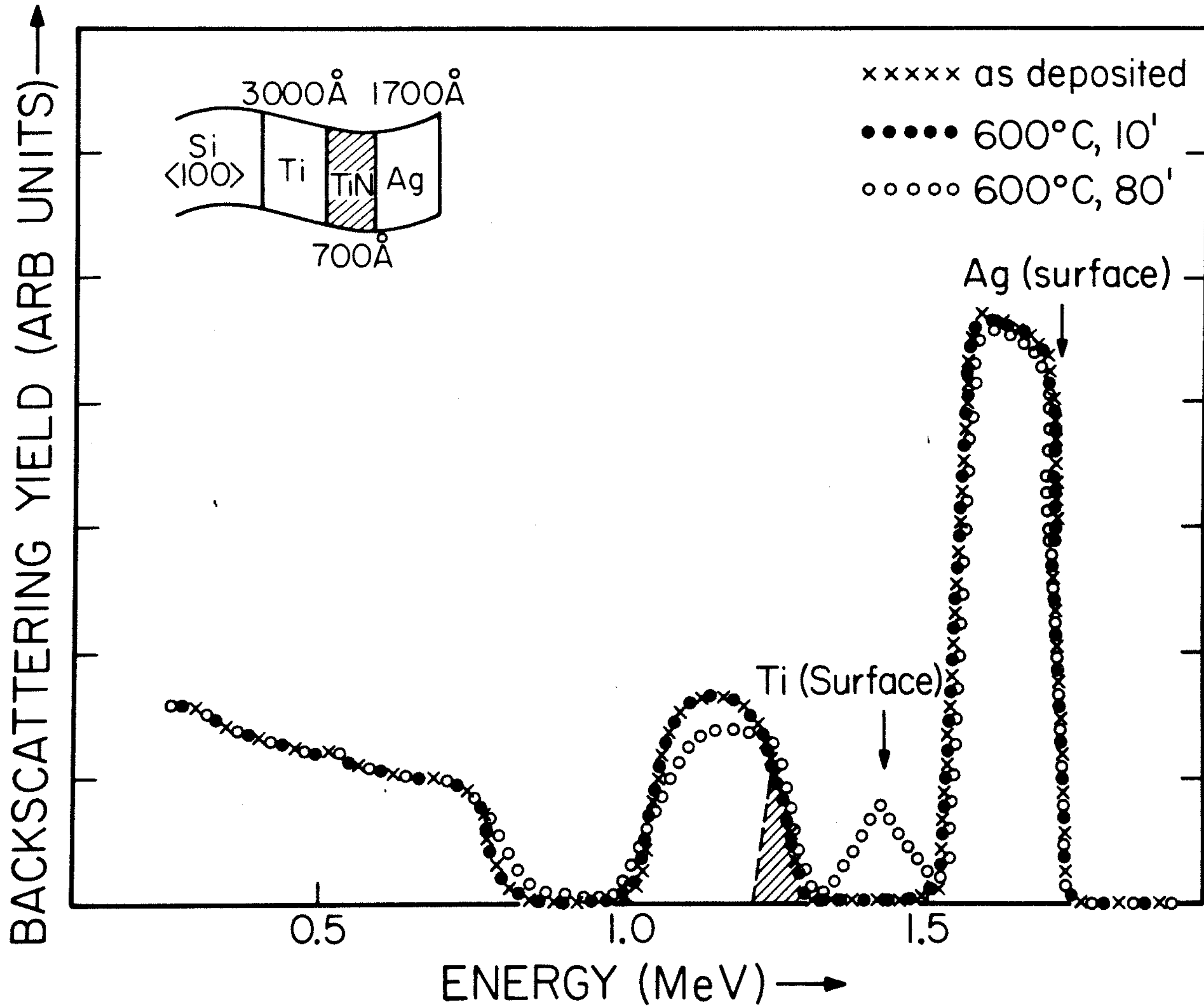

Figure 9 Backscattering spectra of the Si-Ti-TiN-Ag system. The incident ^4He energy is 2 MeV.

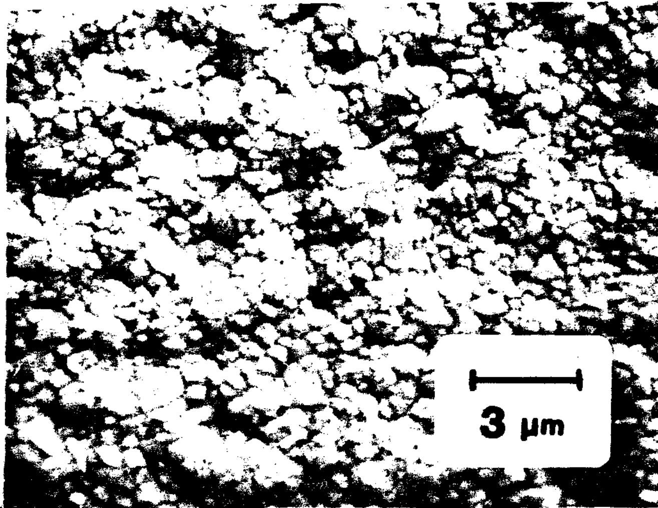

AS DEPOSITED

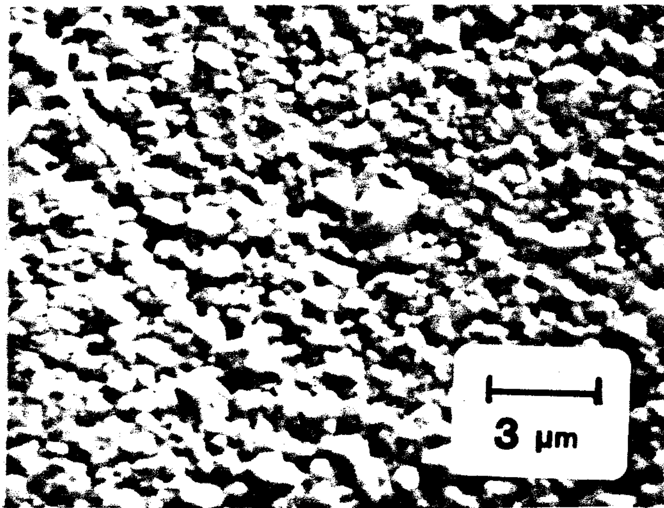

600 °C 80'

Figure 10 SEM micrographs of the Si-Ti-TiN-Ag system before and after a 600°C, 80 min anneal.

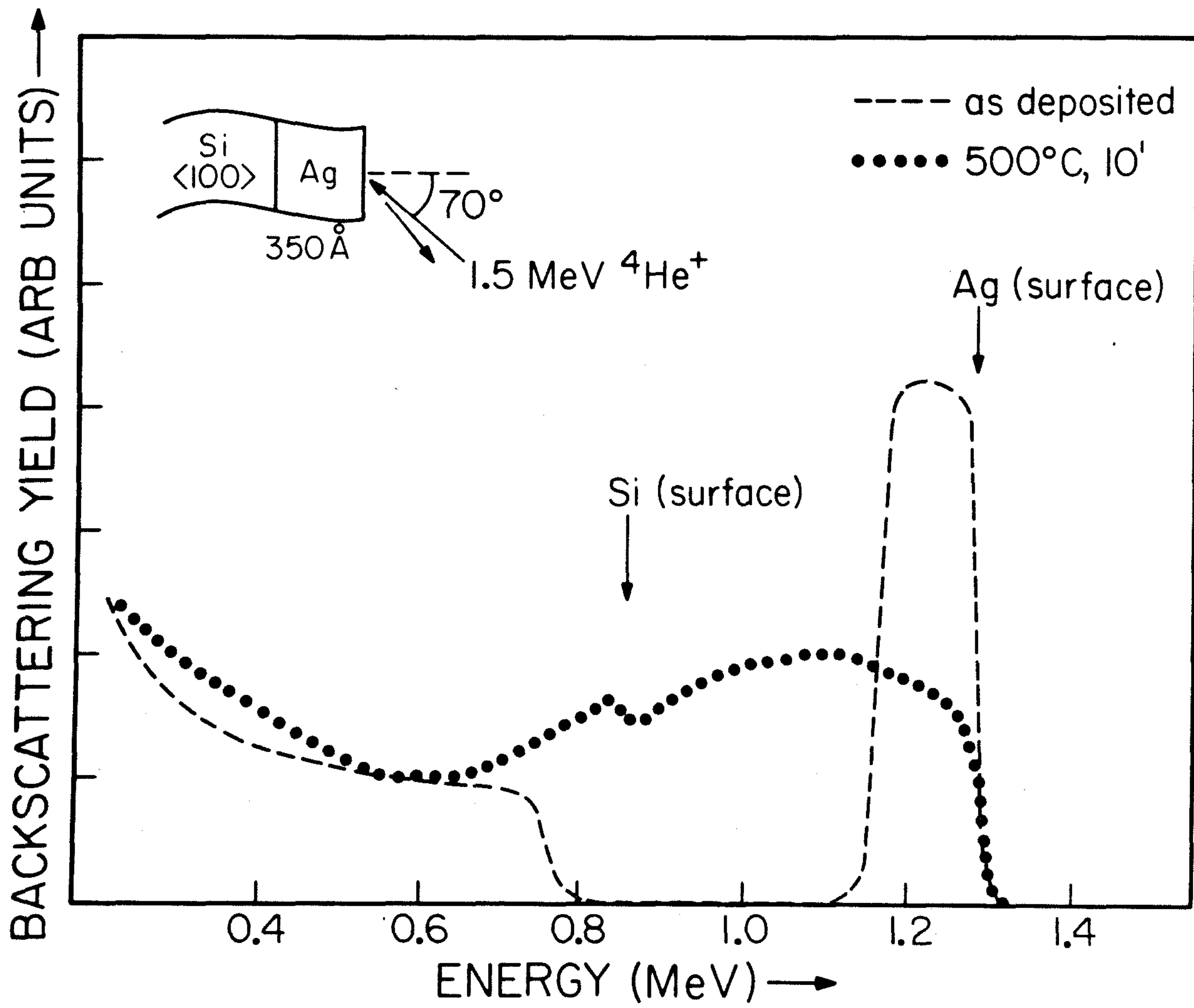

Figure 11 Backscattering spectra of the Si-Ag system. The incident ^{4}He energy is 1.5 MeV.

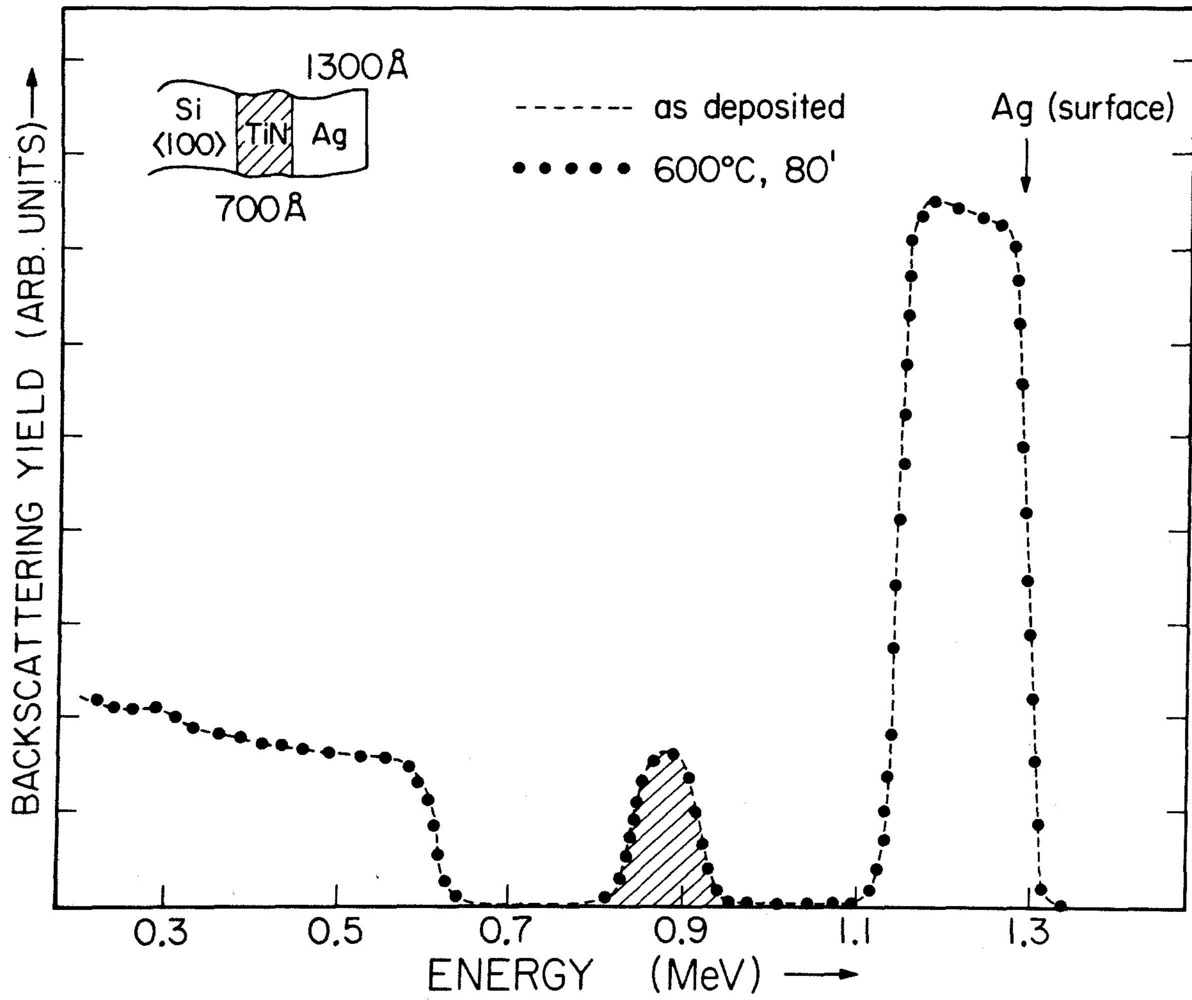

Figure 12 Backscattering spectra of the Si-TiN-Ag system. The incident ^{4}He energy is 1.5 MeV.

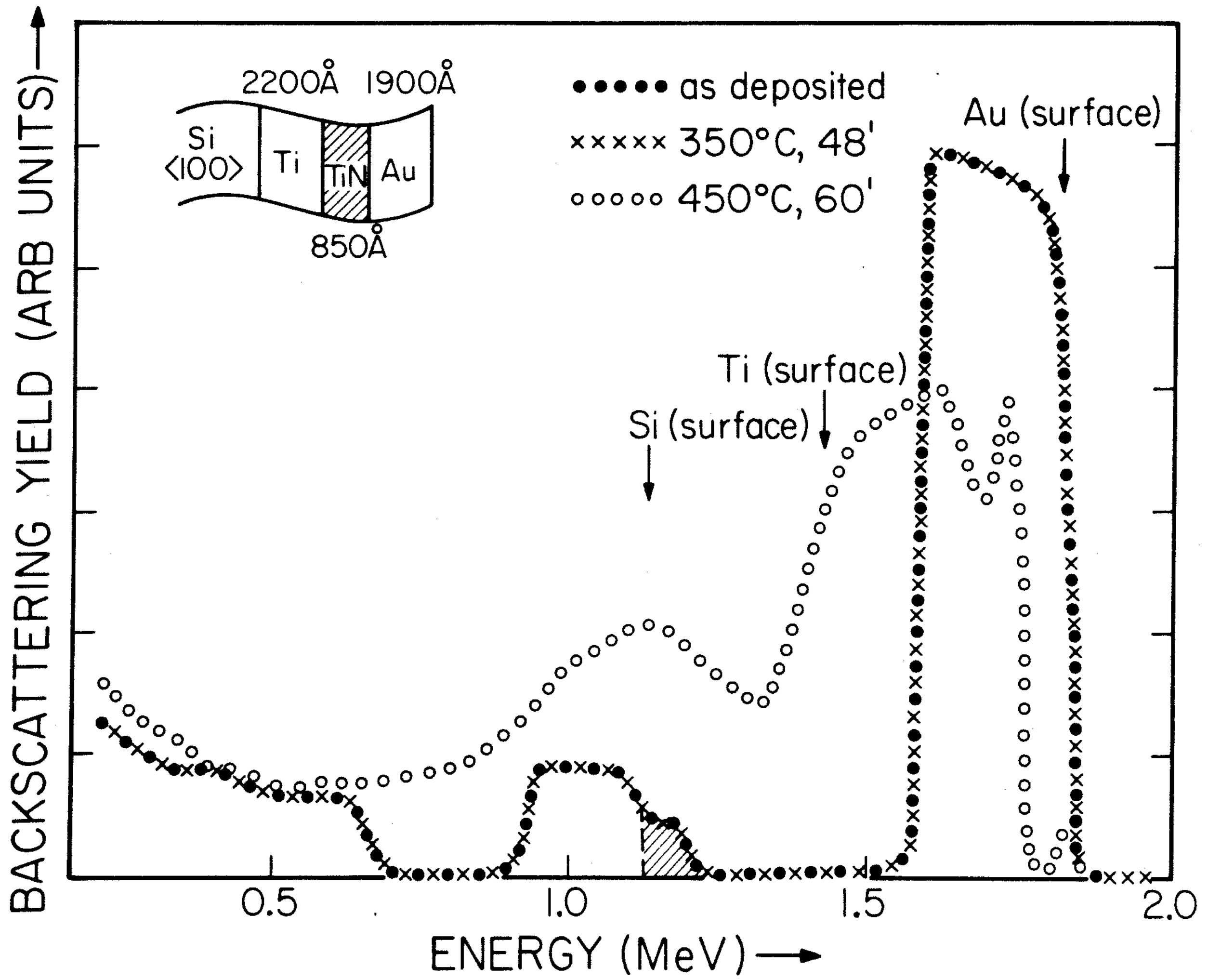

Figure 13 Backscattering spectra of the Si-Ti-TiN-Au system. The incident ^{4}He energy is 2 MeV.

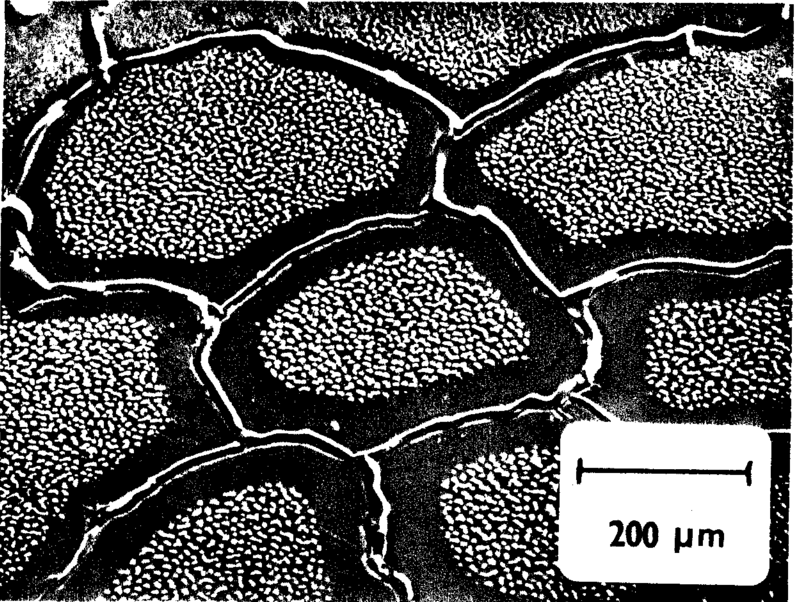

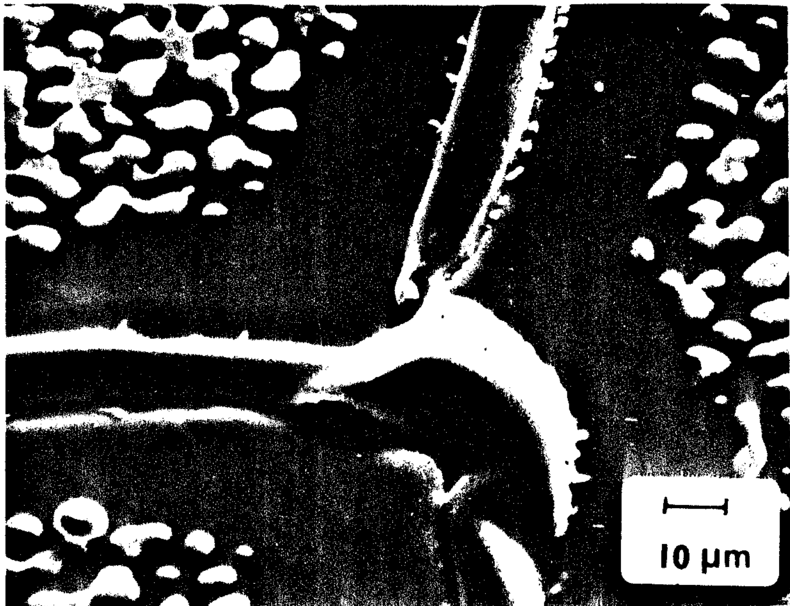

Figure 14 SEM micrographs of the Si-Ti-TiN-Au system after a 400°C, 10 min anneal. Micrograph at the right-hand side is at a higher magnification.

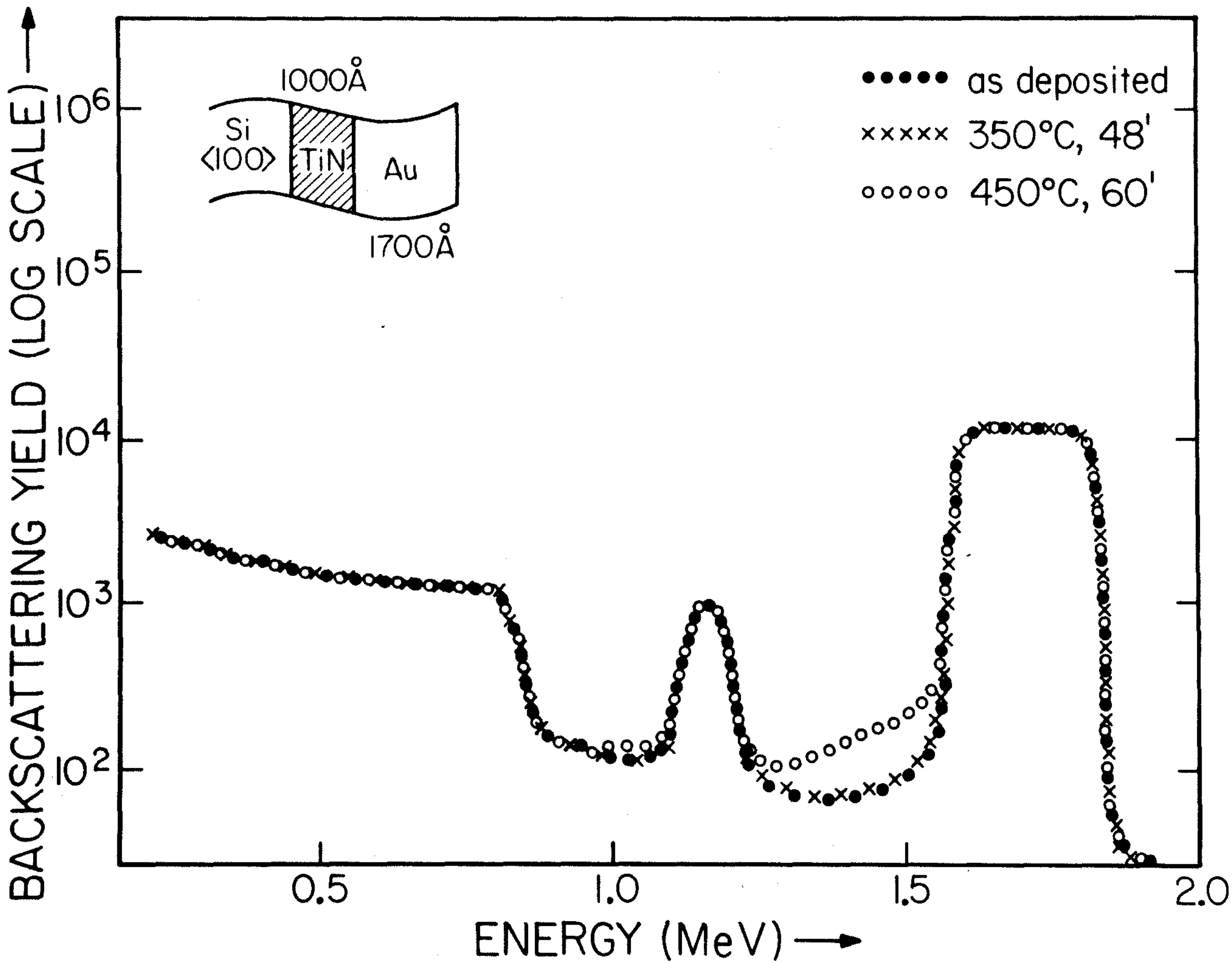

Figure 15 Backscattering spectra of the Si-TiN-Au system. The incident ^{4}He energy is 2 MeV.

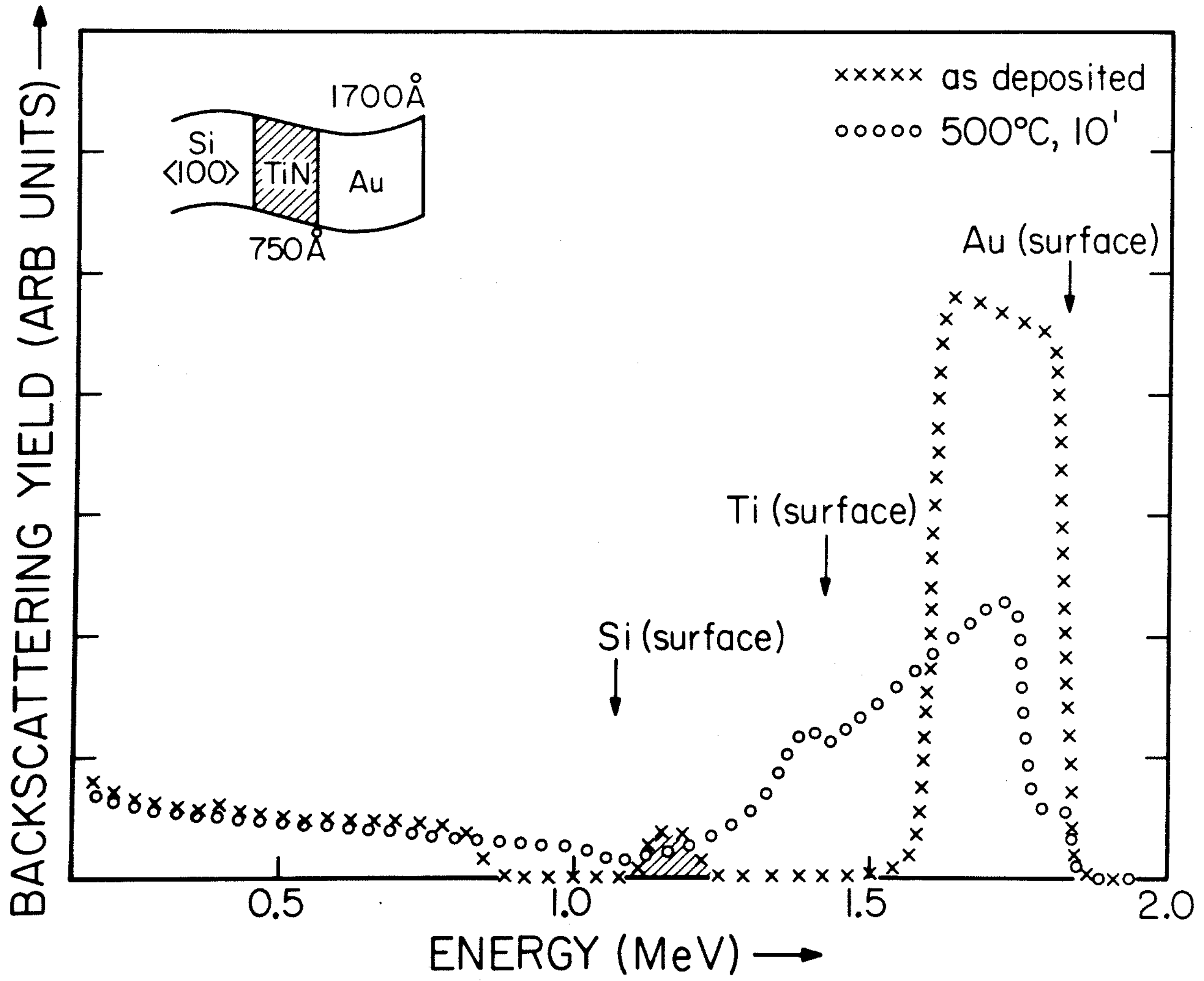

Figure 16 Backscattering spectra of the Si-TiN-Au system, after heat-treatment at 500°C for 10 min. The incident ^{4}He energy is 2 MeV.

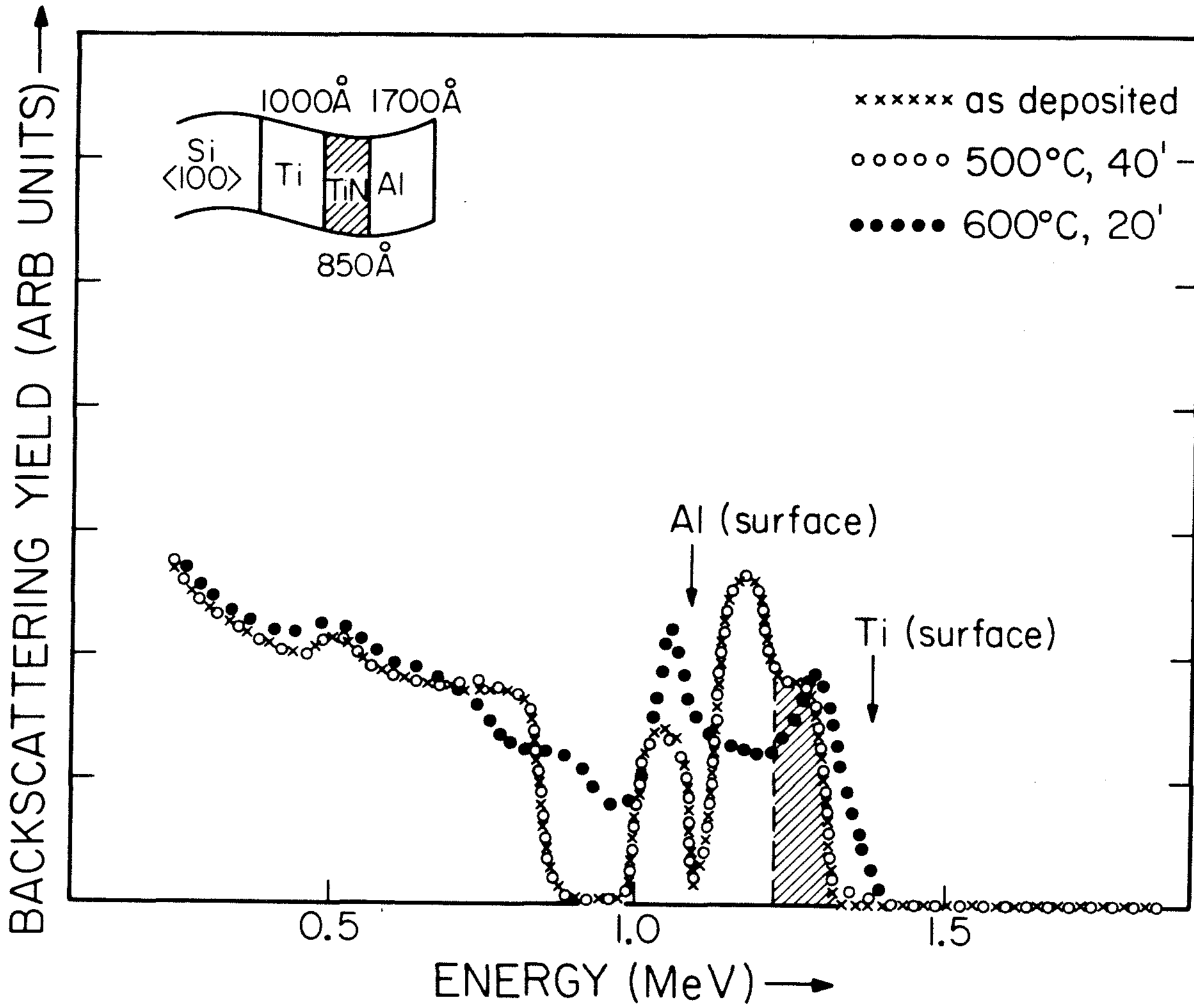

Figure 17 Backscattering spectra of the Si-Ti-TiN-Al system. The incident ^{4}He energy is 2 MeV.

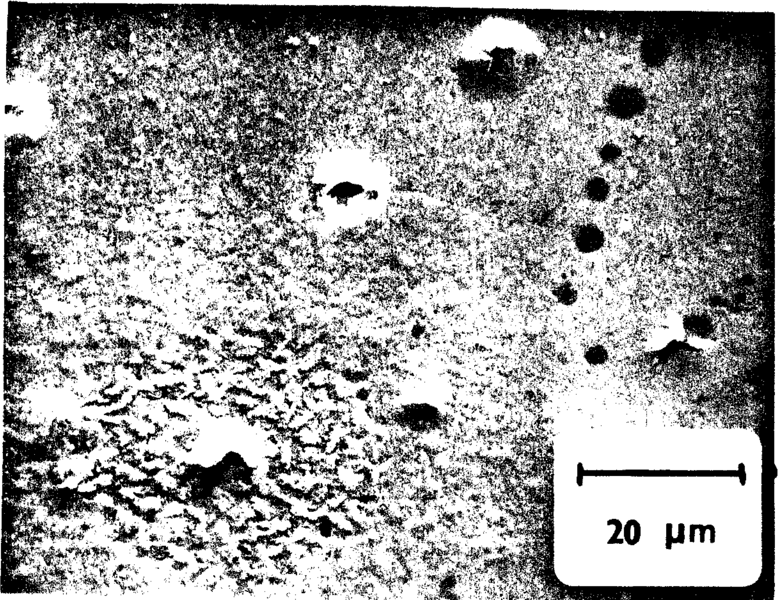

[a]

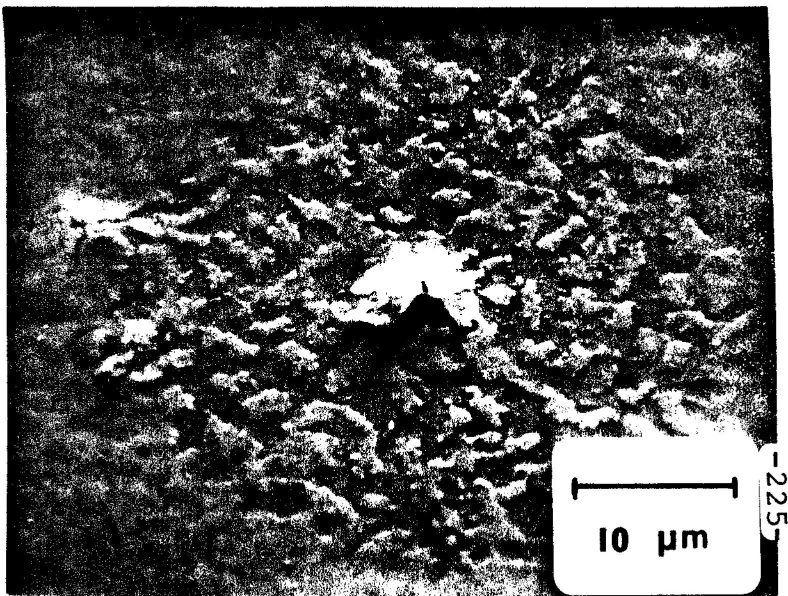

[b]

Figure 18 SEM micrographs of the Si-Ti-TiN-Al system after a 550°C, 10 min anneal. Micrograph (b) shows the "volcano" structure.

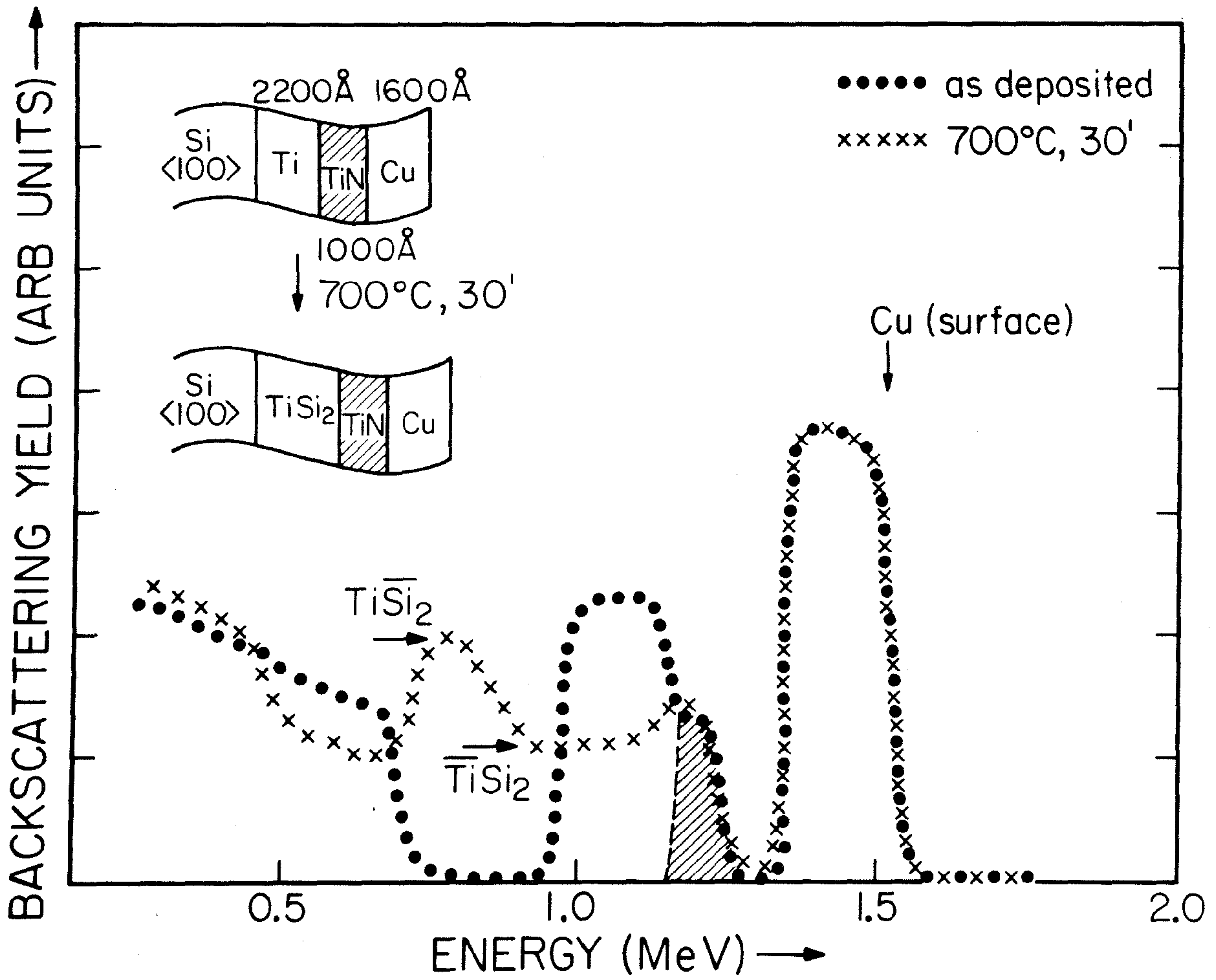

Figure 19 Backscattering spectra of the Si-Ti-TiN-Cu system. The incident ^{4}He energy is 2 MeV.

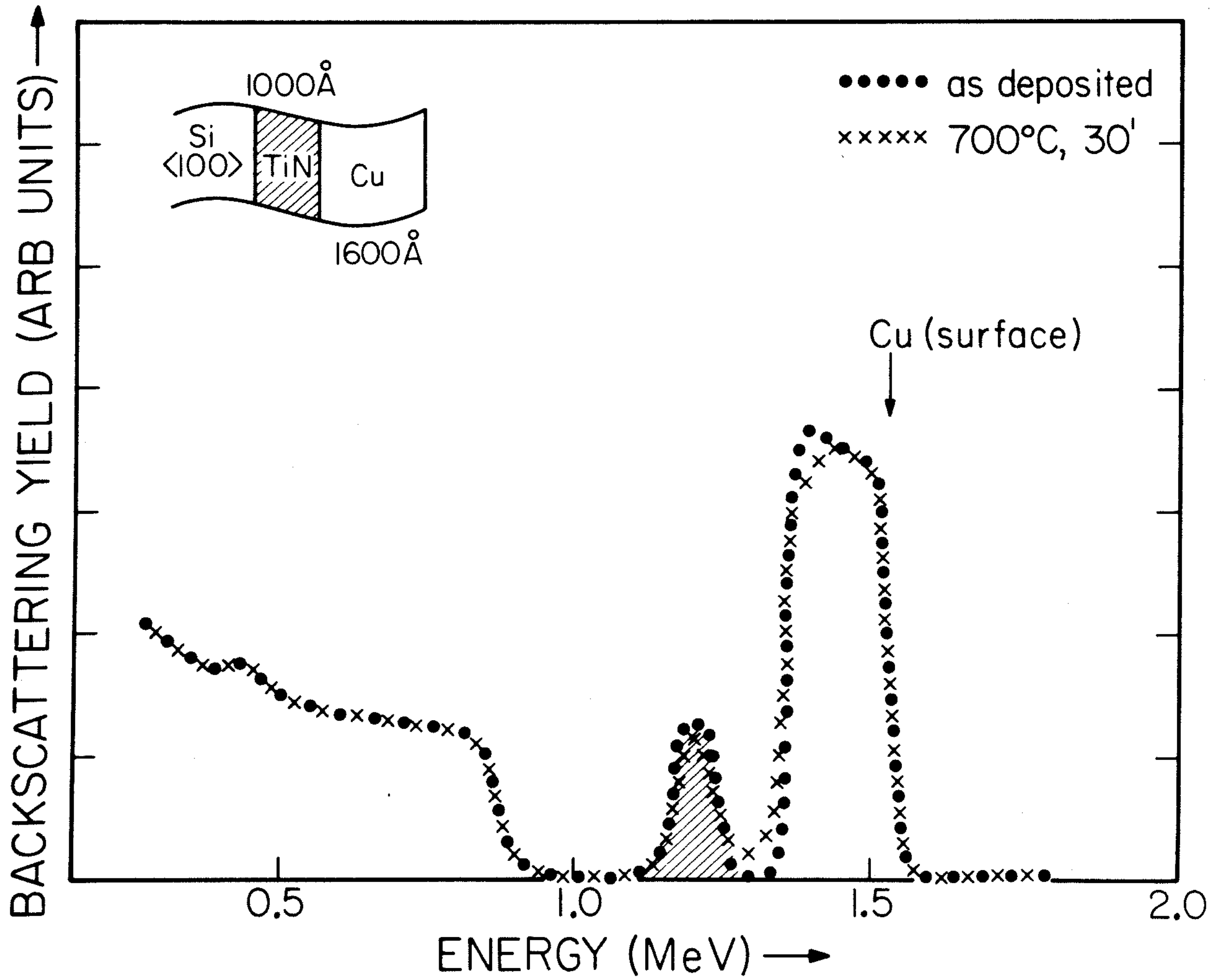

Figure 20 Backscattering spectra of the Si-TiN-Cu system. The incident ^4He energy is 2 MeV.

TABLE 1 Failure Temperatures* of TiN as a Diffusion Barrier for Ti on Si Substrates and Si Substrates.

Metal		Au	Al	Ag	Pd	Cu
Melting Point		1063	660	960	1532	1083
Failure Temperatures with TiN	Ti on Si	370	550	600	>600	>700
	Si	400	550	>600	>600	700
Lowest Metal-Ti Eutectic		830	-	850	735	798
Lowest Metal-Si Eutectic		370	577	830	720	802

*All Temperatures in °C

References

1. J. E. E. Baglin and J. M. Poate, in Thin Films - Interdiffusion and Reactions, edited by J. M. Poate, K. N. Tu and J. W. Mayer (Wiley-Interscience, New York, 1978), p. 305.

2. W. K. Chu, J. W. Mayer and M-A. Nicolet, Backscattering Spectrometry (Academic Press, New York, 1978).

3. J. M. Poate, P. A. Turner, W. J. DeBonte and J. Yahalom, J. Appl. Phys., 46, 4275 (1975).

4. J. M. Harris, Ph.D. Thesis, California Institute of Technology, 1975.

5. A. Hiraki, E. Lugujjo, M-A. Nicolet and J. W. Mayer, Phys. Stat. Sol., A7, 401 (1971).

6. R. W. Bower, Appl. Phys. Lett., 23, 99 (1973).

7. J. K. Howard, R. F. Lever, P. J. Smith and P. S. Ho, J. Vac. Sci. Technol., 13, 68 (1976).

8. T. M. Reith and J. D. Schick, Appl. Phys. Lett., 25, 525 (1974).

9. R. W. Bower, R. E. Scott and D. Sigurd, Solid-State Electronics, 16, 1461 (1973).

CHAPTER 4

APPLICATION OF TITANIUM NITRIDE TO Si SOLAR CELL METALLIZATION SCHEMES

4.1 Introduction

Terrestrial application of the photovoltaic technology demands low-cost and long-term reliable solar cells. Frequently, the failure or degradation of cell performance is caused by the deterioration of electrical contacts near the p-n junction. The Ti-Pd-Ag metallization scheme[1] is presently used by most Si solar cell manufacturers. This system consists of about 1000Å of Ti to provide low contact resistance and tight adherence to the Si and 4μm of Ag to provide good electrical conductivity along the conducting strips. A 1000Å-thick Pd layer is interposed between the two metal layers to prevent the electrochemical reaction between Ti and Ag. Although the Ti-Pd-Ag combination can have satisfactory electrical and mechanical properties after being subjected to a heat and humidity test, it has been reported that the system undergoes structural changes during test exposure[2].

Modern packaging processes for solar cells also require an electrostatic bonding step to encapsulate the cells in glass. During the encapsulation process, the metallization

scheme has to withstand a heat-treatment at 600°C for 10 minutes. At such elevated temperatures interdiffusion takes place at the metal-silicon junction. Consequently, the presence of metallic impurities near the p-n junction can degrade the photovoltaic conversion mechanism by forming recombination centers. In some severe cases, penetration of the metal through the p-n junction can even short out the junction completely. These problems are particularly pertinent to shallow-junction solar cells (∿2000Å) which are often preferred for their high current collection efficiency[3].

In order to solve the contact problem, it seems promising to apply the concept of diffusion barriers[4] to solar cell metallization schemes. The idea is to interpose material "X", the diffusion barrier, between layers A and B so that the undesirable thermal diffusion is suppressed while the electrical and mechanical properties of the A-X-B structure remain unaltered or at least equivalent to the A-B metal combination. An important aspect of the diffusion barrier concept is to free the designer from various metallurgical constraints. Since the choice of metals is generally dictated by metallurgical and processing considerations, the application of an appropriate diffusion barrier may provide more variety to the selection of materials.

In this feasibility study, we have chosen reactively sputtered titanium nitride as the diffusion barrier material. The advantage of the sputtering process is that it is a

well-established technique for large-area coatings. Moreover, pure Ti films can also be prepared in the same sputtering chamber by replacing the sputtering gas with Ar instead of N_2. During the course of this study, it has been found that an interposed layer of Ti (∿1000Å) is often required to enhance the adhesion between various metals and titanium nitride.

4.2 Thermal Instability of the Ti-Pd-Ag System

The thermal degradation of the Ti-Pd-Ag system due to a sintering process at 600°C for 10 min in a flowing nitrogen ambient is illustrated in Fig. 21. The specimen, a n^+-on-p silicon cell, was provided by a solar cell manufacturer (Applied Solar Energy Corporation, City of Industry, California). The junction depth is approximately 2000Å. The front contact is a Ti-Pd-Ag system while the back contact is made of plain silver. After the thermal treatment, both V_{OC} (open circuit voltage), I_{SC} (short circuit current) and the filling factor are observed to be significantly reduced.

In order to understand the I-V characteristic of the solar cell and its relationship to shunt and series resistances, we have shown the simplest equivalent circuit of a solar cell in the operation mode in Fig. 22. The photocurrent is represented by a current generator I_G and is opposite to the forward bias current of the diode, I_D (i.e., the dark current). The total shunt and series resistances across the junction and metallization scheme

are represented by R_{SH} and R_S, respectively. Low R_{SH} values can be caused by surface leakage current along edges of cell, extended crystal defects or metallic bridges across the junction depth. The origin of R_S is from contact resistance to the front and back metal contacts, bulk resistance of the cell base and metallization material, and the sheet resistance of the diffused surface layer. A good Si solar cell should have a R_{SH} value of higher than $10^4 \Omega$ and a R_S value of less than 1Ω for a cell area of 1 cm^2.

In actual cell testing, the load resistor, R_L, is varied from 0 to ∞ while the I-V curve is plotted on an X-Y recorder. From Fig. 22, the I-V relationship is given by the following equations:

$$I \cdot \left(1 + \frac{R_S}{R_{SH}}\right) = I_G - I_D - \left(\frac{V}{R_{SH}}\right) \quad (1)$$

$$I_D = I_O \cdot [\exp\,(q\,V_J/nkT) - 1] \quad (2)$$

$$V_J = V + IR_S \quad (3)$$

where V_J is the voltage across the diode and n is the diode ideality factor. For an ideal p-n junction, the value of n will be 1 (i.e., diffusion current dominated). The value of n will increase to 2 if recombination current becomes significant[5].

When series and shunt resistance effects must be considered, the I-V relationship requires numerical solutions.

However, the effect of R_S and R_{SH} on V_{OC} and I_{SC} can readily be seen from the following arguments. When $R_L = \infty$ (i.e., $I = 0$), V_{OC} is simply the voltage across R_{SH} and will be lowered if R_{SH} decreases. Similarly, when $R_L = 0$ (i.e., $V = 0$), I_{SC} is equal to V_J/R_S and will be lowered if R_S increases. Therefore, by comparing I_{SC} and V_{OC} values before and after various heat-treatments, we can deduce the origin of cell degradation by correlating ΔI_{SC} and ΔV_{OC} to R_S and R_{SH} changes.

In some cases, V_{OC} and I_{SC} are stable after the thermal treatment but the filling factor is decreased. This denotes an increase in the value of n and is probably caused by the presence of more recombination centers within the junction. With the values of R_S and R_{SH} being fixed, the effect of higher n values is to round out the "knee" in the I-V curve.

A qualitative analysis of the I-V characteristics and their dependence on R_S and R_{SH} has been performed by Hovel[6]. By placing various resistors either in series or in parallel with a normal Si cell, a family of I-V curves can be generated using R_S or R_{SH} as the independent parameter. The curves are replotted in Figs. 23(a) and 23(b) and they will be used as a guideline to evaluate the Si solar cells' I-V performance.

To investigate the diffusion properties of the conventional metallization scheme, a multilayered sample was prepared by depositing a Ti-Pd-Ag layer combination on (100) silicon.

Each metal film was prepared by electron beam evaporation. Figure 24 shows backscattering spectra of the system before and after an annealing at 600°C for 5 min in a vacuum furnace (approximately 1×10^{-6} Torr). It is observed that all the titanium has reacted with the palladium and the silver. The diffusion profiles of these metals extend down to the titanium-silicon interface.

These results correlate well with the observed degradation of an actual solar cell after the 600°C thermal treatment (Fig. 21). Since both the I_{SC} and V_{OC} are lowered, the R_{SH} and R_S values are lowered and raised, respectively. The decrease in R_{SH} reflects the fact that the p-n junction can either be contaminated or even short-circuited locally by the presence of metallic elements. The intermixing of Ti-Pd-Ag can lead to an increase in R_S because of the increase in the contact resistance with Si and/or the resistivity of the metal films by forming a ternary alloy.

4.3 TiN as a Diffusion Barrier on Si Solar Cells

The 2 cm x 2 cm n^+-on-p Si solar cells were provided by Applied Solar Energy Corporation with a junction depth of ∿2000Å. The n^+ layer is phosphorus-doped with a concentration of $10^{21}/cm^3$. The p-type substrate (∿10 mil thick) is doped with $10^{16}/cm^3$ of boron and is coated with 4μm of Ag as the back contact. These cells have a typical photoelectric conversion efficiency of 15% when illuminated under air mass zero (AM0) conditions. Prior to TiN deposition, the cells

were cleaned by a dip in an aqueous hydrofluoric acid etch (2% concentration) to remove the native silicon oxide. The metallization pattern on the cells consists of parallel fingers about 1 mm wide and ∿3 mm apart. Mechanical masking procedures were used to define the patterns during TiN deposition and metal evaporation. A sputtering RF power of 1 kilowatt and a nitrogen pressure of 70 mT were used for the reactive sputtering of TiN, with typical deposition rates of ∿100Å per minute. Different TiN thicknesses were obtained by varying the deposition time. The electrical resistivity of the TiN layers was on the order of 500 μΩ-cm. Although lower resistivities can be obtained by higher sputtering powers and lower nitrogen pressures, it has been observed that the adhesion of TiN to Si is satisfactory only at higher nitrogen pressures. Despite the higher bulk resistivity of TiN (approximately a factor of four high than that of evaporated Ti films), the TiN-Ti-Ag system has comparable I-V performance as the Ti-Pd-Ag metallization scheme. This is because R_S is dominated by contact resistances and series resistance <u>along</u> the metallic stripes. With a 4μm-thick and 2-cm long Ag layer as the major electrical conductor, the resistance <u>across</u> the TiN thickness (1000-2000Å) will have negligible contributions to R_S.

The schematic of the metallization layer is shown in Fig. 25. After the TiN layer deposition (500Å to 2000Å in thickness), a thin Ti layer (∿1000Å) was evaporated on top

of the TiN in a separate evaporation chamber followed by a 4μm-thick Ag layer. The Ti layer was used to improve the adhesion between Ag and TiN. To avoid mask registration problems, the Ti and Ag stripes were made only 1/2 mm wide so that they will not overlap with the edges of the TiN layer. A reference sample (i.e., without the TiN layer) was also prepared and tested under identical conditions. Its I-V characteristic curves before and after annealing will be used as a reference to test the effectiveness of the TiN-Ti-Ag metallization scheme.

The purpose of this study is to demonstrate the thermal stability of Si solar cells with TiN as a diffusion barrier. No humidity or thermal cycling test has yet been performed. As an accelerated testing criterion, we have adopted the specifications required by the electrostatic encapsulation process (i.e., 600°C, 10 minutes anneal) because it is of interest to the solar cell industry. However, it should be pointed out that normal processing temperatures for solar cells are between 350°C to 400°C if the advanced packaging technique is not desired.

The 600°C annealing was performed under manufacturing conditions with a flowing nitrogen ambient. No particular attention has been paid to the dryness of the nitrogen gas or the presence of oxygen in the annealing ambient. Prior to the 600°C heat-treatment, all the cells were sintered at 400°C for 10 minutes to minimize contact resistance between

the metallization and Si. This step is essential only for the cells with Ti as the first-contact metal to Si (e.g., Ti-Pd-Ag or Ti-Ag schemes). With TiN as the first-contact metal, good ohmic contact is always assured without any heat-treatment. Nevertheless, for a fair comparison with the Ti-Ag specimen, all the cells were subjected to the same sintering at 400°C before the 600°C anneal.

The I-V curves of the Ti-Ag cell before and after the 600°C anneal are shown in Fig. 26. V_{OC} has dropped from 0.57 volt to 0.14 volt after the heat-treatment. In contrast, I_{SC} has only decreased by $\sim$3%. This implies that the dominant degradation mechanism is caused by a lowering of shunt resistance across the junction. This observation is in good agreement with the diffusion study of Chapter 3 where we have shown the thermal instability of the Si-Ti-Ag system at 600°C (Fig. 8).

The I-V curves of solar cells with the TiN-Ti-Ag metallization scheme are shown in Fig. 27. Thicknesses of the TiN layers are 750Å, 1000Å, 1300Å, and 1700Å on the four different samples. No degradation of V_{OC} can be detected on the samples which indicates that R_{SH} remains constant after the 600°C heat-treatment. However, the filling factor of the I-V curves shows a thickness dependence on the TiN layer and decreases with thinner TiN layers. As discussed previously, this can be caused by recombination current effects at the p-n junction or series resistance

effects as shown in Fig. 23(a) for small increases in R_S.

For the thinner TiN layers (Figs. 27(a) and 27(b)), I_{SC} values are slightly higher after the 600°C anneal. This anomaly is probably due to the unintentional oxidation of the portion of TiN which is not covered by the Ti-Ag stripes. The oxidized TiN, which has low electrical conductivity, becomes translucent to the AM0 illumination. Hence, the active device area of the solar cell is effectively increased and gives higher I_{SC} values. The oxidation properties of TiN thin films have been studied by von Seefeld et al.[7]. They have shown that TiN can be oxidized at 500°C in an oxygen ambient as a Ti-N-O ternary. With higher temperatures (∿600°C), the TiO_2 phase has been identified by X-ray diffraction.

For thicker TiN layers (Figs. 27(c) and 27(d)), no increase in I_{SC} has been observed. This is consistent with the oxidation explanation because the attenuation of light intensity is exponential with the penetration depth. Moreover, a thicker TiN will require a much longer time for complete oxidization.

At a TiN thickness of 1700Å, no change in V_{OC}, I_{SC}, and filling factor can be detected after the 600°C anneal. The data suggest that at least ∿1500Å of TiN is required as a diffusion barrier for the TiN-Ti-Ag metallization scheme.

In conclusion, we have demonstrated the feasibility of using TiN as a high-temperature diffusion barrier material. The TiN-Ti-Ag scheme is chosen because of its simplicity and it should be of interest to test other metallization schemes on solar cells as outlined in Fig.7. In addition, the Si-epitaxial silicide-TiN-metal system should be investigated because the scheme embodies the virtue of both the single-crystal diffusion barrier (i.e., the epitaxial silicide) and the thermodynamically stable diffusion barrier (i.e., TiN).

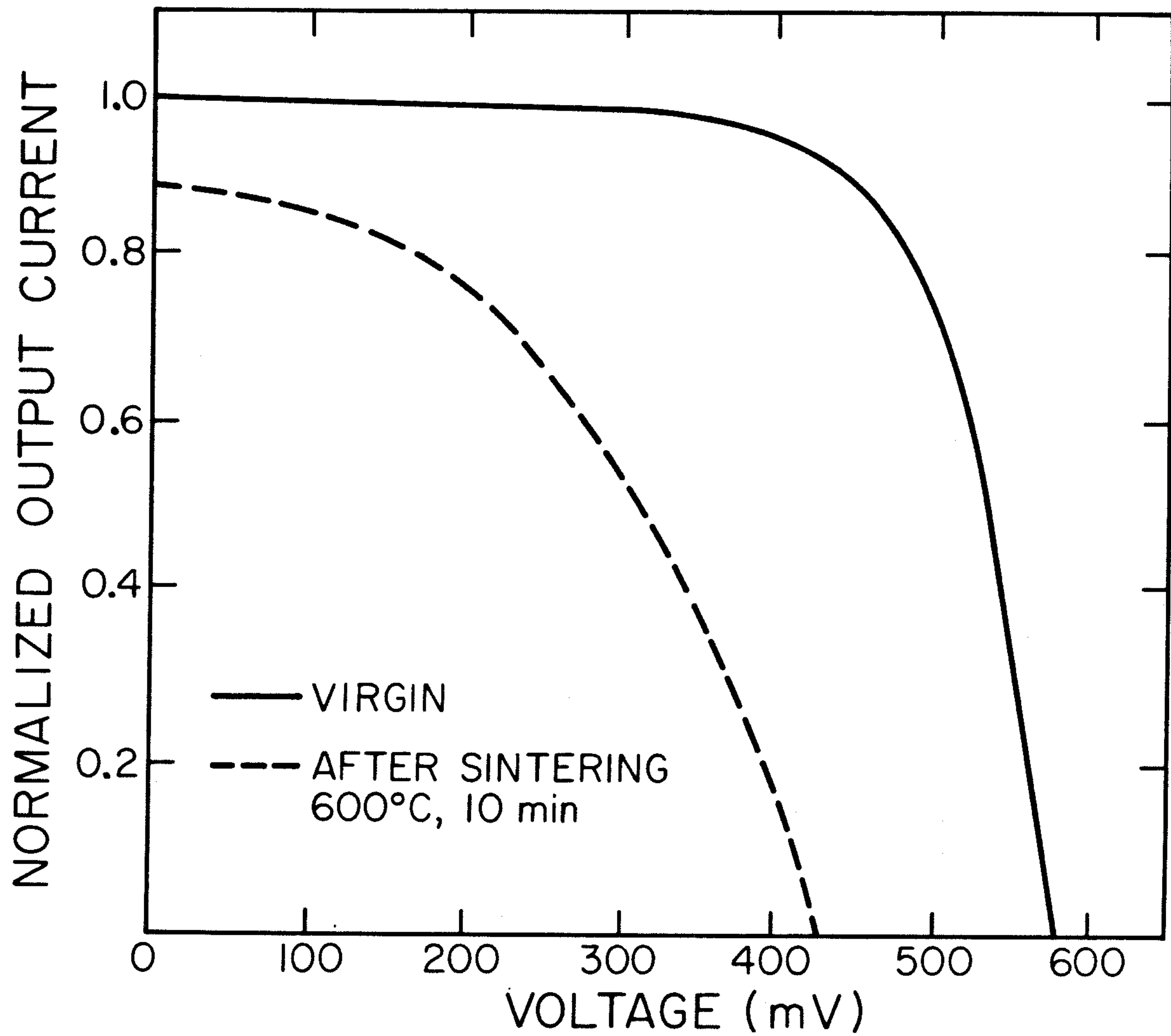

Figure 21 I-V characteristic of a shallow-junction (∿2000Å) Si with the Ti-Pd-Ag metallization scheme under AM0 illumination. The solid line denotes the cell's performance after a 400°C, 10 min anneal. The dashed line shows the degradation after a 600°C, 10 min heat-treatment.

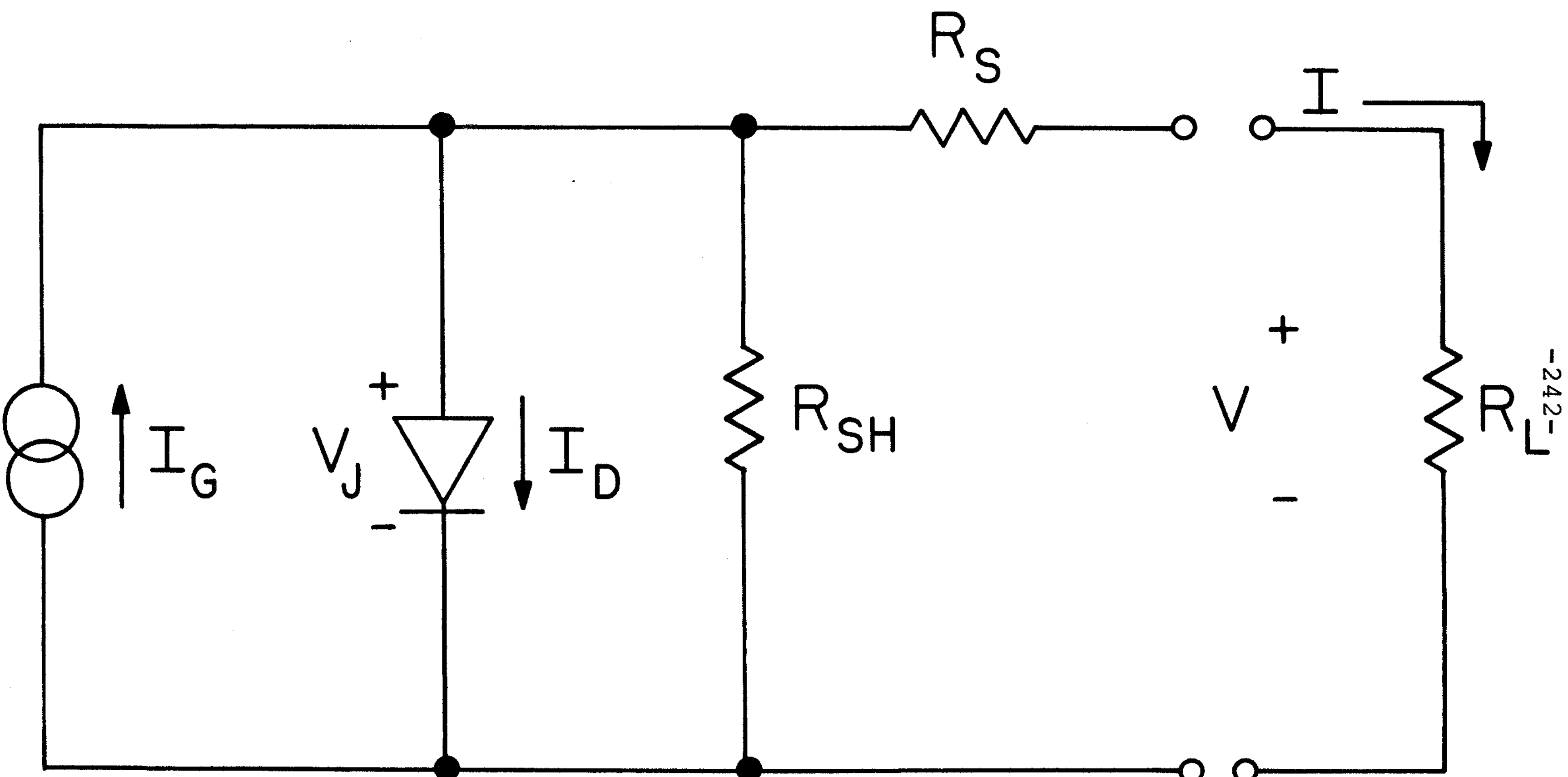

Figure 22 Equivalent-Circuit of a solar cell under illumination.

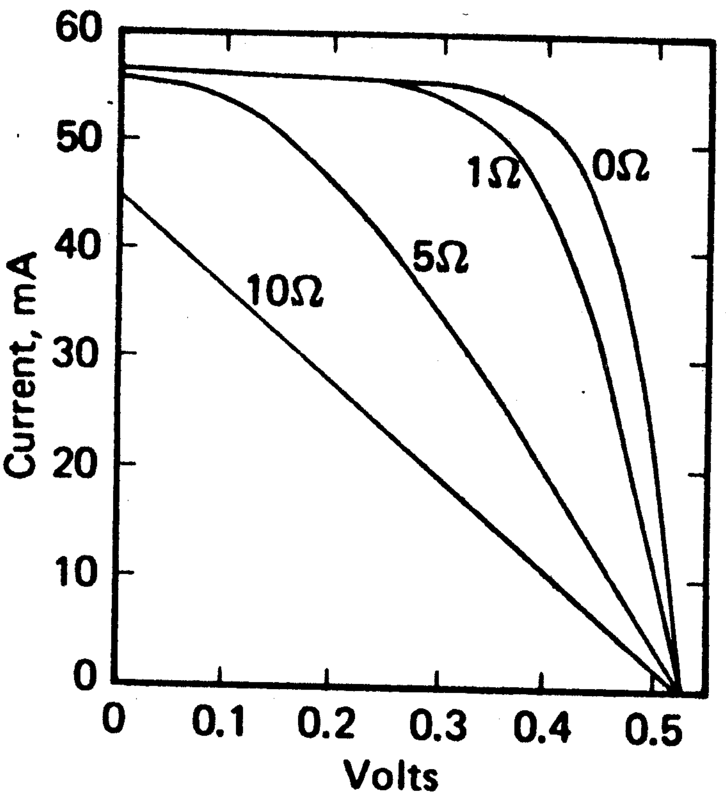

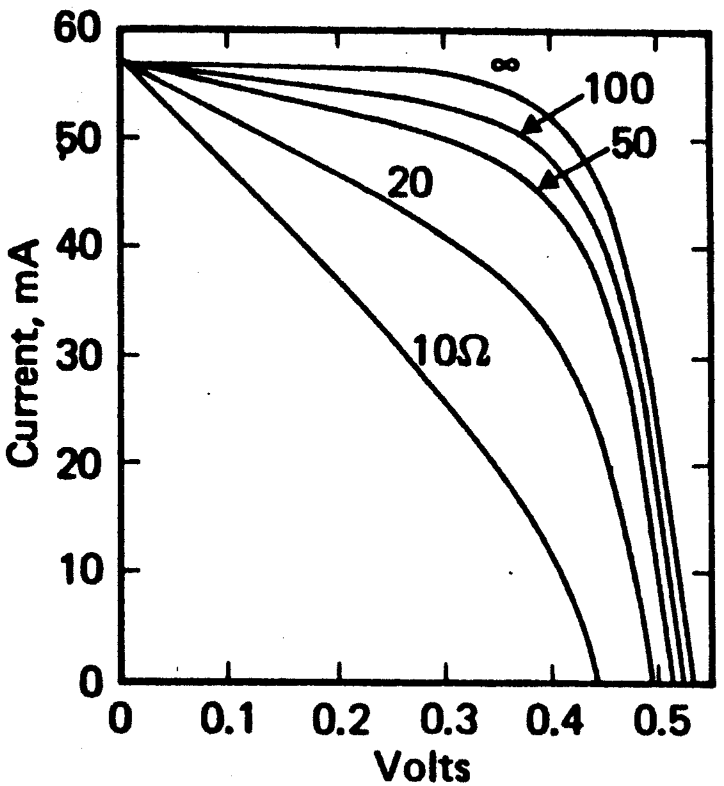

Figure 23 Effects of R_S (a) and R_{SH} (b) on the I-V characteristic of a solar cell [after Hovel [3]].

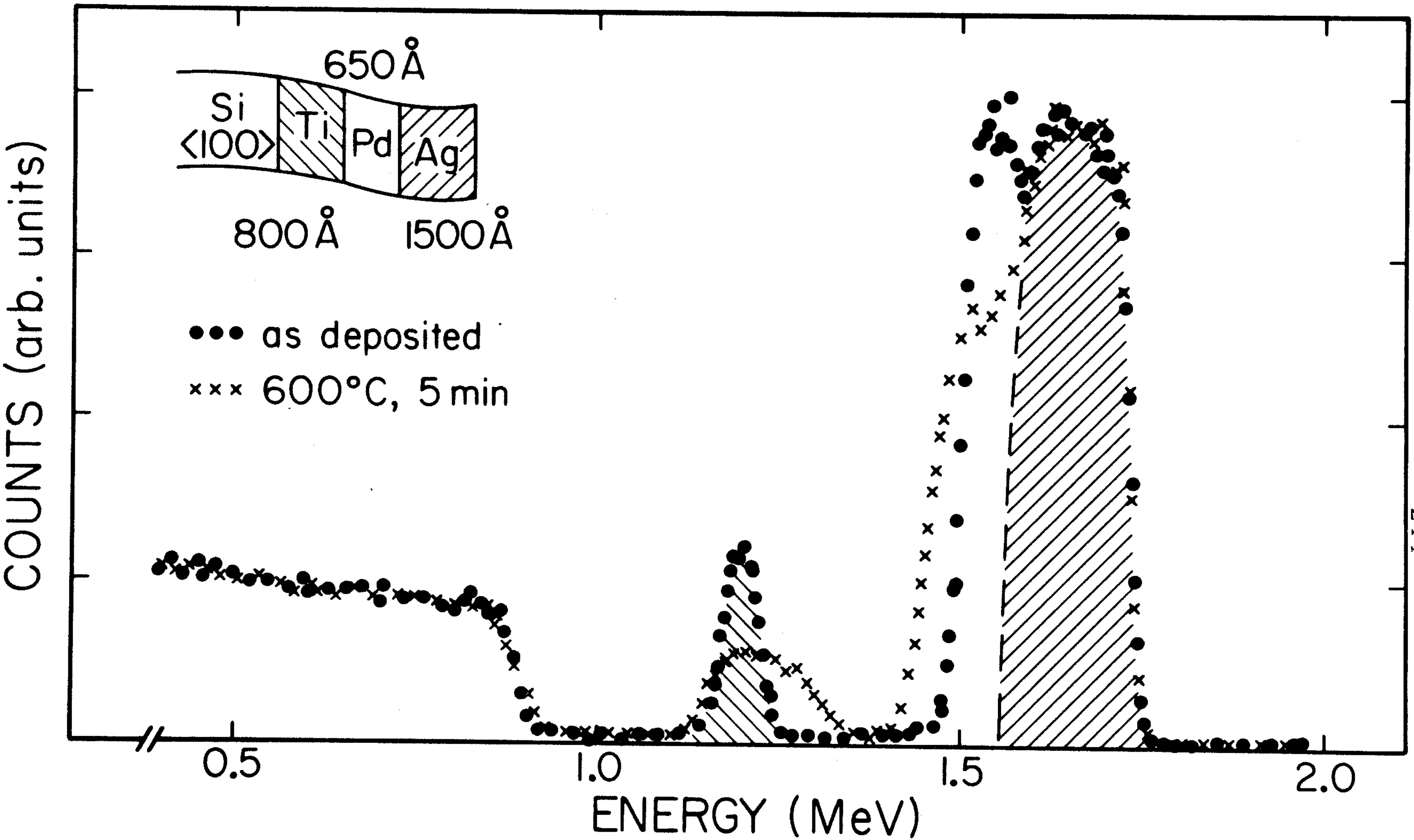

Figure 24 Backscattering spectra of 2 MeV ^{4}He ions obtained from a Ti-Pd-Ag metallization structure, before (•••) and after (xxx) a 600°C, 5 min heat-treatment.

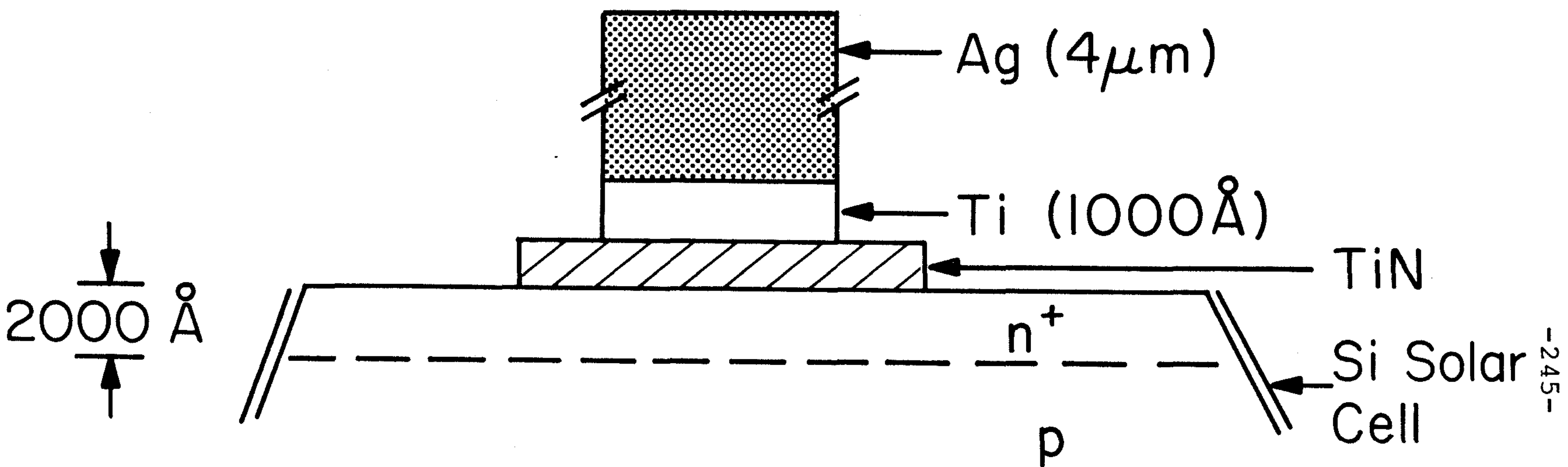

Figure 25 Schematic of the TiN-Ti-Ag metallization system on a Si solar cell.

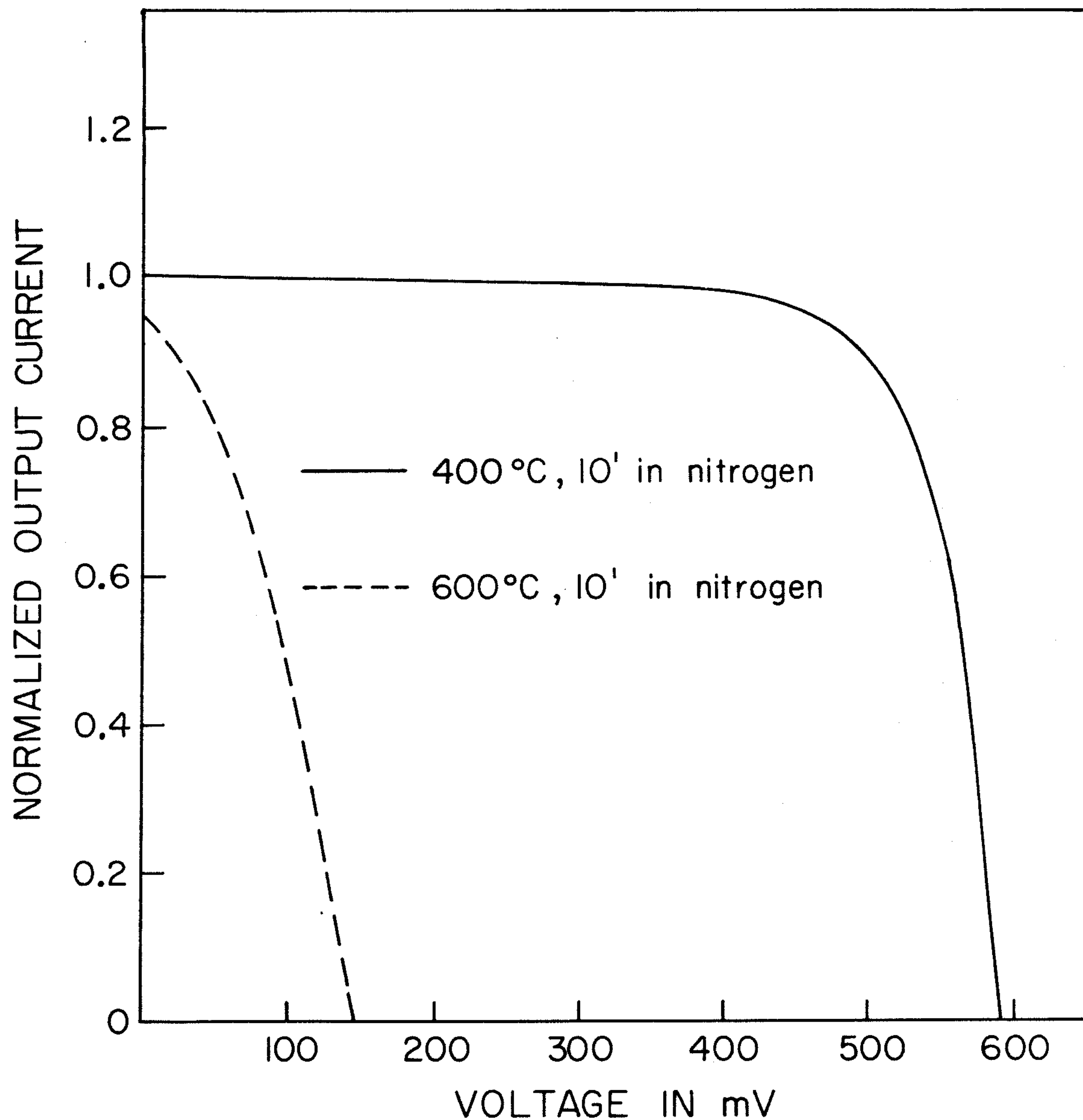

Figure 26 I-V characteristic of a shallow-junction (∿2000Å) Si solar cell with the Ti-Ag metallization scheme before and after a $600^{o}C$, 10 min anneal. The curves are measured with AMO illumination.

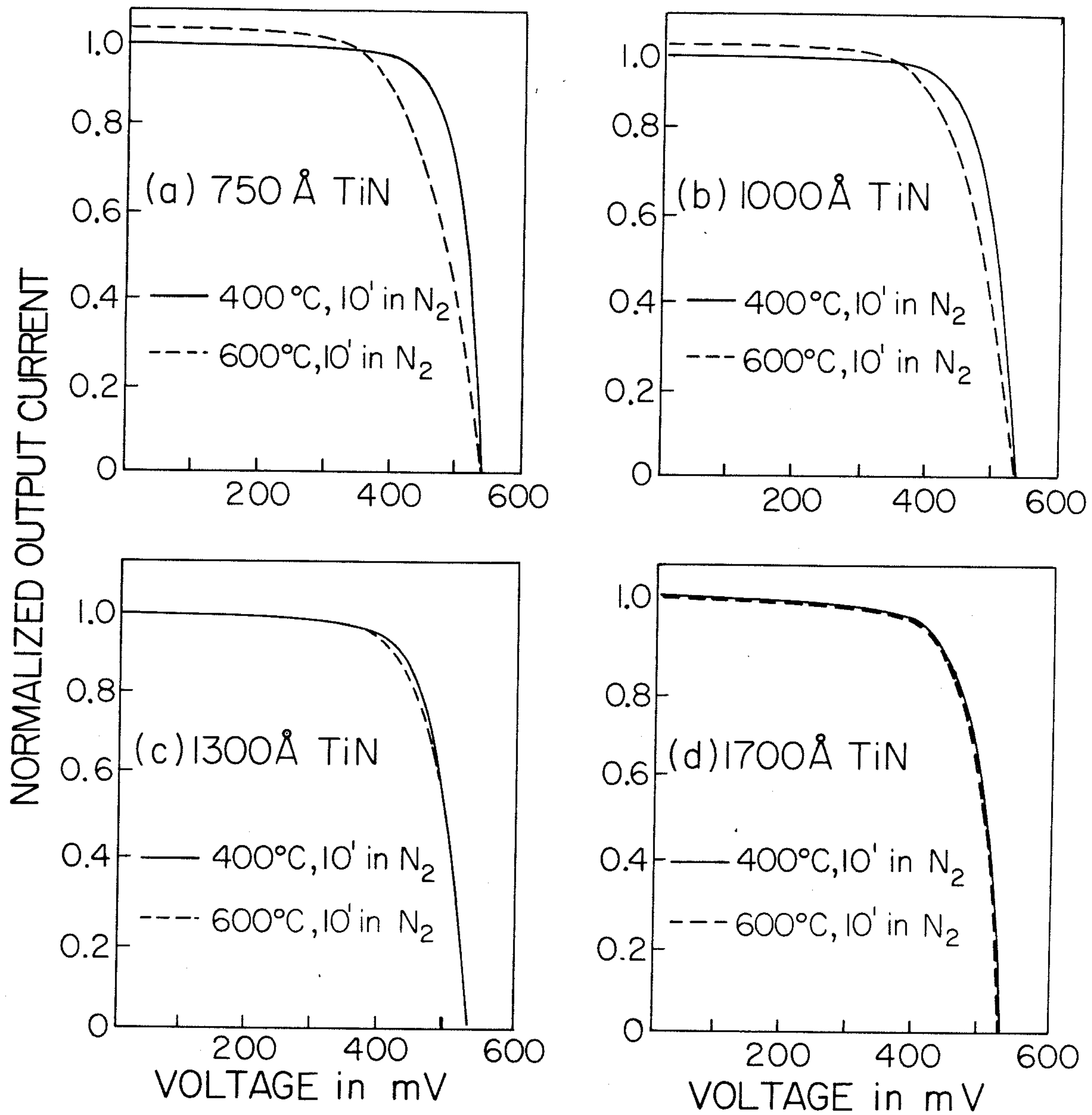

Figure 27 I-V characteristic of shallow-junction (∿2000Å) Si solar cells with TiN-Ti-Ag metallization scheme before and after a 600°C, 10 min anneal. Various TiN thicknesses are used. The curves are measured with AMO illumination.

References

(1) H. Fischer and R. Gereth, IEEE Transactions on Electron Devices, ED-10, 459 (1971).

(2) W. H. Becker and S. R. Pollack, in Proceedings of the 8th IEEE Photovoltaic Specialist Conference, Seattle, Washington (1970), p. 40.

(3) H. J. Hovel, Semiconductors and Semimetals, Vol. II: Solar Cells (Academic Press, New York, 1975), p. 78.

(4) M-A. Nicolet, Thin Solid Films, 52, 415 (1978).

(5) S. M. Sze, Physics of Semiconductor Devices (Wiley-Interscience, New York, 1969), p. 104.

(6) Ref. 3, p. 62.

(7) H. von Seefeld, L. Wielunski and M-A. Nicolet, to be published.